Digital Beamforming for Radio Frequency Interference Suppression in Synthetic Aperture Radar

Zur Erlangung des akademischen Grades eines

DOKTOR-INGENIEURS

von der KIT-Fakultät für
Elektrotechnik und Informationstechnik,
des Karlsruher Instituts für Technologie (KIT)

genehmigte

DISSERTATION

von

M.Sc. Tobias Bollian
geb. in Baden-Baden

Tag der mündlichen Prüfung: 25.10.2019

Hauptreferent: Prof. Dr.-Ing. habil. Alberto Moreira
Korreferent: Prof. Dr.-Ing. Franz J. Meyer

Contents

Zusammenfassung

Fernerkundung mittels Radar mit synthetischer Apertur (SAR) hat sich in ein mächtiges Werkzeug für die regelmäßige Erdbeobachtung von großen Flächen entwickelt, welches unabhängig von den Wetter- und Sonnenlichtbedingungen arbeitet. Jedoch ist Störung der SAR-Aufnahmen durch Radio Frequency Interference (RFI) ein wachsendes Problem. Zudem wird sich die Anzahl der begegneten Störsignale in der Zukunft weiter auf Grund der großen Nachfrage nach drahtlosen Diensten erhöhen. Da die operationelle Frequenz eines SAR-Systems vorgegeben ist durch die physikalischen Eigenschaften welche mit der Fernerkundung bestimmt werden sollen, ist es nicht möglich auf andere Frequenzbänder auszuweichen. Effektive Techniken für eine RFI-Korrektur sind daher maßgebend für den operationellen Erfolg einer SAR-Mission.
In einem konventionellen SAR-System werden bei der RFI-Korrektur auch Anteile des gewünschten SAR-Signals entfernt. Dies kann nur verhindert werden, wenn a-priori Informationen über die Eigenschaften des störenden Signals vorhanden sind. Zudem hängt die Qualität der Korrektur stark von der abgebildeten Szene und der Störung ab.
Eine neue Generation von SAR-Instrumenten setzt auf eine Mehrkanalarchitektur, welche Digital Beamforming (DBF) ermöglicht. Diese Systeme können die empfangenen Signale örtlich filtern und erlauben die Entwicklung von neuen Methoden der RFI-Korrektur. Die Ausleuchtung der Antenne kann nach der Datenaufnahme angepasst werden, um die Aufnahme von Signalen aus der Richtung der RFI-Quelle zu unterbinden. Zudem kann DBF genutzt werden, um das RFI und SAR-Signal aus unterschiedlichen Richtungen separat zu messen. Damit können die Eigenschaften des Störsignals direkt von den Daten bestimmt werden. Diese Arbeit schlägt neuartige RFI-Korrekturverfahren vor, welche auf DBF basieren. Die Methoden nutzen die örtliche Verteilung des SAR-Signals im Range-Doppler-Bereich aus. Diese Verteilung ist veränderlich mit der Zeit und doch vorhersehbar, da die Ankunftszeit des Radarsignals durch die Aufnahmege-

ometrie festgelegt ist. Die vorgeschlagenen, neuen Methoden können in zwei Kategorien aufgeteilt werden. Die erste Methode platziert Nullen in dem Antennenmuster. Die Positionen der Nullen werden innerhalb der SAR-Daten angepasst für eine optimale Unterdrückung der Störsignale. Die Qualität der Filterung wird in dieser Arbeit mit einem speziell hierfür entwickelten Simulator verifiziert. Zudem werden Ergebnisse mit experimentellen Daten eines Flugzeug-SAR präsentiert. Die zweite Methode steuert mehrere, gleichzeitige, digitale Antennenstrahlen in die Richtung der Störsignale um diese zu messen. Auf Grund der gewonnenen Informationen können die Störer von den Daten subtrahiert werden. Zusätzlich können die gemessenen Eigenschaften des Störsignals genutzt werden, um das RFI-Signal für Zeitpunkte zu schätzen, für die eine örtliche Filterung nicht möglich ist. Simulationsergebnisse für diese Methode werden präsentiert.

Abstract

Synthetic Aperture Radar (SAR) has developed into a powerful tool for the frequent Earth observation of large areas, independent of the weather and sunlight conditions. However, the contamination of the acquired SAR data by Radio Frequency Interference (RFI) has become an increasing problem. This observed trend is expected to worsen in the future due to the growing demand for other wireless services. As the SAR center frequency is determined by the physical properties that are to be retrieved, switching frequency bands is not an option. Effective methods to mitigate RFI are therefore critical for the successful operation of a SAR mission.

In a conventional SAR, RFI correction relies on notching methods that also remove parts of the SAR signal. Otherwise, a-priori knowledge about the interfering signal characteristics is required and the filtering performance strongly depends on the observed scene and interference.

New, advanced SAR instruments employ a multi-channel architecture that is capable of Digital Beamforming (DBF). These systems can spatially filter the received signals and give rise to new RFI mitigation techniques. The antenna pattern can be adaptively set after data acquisition to null the angular direction of the impinging RFI signal. Even more, DBF gives the opportunity to individually measure RFI and SAR signals arriving from different directions. This allows to gather information about the interfering signal characteristics from the data. This work proposes novel DBF-based RFI mitigation techniques that utilize the spatial distribution of the SAR signal in the range-Doppler domain. The spatial distribution is variable in time and yet predictable because the arrival time of the radar return is determined by the imaging geometry. The proposed new methods can be divided into two categories. The first new approach adaptively nulls the antenna pattern throughout the SAR data to suppress the RFI signal. A simulator was implemented in the framework of this thesis to verify the performance and a proof-of-

concept with experimental airborne data is presented. The second new approach steers simultaneous digital beams into the direction of the interferers to measure and subtract them from the data. Further, the measured interferer signal characteristics can then be used to estimate the RFI signal for time instances when a spatial filtering is not possible. Simulation results for this approach are presented.

Acronyms and Symbols

List of Constants

c_0	speed of light in vacuum 2.997925 x 10^8 m/s
R_E	mean Earth radius 6371.001 km

Mathematical Notations and Symbols

j	imaginary unit $j = \sqrt{-1}$
a^*	complex conjugate of complex quantity a
a^H	hermitian transpose of complex quantity a
$\in$	element of
$\mathbb{N}$	natural numbers
∂	partial derivative

Acronyms

AM	Amplitude Modulation
AoA	Angle of Arrival
ARM	Autoregressive Model
ARS	Amateur Radio Station
BFSK	Binary Frequency Shift Keying
CW	Continuous Wave
DBF	Digital Beamforming
DDMVDR	Doppler-Dependent Minimum Variance Distortionless Response
DDFMVDR	Doppler-Dependent Frequency Minimum Variance Distortionless Response

EIRP	Equivalent Isotropic Radiated Power
EME	Earth-Moon-Earth
FARS	Frequency Allocations in Remote Sensing
FFT	Fast Fourier Transform
FM	Frequency Modulation
IFFT	Inverse Fast Fourier Transform
INC	Interference-Noise Covariance
IRF	Impulse Response Function
ISLR	Integrated Sidelobe Ratio
ITU	International Telecommunication Union
LCMV	Linearly Constraint Minimum Variance
LMS	Least Mean Square
MEB	Multiple Elevation Beams
MIMO	Multiple Input Multiple Output
MUSIC	Multiple Signal Classification
MVDR	Minimum Variance Distortionless Response
OFDM	Orthogonal Frequency Division Multiplexing
PE	Pulse Extent
PRF	Pulse Repetition Frequency
PSLR	Peak-to-Sidelobe Ratio
PWMVDR	Pulse-Wise Minimum Variance Distortionless Response
RADAR	Radio Detection and Ranging
RDTMVDR	Range-Dependent Time Minimum Variance Distortionless Response
RDFMVDR	Range-Dependent Frequency Minimum Variance Distortionless Response
RFI	Radio Frequency Interference
RLAN	Radio Local Area Network
RNR	RFI-to-Noise Ratio
RSR	RFI-to-Signal Ratio
SAR	Synthetic Aperture Radar

SCORE	Scan On Receive
SFCG	Space Frequency Coordination Group
SL	Symbol Length
SLC	Sidelobe Canceller
SNR	Signal-to-Noise Ratio
SOI	Signal of Interest
SOTR	Space Objects Tracking Radar
SWFMVDR	Segment-Wise Frequency Minimum Variance Distortionless Response
WRC	World Radiocommunication Conference
2DMVDR	Two-Dimensional Minimum Variance Distortionless Response

Lower Case Letters

$\mathbf{a}$	steering vector
a	element phase shift
d	subelement spacing
f_{c}	carrier frequency
f_{D}	Doppler frequency
h_{A}	azimuth chirp
h_{R}	range chirp
k_0	scaling factor
k	time-invariant scaling factor
$\mathbf{k}$	time-variant scaling factor
m	channel number
n	pulse number
p	azimuth sample
r	interferer signal
s	SAR signal
$\mathbf{s}$	signal vector
t	slow time

t_{g} gap duration
u range sample
v number of samples in estimation window
$\mathbf{w}$ beamforming weights
x range domain
$\mathbf{x}$ signal matrix
y cross-range domain
z altitude

Capital Letters

A time-varying amplitude error
A_0 amplitude offset error
B_{W} chirp bandwidth
F number of frequency bins
H platform altitude
H horizontal
H_{a} antenna height
H_{R} range chirp in frequency domain
K number of sources
L_{SA} synthetic aperture length
M number antenna subelements in azimuth
N number antenna subelements in elevation
N_{P} number of integrated pulses
P Capon power spectrum
$\mathbf{R}$ Interference-Noise covariance matrix
$\mathbf{R}_{\mathrm{x}}$ Interference-Noise sample covariance matrix
R slant range distance
R_0 target distance on closest approach
R_1 near range distance
R_2 far range distance
R_{PE} slant range pulse extent

S	range sublook window length
S_{R}	received signal in frequency domain
T_{Int}	integration time
T_{p}	chirp duration
U	range-frequency bin
V	platform velocity
V	vertical

Greek Symbols

δ_{e}	slant range resolution
δp	path delay
$\delta\phi$	phase delay
Δr	range change
γ	interferometric coherence
λ	wavelength
λ_{RFI}	interferer wavelength
ϕ_{a}	azimuth doppler modulation
Φ	time-varying phase error
Φ_0	phase offset error
Ψ	azimuth angle
σ	backscatter coefficient
σ_{a}	amplitude error standard deviation
σ_{n}	power of additive white Gaussian noise process
σ_{Φ}	phase error standard deviation
σ_{s}	power of SAR signal
Θ	angular span of instantaneous SAR signal
Θ_{a}	azimuth beamwidth
Θ_{BW}	elevation beamwidth
Θ_{est}	estimated angular spectrum
θ	elevation angle
θ_{AoA}	estimated angle of arrival

θ_{ASE}	angular signal extent
θ_{d}	angle of arrival of signal of interest
θ_{D}	doppler angle
θ_{l}	look angle
θ_{res}	angular resolution of angular spectrum
θ_{RFI}	interferer signal arrival angle
θ_{t}	antenna tilt angle (in elevation)
τ	fast time

Superscripts and Subscripts

$_{\mathrm{A}}$	azimuth
$_{\mathrm{DBF}}$	denotes a beamformed signal
$_{\mathrm{ext}}$	denotes an extended target
$_{\mathrm{foc}}$	denotes a focused signal
$_{\mathrm{F}}$	filtered
$_{\mathrm{M}}$	main antenna
$_{\mathrm{raw}}$	denotes an unfocused signal
$_{\mathrm{R}}$	receive
$_{\mathrm{RC}}$	range compressed
$_{\mathrm{SOI}}$	signal of interest
$_{\mathrm{T}}$	transmit
$_{\mathrm{ZD}}$	zero Doppler

1. Introduction

1.1. The History of Synthetic Aperture Radar

The dawn of Radio Detection and Ranging (RADAR) is considered to be on December 29th in 1886 when Heinrich Hertz discovered the reflection of electromagnetic waves off metallic plates in Karlsruhe, Germany [1]. However, not realizing the potential of his findings, it took nearly another seventeen years until Christian Hülsmeyer, a German engineer, demonstrated the first radar system for ship detection in 1904. At that time he referred to the radar as Telemobiloskop and failed to attract attention to his invention, mainly due to the lack of suitable amplifiers. Radar was not further developed until the 1930s, when Germany, the United States, Great Britain, France, Italy, the Netherlands, Japan and the Soviet Union started to conduct radar experiments independently of each other and in secret. The first applications were mainly developed for the military and the onset of World War II (WWII) only accelerated radar research. On the morning of December 7th, 1941, before the USA joined WWII, the country's radar unit in Hawaii detected a strong signal return. Not recognizing the importance of the measurements, the radar information was ignored, thereby giving the element of surprise to the Japanese attack on Pearl Harbor.

A turning point for radar was in 1951 when Carl Wiley layed the foundations for Synthetic Aperture Radar (SAR) [2]. Up to this point, the azimuthal radar resolution was determined by the width of the antenna pattern. Thus, the resolution benefited from a long antenna and worsened with range. In contrary, Wiley's discovery utilized the Doppler effect of a moving radar platform to form a synthetic aperture. The resulting resolution was range independent and could be improved by reducing the antenna length. By overcoming the fundamental resolution limits of radars, Wiley provided the stepping stone for spaceborne imaging radars.

Since then, more than 25 civilian spaceborne SAR missions have been launched globally. The missions have evolved from recording images at a resolution of hundreds of meters to a decimeter. They have progressed from providing images of small local patches to

a yearly world coverage, which will be further reduced by the next SAR generation to a new world coverage occuring twice a week. As radars advanced, numerous scientific applications emerged. The collected data are used for example for maritime control, oil spill detection, glacier, land, forest and volcano monitoring, and disaster management after an earthquake. SAR has developed into a powerful Earth observation tool to study the Earth system and its underlying processes.

1.2. Radio Frequency Interference (RFI) in Remote Sensing

Radio Frequency Interferences (RFI) are disturbance signals transmitted by an external source that degrade the system performance. RFI is a global phenomenon, which is continuously growing due to the demand for wireless services and the finite nature of the frequency spectrum [3]. L-band observations of RFI have already been made with the first civilian SAR satellite Seasat [4] over California [5], after it was launched in 1978. Since then, several other remote sensing instruments have reported RFI in their acquired data.

One of these instruments is the L-band mission Aquarius [6, 7]. It is equipped with two instruments: a radiometer at 1.413 GHz and a 5 MHz bandwidth scatterometer centered around 1.26 GHz. The radiometer data over population centers in South America and Africa has been exposed to RFI; interference in the data over Easter Europe and China [8] is especially persistent. No RFI transmissions from the ocean have been detected. The scatterometer, even though its center frequency differs only by 153 MHz, has documented a completely different spatial distribution of the received RFI. The scatterometer is sharing the spectrum with air traffic control and thus data acquired over the mainland of the USA [8] is continuously contaminated. This distribution of RFI around airports is also consistent with observations of the airborne ESTAR radiometer that documented airports as RFI sources [9].

Another instrument is the L-band SAR ALOS PALSAR, which is operating at a center frequency of 1.27 GHz with a bandwidth of up to 28 MHz [10]. Because this instrument is a SAR, the matched filter in the focusing step smears the RFI energy through the image in a haze-like manner [11, 12]. An analysis of this smeared RFI revealed that it caused a radiometric bias of up to 1.3 dB [13] in the data. Multiple observations of

Barrow, Alaska, indicated that the statistics of the RFI itself stayed unchanged over a four year period [11, 12]. This finding suggested that repeated acquisitions might be helpful for the identification and characteriziation of RFI and to help improve the RFI removal from the data. However, an opposite behavior was observed with the SMOS radiometer (1.43 GHz) [14]. The interference measured by this instrument behaved variably in space and time when the years 2010 and 2011 were compared [14]. Though the unwanted signals were stronger over land, RFI was encountered over the ocean, as well. Signals that originated in Spain corrupted the data acquisition of large parts of Northwest Africa. This revealed that, even though the protected band (1.4 GHz - 1.427 GHz are allocated to passive radar only) was a key factor for the system design [14], it was not possible to avoid illegally transmitted signals or unwanted emissions from adjacent bands. The power of the observed RFI covered all ranges: from low power and hard to detect to high power and thus blinding the radiometer [15].
These examples show that RFI is varying locally and temporally because of different frequency regulations in different countries [16]. In addition, the demand for certain services depends on the population density of the area. The spectrum can also be polluted by illegal transmissions or be occupied by military devices. The source of the interference is therefore steadily changing and predictions about the nature of the interfering signals are complicated.
Though RFI is more dominant at lower frequencies [17], such as L-band, it can also occur at higher frequencies. The C-band SIR-C SAR [18], which flew on two Space Shuttle missions in 1994, noticed interference as well. Even at 18.7 GHz, the AMSRE [19] and WINDSAT [20] radiometers experienced a significant increase of RFI from 2006 to 2009 due to the start of a satellite service named DirecTV (18.3 GHz to 18.9 GHz) [21]. This interference was stronger in the winter time because of an increased reflection of the signal off snow [21]. Such a change in the RFI environment can, in the worst case, determine the end of a mission; the European Incoherent Scatter Radar ceased operation in 2009 for this reason [17].
A more recent example of RFI in SAR are ESA's Sentinel-1 [22] satellites launched in 2014 and 2016, which are planned to be acompanied by two additional SAR satellites in the near future, depending on approval of the Earth Explorer mission candidate HARMONY. Sentinel-1 already experienced mutual interference with Radarsat-2 and the Chinese GAOFEN 3 satellite [23], which showed how critical the task of the Space Frequency Coordination Group (SFCG) [24] is to avoid interference between mis-

sions of different space agencies. Also, communication companies are asking to share Sentinel-1's spectrum to meet the demands of the growing Radio Local Area Network (RLAN) market [25]. This is especially troublesome because the affected spectrum had been chosen in the mission's design phase to minimize interference based on the allocations at that time.

Therefore, the Radio Regulations of the International Telecommunication Union (ITU) [16], responsible for the definition of the different services and their operational conditions for each frequency band, has analyzed the impact of a potential RLAN allocation in Sentinel-1's band. Multiple studies have indicated [25] that sharing is not feasible. An extension of the RLAN spectrum in the specific band is therefore not expected, but the decision is still pending as of March 2019. Any modifications of the Radio Regulations can only be made at the World Radiocommunication Conference (WRC), which is an international meeting that takes place every few years [26]. Especially for remote sensing, the Frequency Allocations in Remote Sensing (FARS) technical committee of IEEE Geoscience and Remote Sensing Society was established by scientists and engineers. The committee provides recommendations and input to the WRCs to protect the interest of the remote sensing community [27].

A good example of how remote sensing does not always benefit from frequency allocations is ESA's BIOMASS mission [28]. Even though the BIOMASS has permission to operate in the allocated 432 MHz to 438 MHz band, it is only assigned on a secondary basis. The Space Objects Tracking Radars (SOTR) of the USA are assigned in this frequency band as the primary service [16]. Therefore BIOMASS is not allowed to operate when in line of sight of SOTR because of possible interference to the SOTR [29].

Yet, instruments can not simply switch frequency bands or guarantee RFI-avoidance by receiving a primary frequency allocation. This is because an instrument's operational frequency is not only driven by technology but also by physics. The scattering behavior of the observed physical process dictates the frequencies that can be exploited for remote sensing. For example, forest applications benefit from the higher penetration of electromagnetic waves at lower frequencies. This increases the radar backscatter's sensitivity to high biomass densities [28]. Furthermore, the temporal decorrelation between repeat passes is reduced due to the increased penetration of the signal and the increased signal return from tree branches and trunks, which are stable over time. Missions that depend on P- or L-band have to find ways to coexist with present RFI sources, whereas missions operating at other frequencies need to prepare for a possible contamination in the future.

Recent and future SAR missions at P-band are BIOMASS [28], EcoSAR [30] and AirMOSS [31]. Examples for L-band SAR sensors and missions are DBSAR-1 [32], DBSAR-2 [33], ALOS-2 [34], ALOS-4 [35], NISAR [36], SAOCOM [37] and Tandem-L [38]. RFI poses a major challenge to the scientific operation of these SAR systems. Interference can emerge in the operational mode and bias the measured backscatter, corrupt polarimetric signatures (Fig. 1.1) and decorrelate interferometric SAR data [5, 11]. Further, a degradation of polarimetric and geometric calibration [39] efforts during a mission's commissioning phase occurs if calibrations sites are impacted by RFI. Any resulting errors will affect future measurements even in the absence of interference. The mitigation of RFI is therefore critical to ensure the integrity of derived science products.

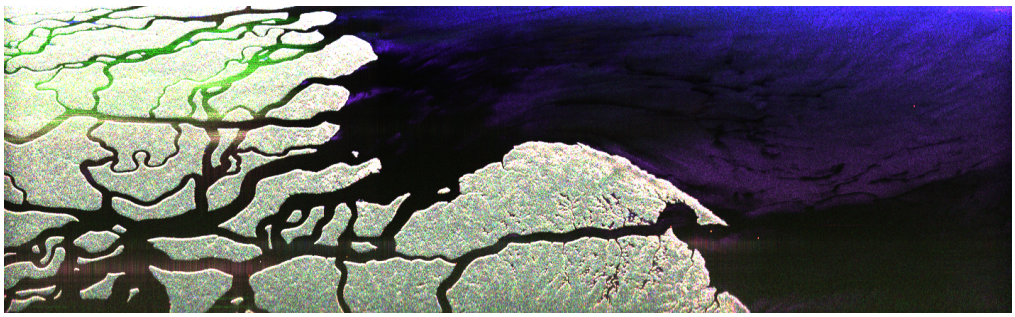

(a)

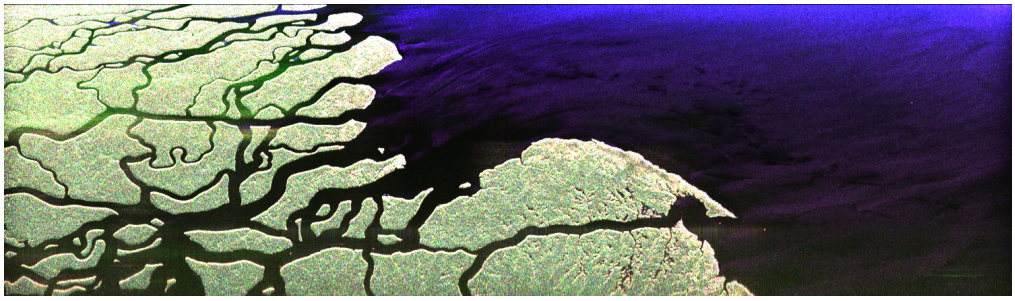

(b)

Fig. 1.1.: Pauli decomposition images of fully polarimetric DBSAR-1 data acquired on September 13, 2011. a) Strong RFI corrupts polarimetric signatures over the river in upper left corner. b) Much weaker RFI smears through image during repeated flight 24 minutes later.

1.3. State-of-the-Art RFI Mitigation

Conventional RFI mitigation techniques can be grouped into three categories [40]: notching methods [11, 41, 42], subtraction methods and filter methods. Notching methods remove samples from the data that are corrupted by RFI. This is done either in the time or frequency domain depending on the nature of the interference. For example, narrowband RFI can easily be notched in the frequency domain (Fig. 1.2a) but is spread in the time domain. The advantage of notching is the fast implementation at a low computational cost. Disadvantages include a Signal-to-Noise Ratio (SNR) drop due to a loss of part of the desired signal, an inevitable distortion of the SAR Impulse Response Function (IRF) and an increase of its sidelobes [41].
The subtraction methods aim at estimating and modelling the RFI based on a-priori information [40, 43, 44]. The estimated interference is then coherently subtracted (Fig. 1.2b) without distorting the SAR signal. However, results depend on how well the assumed model fits the RFI.
Filtering methods often implement adaptive filters as, for example, the Least Mean Square (LMS) filter in [45, 46]. Commonly, a delayed version of the input signal is used as reference RFI signal (Fig. 1.2c) under the assumption that a time delay of few samples decorrelates the wide-band SAR signal, while the narrow-band RFI stays unaffected. A transfer function that minimizes the residual error introduced by RFI can be estimated. Convergence and performance of the filter rely on a careful selection of the filter parameters, which depend on the SAR-to-RFI level.
Another filtering method is spatial filtering by shaping the antenna pattern. Spatial filtering depends on the interferer's location and is independent of statistics of the interfering signal and the SAR-to-RFI ratio. This can be achieved with auxilliary antennas that act as a sidelobe canceller (SLC) [47–49]. The information that is gathered with the auxiliary antennas is coherently subtracted and the antenna pattern is nulled towards the interferer. The SLC has been investigated in the context of SAR in [50–52]. In [53], the phased array of the SAR is used for an interferer with known angle of arrival (AoA) or several auxiliary antennas are used to adapt the antenna pattern for interferer cancellation on a pulse-by-pulse basis. This method is performed at the cost of the additional auxililary antennas or the reduced size of the main antenna.
Regardless of the chosen approach, an RFI mitigation is only possible if the interferer power is not driving the received radar signal into saturation.

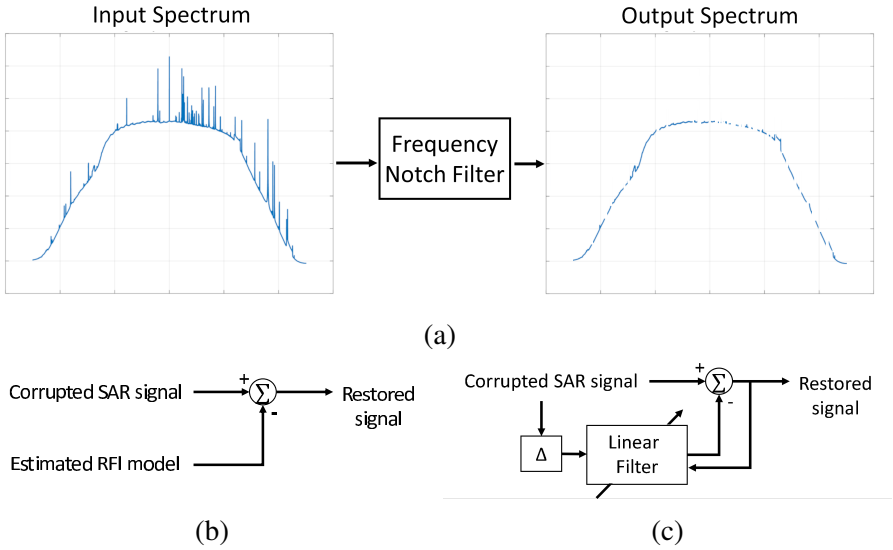

Fig. 1.2.: Conventional RFI mitigation techniques: a) Notch filter applied in the frequency domain. Samples corrupted by narrowband RFI are replaced with zeros. b) Subtraction techniques model the interference signal based on a-priori knowledge and subtract the estimate coherently. c) A Least Mean Square filter with the delayed signal input as reference signal. The transfer function of the linear filter is iteratively adapted to minimize the signal error.

1.4. Motivation and Scope of Work

The next generation of SAR systems incorporates a multichannel architecture that opens up new opportunities for the mitigation of RFI. The individual recording of multiple subelements of an antenna array allows for digital beamforming (DBF) [54], a technique that is used to synthesize antenna patterns post-data acquisition [55]. Therefore, the interferer Angle-of-Arrival (AoA) and thus the optimal antenna pattern to spatially filter RFI can be estimated from the data. In addition, all possible antenna patterns can be synthesized simultaneously, which eliminates the need for separate auxiliary antennas.
The objective of this thesis is to analyze how the DBF capability can be used to separately measure the RFI, which is then removed from the contaminated SAR data. Since digital antenna arrays allow to form an individual antenna pattern on a sample-by-sample basis, it is desirable to select the beamforming weights adaptively throughout the data. This is especially important because the SAR data might not only be contaminated with RFI but also by range-varying ambiguities. Thus, for an

arbitrary two-dimensional array, an optimal RFI suppression algorithm minimizes the combined energy of interference and ambiguities locally within each pulse. This work will investigate how this is possible by utilizing the spatial distribution of the SAR signal, which is inherent to its imaging geometry. In elevation, the AoA of the instantaneous echo signal sweeps within the receive window [56] and therefore allows for an improved detection of interferences. In the same manner as the Scan-on-Receive (SCORE) technique [56, 57] is commonly used in DBF SAR to steer the main beam within the receive window, the antenna pattern for RFI mitigation can be adaptively set for each range line. In azimuth, the AoA depends on the Doppler frequency and thus enables a nulling in along-track after a transformation into the range-Doppler domain. Depending on the size of the two-dimensional antenna array, one or both dimensions can be used.

The work is structured as follows: a summary of SAR and its theoretical background, as well as SAR performance parameters, are given in Chapter 2. This is followed by a brief introduction to DBF, its current applications in SAR and a discussion of the idea of RFI mitigation using DBF. An overview of current and future DBF SAR missions is provided. Then, expected interference sources and their characteristics at P- and L-band are listed. The simulation model that is used throughout this thesis is presented for the SAR and the RFI signal. In the end, an error model for the performance evaluation is introduced and simulation results of the impact on the SAR imaging quality are presented.

Chapter 3 addresses the adaptive antenna pattern notching with DBF for RFI mitigation and proposes novel methods that utilizes the spatial distribution of the SAR signal in the range-Doppler domain. Several new algorithms with varying computational load are presented for DBF SAR systems with multiple channels in elevation, in azimuth and in both dimensions. The effectiveness of these new algorithms is assessed for different interference scenarios and system parameters for DBF are varied to analyze the benefit of larger antenna arrays.

Next, Chapter 4 is providing an RFI analysis of experimental airborne SAR data. Two new RFI detection methods are proposed and their performance is evaluated. A verification of the novel mitigation algorithms for DBF in range from the previous chapter is performed. The improvement of the image quality is assessed by means of the interferometric coherence of a single-pass interferogram. In addition, the interference in the SAR data is geolocated by analyzing the change of the interferer's angle of arrival over time.

The mitigation approaches developed so far rely on the availability of the individual channel data. In a spaceborne scenario this requires an on-board processing or down-linking of all channels, which is not possible. These drawbacks can be overcome with the new approach proposed in Chapter 5, which utilizes digital auxiliary beams that can be simultaneously formed with DBF. The goal of this novel method is to extract information about the interfering signal with these additional simultaneous beams. A downlinking of the digital auxiliary beams is feasible because of the reduced data rate compared to transmitting all channels and thus the beams can be used to remove the RFI during post-processing on the ground. In addition, this chapter investigates how these novel digital auxiliary beams can be used in a scan-on-receive system to remove RFI even for time instances when the interference is non-orthogonal to the SAR signal (and can not be filtered).

Chapter 6 ends this thesis with a summary of the findings of this work. A conclusion of the benefits of DBF for RFI mitigation is drawn and an outlook for the future is given.

2. Theoretical Background

2.1. Chapter Overview

This chapter presents the theoretical background needed for the understanding of this work. A basic overview of SAR is given in Section 2.2 along with a presentation of performance parameters used for evaluation of the image quality. This is followed by an introduction to DBF in Section 2.3. Existing DBF techniques for SAR and the idea behind the research of this work are both expressed in this section. DBF SAR systems that benefit of this thesis are listed in Section 2.3.4. Next, the frequency allocations at P- and L-band for current and future SAR missions are discussed in Section 2.4. A summary of the characteristics of amateur radio stations is provided. Section 2.5 introduces a simulation model for the SAR and RFI signal. Then, an error model (Section 2.5.3) is presented to compare the performance of the RFI mitigation techniques presented in this thesis.

2.2. Synthetic Aperture Radar (SAR)

2.2.1. Principles of SAR

This section gives a brief summary of the basic principles of SAR based on [58–61]. A SAR is a radar on a moving platform with the imaging geometry depicted in Fig. 2.1. The radar is located at a height of $\mathrm{z} = H$ and is capable of transmitting linear frequency modulated radar pulses that can be described by

$$h_{\mathrm{R}}(\tau) = e^{j\pi \frac{B_{\mathrm{W}}}{T_{\mathrm{p}}} \left(\tau - \frac{T_{\mathrm{p}}}{2}\right)^2} \cdot \mathrm{rect}\left[\frac{\tau - T_{\mathrm{p}}/2}{T_{\mathrm{p}}}\right], \tag{2.1}$$

where B_{W} is the chirp bandwidth and T_{p} the chirp duration. The rect-function limits the chirp duration to the fast-time interval $0 \leq \tau \leq T_{\mathrm{p}}$.
While the radar is transmitting these pulses with a pulse repition frequency PRF, it is

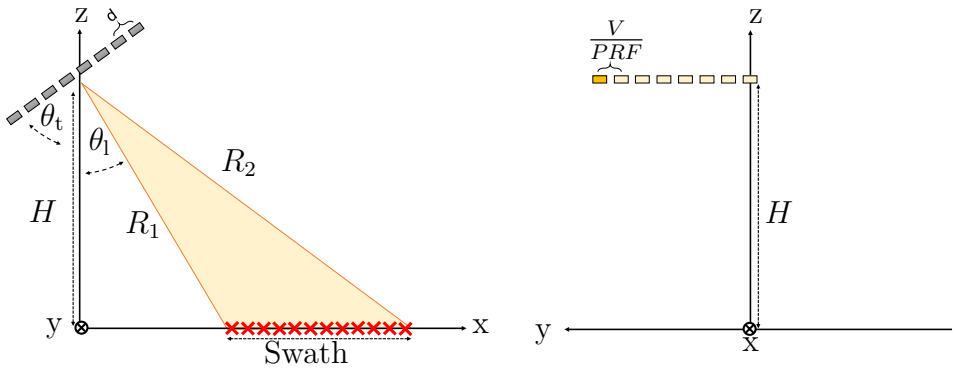

Fig. 2.1.: Cross-section of simulated radar geometry. An antenna array (gray boxes) with element spacing d is located at height H and tilted by θ_t. The illuminated swath is ranging from slant-range values R_1 to R_2. The platform is moving in positive y-direction with velocity V and transmits radar pulses at $t = nPRF$ $(n \in \mathbb{N})$. PRF is the pulse repetition frequency. The yellow boxes represent the current and previous transmit positions.

moving in the y-direction. The slow-time t represents the time of the platform movement in this direction, which is often refered to as azimuth direction. Consequently, each pulse is transmitted at $t = nPRF$ $(n \in \mathbb{N})$. The pulse sequence transmitted at carrier frequency f_c is given by

$$s_T(\tau, t) = h_R(\tau) \cdot e^{j2\pi f_c(t+\tau)}. \tag{2.2}$$

Because of the relative movement between the radar platform and the targets on ground, the range distance R to a target is changing in slow-time according to

$$R(t, R_0) = \sqrt{R_0^2 + V^2 t^2} \approx R_0 + \frac{V^2 t^2}{2R_0} \tag{2.3}$$

with the platform velocity V and the range distance R_0 to the target at the closest approach.

Each transmitted pulse travels to an arbitrary target on the ground and back to the radar. The time span between transmission of the pulse and receipt of the radar return is called round-trip time. Since the chirp signal begins to transmit at $\tau = 0$, the wavefront of the returned signal within each receive window $t = nPRF$ arrives at the receive antenna at

$$\tau = \frac{2R(t, R_0)}{c_0}. \tag{2.4}$$

In addition, a phase modulation $\phi_{\mathrm{a}}(t, R_0)$ in azimuth is introduced by the time-varying $R(t, R_0)$ and described by

$$h_{\mathrm{A}}(t, R_0) = e^{j\phi_{\mathrm{A}}(t,R_0)} \tag{2.5}$$

with

$$\phi_{\mathrm{A}}(t, R_0) = -\frac{4\pi}{\lambda} R(t, R_0). \tag{2.6}$$

With Eq. (2.3) and Eq. (2.6), it can be shown that, for small squint angles, this phase modulation yields a linear Doppler frequency shift of

$$f_{\mathrm{D}}(t) = \frac{1}{2\pi}\frac{\partial}{\partial t}\phi_{\mathrm{A}}(t, R_0) \approx -\frac{1}{2\pi}\frac{\partial}{\partial t}\frac{4\pi}{\lambda}\left(R_0 + \frac{V^2 t^2}{2R_0}\right) = -\frac{2V^2 t}{\lambda R_0}, \tag{2.7}$$

which thus results in a linear frequency modulation in the azimuth direction.
Therefore, the received SAR signal of an ideal point target with backscatter coefficient σ can be described with a shift of Eq. (2.2) by the round-trip time and by accounting for the azimuth modulation (Eq. (2.6)):

$$s_{\mathrm{R}}(\tau, t, R_0) = \sigma \cdot h_{\mathrm{R}}\left(\tau - \frac{2R(t, R_0)}{\mathrm{c}_0}\right) \cdot h_{\mathrm{A}}(t, R_0). \tag{2.8}$$

2.2.2. Signal Processing

An image can be formed from the received data, by realizing that the target return is composed of the two separate linear chirps $h_{\mathrm{R}}(\tau)$ and $h_{\mathrm{A}}(t, R_0)$. Then, a matched filter can be used to compress each chirp [58–61]. This procedure can be applied most efficiently in the frequency domain using Fast Fourier Transforms (FFTs). The range compression in the frequency domain is performed with

$$S_{\mathrm{RC}}(f) = S_{\mathrm{R}}(f) H^*_{\mathrm{R}}(f). \tag{2.9}$$

Note that $S_{\mathrm{RC}}(f)$ is the range-compressed signal in the frequency domain. $S_{\mathrm{R}}(f)$ and $H_{\mathrm{R}}(f)$ represent the frequency domain signal of Eq. (2.8) and Eq. (2.1), respectively. After pulse compression, the pulse is transformed back into the time domain with an Inverse FFT (IFFT). The output of the matched filter is the IRF of the radar for an ideal point target. The real and imaginary parts of the chirp $h_{\mathrm{R}}(\tau)$ and its range-compressed IRF are plotted in Fig. 2.2. Note that the 3dB width of the IRF is inversely proportional to the chirp bandwidth.

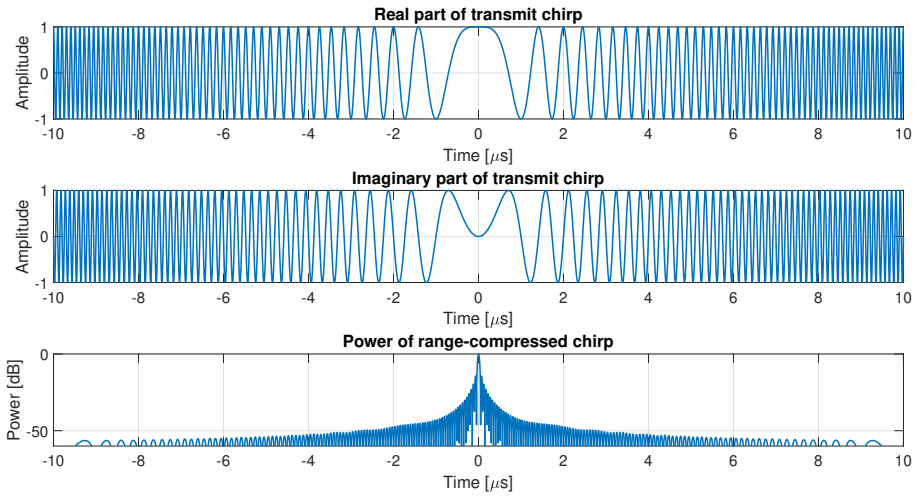

Fig. 2.2.: Real and imaginary part of a transmit chirp with a pulse duration of 20 μs and a bandwidth of 20 MHz (top and middle). Bottom: the chirp after pulse compression with a matched filter shows the SAR impulse response function.

In the same manner as in the range direction, a matched filter can be applied in the azimuth direction. Here, the azimuth chirp $h_{\mathrm{A}}(t, R_0)$ is range-dependent. As before, the resolution is inversely proportional to the bandwidth of the chirp, which is the Doppler bandwidth here. To improve the azimuth resolution, the antenna beam in azimuth needs to be widened. This results in an observation of the target over a larger span of Doppler angles and consequently a larger Doppler bandwidth.

2.2.3. SAR Performance Parameter

The SAR IRF characterizes the response of an ideal point target in the focused image. The shape of the IRF is two-dimensional and is determining the image quality. It can be used for evaluation purposes. From the IRF, the following parameters [62–64] can be derived for range and azimuth each:

Gain [dB] The power in the mainlobe. For this analysis, the gain is normalized to 0 dB with respect to the ideal gain.

Phase [deg] The phase of IRF at peak value.

Resolution [m] The slant-range resolution δ_{e} is defined by the 3 dB width of the

mainlobe. It is the spatial distance between the two points where the mainlobe drops by 3 dB (Fig. 2.3).

PSLR [dB] The Peak-to-Sidelobe Ratio is the ratio of the mainlobe peak value to the peak value of the strongest sidelobe. For this analysis, the strongest sidelobe is selected inside a window centered on the main peak with a side length of $20\delta_\mathrm{e}$ (Fig. 2.3).

ISLR [dB] The Integrated Sidelobe Ratio is the ratio of the energy within the mainlobe to the energy outside of this area (integrated over a window centered on the main peak with a side length of $20\delta_\mathrm{e}$). In Fig. 2.3, the ISLR is the ratio of the energy in the blue area and the red area. Mathematically, the ISLR is expressed as

$$ISLR = \frac{\int_{-\delta_\mathrm{e}}^{\delta_\mathrm{e}} |s_\mathrm{RC}(x)|^2 \mathrm{d}x}{\int_{-10\delta_\mathrm{e}}^{10\delta_\mathrm{e}} |s_\mathrm{RC}(x)|^2 \mathrm{d}x - \int_{-\delta_\mathrm{e}}^{\delta_\mathrm{e}} |s_\mathrm{RC}(x)|^2 \mathrm{d}x}. \tag{2.10}$$

Coherence A powerful measure in SAR interferometry is the complex coherence. It is a quantity of accuracy for the measured interferometric phase [65] and holds valuable information about the physical properties of volume scatterers [66]. The complex coherence between two signal s_1 and s_2 is defined [67] as a normalized correlation of the signals with values between 0 (no correlation) and 1 (fully correlated). It is commonly approximated with spatial averaging over n pixels to

$$\gamma = \frac{\sum_{k=1}^{n} s_{1,k} \cdot s_{2,k}^*}{\sqrt{\sum_{k=1}^{n} s_{1,k} \cdot s_{1,k}^*} \cdot \sqrt{\sum_{k=1}^{n} s_{2,k} \cdot s_{2,k}^*}}. \tag{2.11}$$

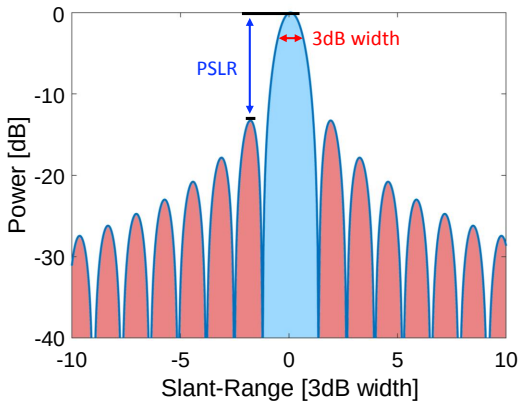

Fig. 2.3.: Illustration of the SAR performance parameters defined by the IRF in one dimension: the resolution is defined by the 3 dB width of the main peak (red arrows), the PSLR is the power ratio between the main peak and the second highest sidelobe, the ISLR is the ratio of the power located inside the main peak (blue area) to the power in the sidelobes (red area).

2.3. Digital Beamforming (DBF)

2.3.1. Principles of DBF

A planar wave that is impinging an antenna array with N elements is arriving at each subelement with a path delay [68, 69]. This path delay is dependent on the subelement spacing d and can be derived with geometrical relations according to Fig. 2.4. The additional delay δp for the $(n-1)$th element is

$$\delta p = (n-1)d\sin\theta. \tag{2.12}$$

With the relation

$$\frac{\delta\phi}{2\pi} = \frac{\delta p}{\lambda} \tag{2.13}$$

the path delay can be converted into the phase delay

$$\delta\phi = 2\pi(n-1)\frac{d}{\lambda}\sin\theta. \tag{2.14}$$

The signal from a certain AoA can be amplified by applying the conjugate of the phase delay $\delta\phi$ as weights to each subelement [70]. This results in an electronical steering of the antenna beam towards that angular direction. In conventional phased array

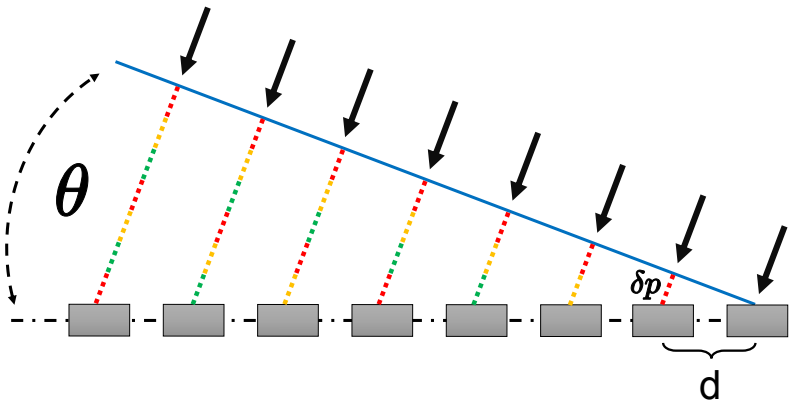

Fig. 2.4.: A plane wave (black arrows) that arrives at an antenna array experiences a path delay δp at each subelement. The delay is dependent on the angle of arrival θ and the element spacing d.

radars [71], the weights between channels are set prior to A/D conversion of the signal. This allows to sum the N signals before the sampling process. While this keeps the data rate low, there are advantages that come with sampling each subelement individually before the summation. If all subelements (or channels) are sampled individually, DBF is possible. This comes at the expense of a more complex system and a data rate that is increased by the factor N. Because the data stream of each channel is now available individually, this allows to set the weights during post-processing. This can be used to adaptively change the antenna pattern based on the received data or to synthesize multiple beams simultaneously. Because DBF changes the gain in defined directions, it is commonly referred to as a spatial filter [55].

2.3.2. SAR Applications

Several applications of DBF for SAR systems have been proposed and include the following:

Displaced Phase Centers To avoid azimuth ambiguities, the PRF has to be set high enough to ensure a sufficient sampling of the Doppler bandwidth. Because the azimuth resolution is coupled to the Doppler bandwidth, a finer resolution requires a higher PRF. However, an increased PRF reduces the unambiguous swath width that can be sampled in range. This is a fundamental limitation of conventional SAR systems that can either achieve a wide swath or a high azimuth resolution. DBF can overcome this limitation

by arranging multiple channels in azimuth [54, 72]. For each pulse, one phase center per channel can be recorded and the PRF can be reduced by the factor N. If the platform moves one half of its antenna length in between pulses, then the Doppler spectrum can be recovered. This allows the SAR to achieve a high azimuth resolution and a wide swath simultaneously at the expense of more channels and processing. Advanced algorithms are also capable of recovering the spectrum for deviating platform velocities [73, 74].

Scan on Receive An increased illuminated swath reduces the gain of the transmit beam. This can be compensated in DBF systems by an increased height of the receive antenna which improves the gain and thus the SNR. The SNR improvement is a result of the narrowing antenna pattern. Naturally, this also decreases the beamwidth of the receive beam. However, DBF systems are capable of steering the narrow beam during the receive window. It can be steered towards the instantaneous direction of the ground return in a SCORE manner [56, 57]. Note that a dispersive beam is required if the beamwidth is smaller than the pulse extent on the ground [75].

Multiple Elevation Beams An extension of the SCORE operation is the implementation of multiple elevation beams (MEB) [76, 77]. As the swath size increases, signal returns from multiple ranges arrive at the antenna simultaneously. It is therefore necessary to separate them with a spatial filter. Returns from different beams are separated by moving multiple narrow beams across the swath in SCORE mode.

Ambiguity Suppression The ability to modify the antenna pattern with DBF allows for a notching of range and azimuth ambiguities [78]. Residual range ambiguities can also be removed with the information collected by MEB [79].

Dual Track Mode For airborne DBF systems, a wide illumination with the transmit beam allows for a mapping of both sides of the flight track simultaneously. The spatial filtering can separate both sides in post-processing. This was successfully demonstrated with DBSAR [80]. The swath size of an airborne DBF SAR can be doubled compared to a conventional airborne SAR.

Orthogonal Waveforms Multiple-input multiple-output (MIMO) SAR are transmitting multiple transmit chirps at once [81, 82]. For example, a horizontally and ver-

tically polarized pulse can be transmitted at the same time [83]. This is possible if the waveforms are orthogonal to each other for short-term shifts. As a result, the matched filter extracts one waveform at the center of the IRF and suppresses the other. The energy of the orthogonal waveform is displaced in the IRF. However, with DBF systems in SCORE, only the center of the IRF is kept. The ability to transmit pulses in both polarizations at once allows to use the same instrument PRF for a fully polarimetric system as for a dual-polarization system and thus avoids a halfening of the swath width. A further application of MIMO SAR is the beamforming of the transmit beam during post-processing [84]. Instead of illuminating a wide swath with low gain, a narrow transmit beam can be steered along with the receive beam to improve the SNR.

Simultaneous Modes of Operation Conventional SAR implement different operational modes to trade off between azimuth resolution and length of the recorded flight path. In Stripmap mode, the antenna is pointing orthogonally to the flight track to map a constant Doppler spectrum along the entire flight path. Another option is to steer the antenna in azimuth to illuminate a constant spot on the ground. This increases the Doppler spectrum and thus the azimuth resolution. This mode is called Spotlight and it results in a loss of part of the flight path. With DBF SAR, both modes can be implemented simultaneously and/or the spotlight mode can be implemented on the entire flight path by steering the beam in post-processing.

2.3.3. DBF for RFI Mitigation

As discussed in Section 1.2, RFI in remote sensing is a growing issue. This work investigates how DBF can be used to blind the radar towards the direction of interferences (Fig. 2.5). In the same manner as in a conventional SAR, the desired ground return (green arrow) is extracted by steering the beam towards its angular direction (blue pattern). An interference source in the scene or outside of the swath is entering the antenna throught the sidelobes (red arrow). Depending on the strength of the interferer it can degrade the SAR data. A notch can be placed in the antenna pattern in the direction of the interferer (orange pattern) while preserving the main beam. This is equivalent to a spatial filtering and requires either a priori knowledge about the AoA of the interferer or it needs to be estimated from the data. Conventional phased arrays require to pick the antenna pattern before the data collection and thus can only adapt after the interference

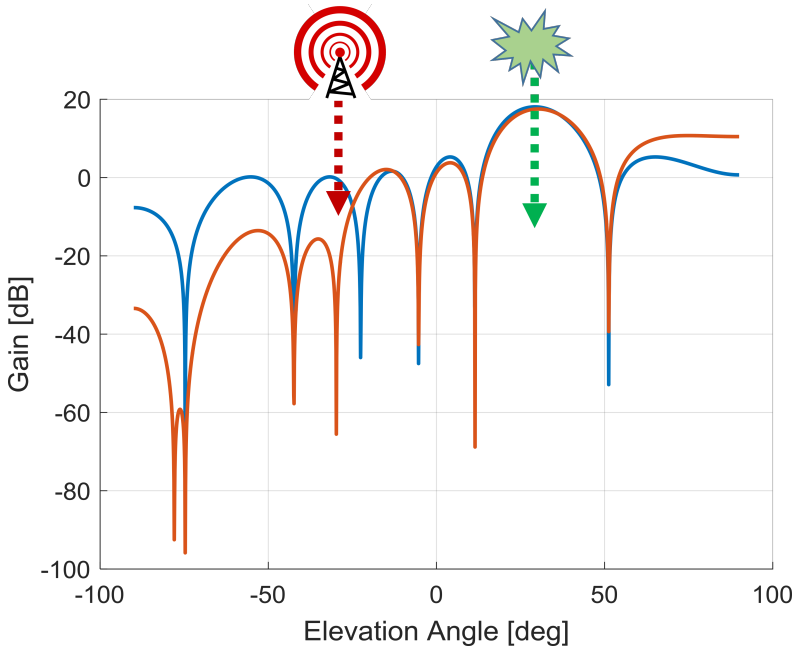

Fig. 2.5.: Illustration of RFI mitigation with DBF: the SAR signal (green arrow) in the mainlobe is degraded by an interferer (red arrow) that is visible through the sidelobes (blue pattern). DBF nulls the antenna pattern to suppress the interferer (orange pattern).

occurs or require auxiliary antennas. In addition, there is no capability to estimate the AoA and DBF overcomes this limitation. An estimation of the AoA from the multi-channel data is possible and the antenna pattern can be changed during post-processing. The idea is that this can be used to improve the RFI mitigation. Note that for an antenna array with N channels, this comes at the cost of an additional data amount by a factor of N and an increased computational load. A fundamental limitation of DBF is that an interferer inside the mainlobe can not be notched without collapsing the gain in the antenna pattern. This makes the SAR signal sensitive to a mispointing of the main beam or results in a complete loss of the SAR signal. An approach to overcome this limitation is investigated in Chapter 5.

2.3.4. Current and Future Missions with DBF

DBF SAR systems overcome fundamental limitations of conventional SAR systems. Therefore, DBF is the baseline for future SAR-based Earth observation missions. An overview of current airborne and future spaceborne missions is compiled in Table 2.1. The concepts for additional systems are in development, such as a DBF capability for ESA's next generation of Sentinel-1 satellites [85]. Hence, the number of SAR that can benefit of an RFI mitigation with DBF is expected to grow in the future.

Table 2.1.: A compilation of current and future SAR missions with DBF capability.

Mission	Platform	Band	Elevation Channels	Azimuth Channels	Antenna
EcoSAR [30]	Airborne	P	8 per wing	1	Planar
DBSAR-1 [32]	Airborne	L	8	1	Planar
DBSAR-2 [33]	Airborne	L	8	1	Planar
DBFSAR [86]	Airborne	X	12	1	Planar
X-band SAR [87]	Airborne	X	16	4	Planar
Ka-band SAR [88]	Airborne	Ka	8	3	Planar
Tandem-L [89]	Spaceborne	L	32	6	Reflector
NISAR [36]	Spaceborne	L	12	1	Reflector
NISAR [90]	Spaceborne	S	24	1	Reflector
TerraSAR-X [91]	Spaceborne	X	1	2	Planar
HRWS [76]	Spaceborne	X	12	4	Planar

2.4. Radio Frequency Interference

RFI is a consequence of the finiteness of the natural resource frequency spectrum and the increasing demand for wireless technology. Because the spectrum is becoming more crowded it is necessary to find ways to: a) avoid mutual interference and b) remove RFI from collected data. This is especially important at P- and L-band, the currently most congested bands used by SAR systems. Therefore, the following subsections give an overview of frequency allocations for current and future P- and L-band SAR (Section 2.4.1) and characteristics of Amateur Radio Stations (ARS) in this band (Section 2.4.2).

2.4.1. P- and L-Band Frequency Allocations

Current and future L-band SAR missions are operating in the 1215 MHz to 1300 MHz band. The frequency allocations according to [16] are listed in Table 2.2. The Earth exploration allocation is for the SAR instruments. The remaining entries give an overview of possible interference sources. It is presumed that the possibility of an interfering Earth exploration satellite or a spacecraft conducting space research can be disregarded, as the avoidance of these kind of disturbances is the goal of the Space Frequency Coordination Group (SFCG). Interfering signals from a radio navigation satellite (e.g., GPS L2 band, upcoming Galileo mission, etc.) would result in indirect interference that bounces off the Earth's surface. As this kind of interference is not spatially localized, an RFI mitigation with DBF (purpose of this thesis) can be ruled out from the beginning. It is therefore assumed that the residual power from the reflected signals can be neglected for an active remote sensing instrument such as SAR. This reduces the list of legal RFI threats to radiolocation services and amateur radio services. Radiolocation services are most likely operating at fixed positions (e.g., airports) with the exception of military radiolocation services. They are responsible for the strong RFI observed in the mainland of the USA [8] mentioned in Section 1.2. Radiolocation services are assumed to transmit a systematic signal that can be modelled. Their fixed position and systematic signal allow to make good predictions about regions affected by interference and the nature of the RFI signal. The unknown impact at L-band are the ARS transmitting in the 1240 MHz to 1300 MHz band. Expected characteristics of ARS are listed in Section 2.4.2.

Table 2.2.: Frequency allocations in the spectrum 1215 MHz - 1300 MHz occupied by current and future L-band SAR missions according to [16].

1215 MHz to 1240 MHz	**1240 MHz to 1300 MHz**
EARTH EXPLORATION-SATELLITE (active)	EARTH EXPLORATION-SATELLITE (active)
RADIOLOCATION	RADIOLOCATION
RADIONAVIGATION-SATELLITE (space-to-Earth), (space-to-space)	RADIONAVIGATION-SATELLITE (space-to-Earth), (space-to-space)
SPACE RESEARCH (active)	SPACE RESEARCH (active)
	Amateur

A summary of potential interferers at P-band (353 MHz - 535 MHz) is given in Table 2.3. The table excludes passive services (e.g., astronomy) and space-to-space services that are unlikely to cause interference. For spaceborne missions, the frequency allocation for SAR is limited to 6 MHz in the 432 MHz to 438 MHz band. Threats in this band

are radiolocation services and windprofilers, as well as ARS. Radiolocation services and wind profilers are expected to transmit a predictable signal which is helpful for the RFI mitigation. In addition, they are, except for military radars, most likely positioned at fixed locations. Hence, spatial RFI mitigation with DBF could be effective to suppress them. As in L-band, the ARS remains an unknown impact and the biggest threat. For airborne radars the increased bandwidth yields a larger list of possible interferers. While space-to-Earth interference is assumed to be neglectible, Earth-to-space interference is not. Because of the reduced altitude and swath of airborne systems, this could be combated by agreements with local entities to stop transmission during the short acquisition time of the airborne system. However, this is not feasible for broadcasting systems that are located in the upper spectrum (470 MHz to 535 MHz). A spatial filter for fixed interferers, such as TV towers, is conceivable.

Table 2.3.: Interfering frequency allocations in the spectrum 353 MHz - 535 MHz occupied by current and future P-band SAR missions according to [16].

Fixed, Mobile	237.0 MHz - 328.6 MHz, 335.4 MHz - 399.9 MHz, 406.1 - 430.0 MHz, 440.0 MHz - 535.0 MHz
Aeronautical Radionavigation (Instrument Landing Systems)	328.6 MHz - 335.4 MHz
Mobile-satellite (space-to-Earth)	387.0 MHz - 390.0 MHz, 400.15 MHz - 401.0 MHz
Mobile-satellite (Earth-to-space)	399.9 MHz - 400.05 MHz, 406.0 MHz - 406.1 MHz, 455.0 MHz - 456.0 MHz, 459.0 MHz - 460.0 MHz
Standard frequency and time signal satellite	400.05 MHz - 400.15 MHz
Metereological satellite (space-to-Earth)	400.15 MHz - 401.0 MHz
Space research (space-to-Earth)	400.15 MHz - 401.0 MHz
Metereological aids	400.15 MHz - 406.0 MHz
Space operation (space-to-Earth)	401.0 MHz - 402.0 MHz
Metereological satellite (Earth-to-space)	401.0 MHz - 403.0 MHz
Wind profiler	420.0 MHz - 435.0 MHz, 438.0 MHz - 450.0 MHz
Radiolocation	430.0 MHz - 450.0 MHz
Amateur	430.0 MHz - 440.0 MHz
Earth exploration satellite (active)	432.0 MHz - 438.0 MHz
Metereological satellite (space-to-Earth)	460.0 MHz - 470.0 MHz
Broadcasting	470.0 MHz - 535.0 MHz

2.4.2. Amateur Radio Station Characteristics

Typical amateur radio operations are dialogues between two or more operators, ranging from brief exchanges to long discussions [92]. A number of contests are carried out throughout the year with the goal to contact as many amateur stations as possible. Characteristics of radio amateur systems for use in sharing studies are published in the ITU recommendation M.1732-2 [93]. The ITU assumes that systems in the 1.2-1.3 GHz band transmit with an Effective Isotropic Radiated Power (EIRP) of 1 dB to 45 dB. Generally, one would assume that the directivity of the radiating antenna is aligned horizontally to the Earth surface (Fig. 2.6). This would increase the one-way path from a possible interferer to a satellite at 745 km altitude (neglecting tropospheric ducting) by 2425 km, resulting in an additional attenuation of 12.58 dB (total loss: 141 dB) compared to a vertical directivity. Hence, if the interferer is pointing directly towards the satellite, RFI powers at the antenna input of up to -96 dB are expected. This might not saturate a SAR system but is still above the noise floor. An exception is the operation of Earth-Moon-Earth (EME) systems, which use the moon as a reflector to increase their covered distance. These systems have higher EIRP values from 40 dB to 68 dB [93] and are directed towards the moon. An interference and saturation of SAR systems with EME systems would be possible if the radar were in the line of sight between the amateur radio station and the moon. This interference scenario would be limited to an operation during evening or night hours.

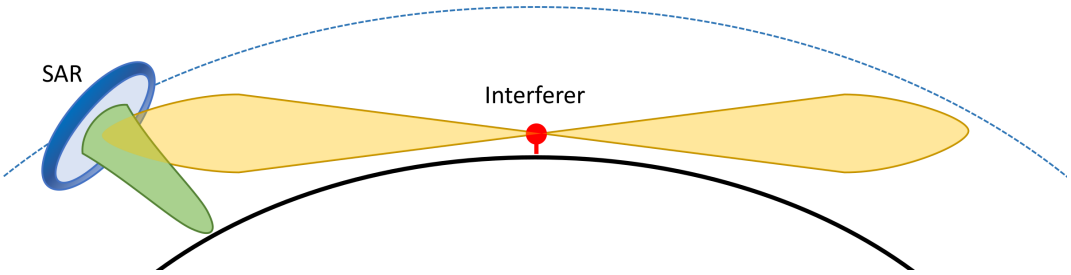

Fig. 2.6.: Interference of a spaceborne radar by an interferer with horizontal directivity.

Probably the most popular form of amateur radio is the transmission of voice. The available modes can be classified into analog (AM, FM, etc.) and digital signals. Due to the nature of speech, the expected short-term stationarity of these signals is in the order of milliseconds. For a digital signal, the short-term stationarity depends on the Baud rate (or symbol rate) of the signal. A digital mode for speech transmission is Digital Voice.

Several different protocols exist, with most using rates of only a few hundred Baud. An upper limit for voice transmission is offered by the D-STAR protocol, which transmits up to 9600 Baud. In addition, modes for digital data transmission include Packet, PSK31, NBDP, RTTY and other modes. Even though no limit for the Baud rates exist, common standards use baud rates on the order of 100 bauds with the highest baud of up to 9600 used by packet radio. An exception to this is the transmission of analog or digital TV signals by amateur stations. No upper limit is regulated, though, for example, German DVB-C stations transmit with 6900 Baud.

2.5. Simulation Models

2.5.1. Synthetic Aperture Radar

In the framework of this thesis, the antenna is a linear array that consists of N elements in elevation with element spacing d (Fig. 2.1). Note that the presented model can be extended to a two-dimensional array with $N \cdot M$ elements without loss of generality, hereof M elements distributed in the azimuth direction. In the following, a tilt angle of $\theta_\mathrm{t} = 0°$ in accordance with the experimental data in Chapter 3 is assumed, as well as an antenna array aligned in elevation (no elements in azimuth were available for the experimental data). The transmit beam of the radar results in an illuminated swath that covers the slant ranges $R_1 \leq R \leq R_2$. The stop-and-go approximation is used, which assumes a stationary radar position during pulse transmission and reception. In between pulses, the platform is travelling with a constant velocity V along the y-axis. The transmitted chirps are modelled with Eq. (2.1) as discussed in Section 2.2.1. Hereby, the transmit gain and propagation loss are neglected, as only the relative received power between SAR signal and interferer signal at the antenna input is of interest in this thesis. On the ground, the signal is scattered back by an extended target (red crosses in Fig. 2.1) that is located on the x-y-plane. The backscattering coefficient $\sigma(\mathrm{x}, \mathrm{y})$ of the extended target is modelled as a circular-symmetric complex Gaussian random vector, that has a Rayleigh distributed amplitude and a uniformly distributed phase. Then, the scattered signal propagates back towards the antenna and, after a round-trip time of $\tau = 2R/c_0$, the reflection from a point at $x = \sqrt{\frac{\tau^2 c_0^2}{4} - H^2}$ ($\frac{\tau c_0}{2} > H$) starts to arrive at the antenna. Due to the pulse extent, the return from that point is not received until $\tau = 2R/c_0 + T_\mathrm{p}$. As before, the propagation loss and antenna gain are neglected. The array geometry at the antenna

results in an arrival time delay between the antenna elements and hence in a phase shift $a(\tau, m)$ at the m-th element:

$$a(\tau, m) = e^{j2\pi m \frac{d}{\lambda} \sin(\theta_{\mathrm{l}}(\tau))}, \tag{2.15}$$

where the elevation look angle θ_{l} is calculated for a flat Earth model as:

$$\theta_{\mathrm{l}}(\tau) = \cos^{-1}\left(\frac{2H}{\tau c_0}\right). \tag{2.16}$$

Note that this is a valid approximation for the airborne experimental data of Chapter 3. In case of a spaceborne geometry with Earth radius R_{E} such as in [75], Eq. (2.16) is computed via:

$$\theta_{\mathrm{l}}(\tau) = \cos^{-1}\left(-\frac{H^2 + 2R_{\mathrm{E}}H + \frac{\tau^2 c_0^2}{4}}{\tau c_0 (H + R_{\mathrm{E}})}\right). \tag{2.17}$$

For an infinitely large R_{E}, Eq. (2.16) and Eq. (2.17) become identical.
Ignoring the synthetic aperture for now and substituting $y = Vt$, the zero Doppler contributions of each target in the simulated multi-channel baseband image can be written as

$$s_{\mathrm{R,zd}}(\tau, t, m) = \left[a(\tau, m) \cdot \sigma\left(\sqrt{\frac{\tau^2 c_0^2}{4} - H^2}, Vt\right) \cdot \mathrm{rect}\left[\frac{\tau c_0 - R_1 - R_2}{2R_1 - 2R_2}\right]\right] * h_{\mathrm{r}}(\tau). \tag{2.18}$$

Here, the rect-function limits the backscatter coefficient $\sigma(\mathrm{x}, \mathrm{y})$ to the swath extent $R_1 \leq R \leq R_2$. $a(\tau, m)$ defines the phase shifts between the antenna elements for each scatterpoint in $\sigma(\mathrm{x}, \mathrm{y})$. Note that $a(\tau, m)$ is applied before the return from each angle is spread with the chirp convolution in range.
As a final step, the Doppler modulation is included with a convolution by h_{A} (Eq. (2.5)) in azimuth. The result corresponds to a range cell migration corrected raw image. The simulated multi-channel SAR signal $s_{\mathrm{R}}(\tau, t, m)$ in baseband is given by

$$s_{\mathrm{R}}(\tau, t, m) = s_{\mathrm{R,zd}}(\tau, t, m) * h_{\mathrm{A}}(\tau, t). \tag{2.19}$$

Because the simulated image is of discrete nature, the signal model in Chapter 3 is

$$s_{\mathrm{R}}(u, p, m) = s_{\mathrm{R,zd}}(u, p, m) * h_{\mathrm{A}}(u, p), \tag{2.20}$$

where u represents the fast time range samples and p the pulses acquired in slow time. The investigation is limited to distributed targets, which represent the worst-case scenario as discussed in Appendix A. A better performance can generally be assumed for point-like targets.

2.5.2. Radio Frequency Interference

Next, the signal is contaminated with an RFI signal. For this, the spatial location of the interferer is described with the angle-of-arrival θ_{RFI} of the RFI signal relative to the planar antenna array. θ_{RFI} is assumed constant during the simulations that are restricted to a few hundred pulses. As before, the propagation loss is disregarded because the RFI signal power will be scaled at the antenna input to analyze different RFI-to-Signal Ratios (RSR). The measured RFI signal RFI for an interfering signal r with wavelength λ_{RFI} is modelled at baseband with

$$RFI(\tau, t, m) = r(\tau, t) \cdot e^{j2\pi m \frac{d}{\lambda_{\mathrm{RFI}}} \sin(\theta_{\mathrm{RFI}})}. \tag{2.21}$$

Hereby, the phase term represents the θ_{RFI}-dependent phase difference between the receive channels. The signals are modulated with a one-way Doppler shift of the range at the image center, though the Doppler is the same for each channel and does therefore not affect a spatial filter.
Two different kinds of interferers are simulated throughout the thesis.
For a continuous-wave (CW) interferer, r in baseband is

$$r(\tau, t) = e^{j2\pi(f_{\mathrm{RFI}} - f_{\mathrm{c}})\tau} \cdot e^{j2\pi(f_{\mathrm{RFI}} - f_{\mathrm{c}})t}. \tag{2.22}$$

For the simulation of a communication signal with symbol length SL, a random discrete vector c with uniformly distributed ones and zeros is simulated. The vector is then modulated onto a BFSK signal of frequency f_1 and f_2. The resulting signal is shifting between two CW-interferers with instantaneous frequency $f_{\mathrm{RFI}}(\tau, t)$, given by

$$f_{\mathrm{RFI}}(\tau, t) = \begin{cases} f_1 & : \left\lfloor c\left(\frac{t+\tau}{SL}\right)\right\rceil = 0 \\ f_2 & : \left\lfloor c\left(\frac{t+\tau}{SL}\right)\right\rceil = 1. \end{cases} \tag{2.23}$$

2.5.3. Error Model

Description

Figure 2.7a illustrates the use of an additive error model because RFI is of an additive nature. The black vector represents the SAR signal vector. An additive error with fixed amplitude (blue-dashed vector) will displace the SAR signal vector to a location on the green-dashed circle. The exact position is determined by the relative phase of the interferer which can rotate the error vector along the red line. It is evident that the resulting amplitude error will depend on the interferer phase, which results in amplification or attenuation of the signal for constructive and deconstructive interference, respectively. This means that the additive amplitude error alone gives no indication of the resulting signal amplitude. To ensure that the radiometric budget is met, one can not set a fixed limit to the phase and amplitude error but only to the combination of both. Further, the resulting signal phase error will depend on the ratio of the RFI amplitude (blue-dashed) to the SAR amplitude (black) and the RFI phase (red). The larger the relation of the RFI amplitude is relative to the SAR amplitude, the greater the introduced phase error for a fixed RFI amplitude. In the same manner, the additive phase error alone gives no indication of the resulting signal phase. Given these points, the interdependency of the signal error on the RFI amplitude, RFI phase and SAR amplitude makes the additive error model a disadvantageous choice.
In contrast, a multiplicative error model is illustrated in 2.7b. Note that a conversion between both models is straightforward. For this model, the multiplicative amplitude error describes the resulting amplitude (blue-dashed) and the multiplicative phase error describes the resulting signal phase (red). Both errors are decoupled and a fixed limit for both errors can be defined individually. For this reason, the error model used in this thesis is multiplicative and given by

$$s_{\mathrm{Err}}(\tau,t) = \Big[A_0 + A(\tau,t)\Big] \cdot s_{\mathrm{R,DBF}}(\tau,t) \cdot e^{j\Phi_0} \cdot e^{j\Phi(\tau,t)}, \tag{2.24}$$

where A_0 and Φ_0 are constant amplitude and phase offsets and $A(\tau,t)$ and $\Phi(\tau,t)$ are time-varying errors. $s_{\mathrm{R,DBF}}(\tau,t)$ is the beamformed $s_{\mathrm{R}}(\tau,t,m)$ signal. The four parameters are derived from the raw data because the simulated SAR signal is an extended target that does not undergo a processing gain (Appendix A). $A(\tau,t)$ and $\Phi(\tau,t)$ are expressed with their respective standard deviations σ_{A} and σ_{Φ}.

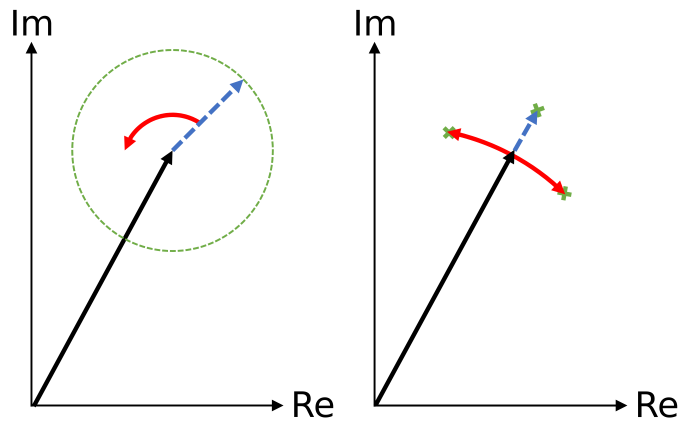

(a) (b)

Fig. 2.7.: a) Additive error model: SAR signal (black vector) imposed with additive RFI (blue-dashed vector). A phase change of the interferer (red) causes the measured signal to be within the green-dashed circle. The resulting amplitude error depends on both RFI amplitude and phase. The resulting phase error depends on amplitude and phase as well. b) Multiplicative error model: SAR signal (black vector) that is affected by multiplicative amplitude error (blue-dashed vector) and multiplicative phase error (red). The resulting amplitude error depends on the multiplicative amplitude, the resulting phase error on the multiplicative phase.

Impact on SAR Performance Parameters

With the previously defined error model and the performance parameters from Section 2.2.3, it is now possible to simulate the maximum allowed errors that meet a desired error budget. First, the impact of the error model on the amplitude budget is discussed. Due to the nature of the error model, an amplitude offset A_0 directly translates into an amplitude offset. For extended targets, the amplitude standard deviation σ_A in the raw data represents the amplitude deviation in the focused image. The overall amplitude error within one standard deviation can therefore be described with

$$20\log_{10}(A_0 + |\sigma_\mathrm{A}|). \tag{2.25}$$

The resulting overall amplitude error is plotted in Fig. 2.8a. For σ_A smaller than -40 dB, the overall amplitude error is controlled by A_0 alone. For larger values the amplitude standard deviation starts to influence the error and takes over the dominant role for $\sigma_\mathrm{A} > 30$ dB. As an example, it is assumed that the overall amplitude error shall not ex-

ceed 0.5 dB. 0.2 dB is allocated to amplitude offset errors A_0. For an error budget that is met within one standard deviation, this would result in a requirement of $\sigma_{\mathrm{A}} \leq -38.5$ dB.

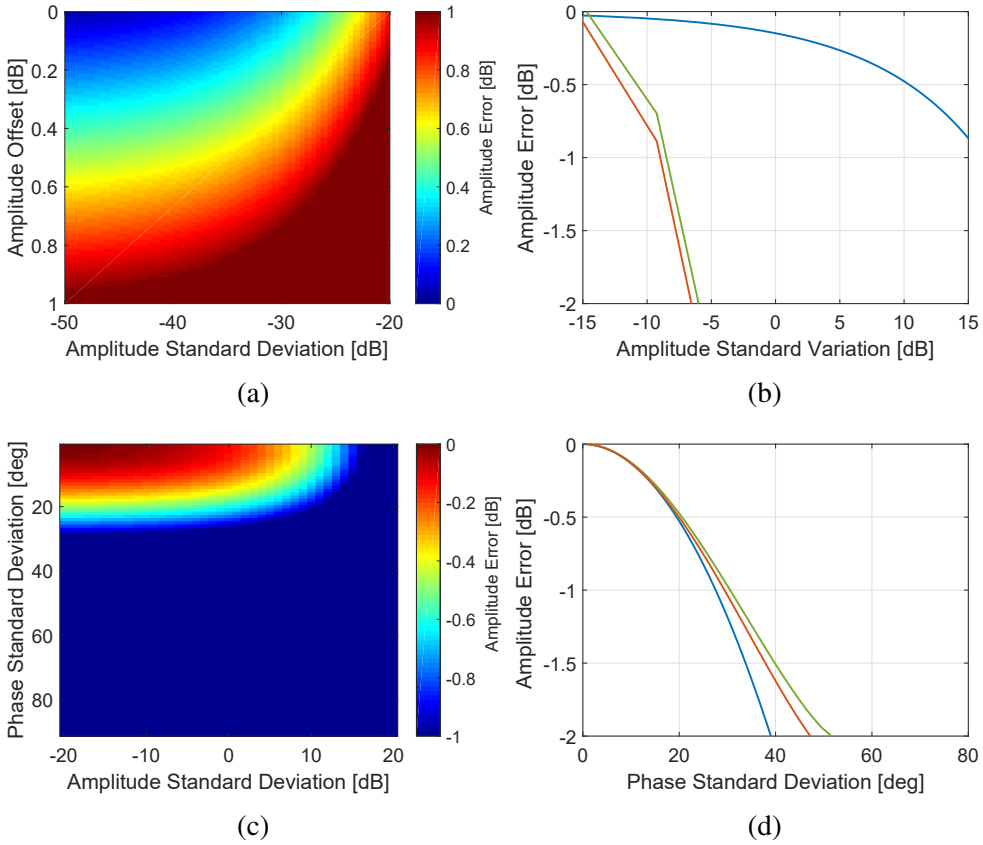

Fig. 2.8.: a) Resulting amplitude error for an extended target according to Eq. (2.25), b) Amplitude error for a point target after the matched filter for Gaussian (blue) RFI and CW RFI (green minimum error, orange maximum error), c) Amplitude error for a point target in dependency of time-varying amplitude and phase errors, d) Amplitude error for a point target in dependency of a time-varying phase error.

The impact on a point target is shown in Fig. 2.8b. The impact is simulated for normally distributed errors σ_{A} and σ_{Φ} (blue line). In addition, the influence of a CW interferer on the RFI is simulated for different f_{RFI} and RFI-to-Signal Ratios (RSR). The resulting error model parameters are calculated and the upper and lower bound of the error is plotted in green and orange, respectively. Note that for CW interferers, σ_{A} shows a direct correlation with σ_{Φ} and thus both errors are separable.

In the case of a CW interferer, the selected budget is exceeded for $\sigma_{\mathrm{A}} > -13.4$ dB. It is evident that the radiometric accuracy for point targets requires a less strict limitation of the errors because the integration with the matched filter reduces the error. For a Gaussian interferer, the error would be reduced by $\sqrt{N_{\mathrm{P}}}$, where N_{P} represents the number of integrated pulses.

While the phase error σ_{Φ} does not influence the radiometric accuracy of extended targets, it does affect the matched filtering of a point target. The resulting error in dependence of σ_{A} and σ_{Φ} is shown in Fig. 2.8c. Clearly, for the previously defined requirement of $\sigma_{\mathrm{A}} \leq -38.5$ dB, the influence of σ_{Φ} on the matched filtering is more important than σ_{A}. Therefore, a one dimensional plot of σ_{Φ} is shown in Fig. 2.8d. For the previously selected maximum amplitude error, the requirement is $\sigma_{\Phi} \leq 18°$. The radiometric budget is met for both point and extended targets if $A_0 \leq 0.2$ dB, $\sigma_{\mathrm{A}} \leq -38.5$ dB and $\sigma_{\Phi} \leq 18°$.

Next, the impact of the error model on a phase error budget is discussed. Phase errors Φ_0 directly translate into a phase offset. If a total budget of 20° is assumed with 2° assigned to Φ_0, this allows the phase standard deviation σ_{Φ} to be up to 18° to meet the amplitude budget for extended targets. The 2D plot of Fig. 2.9a shows the phase error offset for a point target with normal errors. For the previously defined $\sigma_{\mathrm{A}} \leq -38.5$ dB, the phase standard deviation is the dominant contribution. For the defined $\sigma_{\Phi} \leq 18°$, the introduced phase offset is a fraction of a degree for both kinds of simulated interferer types (Fig. 2.9b) and meets the budget. In addition, σ_{A} of a CW interferer causes neglegible phase errors for its permitted values (Fig. 2.9c). In conclusion, the error budget defined for the amplitude budget is also valid for the phase budget: $\sigma_{\Phi} \leq 18°$.

Appendix B shows that the impact of the error model on resolution, PSLR, ISLR and coherence. It can be concluded, that the worst case scenario is covered by an analysis of the amplitude and phase errors imposed by RFI on a distributed target.

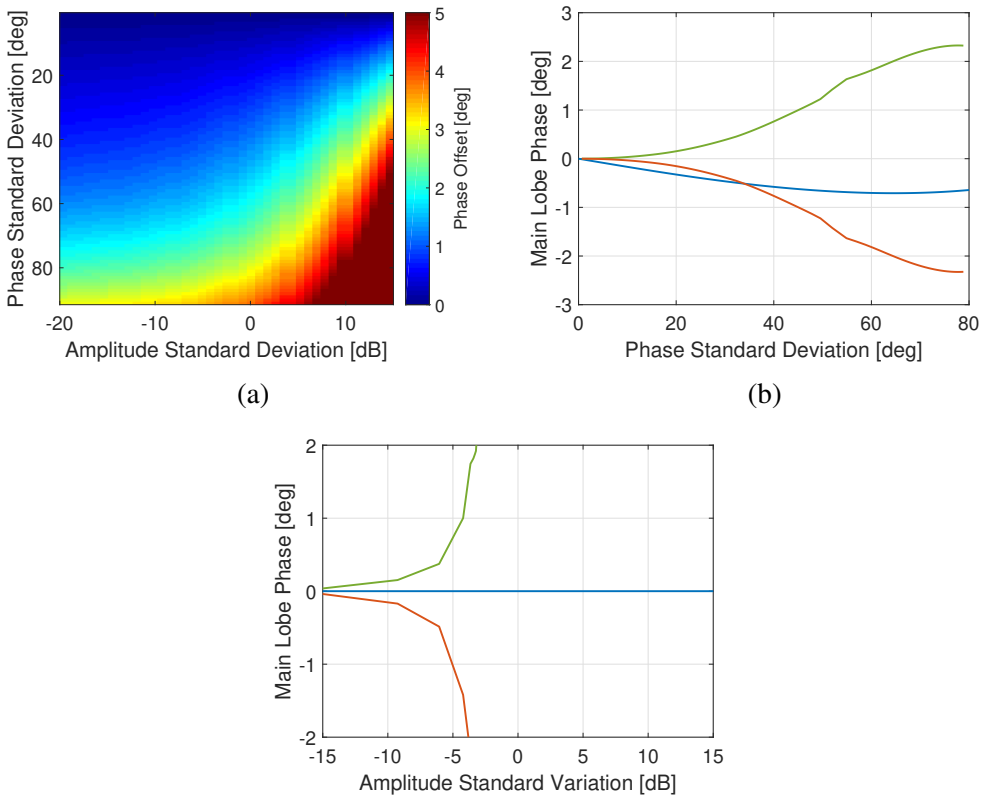

Fig. 2.9.: a) Phase error for an extended target in dependency of time-varying amplitude and phase errors, b) Phase error for point target in dependency of time-varying phase errors, c) Phase error for point target in dependency of time-varying amplitude errors. The green and orange curves represent the minimum and maximum error for a CW interferer.

3. Adaptive Antenna Pattern Notching for RFI Mitigation

3.1. Chapter Overview

This chapter discusses RFI mitigation in SAR data by means of notching the antenna pattern. As a consequence of the notching, interferer signals outside of the main beam are suppressed while the SAR signal is preserved. This spatial filter technique can be applied if all receive channels are available, such as is the case for an airborne system or for future spaceborne systems with enough computational on-board capabilities. The theoretical background for this approach is presented in Section 3.2. Based on the existing methods, new algorithms are derived that utilize the spatial distribution of the SAR signal, which is inherent to its imaging geometry. This is done for a system with multiple channels in elevation and/or in azimuth in Section 3.3. The potential of the newly introduced algorithms is then analyzed in Section 3.4 for different interference scenarios. A summary of the findings is given in Section 3.5.
Part of the results presented in this chapter has been published in [94].

3.2. Theoretical Background

3.2.1. Minimum Variance Distortionless Beamformer

A spatial suppression of RFI can be achieved with adaptive beamforming. Hereby, the main beam is preserved in the direction of the signal of interest (SOI) but nulls are placed in the antenna pattern towards the direction of the interferers. A well-researched adaptive beamformer for this purpose is the Minimum Variance Distortionless (MVDR) (or Capon) beamformer [55, 95–97]. The preservation of the SOI is guaranteed by requiring a unity gain in its direction with

$$\mathbf{w}^H \mathbf{a}(\theta_\mathrm{d}) = 1, \tag{3.1}$$

where $\mathbf{w}$ is the vector containing the optimal beamforming weights, θ_d is the AoA of the SOI and $\mathbf{a}(\theta)$ is the steering vector. The steering vector represents the phase delay between the N channels for a signal impinging the antenna from direction θ and depends on the element spacing d:

$$\mathbf{a}(\theta) = \begin{bmatrix} 1 & \mathrm{e}^{j2\pi d/\lambda \sin(\theta)} & \dots & \mathrm{e}^{j2\pi d/\lambda (N-1) \sin(\theta)} \end{bmatrix}. \tag{3.2}$$

Simultaneously, the Signal-to-Noise-plus-Interference ratio is maximized by minimizing the beamformed Interference-Noise-Covariance (INC) matrix according to:

$$\min \mathbf{w}^H \mathbf{R} \mathbf{w} \tag{3.3}$$

Here, $\mathbf{R}$ is the INC matrix which is discussed in Section 3.2.2. It can be shown that the optimal weights $\mathbf{w}$ that fullfill Eq. (3.1) and Eq. (3.3) can be computed via

$$\mathbf{w}(\theta_\mathrm{d}) = \frac{\mathbf{R}^{-1}\mathbf{a}(\theta_\mathrm{d})}{\mathbf{a}^H(\theta_\mathrm{d})\mathbf{R}^{-1}\mathbf{a}(\theta_\mathrm{d})}. \tag{3.4}$$

A drawback of the MVDR is its sensitivity to errors of the steering vector $\mathbf{a}(\theta)$ [98–101], that can be introduced by instrument calibration errors or by inaccuracies in the knowledge of θ_d, e.g. due of topography [102]. Note that the SCORE operation of a DBF SAR is affected by the same inaccuracy of the steering vector as mentioned in [102]. Without loss of generality, the MVDR can be substituted in the developed algorithms by other beamformers, such as the Linearly Constraint Minimum Variance (LCMV) [103] beamformer. Then, uncertainties of the AoA can be addressed by broadening the mainlobe with the LCMV, which adds further constraints. However, this comes at the cost of the number of nulls that can be placed. Hence, it is assumed for the rest of this work that $\mathbf{a}(\theta)$ is known well enough to perform SCORE and the MVDR is sufficient.

3.2.2. Interference-Noise-Covariance Estimation

The MVDR beamformer solution of Eq. (3.4) relies on knowledge about the INC matrix $\mathbf{R}$. Because $\mathbf{R}$ is generally not known, it needs to be approximated by estimating the

sample covariance matrix over v samples via

$$\mathbf{R}_{\mathrm{x}} = \frac{1}{v} \sum_{k=1}^{v} \mathbf{x}(k)\mathbf{x}^{H}(k), \tag{3.5}$$

where $\mathbf{x}(k)$ is the signal matrix with a number of rows equivalent to the channel count N. Each row is the received signal from a receive channel. However, $\mathbf{R}_{\mathrm{x}}$ can only be estimated on the received signal that is composed not only of the interference and noise but also of the SOI. As a result, the MVDR tries to minimize the SAR signal too, which is a disadvantage. A solution for this was presented in [104], where the transmission of the SAR pulse is skipped periodically or randomly. In this way, the authors estimate the INC on noise pulses in the absence of the SAR signal. This approach requires the use of frequent noise pulses to adapt to a changing interferer environment and because the interferer's AoA might change due to the relative motion. A new SAR technique called Staggered SAR is changing the PRF from pulse to pulse with the goal to remove blind ranges in the SAR image [105–108]. Consequently, Staggered SAR introduces missing samples, whose range position varies across the image. Staggered SAR still performes well because not more than one consecutive sample is missed at the same range. This cannot be achieved with frequent noise pulses as proposed in [104]. Further, pulsed radars might not affect every pulse in the image and could be missed. And especially communication signals with time bursts can lead to many different interferer constellations (and thus INC matrices) inside the same receive window. It is therefore desired to compute many INC estimates without relying on noise pulses or tight calibration windows.

In [109], the authors propose a reconstruction of the INC that makes use of the Capon spatial spectrum estimator [95]:

$$P(\theta) = \frac{1}{\mathbf{a}^{H}(\theta)\mathbf{R}_{\mathrm{x}}^{-1}\mathbf{a}(\theta)}. \tag{3.6}$$

$P(\theta)$ gives an estimate of the power that is impinging the antenna from the direction θ. By integrating $P(\theta)$ over angular regions that are not occupied by the SOI, the INC can be reconstructed as shown in [109]:

$$\mathbf{R} = \int_{\bar{\Theta}} P(\theta)\mathbf{a}(\theta)\mathbf{a}^{H}(\theta)\,\mathrm{d}\theta = \int_{\bar{\Theta}} \frac{\mathbf{a}(\theta)\mathbf{a}^{H}(\theta)}{\mathbf{a}^{H}(\theta)\mathbf{R}_{\mathrm{x}}^{-1}\mathbf{a}(\theta)}\,\mathrm{d}\theta. \tag{3.7}$$

Note that Θ is the angular area occupied by the SOI. This approach is appealing for a SAR system because the AoA of the SOI, which changes with fast time and Doppler, is predetermined by the SAR imaging geometry. Therefore, in Section 3.3, the MVDR and the INC reconstruction of Eq. (3.7) are expanded into multiple RFI mitigation algorithms that are directly applicable to SAR.

3.2.3. The Angular Extension of SAR Signals

The long chirps that are generally used in SAR cause every point on the ground to be illuminated by a duration of T_p. As a consequence, target returns from multiple elevation angles are arriving at the antenna simultaneously. This instantaneous illuminated area on the ground is the pulse extent (PE) illustrated in Fig. 3.1a, which covers the slant range distance [75]

$$R_\mathrm{PE} = \frac{T_\mathrm{p} c_0}{2}. \tag{3.8}$$

Because returns from the entire PE are received at once, the angular spectrum (Eq. (3.6)) estimated on the raw data is occupied by the SAR signal from multiple ranges (and thus AoAs) simultaneously. This is shown in Fig. 3.1b for a complex-circular Gaussian SAR signal that is simulated over look angles spanning from 24° to 60°. To reduce the PE, the data can be range compressed. The resulting compressed PE reduces the area in the spatial spectrum in Fig. 3.1c. The range-time dependency of the AoA that is inherent to the imaging geometry is evident. Another possibility to reduce the PE is to create frequency sublooks with bandpass filters in the frequency domain. Because the transmit chirp is modulated with a linear frequency ramp (Fig. 3.1d), this bandpass filter in the frequency domain results in a reduction of the PE. This comes at the price of having to perform the RFI mitigation individually on each frequency sublook and therefore increases the processing time. Further implications and better options are discussed in Section 3.3. In the following, the spatial PE is referred to as the angular signal extent in the angular elevation spectrum.

A similar angular signal extent of the SAR signal can be observed in azimuth as well. Returns from a wide span of Doppler angles arrive simultaneously at the antenna. As illustrated in Fig. 3.2a, the SAR is receiving multiple returns from a target on the ground (red marker) while it is moving over the target. The resulting ground extent due to this Doppler angle span is shown in Fig. 3.2b. In azimuth the extent on ground depends on the opening angle Θ_a of the aperture and the slant range distance R_0 and is equivalent to

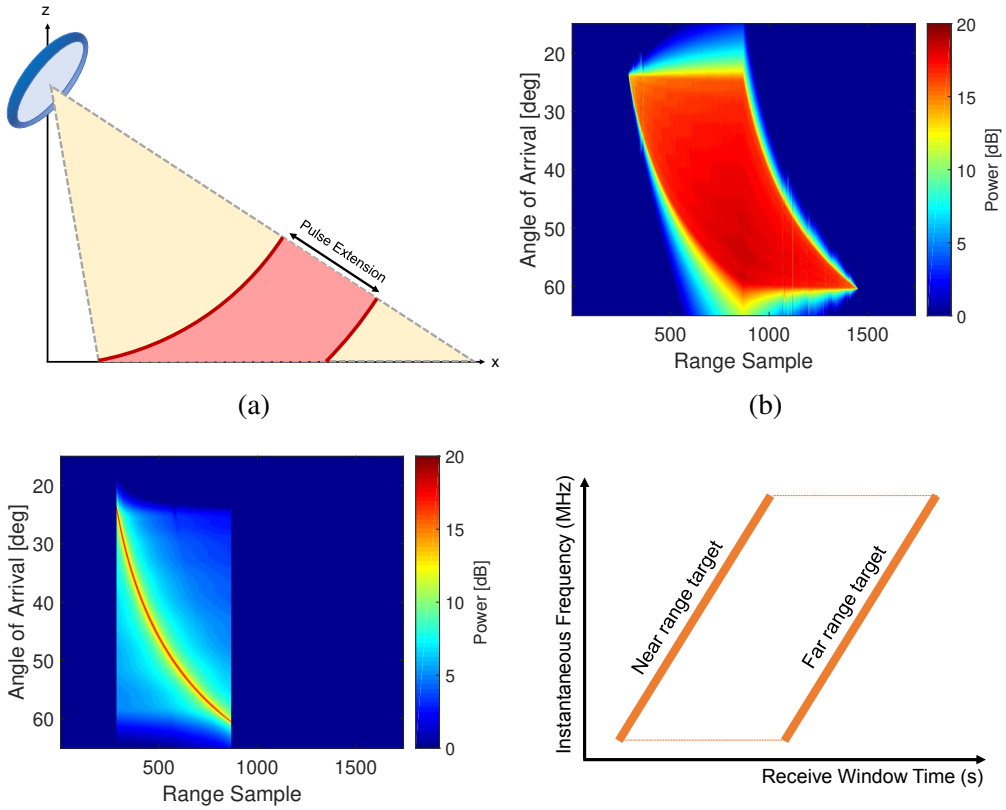

Fig. 3.1.: a) Illustration of the pulse extension in red. Returns from all targets within the red zone arrive at the radar simultaneously. As the pulse propagates, the pulse extension travels on ground. b) Capon spatial spectrum (power from AoA) vs. range sample for raw SAR signal. The signal is simulated with a complex-circular Gaussian backscatter between 24° and 60° AoA. The transmit pulse duration is 20 μs. The radar is receiving energy from a wide span of AoAs at each range because of the pulse extension. c) Capon spatial spectrum vs. range sample for range-compressed SAR signal. The energy is compressed to the instantaneous range. d) Instantaneous frequency of near and far range target within the receive window for a transmit pulse that is modulated with a linear frequency.

the synthetic aperture length [60]

$$L_{\mathrm{SA}} = \Theta_{\mathrm{a}} R_0. \tag{3.9}$$

Due to this relative motion, a Doppler shift is introduced, which leads to a chirp in

azimuth. The Doppler shift is depending on the AoA in azimuth. Note that the color in Fig. 3.2b represents the changing Doppler and hence the AoA in azimuth. Doppler subapertures can be performed to process the wide beam on multiple narrow beams.

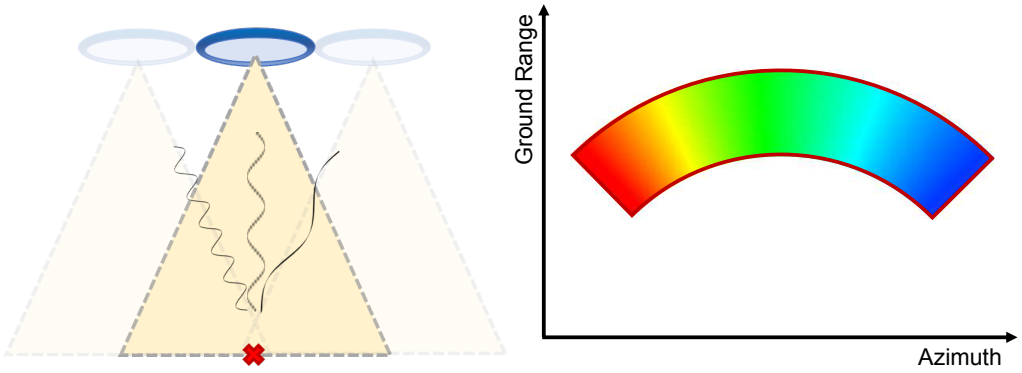

(a) (b)

Fig. 3.2.: a) The beamwidth in azimuth allows the SAR to record the Doppler chirp caused by the relative motion between radar and target (red mark). Additionally, it also causes the illumination of a wide span of Doppler angles in the azimuth direction. b) Two-dimensional ground extent. The height is given by the PE in range, whereas the angular span is a result of the Doppler angle span. The color scheme illustrates the change of the Doppler frequency and azimuth AoA.

3.3. Proposed RFI Mitigation Algorithms using DBF

In this section, newly developed RFI removal algorithms, which make use of the spatial distribution of the SAR signal, are presented. They are based on the MVDR beamformer with an INC estimation according to Eq. (3.7). Thus, the INC is estimated by integrating over the angular spectrum $\bar{\Theta}$ that is not occupied by the instantaneous SAR return Θ (Fig. 3.3). As a result, the angular signal extent of the pulse is generating an RFI detection gap. All interfering sources that are in this angular area can not be detected. Fig. 3.4 shows the angular signal extent θ_{ASE} versus look angle for an airborne ($H = 3\ km$) and spaceborne ($H = 600\ km$) SAR system operating with a chirp duration of $T_{\mathrm{P}} = 20\ \mu s$. It is evident, that the angular signal extent is especially critical in the case of an airborne system. Using a flat Earth approximation (for the computation of the spaceborne scenario see [75]), the angular extent is given by

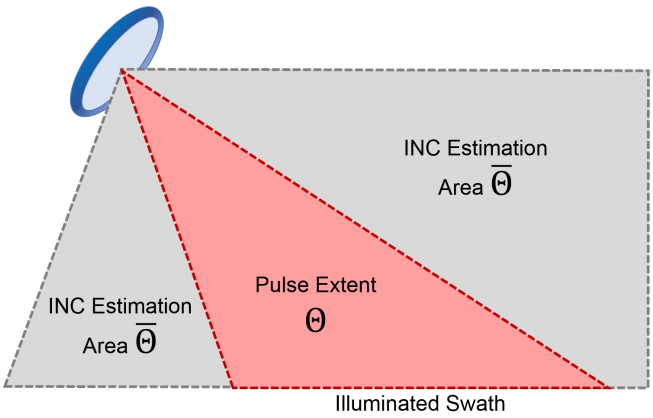

Fig. 3.3.: The estimation of the INC matrix in the presence of the SAR signal is achieved by integrating the angular spectrum over the angular area $\bar{\Theta}$. The instantaneous SAR signal occupies the angular area Θ .

$$\theta_{\mathrm{ASE}}(\theta_{\mathrm{l}})|_{\Delta r=\frac{\tau_{\mathrm{P}} c_0}{2}} = \arccos\left(\frac{H\cos\theta_{\mathrm{l}}}{H+\Delta r\cos\theta_{\mathrm{l}}}\right) - \theta_{\mathrm{l}} \tag{3.10}$$

It can be concluded that θ_{ASE} becomes zero for infinitely large H and approaches $\theta_{\mathrm{ASE}} = 90° - \theta_{\mathrm{l}}$ for small H.

By performing a range compression, as proposed in this thesis, θ_{ASE} can be reduced (green line in Fig. 3.4) to below one degree, as is the case for the spaceborne scenario (blue line) without range compression. In the same manner, the spaceborne signal could be range-compressed for a further reduction. However, this poses a challenge for the on-board processing.

This raises the question if the θ_{ASE} of a spaceborne geometry does require a further reduction that can be achieved with range compression. After the angular spectrum estimation, the SAR signal will occupy an angular area Θ_{est} equivalent to θ_{ASE} plus half the angular resolution θ_{res} of the spectrum estimator on both sides. Thus,

$$\max(\Theta_{\mathrm{est}}(\theta_{\mathrm{l}})) - \min(\Theta_{\mathrm{est}}(\theta_{\mathrm{l}})) = \theta_{\mathrm{ASE}}(\theta_{\mathrm{l}}) + \theta_{\mathrm{res}}, \tag{3.11}$$

which sets a limit for separating the instantaneous SAR signal from surrounding interferers. Now, a conservative approach for the antenna pattern notching would be to only place nulls outside of the instantaneous mainlobe because this allows for a good beamforming performance even if the system calibration is degraded (as is the case for the

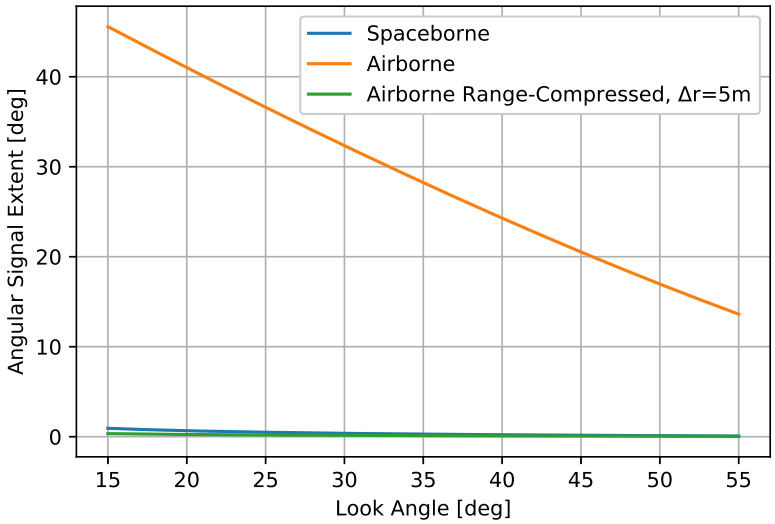

Fig. 3.4.: Angular signal extent in elevation for SAR systems operating with a 20 μs chirp at $H = 3\ km$ (airborne, orange), at $H = 600\ km$ (spaceborne). The green line represents the airborne system after range compression.

real data of Chapter 4). A notching inside the outer parts of the mainlobe is still possible with a very good instrument calibration. However, placing a notch inside the mainlobe if there are errors in the calibration results in a deformed mainlobe. Thus, the gain at the main peak can not be predicted very well and this will degrade the radiometric calibration and increase the sensitivity to mispointing. The beamwidth depends on the antenna height H_a in elevation and on the antenna length L_a in azimuth. Θ_BW in elevation can be approximated for a linear array to [60]:

$$\Theta_\mathrm{BW} \approx \frac{\lambda}{H_\mathrm{a}} = \frac{\lambda}{Nd}\bigg|_{d=0.5\lambda} = \frac{2}{N} \tag{3.12}$$

and is plotted in Fig. 3.5. Thus,

$$\theta_\mathrm{ASE} + \theta_\mathrm{res} < \theta_\mathrm{BW}. \tag{3.13}$$

Note, that θ_res depends on the used spectral estimator, the antenna length, N, the SNR and the number of samples v used for the estimation. More complex spatial estimators [110–112] better resolve signals in the angular domain but come with the cost of an

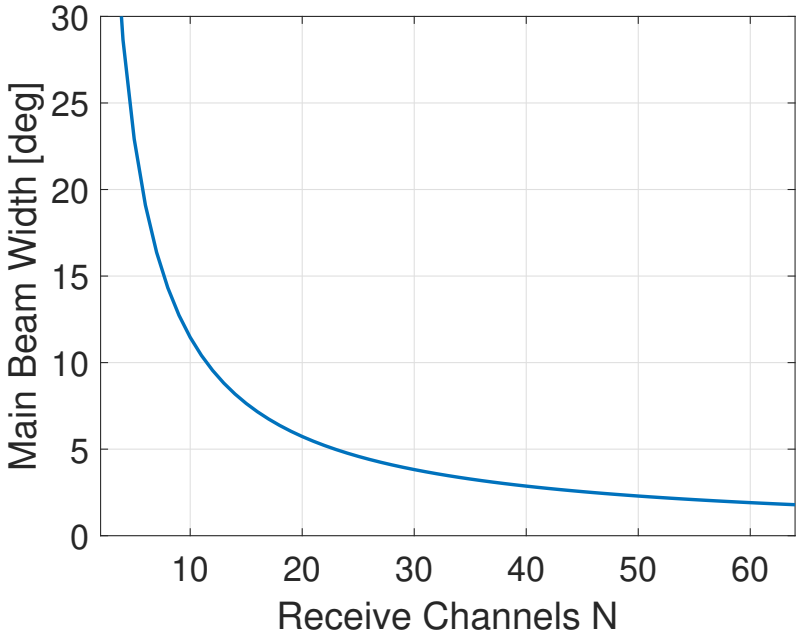

Fig. 3.5.: a) Main beamwidth of antenna pattern synthesized with N subelements with spacing $d = 0.5\lambda$. Note that the beamwidth is defined by the resulting antenna length.

increased processing. Nevertheless, this suggests that a further range compression for a spaceborne system would only be required, if a very narrow beamwidth or a very long transmit chirp were used. A narrow beamwidth requires the use of dispersive beams (frequency sublooks) to compensate the pulse extension loss [75]. This results in an inherent reduction of θ_{ASE}, as the pulse duration will be split among the frequency sublooks.
In the following, algorithms of three different categories are presented. First, DBF algorithms for a system with N channels in elevation are presented in Section 3.3.1. Next, they are adapted for systems with M channels in azimuth in Section 3.3.2. Without loss of generality, algorithms from both categories can be selected and combined for a system that is capable to perform DBF in both dimensions. This allows for a two-dimensional integration of the INC and can reduce the RFI detection gap further. However, applying both categories to a system with $M \cdot N$ channels in a sequential manner impairs the effectiveness of the algorithms ($N-1$ are set in range first and then $M-1$ in azimuth, which results in a suboptimal performance of the MVDR). The last category (Section 3.3.3) describes a method for two-dimensional MVDR beamforming that is in theory able to

place a total of $(N-1)(M-1)$ notches due to the increased degree of freedom.

3.3.1. DBF in Elevation

Pulse-Wise MVDR

The fastest approach is to estimate the INC on a pulse-wise basis in the time domain as shown in Fig. 3.6. For each pulse p of the signal represented in Eq. (2.20), the sample covariance of Eq. (3.5) is computed on

$$\mathbf{x}_p(u,m) = s_{\mathrm{R}}(u,p,m). \tag{3.14}$$

The result is inserted into Eq. (3.7) for

$$\theta_{\mathrm{l}}(u_{\min}) - \frac{\theta_{\mathrm{res}}}{2} \leq \Theta \leq \theta_{\mathrm{l}}(u_{\max}) + \frac{\theta_{\mathrm{res}}}{2}. \tag{3.15}$$

Note that $\theta_{\mathrm{l}}(u)$ of range sample u is defined by Eq. (2.17). Next, the pulse-dependent weights $\mathbf{w}_p$ are calculated with Eq. (3.4). Each pulse is then individually beamformed with $\mathbf{w}_p$.

Throughput can be further improved by recalculating the beamform weights only every other pulse. However, this makes the filter vulnerable to pulsed RFI that is not present in each pulse.

Regardless of the choice, the estimation of the INC can not be computed in the entire illuminated swath, which is equivalent to the angular area Θ occupied by the angular extent of all ground returns (Fig. 3.3). Hence, the Pulse-Wise MVDR (PWMVDR) is blind to interferers located inside the SAR swath. It's main purpose is the mitigation of out-

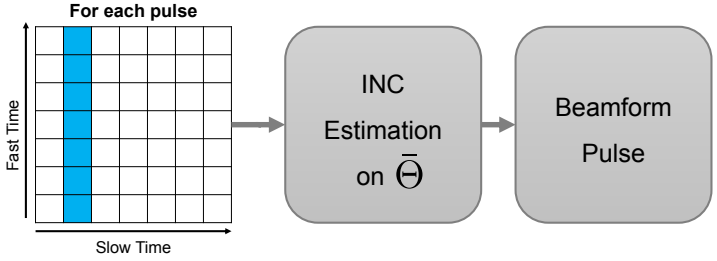

Fig. 3.6.: Pulse-Wise MVDR RFI mitigation with DBF. A mitigation of $N-1$ interferers per pulse is possible.

of-swath interference. This only makes the PWMVDR a good choice for acquisitions in forest or isolated areas where no interference is expected in the imaged area itself. Images of urban areas or of areas that are expected to be contaminated by interference (e.g., an airport in the image) can not be efficiently filtered. A total of $N-1$ notches are fixed for the entire pulse to minimize the interference on a global scale. Depending on the interference, especially for a number of interferers close to or larger than $N-1$, this can limit the performance.

Segment-Wise Frequency MVDR

A similar approach to the Pulse-Wise MVDR can be implemented in the range-frequency domain. The following algorithm is depicted in Fig. 3.7. First, a range FFT is performed on the data. Let the range-frequency azimuth-time signal of Eq. (2.20) be described with $S_{\mathrm{R}}(U,p,m)$, where U represents the range-frequency bins. Then, the INC is estimated for each frequency bin U to

$$\mathbf{x}_U(p,m) = S_{\mathrm{R}}(U,p,m). \tag{3.16}$$

This requires the algorithm to be performed on a small segment of multiple pulses. Again, the result is inserted into Eq. (3.7) for

$$\theta_{\mathrm{l}}(u_{\min}) - \frac{\theta_{\mathrm{res}}}{2} \leq \Theta \leq \theta_{\mathrm{l}}(u_{\max}) + \frac{\theta_{\mathrm{res}}}{2}. \tag{3.17}$$

Each frequency bin line is then beamformed with the MVDR weights $\mathbf{w}_U$. Because each frequency bin is filtered with individual beamforming weights, the Segment-Wise Frequency MVDR (SWFMVDR) is able to place $N-1$ fixed notches at each frequency

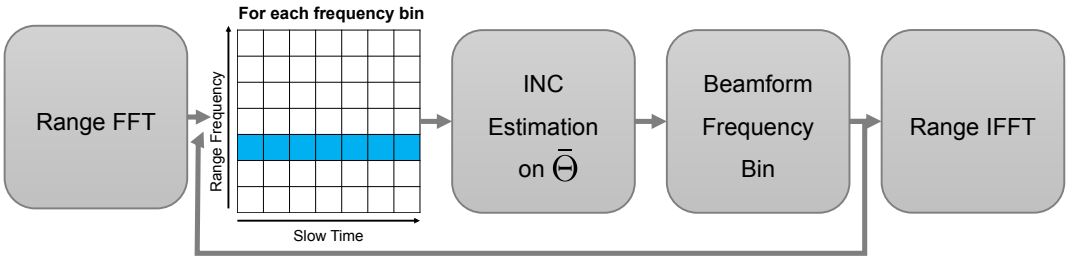

Fig. 3.7.: Segment-Wise Frequency MVDR RFI mitigation with DBF. A mitigation of $N-1$ interferers per frequency bin is possible.

bin. Hence, for a total number of F frequency bins, the total number of notches in the segment is $(N-1)F$. However, as before, the angular spectrum contains the information of the entire angular ground extent. The SWFMVDR is also blind to interferers in the entire illuminated swath (Fig. 3.3) because the entire pulse was used for the FFT. Therefore, it addresses out-of-swath interferers. The advantage of this approach is that the notches are variable in the frequency domain. An image that is contaminated with many narrow band interferers (e.g., more than $N-1$) benefits from this approach over the Pulse-Wise MVDR.

Range-Dependent Time MVDR

It is important to reduce the RFI detection gap of the INC estimation (angular extent of SAR signal) if the RFI mitigation is to be improved. Instead of performing pulse-wise operations, the INC estimation can be performed for different range lines. This reduces the RFI detection gap to the angular extent of the instantaneous SAR signal, which, in elevation, is defined by the PE. Fig. 3.8 illustrates the reduction of the RFI detection gap. The advantage over Fig. 3.3 is clearly visible.
As discussed in Section 3.2.3, an airborne system benefits of an additional range compression of the data prior to the INC estimation. For a spaceborne system, this is generally not necessary and thus the range compression and range decompression steps applied in the following algorithms can be omitted. As shown in Fig. 3.9, the INC can then be estimated on each range line of a small azimuth segment with

$$\mathbf{x}_u(p,m) = s_{\mathrm{R}}(u,p,m). \tag{3.18}$$

The number of pulses in the segment needs to be small enough to keep the AoA change of the interferer (caused by the relative motion) small, otherwise multiple notches need to be placed towards the same interferer to widen the notch. On the other hand, the estimate accuracy of the INC increases with the number of pulses. The angular integration area for the INC estimation is adaptively changed in range for an integration over all angles except for

$$\theta_{\mathrm{l}}(u) - \frac{\theta_{\mathrm{res}}}{2} \leq \Theta \leq \theta_{\mathrm{l}}(u) + \frac{\theta_{\mathrm{res}}}{2}. \tag{3.19}$$

Thus, the instantaneous RFI detection gap for each line is reduced to the resolution of the IRF (if range compressed) and depends on the transmit chirp parameters. Each range

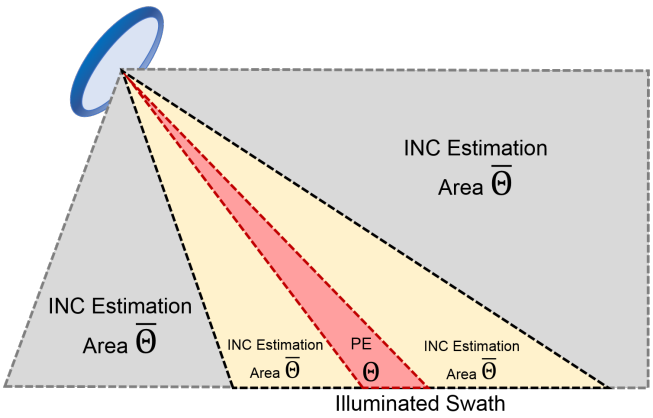

Fig. 3.8.: After range compression, the PE in each range line is reduced to the resolution of the IRF. The INC can be estimated on part of the illuminated swath in a range-dependent manner to reduce the RFI detection gap.

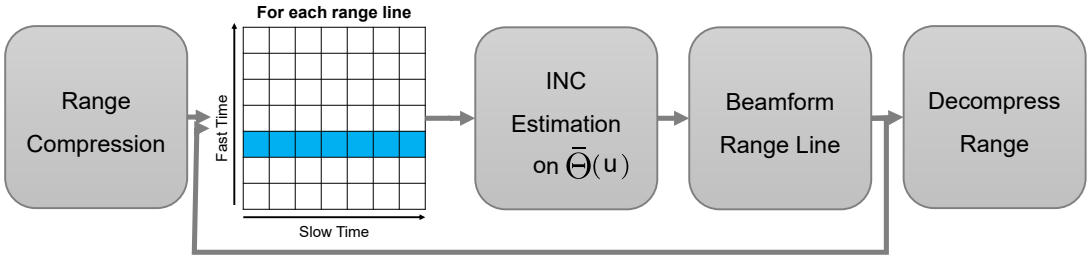

Fig. 3.9.: Range-Dependent Time MVDR RFI mitigation with DBF. A mitigation of $N-1$ interferers per range line u is possible.

line is individually beamformed with $\mathbf{w}_u$. If needed, a decompression in range can now be performed. The number of instantaneous notches is $N-1$, but the notches are variable in range. This results in a local minimization of the interferer energy. In addition, the Range-Dependent Time MVDR (RDTMVDR) is also capable of automatically notching range-dependent ambiguities and orthogonal waveforms.

Range-Dependent Frequency MVDR

An extension of the Range-Dependent Time MVDR is the Range-Dependent Frequency MVDR (RDFMVDR) shown in Fig. 3.10. Here, the raw data can be range compressed as well to reduce the PE (e.g., necessary for the airborne case as discussed in 3.3). Instead of performing an INC estimation for each range line, the Range-Dependent Frequency MVDR is computing the range FFT on small and non-overlapping range windows of

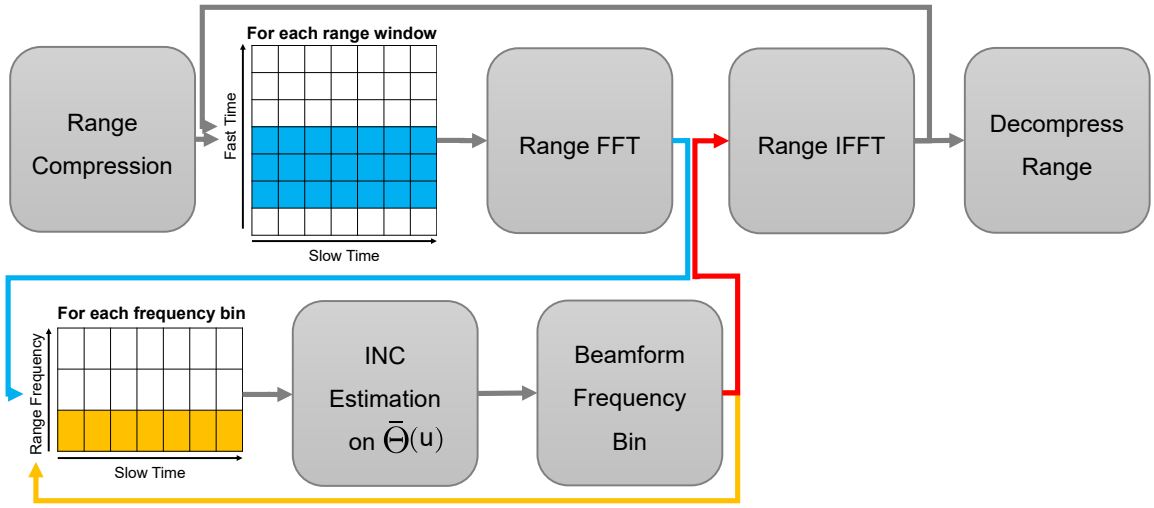

Fig. 3.10.: Range-Dependent Frequency MVDR RFI mitigation with DBF. A mitigation of $N-1$ interferers per range window and frequency bin is possible. Range window is centered around range sample u.

length S (e.g., $S = 64$) from u_{start} to $u_{\text{end}} = u_{\text{start}} + S$. This is illustrated with the blue arrow in Fig. 3.10. The INC estimation is then performed for each frequency bin U of each small range window on

$$\mathbf{x}_{u_{\text{start}},U}(p,m) = \text{FFT}\left\{ s_{\text{R}}(u,p,m)\Big|_{u_{\text{start}} \le u \le u_{\text{end}}} \right\}(U,p,m). \tag{3.20}$$

Hereby, the angular extent occupied by the instantaneous SAR signal is given by

$$\theta_{\text{l}}(u_{\text{start}}) - \frac{\theta_{\text{res}}}{2} \le \Theta \le \theta_{\text{l}}(u_{\text{end}}) + \frac{\theta_{\text{res}}}{2}. \tag{3.21}$$

Next, each frequency bin line is beamformed (yellow arrow in Fig. 3.10) with the weights $\mathbf{w}_{u_{\text{start}},U}$ and a range IFFT is performed (red arrow in Fig. 3.10). The steps are then repeated for the next range window (gray arrow in Fig. 3.10). In the end, the beamformed data can be decompressed in range again.

The Range-Dependent Frequency MVDR has an increased computational load compared to the Range-Dependent Time MVDR, but the utilization of the frequency domain gives it the ability to place $(N-1)S$ antenna pattern notches in each range line. This is an advantage if multiple interferers are spread over the frequency spectrum and thus can be notched separately with a frequency separation. Note that the separation capabilities

are limited due to the short window size and resulting spectral leakage effects [113] (This could be solved by a windowing in the time domain). An increase of the FFT window in range reduces spectral leakage but increases the RFI detection gap, because multiple range lines and thus a larger angular extent is occupied by the instantaneous SAR signal. The full potential of the Range-Dependent Frequency MVDR can be utilized with a wide-band SAR system. The advantage of the Range-Dependent Frequency MVDR over a conventional subband processing with range sublooks is discussed next.

On the Utilization of Range-Frequency Sublooks

Instead of applying the Range-Dependent Frequency MVDR, one could also use the Range-Dependent Time MVDR on multiple range-frequency sublooks. Both approaches are capable of spreading the antenna pattern notches in range and in frequency. The difference between both methods is the resulting instantaneous PE. As before, let S be the number of frequency bins for the Range-Dependent Frequency MVDR. In addition, we represent the number of sublooks for the Range-Dependent Time MVDR with S as well for the following comparison. Consequently, both algorithms are capable of placing a total of $(N-1)S$ antenna pattern notches, with $N-1$ notches per subband. This is beneficial in case the RFI sources are spread over the frequency domain.
The slant range resolution of the focused image is approximated by [60]

$$\delta_{\mathrm{e}} = \frac{k_0 c_0}{2B_{\mathrm{W}}}. \tag{3.22}$$

Note that B_{W} represents the chirp bandwidth of the entire received chirp before sublook processing. k_0 is a scaling factor set by the amplitude weighting in the frequency domain. For a rectangular window, $k_0 = 0.89$ [60]. Thus, the instantaneous PE with S range-compressed sublooks is

$$PE_{sub} = S\delta_{\mathrm{e}}. \tag{3.23}$$

The instantaneous PE for the current range window of the Range-Dependent Frequency MVDR with length S is given by

$$PE_{RDF} = \delta_{\mathrm{e}} + S\frac{c_0}{2f_{\mathrm{s}}}. \tag{3.24}$$

f_{s} is the sampling frequency of the data. It is assumed that k_0 is identical in both cases.

The Range-Dependent Frequency MVDR is superior if the instantaneous PE is smaller:

$$PE_{sub} - PE_{RDF} > 0 \tag{3.25}$$

Inserting Eq. (3.23) and Eq. (3.24) into Eq. (3.25) yields

$$S > \frac{1}{1 - \frac{c_0}{2 f_\mathrm{s} \delta_\mathrm{e}}} = \frac{1}{1 - \frac{B_\mathrm{W}}{f_\mathrm{s} k_0}} \tag{3.26}$$

for

$$\frac{f_\mathrm{s} k_0}{B_\mathrm{W}} > 1. \tag{3.27}$$

In case of the experimental data that is used in Chapter 4, the Range-Dependent Frequency MVDR is superior for $S > 1.86$.

Pulsed-RFI MVDR

Interferers that transmit continuously during the flyby time of the radar can be mitigated with the previous algorithms. However, RFI signals that appear as short pulses in the SAR data benefit from small INC estimation windows in range (Fig. 3.11). Similar to the Range-Dependent Time MVDR, the INC estimation is performed on range-dependent windows. For the Pulsed-RFI MVDR, the windows are restricted to the individual pulse according to

$$\mathbf{x}_{u_\mathrm{start},p}(u,m) = s_\mathrm{R}(u,p,m)\Big|_{u_\mathrm{start} \leq u \leq u_\mathrm{end}}. \tag{3.28}$$

Hereby, the angular extent occupied by the instantaneous SAR signal is given by

$$\theta_\mathrm{l}(u_\mathrm{start}) - \frac{\theta_\mathrm{res}}{2} \leq \Theta \leq \theta_\mathrm{l}(u_\mathrm{end}) + \frac{\theta_\mathrm{res}}{2}. \tag{3.29}$$

3.3.2. DBF in Azimuth

In the case of a SAR with M channels in azimuth, the Pulse-Wise MVDR and Segment-Wise Frequency MVDR are also applicable but limited to the same constraints. Instead of being blind in the PE extending into the range direction, the filter is blind over the Doppler angle extent in azimuth (Fig. 3.2b and Fig. 3.12a). Unlike before, an azimuth compression is not useful as each focused point is containing information from all AoA

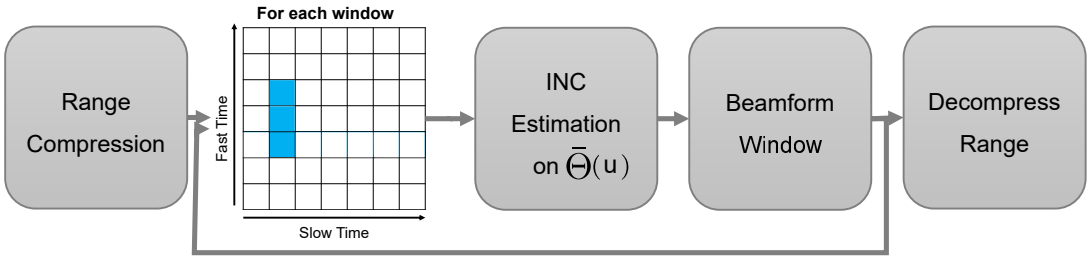

Fig. 3.11.: A pulsed MVDR RFI mitigation with DBF. A mitigation of $N-1$ interferers per window is possible.

over the synthetic aperture. Instead, the data are converted into the range-Doppler domain because the AoA is correlated with the Doppler frequency. The resulting Doppler frequency in each column is occupying its unique AoA as illustrated in Fig. 3.12b. Note that the PE in range is not relevant to a system with DBF in azimuth as it can not distinguish elevation angles. Two different algorithms that utilize the spatial distribution of the SAR signal in the Doppler plane are presented.

Doppler-Dependent MVDR

For the Doppler-Dependent MVDR (DDMVDR), the data are first converted to the range-Doppler domain via an azimuth FFT as shown in Fig. 3.13. This is performed on small azimuth segments and not on the entire image. Processing in chunks (e.g., 500 pulses) allows to adjust to a slow-time dependency of the RFI because of the platform motion. The data in each column represent a separate Doppler frequency. The INC estimation is thus performed column-wise on

$$\mathbf{x}_{f_\mathrm{D}}(u,m) = \mathrm{FFT}\left\{s_\mathrm{R}(u,p,m)\right\}(u,f_\mathrm{D},m). \tag{3.30}$$

Note that f_D refers to the Doppler frequency and θ_D to the Doppler angle. The Doppler angle extent in azimuth is changed adaptively according to the known imaging geometry so that

$$\theta_\mathrm{D}(f_\mathrm{D}) - \frac{\theta_\mathrm{res,a}}{2} \leq \Theta \leq \theta_\mathrm{D}(f_\mathrm{D}) + \frac{\theta_\mathrm{res,a}}{2}. \tag{3.31}$$

Note that $\theta_\mathrm{res,a}$ represents the angular azimuth resolution in this case. Each column is beamformed and an azimuth IFFT is applied. The algorithm is the equivalent to the Range-Dependent Time MVDR but adapted to the Doppler plane for a system with DBF in azimuth.

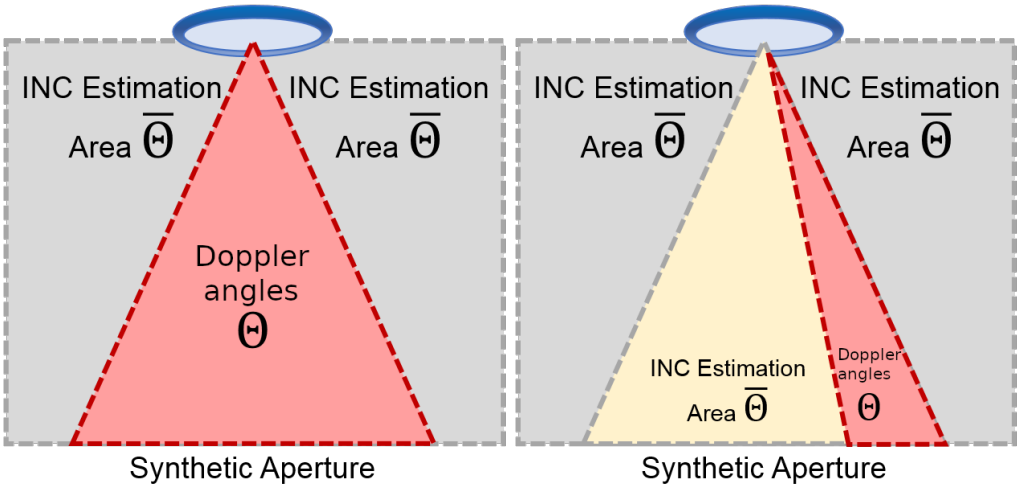

(a) (b)

Fig. 3.12.: a) At each time instance, the radar is receiving returns from the entire synthetic aperture. The Pulse-Wise MVDR and Segment-Wise Frequency MVDR are therefore blind to interference within the synthetic aperture due to the Doppler angle extent in azimuth. b) In the range-Doppler domain, the AoA in azimuth is correlated with the Doppler frequency. This can be utilized to reduce the RFI detection gap because the instantaneous Doppler angle is different in each Doppler bin.

Doppler-Dependent Frequency MVDR

An additional range FFT is applied for the Doppler-Dependent Frequency MVDR (DDFMVDR). As displayed in Fig. 3.14, the resulting two-dimensional frequency image chunk is then beamformed in individually windows on

$$\mathbf{x}_{U,f_\mathrm{D}}(U, f_\mathrm{D}, m) = \mathrm{FFT2D}\left\{s_\mathrm{R}(u, p, m)\right\}(U, f_\mathrm{D}, m)\Big|_{U_\mathrm{start}\leq U\leq U_\mathrm{end}, f_\mathrm{D,start}\leq f_\mathrm{D}\leq f_\mathrm{D,end}}. \tag{3.32}$$

Again, the Doppler extent in azimuth is changed adaptively according to the known imaging geometry so that

$$\theta_\mathrm{D}(f_\mathrm{D,start}) - \frac{\theta_\mathrm{res,a}}{2} \leq \Theta \leq \theta_\mathrm{D}(f_\mathrm{D,end}) + \frac{\theta_\mathrm{res,a}}{2}. \tag{3.33}$$

The dimensions of the window can be choosen at will but represent a trade off between: a) the sample number for the INC estimation, b) the frequency resolution of the window

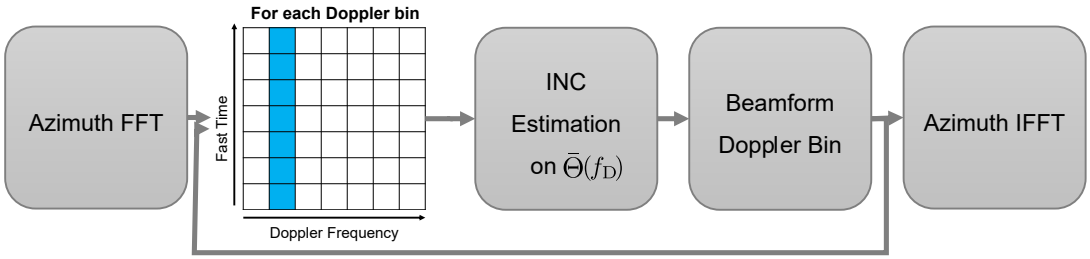

Fig. 3.13.: Doppler-Dependent MVDR RFI mitigation with DBF. A mitigation of $M-1$ interferers per Doppler bin is possible.

and c) the Doppler resolution and hence the RFI detection gap of the algorithm. In the end, the beamformed data are converted back to the time domain. The increased processing gives the ability to change the notches adaptively over the bandwidth of the range chirp.

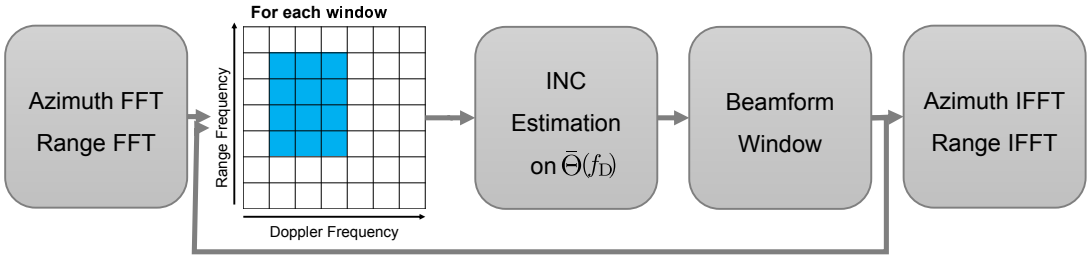

Fig. 3.14.: Doppler-Dependent Frequency MVDR RFI mitigation with DBF. A mitigation of $M-1$ interferers per window is possible.

3.3.3. Two-Dimensional DBF

A two-dimensional antenna array with N channels in elevation and M channels in azimuth consists of $N \cdot M$ channels. It is therefore possible to place $(N-1)(M-1)$ antenna pattern notches at the cost of an increased computational load. In addition, the two-dimensional angular resolution of the targets allows a significant reduction of the PE and Doppler angle extent. The angular extent of the ideal point target, shown in Fig. 3.15 in yellow, can be reduced to a small patch via range compression (e.g., necessary for the airborne case as discussed in 3.3) and conversion to the range-Doppler domain.
The RFI filtering can then be applied with a two-dimensional MVDR (2DMVDR),

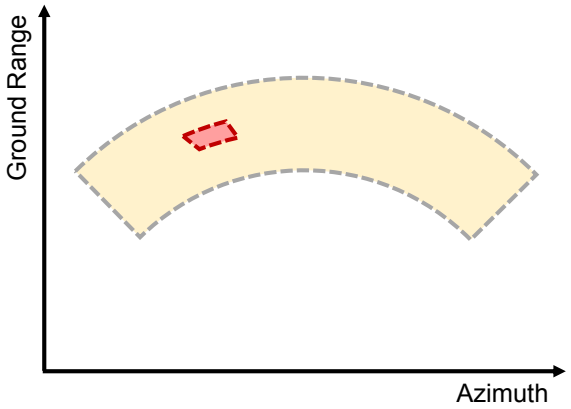

Fig. 3.15.: The pulse and Doppler extent of an ideal point target projected onto the ground (yellow). Two-dimensional DBF is capable of separating the extent to small patches (red box) in the range-compressed Doppler domain. This reduces the RFI detection gap of the INC estimation.

shown in Fig. 3.16. The INC estimation is applied to multiple windows

$$\mathbf{x}_{u,f_\mathrm{D}}(u, f_\mathrm{D}, m) = \mathrm{FFT}\left\{s_\mathrm{R}(u, p, m)\right\}(u, f_\mathrm{D}, m)\Big|_{u_\mathrm{start}\le u\le u_\mathrm{end}, f_\mathrm{D,start}\le f_\mathrm{D}\le f_\mathrm{D,end}}. \quad (3.34)$$

The windows are then beamformed. Again, the dimensions of the window are a trade off between instantaneous angular extent and sample size for the INC estimation. The integration is limited in both dimensions by

$$\theta_\mathrm{l}(u_\mathrm{start}) - \frac{\theta_\mathrm{res}}{2} \le \Theta \le \theta_\mathrm{l}(u_\mathrm{end}) + \frac{\theta_\mathrm{res}}{2} \quad (3.35)$$

and

$$\theta_\mathrm{D}(f_\mathrm{D,start}) - \frac{\theta_\mathrm{res,a}}{2} \le \Theta \le \theta_\mathrm{D}(f_\mathrm{D,end}) + \frac{\theta_\mathrm{res,a}}{2}. \quad (3.36)$$

By performing the 2DMVDR on small azimuth chunks, the RFI variability due to the moving platform can be better compensated. Additionally, the impact of topography can be better handled. For a radar with a wide aperture (long integration time), the algorithm should be applied on multiple azimuth sublooks if the topography variation is large. An alternative would be an integration of the 2DMVDR into a backprojection focusing algorithm [114, 115].

3.3.4. Summary of Proposed Algorithms

The methods proposed in this chapter are summarized in Table 3.1.

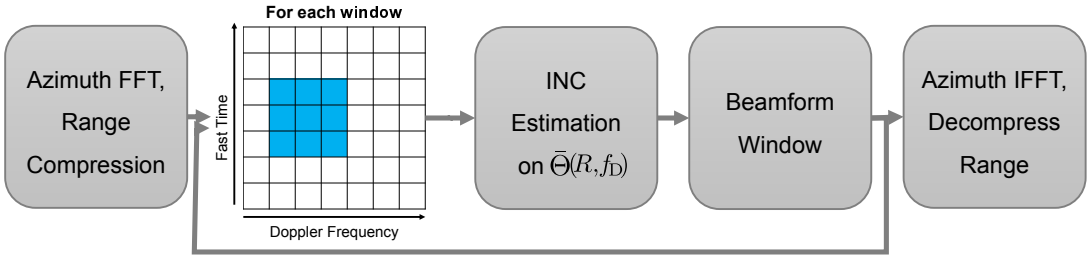

Fig. 3.16.: Two-dimensional MVDR RFI mitigation with DBF. A mitigation of $(N-1)(M-1)$ interferers per window is possible.

Table 3.1.: Summary of the presented algorithms.

Algorithm	DBF Type	N-1 nulls per	RFI Type	Advantage	Disadvantage
Pulse-Wise	Elevation	per pulse	Both	Fast, for scenes without expected in-swath interference	Blind in-swath
Segment-Wise Frequency	Elevation	per frequency bin	Continuous	Fast, for scenes without expected in-swath interference	Blind in-swath
Range-Dependent Time	Elevation	per range line	Continuous	Recovers part of swath despite in-swath interference	Processing time
Range-Dependent Frequency	Elevation	per range window and frequency bin	Continuous	Recovers part of swath despite in-swath interference. Beneficial for smaller antenna arrays.	Increased processing time
Pulsed-RFI	Elevation	per range window	Pulsed	Suitable for pulsed RFI scenarios. Recovers in-swath interference	Not detecting weak CW interference
Doppler Dependent	Azimuth	per Doppler frequency bin	Continuous	Fast, for scenes without expected in-swath interference	Blind in-swath
Doppler Dependent Frequency	Azimuth	per range-Doppler window	Both	Suitable for CW and pulsed in-swath interference	Processing time
2D	Both	per range-Doppler window	Both	Capable of placing most notches and can recover largest swath percentage	Processing time

3.4. Simulations for DBF in Elevation

The previous sections introduced new RFI mitigation algorithms for SAR based on DBF. The goal of this section is to analyze and to compare the performance of the algorithms that utilize DBF in range, before they are applied to experimental data in Section 4 (which was recorded with a DBF in elevation system). For this purpose, a simulator was implemented in the framework of this thesis.

3.4.1. Simulation Steps and Parameters

As an initial step, the implemented simulator simulates the multi-channel SAR raw data (as formulated in Section 2.5) in baseband as if acquired by a planar antenna at an altitude of 3.2 km. The channel spacing is half a wavelength. The channel number (number of array elements) N ranges from 2 to 64. Even though the total length of antennas are proportional to the number of elements, this is an inevitable design requirement for DBF antennas. Having antenna elements longer than half wavelength would increase grating lobes in the antenna pattern, significantly impacting the DBF performance.
It is therefore important to note that two effects are visible in the simulations. First, the increased number of N increases the number of notches that can be placed in the antenna pattern. The ability of the algorithms to handle a specific number of interferers can therefore be attributed to the increase of the number of antenna subelements N. On the other hand, the increased antenna length sharpens the main beam. It improves the angular resolution that separates the instantaneous SAR signal from the interferer signals in the angular domain. Therefore, the increased antenna length is responsible for the improvement of the total percentage of the swath that can be recovered with increasing antenna size.
The observed scene is simulated from an incidence angle of 21° to 60° and with a complex-circular Gaussian backscatter. The transmit chirp of the simulated system is 20 μs long and occupies a bandwidth of 120 MHz (in accordance with the airborne experimental data available in Chapter 4), sampled at 290 MHz. A total of 500 pulses are simulated at a center wavelength of λ. Note that the complex-circular Gaussian backscatter allows to simulate the 500 pulses without moving the platform (in contrary to the case of a non-Gaussian target). The SNR of the raw data is set to two values: a) 0 dB to simulate the worst case of an extended target with identical SNR in the focused image and b) 37.63 dB which is equivalent to the range gain of a point target for

Table 3.2.: Parameters used for the simulation of the SAR and RFI data

Parameter	**Value**
Elevation Channels	2 to 64
Channel Spacing	0.5λ
Sample Frequency	290 MHz
Center Frequency	435 MHz
Pulse Bandwidth	120 MHz
Pulse Duration	20 μs
Near Range Angle	21°
Far Range Angle	60°
Platform Altitude	3.2 km
Number of Pulses	500
Backscatter Amplitude	Rayleigh distribution
Backscatter Phase	Uniform distribution between 0° and 360°
SNR	0 dB, 37.63 dB
RFI Type	Continuous Wave

the simulated chirp. Next, an RFI signal is simulated that is received by the same multi-channel SAR system. The RFI type is a CW interferer (note that the effect of wide-band RFI is discussed in Section 3.5). The exact RFI specifications (location and transmit frequency) are presented in the following subsection. All parameters are summarized in Table 3.2. The data are then processed according to Fig. 3.17. Both SAR and RFI data, are compressed in range (Note that this is only necessary in the airborne scenario to reduce the angular pulse extent. This is not necessary in the spaceborne case and could also be achieved with dispersive beams). SCORE beamforming is applied to the SAR data to produce the ideal reference data. The contaminated multi-channel data are synthesized by adding the range-compressed SAR and RFI data. The contaminated dataset is then processed with the previously presented RFI mitigation algorithms. Because the channels are aligned in elevation, the selected algorithms are the Pulse-Wise MVDR, Range-Dependent Time MVDR and Range-Dependent Frequency MVDR. The output of the algorithm is the recovered data. Finally, the recovered data are divided by the ideal reference data. The output is thus a residual error image that can be analyzed further according to the previously presented multiplicative error model (see error model in Section 2.5.3).

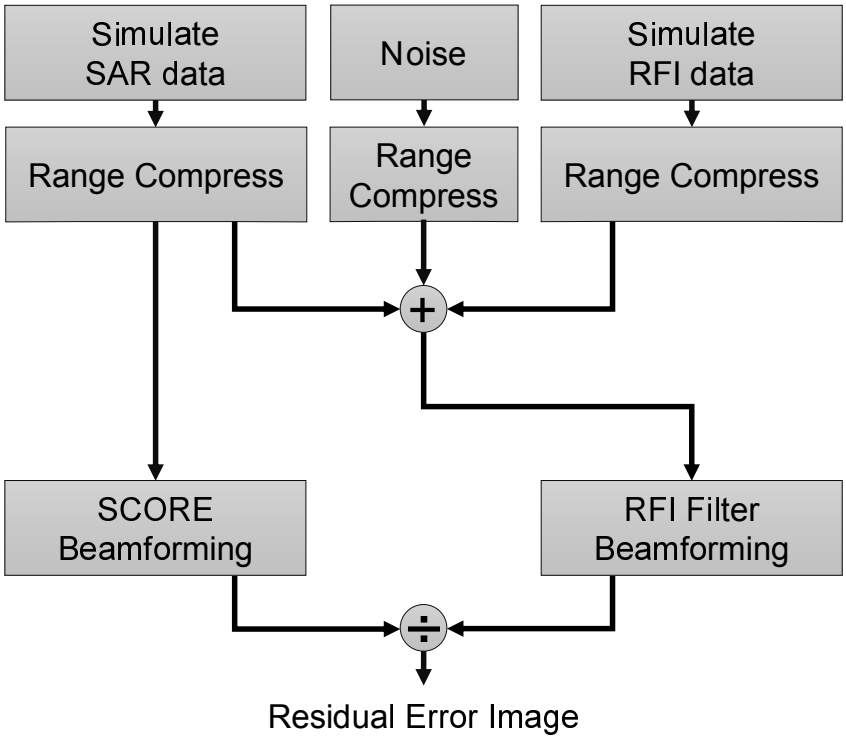

Fig. 3.17.: Simulation chain for the performance evaluation of the RFI mitigation. The simulated SAR and RFI data are range compressed individually. The range-compressed SAR data are then beamformed with SCORE to create the ideal reference data. Contaminated data are produced by summing the range-compressed SAR and RFI data. The contaminated data are then corrected using the algorithms. In the end, the algorithm output is divided by the reference data to produce the residual error image.

3.4.2. Simulated Interference Scenarios

Four different interferer scenarios are considered for the performance analysis with the implemented simulator. The number of interferers is different in each case. This allows the testing of the algorithms under different conditions and to determine their filtering capabilities. The scenarios are described next.

Scenario A

The first scenario consists of a single interfering source that is located outside of the swath at -20° and transmits a CW at a baseband frequency of 40 MHz[1]. A single in-

[1]The effect of wide-band RFI is discussed in Section 3.5.

terferer represents the easiest case and it is expected that all algorithms can filter the interferer regardless of the number of available channels. Because the interferer is outside of the swath, it is possible to fully recover the SAR data. This scenario is depicted in Fig. 3.18.

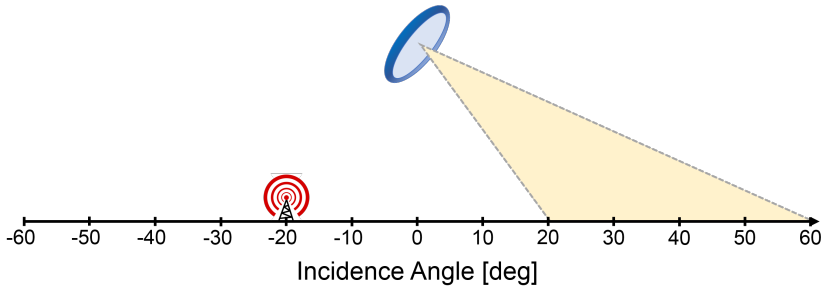

Fig. 3.18.: Scenario A: A single interferer is located outside the swath at -20°. It is transmitting a signal at 40 MHz in baseband.

Scenario B

An additional interferer is placed inside the swath at 40° for Scenario B. This interferer is transmitting at a baseband frequency of 25 MHz. Because it is located inside the swath, the SAR signal can not be recovered in its angular proximity. However, it is expected that the filters can recover part of the swath. The percentage of the swath that can be recovered will depend on the algorithm capabilities.

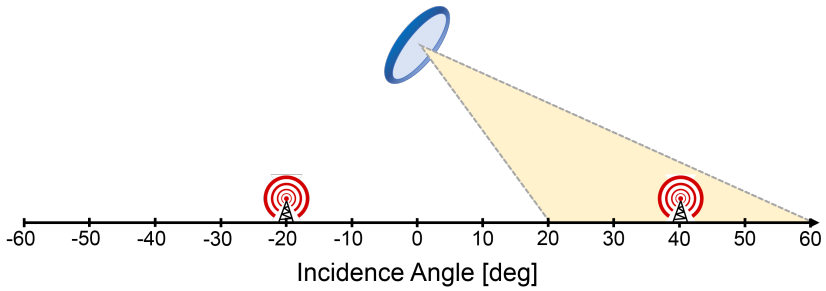

Fig. 3.19.: Scenario B: Two interferers are present. The first interferer is outside the swath at -20° with baseband frequency 40 MHz. The second interferer is inside the swath at 40° with a baseband frequency of 25 MHz.

Scenario C

The number of interferers is increased to 11 for Scenario C. All interferers are located outside of the swath, which makes a full recovery of the SAR signal possible. The interferers are equally spaced in 5° intervals starting from -50° to 0°. Each interferer is transmitting at a different frequency, starting from -60 MHz to 25 MHz in baseband with a 5 MHz spacing. The quality of the recovery is expected to depend on the number of channels N and on the used algorithm.

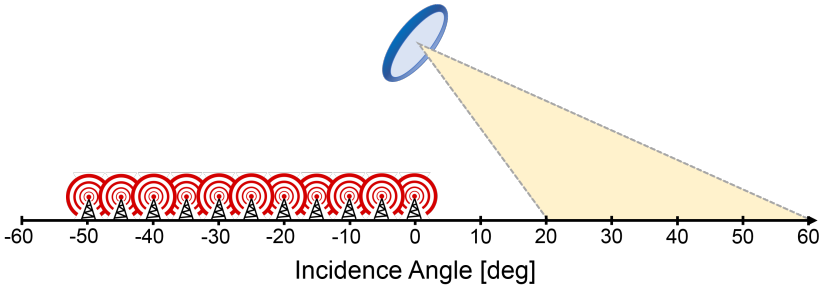

Fig. 3.20.: Scenario C: 11 interferers are present and outside of the swath. Locations range from -50° to 0° in 5° intervals. Transmitting frequencies range from -60 MHz to 25 MHz in baseband with 5 MHz spacing.

Scenario D

The number of interferers remains at 11 for Scenario D. However, the interferer spacing is changed and four interferers are moved inside of the swath, which prevents a full recovery of the SAR signal. The interferers are now equally spaced in 10° intervals

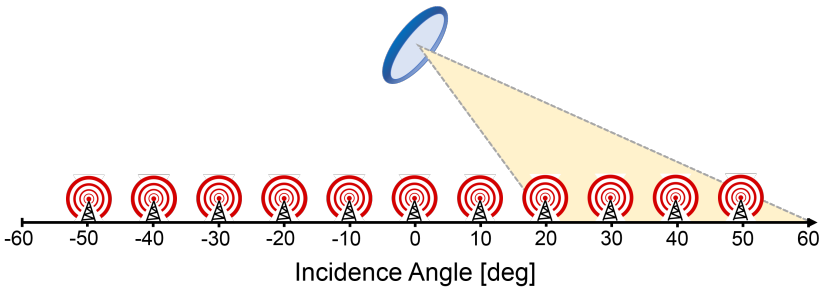

Fig. 3.21.: Scenario D: 11 interferers are present. They are located inside and outside of the swath. Locations range from -50° to 50° in 10° intervals. Transmitting frequencies range from -60 MHz to 25 MHz in baseband with 5 MHz spacing.

starting from -50° to 50°. The interferers transmitting frequencies stay the same (starting from -60 MHz to 25 MHz in baseband with a 5 MHz spacing). Reconstructing the SAR data is a challenge because the in-swath interferers are spread over the entire swath. The recovery is expected to improve with the number of channels. However, the Range-Dependent Frequency MVDR is expected to perform the best in this scenario because of its ability to change the notches adaptively in the frequency domain.

3.4.3. Simulation Results

An important aspect of the presented algorithms is the estimation of the INC matrix by integrating a spatial spectrum estimate. The spatial spectrum is estimated with the Capon method because of its robustness against false peaks in the spectrum and its low computational complexity. This choice comes at the expense of a worsening angular resolution θ_{res} with smaller SNR. In Fig. 3.22 the spatial spectrum estimate for a range line of Scenario A is shown. Because the data are compressed in range, the instantaneous SAR signal return from the picked range line is coming from 54°. The RFI source is located at -20°. Note that the spectrum estimation is performed at the center frequency of the radar. Because the interferer is shifted from the center frequency, this causes an angular offset $\Delta\theta_{\mathrm{RFI}}$ in the spatial estimate, as the phase ramp induced for θ_{RFI} at the interferer frequency f_{RFI} is equivalent to a phase ramp of different AoA at f_{c}:

$$\frac{2\pi d f_{\mathrm{c}}}{\mathrm{c}_0} \sin\left(\theta_{\mathrm{RFI}}\right) = \frac{2\pi d f_{\mathrm{RFI}}}{\mathrm{c}_0} \sin\left(\theta_{\mathrm{RFI}} + \Delta\theta_{\mathrm{RFI}}\right). \tag{3.37}$$

This shift is acceptable because once the algorithm places a notch in the antenna pattern towards $\theta_{\mathrm{RFI}} + \Delta\theta_{\mathrm{RFI}}$ for f_{c}, it is effectively placing a notch towards θ_{RFI} for f_{RFI}. It is also evident from Fig. 3.22 that the two different SNRs yield different resolutions in the spatial spectrum. While the SNR of 37.63 dB shows a good ability to resolve both signals accurately and with low sidelobes, the SNR of 0 dB results in wide peaks with high sidelobes. Note that an improved resolution θ_{res} can be achieved with more complex spectrum estimators at the cost of computational load. In the following subsections it will be shown that the algorithms still perform reasonably good at SNR of 0 dB. However, the resolution θ_{res} in the spatial spectrum impacts the ability to suppress interference in the swath as the widening peak increases the visible PE. For the SNR = 0 dB simulation, the integration gap around the PE is therefore choosen so that the INC is not integrated

over the instantaneous SCORE main beam, as discussed before. By this means, a notch that is placed close to the instantaneous SAR signal because of the widened PE does not degrade the antenna pattern. For the SNR = 37.63 dB simulation, this integration gap is reduced to a quarter of the main beamwidth because the signals are better resolved in the spatial spectrum and demonstrate what is possible with more complex spatial estimators [110–112].

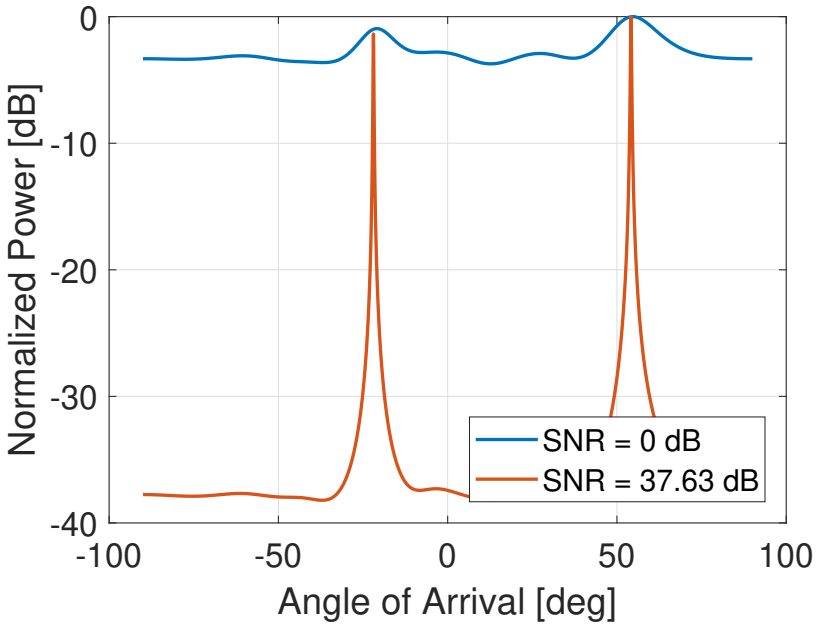

Fig. 3.22.: Capon spatial spectrum estimate of range-compressed range line with instantaneous SAR signal coming from 54° and RFI source at -20°.

Scenario A

Scenario A consists of a single interferer outside of the swath. For this reason, a spatial filter seems to be ideal to suppress the RFI and a full recovery of the swath is expected. Figure 3.23 shows the phase standard deviation of the residual error image (as defined in Section 2.5.3) measured in each range line (and thus at different incidence angles) before and after spatial filtering with the Range-Dependent Frequency MVDR beamformer (SNR = 37.63 dB). The RFI-to-Noise Ratio (RNR) is varied along the y-axis from -20 dB to 40 dB and represents the power at each subelement. It is expected that the more elements N the antenna array has, the stronger RFI powers it can suppress

because more notches are available. Figure 3.23a and Fig. 3.23c show the error before the spatial filter is applied for N = 8 and N = 32, respectively. The first observation is that the degradation of the data begins earlier for N = 8 at a RNR of -15 dB. The reason for this is that the longer array (N = 32) achieves a higher gain towards the swath and thus has a higher RFI suppression that is inherent to the antenna pattern. The data start to degrade for N = 32 at a RNR of -5 dB. The ripples in the error image are caused by the SCORE operation that results in the interferer passing through the nulls and peaks of the sidelobes. The residual phase standard deviation error after applying the Range-Dependent Frequency MVDR beamformer is shown in Fig. 3.23b (N = 8) and Fig. 3.23d (N = 32). It is evident that the residual error drops back to the noise floor for both cases. The mean μ_{σ_Φ} and variance $\sigma^2_{\sigma_\Phi}$ of the phase standard deviation error σ_Φ is computed and the 3-sigma phase standard deviation error is defined as

$$\mu_{\sigma_\Phi} + 3\sigma_{\sigma_\Phi}. \tag{3.38}$$

The difference between the ideal noise floor and the residual after filtering RFI is plotted as the 3-sigma phase standard deviation error increase in Fig. 3.24. Figure 3.24a through Fig. 3.24f show the results for N = 2, 4, 8, 16, 32 and 64, respectively. The solid colored lines represent the different algorithms for SNR = 0 dB and the dashed colored lines represent them for SNR = 37.63 dB.

The black lines show the 3-sigma increase before the algorithms are applied (note that the black line performs best in the absence of RFI because the algorithms introduce a small processing noise). They are showing low values for low RNR and suddenly increase when the RFI starts to degrade the data. From Fig. 3.24a through Fig. 3.24f it is evident that the sudden data degradation occurs at higher RNR values with increasing antenna array length because of the aforementioned reason. The results of the Pulse-Wise MVDR algorithm are shown in blue. Starting from N = 8 , the 3-sigma increase is below 2.5° regardless of SNR and RNR. For lower N, the Pulse-Wise MVDR is not behaving stably. As N increases, the maximum 3-sigma increase drops. For N = 16 the increase is below 1° and for higher N it is only a fraction of a degree. The Range-Dependent Time MVDR is shown in orange and shows a stable behavior even for N = 2. However, at N = 2 it is only able to suppress the RFI up to a RNR of 0 dB for SNR = 0 dB (up to a RNR of 5 dB for SNR = 37.63 dB). This is because only one narrow notch can be placed which makes the algorithm sensitive to a slight misplacement of the notch.

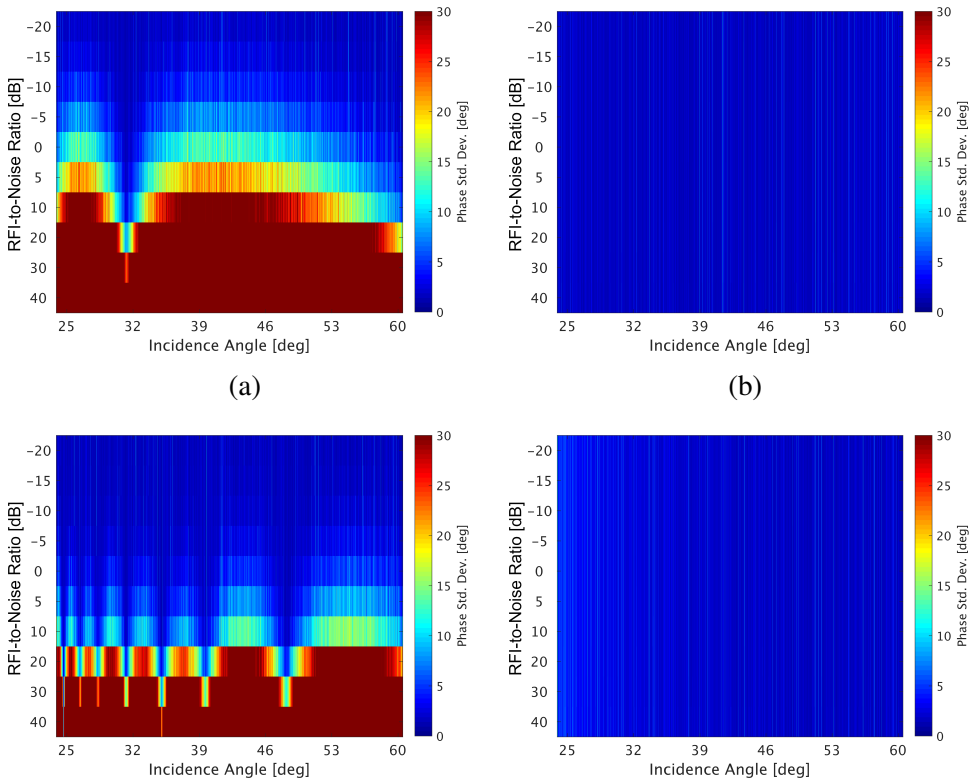

Fig. 3.23.: The phase standard deviation of the residual error image of scenario A for different RFI-to-Noise Ratios vs. the incidence angle of the instantaneous SAR signal. The SNR is 37.36 dB. a) No RFI mitigation for $N = 8$, b) After Range-Dependent Frequency MVDR beamforming for $N = 8$, c) No RFI mitigation for $N = 32$, d) After Range-Dependent Frequency MVDR beamforming for $N = 32$. The Range-Dependent Time MVDR beamformer performs similar.

For larger N, a wider notch is placed that suppresses the RFI even if a slight misplacment occurs. For $N = 4$, the 3-sigma increase of the Range-Dependent Time MVDR is constantly below 3° and for $N = 8$ it is constantly below 1.5°. After N exceeds 16, the algorithm reaches its best performance with a 3-sigma increase below 0.43°. A further increase of N does not improve the algorithm anymore. In addition, the constant 3-sigma increase causes a degradation of the data by these 0.43° compared to the uncorrected case for low RNR. The Range-Dependent Frequency MVDR beamformer (green) shows a similar behavior to the Range-Dependent Time MVDR. The maximum error shown by the green curves are below the orange curves for $N = 2$ to 8. Hence,

the Range-Dependent Frequency MVDR beamformer shows a better performance than the Range-Dependent Time MVDR because the available notches can be distributed differently at different frequencies. This changes for larger N and the maximum and constant 3-sigma increase at N = 16 is 0.62. This can be explained by the fact that the Range-Dependent Frequency MVDR injects a higher artifical noise floor than the Range-Dependent Time MVDR. This is likely due to the additional processing with windows in the frequency domain. This artificial noise floor rises close to 2° for N = 32 to 64. Overall, all presented RFI suppression algorithms based on DBF are able to handle scenario A, which consist of a single interferer outside of the swath. However, the Pulse-Wise MVDR shows an inferior behavior for N below 16 but achieves a better suppression if a lot of notches are available (and only out-of-swath interference is present). The Range-Dependent Time MVDR and Range-Dependent Frequency MVDR inject artificial noise that can degrade the data in the absence of RFI.

The maximum 3-sigma phase offset increase at RNR = 40 dB is plotted in Fig. 3.25a in dependency of array length N. Due to the scaling of the y-axis, the black line for the error pre-filtering is not visible in the plot. All algorithms show an improvement up to N = 8, which resembles the minimum array length to suppress the interferer at the given RNR. Again, the Pulse-Wise MVDR improves with increasing length while the Range-Dependent Time MVDR and Range-Dependent Frequency MVDR inject an artifical noise floor that is increasing slightly with N. Note that the maximum 3-sigma phase offset increase of this artificial noise floor is 0.8°.

The maximum 3-sigma amplitude offset increase at RNR = 40 dB is plotted in Fig. 3.25b. This error directly affects the radiometric budget. For N below 8 the RFI suppression is not sufficient and a high amplitude error is introduced. This is due to the RNR of 40 dB. For N = 8, the Range-Dependent Frequency MVDR shows the best suppression with an amplitude error of 0.2 dB followed by the Range-Dependent Time MVDR with an amplitude error of 0.3 dB. The worst suppression is reached by the Pulse-Wise MVDR with a remaining amplitude error of 0.53 dB. The error drops further for all algorithms with increasing N. It is evident that the Pulse-Wise MVDR is capable of removing the amplitude error for N larger than 32 to a residual of 0.05 dB. The Range-Dependent Time MVDR and Range-Dependent Frequency MVDR have a remaining amplitude error of 0.12 dB and 0.09 dB, respectively.

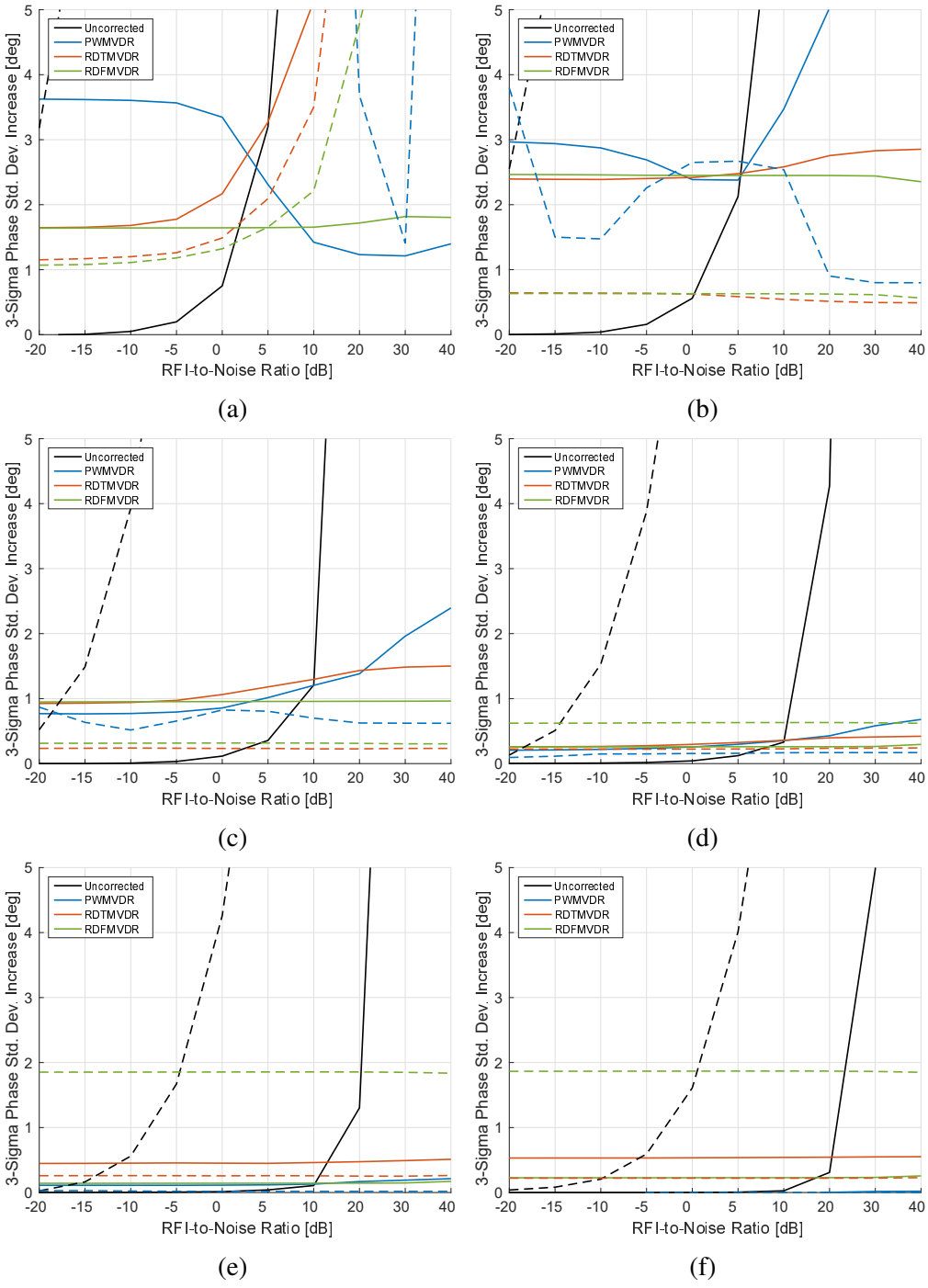

Fig. 3.24.: The 3-sigma phase standard deviation error of the residual error image of Scenario A vs. RFI-to-Noise Ratio. The plots are shown for SNR = 0 dB (solid lines) and SNR = 37.36 dB (dashed lines). a) $N = 2$, b) $N = 4$, c) $N = 8$, d) $N = 16$, e) $N = 32$, f) $N = 64$

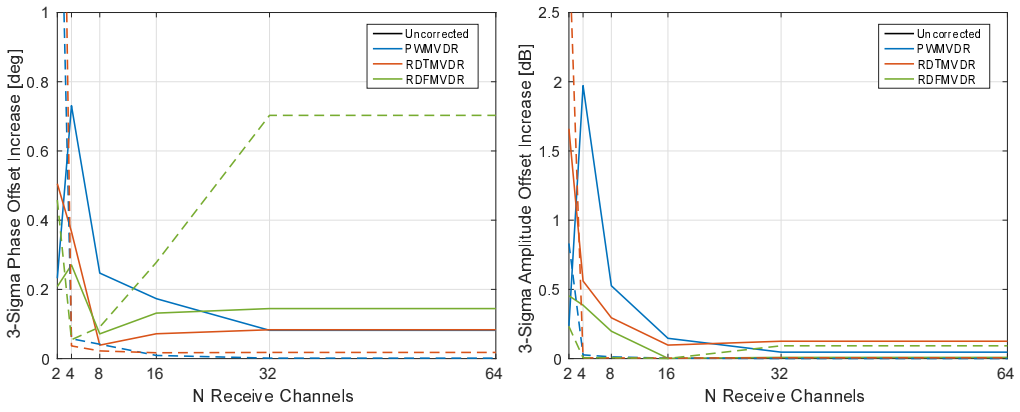

(a) (b)

Fig. 3.25.: The 3-sigma error increase of the residual error image of scenario A at an RFI-to-Noise Ratio of 40 dB vs the antenna array length. The plots are shown for SNR = 0 dB (solid lines) and SNR = 37.36 dB (dashed lines). a) Phase offset, b) Amplitude offset.

Scenario B

For scenario B, an additional interferer is put inside the swath at 40°. Because DBF is a spatial filter, part of the swath can not be recovered. The extent of the lost swath depends on the interferer power, the available notches (thus N), the beamwidth (thus antenna length) and the applied algorithm. Figure 3.26 shows the phase standard deviation of the residual error image measured in each range line before and after the Range-Dependent Frequency MVDR is applied (SNR = 37.63 dB). Again, the RNR is varied along the y-axis from -20 dB to 40 dB and represents the power at each subelement. Figure 3.26a and Fig. 3.26c show the error before the spatial filter is applied for N = 8 and N = 32, respectively. The first observation is that the degradation of the data sets for both figures already started at -20 dB. The degradation is more significant than for scenario A because the interferer inside the swath is not suppressed by the sidelobes. However, the entire swath is lost sooner for N = 8 than for N = 32 due to the narrower antenna pattern of the longer antenna. This results in a partial interference suppression with the SCORE operation when the instantaneous main beam is not looking into the interferer. The residual phase standard deviation error applying the Range-Dependent Frequency MVDR beamformer is shown in Fig. 3.26b (N = 8) and Fig. 3.26d (N = 32). The residual error drops back to the noise floor in both cases up to a RNR of about 5 dB. For stronger RNR, the interferer is causing a local degradation in the proximity of the

interferer position. As expected, the width of the lost area around the interferer decreases with increasing N (which here results in a longer antenna and thus a smaller instantaneous main beam). This is a fundamental limitation of DBF that can not be overcome by shaping the antenna pattern alone. Note that the remainder of the swath is recovered with the RFI suppression.

The amount of the lost swath is further analyzed in Fig. 3.27. Figure 3.27a shows the phase standard deviation error at RNR 40 dB for each range line after the mean phase standard deviation error of the noise floor is subtracted (N = 16). The black lines show the error if no correction is performed. Note that the lower curve is due to the SNR of 0 dB, whereas the higher black curve represents a SNR of 37.63 dB. The blue lines show the error after the Pulse-Wise MVDR is applied. The more saturated blue shows the higher SNR. For both SNR, the Pulse-Wise MVDR is not effective in restoring part of the swath. This is expected because the Pulse-Wise MVDR is blind to the in-swath interferer due to the PE. As a consequence, the antenna pattern is the regular Scan-On-Receive pattern. As the radar scans in elevation to look at different incidence angles, the fixed interferer is wandering through the sidelobes and periodic drops occur when the interferer is in an antenna pattern null. The orange lines show the result of the Range-Dependent Time MVDR beamformer. Part of the swath in the proximity of the interferer is lost, but the remaining part of the swath is restored. Note that, though the interferer is located at 40°, the antenna pattern sees it at a shifted angle due to the frequency offset from the center frequency (discussed in Section 3.4.3). The more saturated orange line for the better SNR case shows a smaller loss of the swath. The higher SNR can resolve the interferer position and the instantaneous SAR signal better because of the resolution in the Capon spectral estimate. The notch can therefore be placed closer to the instantaneous SAR AoA. The same behavior can be noticed for the Range-Dependent Frequency MVDR beamformer in green. However, the Range-Dependent Frequency MVDR is superior to the Range-Dependent Time MVDR because more of the swath can be recovered. The reason for this is that the Range-Dependent Frequency MVDR can place the notches more effectively due to the additional processing in the frequency domain. It can place different notches for the in-swath and out-of-swath interferer. The same plot is shown for N = 64 in Fig. 3.27b. The difference between this plot and the plot for N = 32 is that more of the swath is recovered because the main beamwidth is getting smaller. In addition, the resolution of the Capon spectral estimate improves with N and thus the resolution is improved for low SNR too.

The percentage of the recovered swath in dependency of N is plotted from Fig. 3.27c through Fig. 3.27e for the phase standard deviation, the phase offset and the amplitude offset, respectively. The recovered swath in the figures has a phase standard deviation error below 20°, a phase offset below 5° and an amplitude offset below 0.5 dB. For all parameters, some amount of swath can be recovered for N larger than 4. The lost swath halfens for a doubling of the anntenna length, which is due to the resulting halfening of the antenna pattern main beam. As a consequence, the improvement with N up to N = 16 is large and then starts to get smaller. In addition, it is evident that it is necessary to use the range-dependent algorithms to recover the swath. The Range-Dependent Frequency MVDR is especially superior for a smaller N. With increasing N, when a multiple of notches is available per interferer, the higher computational load can not be justified anymore and the benefit over the Range-Dependent Time MVDR diminishes.

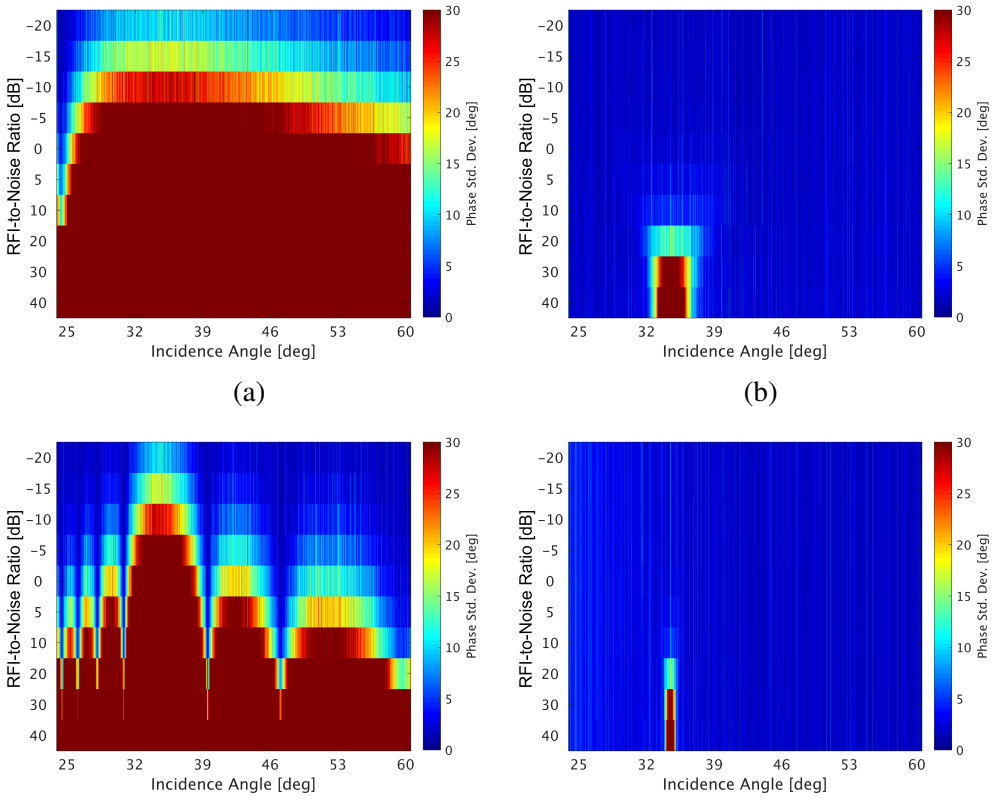

Fig. 3.26.: The phase standard deviation of the residual error image of scenario B for different RFI-to-Noise Ratios vs. the incidence angle of the instantaneous SAR signal. The SNR is 37.36 dB. a) No RFI mitigation for $N = 8$, b) After Range-Dependent Frequency MVDR beamforming for $N = 8$, c) No RFI mitigation for $N = 32$, d) After Range-Dependent Frequency MVDR beamforming for $N = 32$. The results of the Range-Dependent Time MVDR beamforming are similar, though the corrupted area increases slightly in elevation due to the less optimal notch placement.

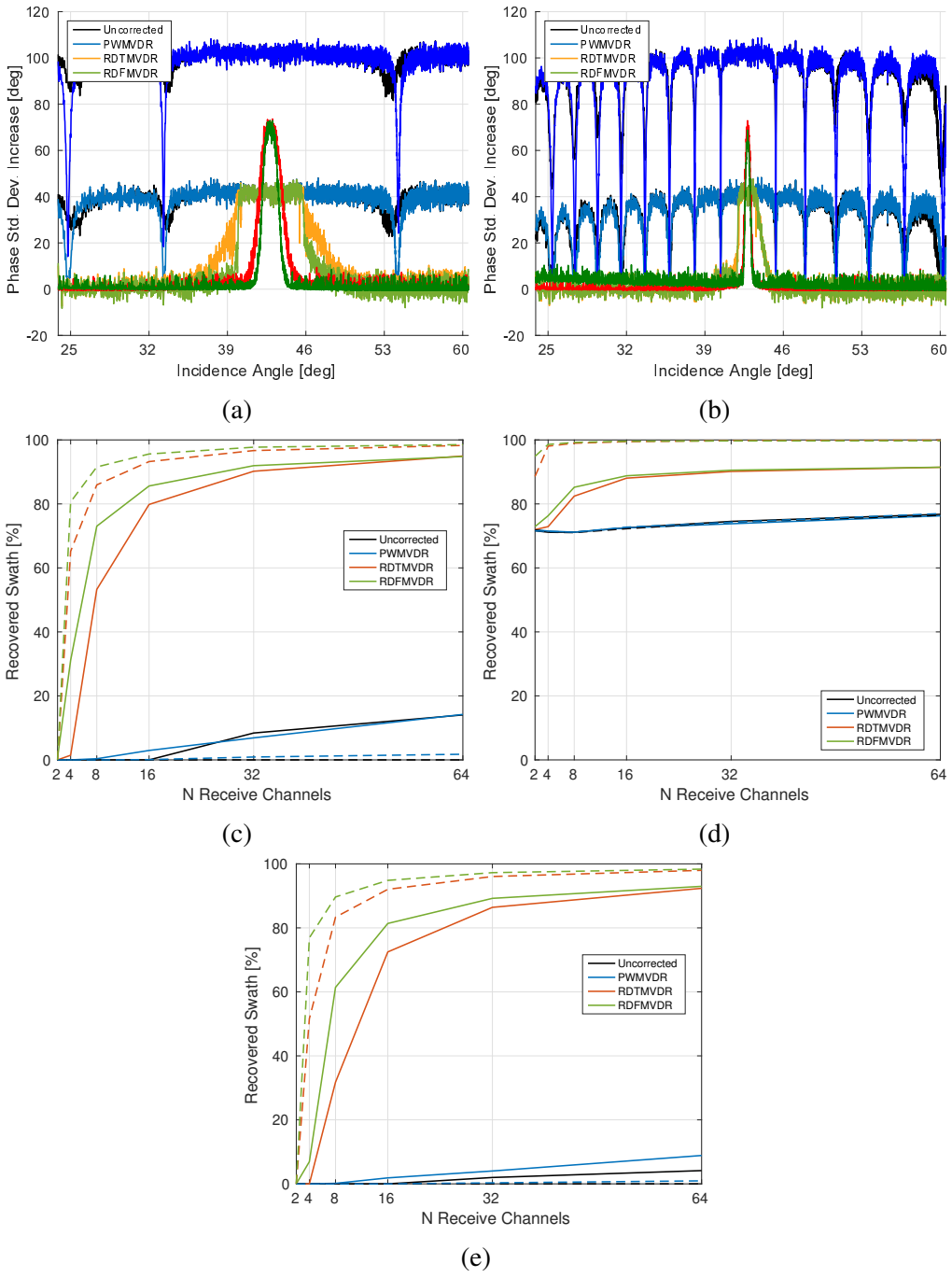

Fig. 3.27.: The phase standard deviation increase of the residual error image for scenario B at an RFI-to-Noise Ratio of 40 dB. SNR = 0 dB (pale and solid lines) and SNR = 37.36 dB (saturated and dashed lines). a) Error plotted vs. incidence angle for N = 16, b) Error plotted vs. incidence angle for N = 64, c) The percentage of the recovered SAR swath that is within the phase std. dev. limits of 20°, d) The percentage of the recovered SAR swath that is within the phase offset limits of 5°, e) The percentage of the recovered SAR swath that is within the absolute amplitude budget of 0.5 dB.

Scenario C

As before, Fig. 3.28 shows the phase standard deviation of the residual error image measured in each range line before and after spatial filtering with the Range-Dependent Frequency MVDR beamformer (SNR = 37.63 dB). Figure 3.28a and Fig. 3.28c show the error before the spatial filter is applied for N = 8 and N = 32, respectively. All the interferers in scenario C are placed outside the swath and an initial suppression by the antenna pattern sidelobes occurs. Therefore, the data degradation does not start until RNR = -15 dB and RNR = -5 dB. Even though there are 11 interferers and Fig. 3.28b shows the spatial filter for N = 8, the full swath can be recovered. Fewer notches than interferers are needed if all interferers are outside the swath, as is the case here, because a wide notch can suppress multiple close interferers. Hence, only a few notches are sufficient to improve the sidelobe suppression over a wide span of angles. However, even higher RFI powers could be suppressed if N were increased. As expected, increasing N to 32 in Fig. 3.28d results in a full recovery and is only shown for completeness.
Next, Fig. 3.29 shows the 3-sigma phase standard deviation error for scenario C. As before, N increases from 2 to 64 and the beginning of the degradation (black line) is pushed to higher values. In the same manner, the colored curves after the spatial filtering are pushed to the lower left corner as N increases. Because of the amount of interferers, the filtering with few notches and thus for low N is degrading for high RNR. As in scenario A (single interferer) it can be observed that the fastest algorithm, the Pulse-Wise MVDR, performs the worst and the most complex algorithm, the Range-Dependent Frequency MVDR, the best. The disadvantage of the Range-Dependent Frequency MVDR is, besides the high computational load, an artifical noise floor that is injected and that becomes visible for large N. This artificial noise is on the order of 1.5°.
The maximum 3-sigma phase offset increase at RNR = 40 dB is plotted in Fig. 3.30a. The range-dependent algorithms show a phase offset of less than a degree above N = 8. For high N, the limit of the phase offset reconstruction is 0.15° for the Range-Dependent Time MVDR and 0.7° for the Range-Dependent Frequency MVDR. The maximum 3-sigma amplitude offset increase at RNR = 40 dB is plotted in Fig. 3.30b. Again, this error directly affects the radiometric budget. For N below 8 the RFI suppression is not sufficient and a high amplitude error is introduced. This is due to the RNR of 40 dB. For N = 8, the Range-Dependent Frequency MVDR shows the best suppression with an amplitude error of 1.25 dB. The error drops further for all algorithms with

increasing N. It is evident that the Pulse-Wise MVDR is capable of removing the amplitude error for N larger than 32. On the contrary, the Range-Dependent Time MVDR has a remaining amplitude error of 0.09 dB and the Range-Dependent Frequency MVDR a remaining amplitude error of 0.2 dB. While the range-dependent algorithms show a better behavior for lower N, for large N the amplitude error of the Pulse-Wise MVDR is the best (if no interferer is inside the swath).

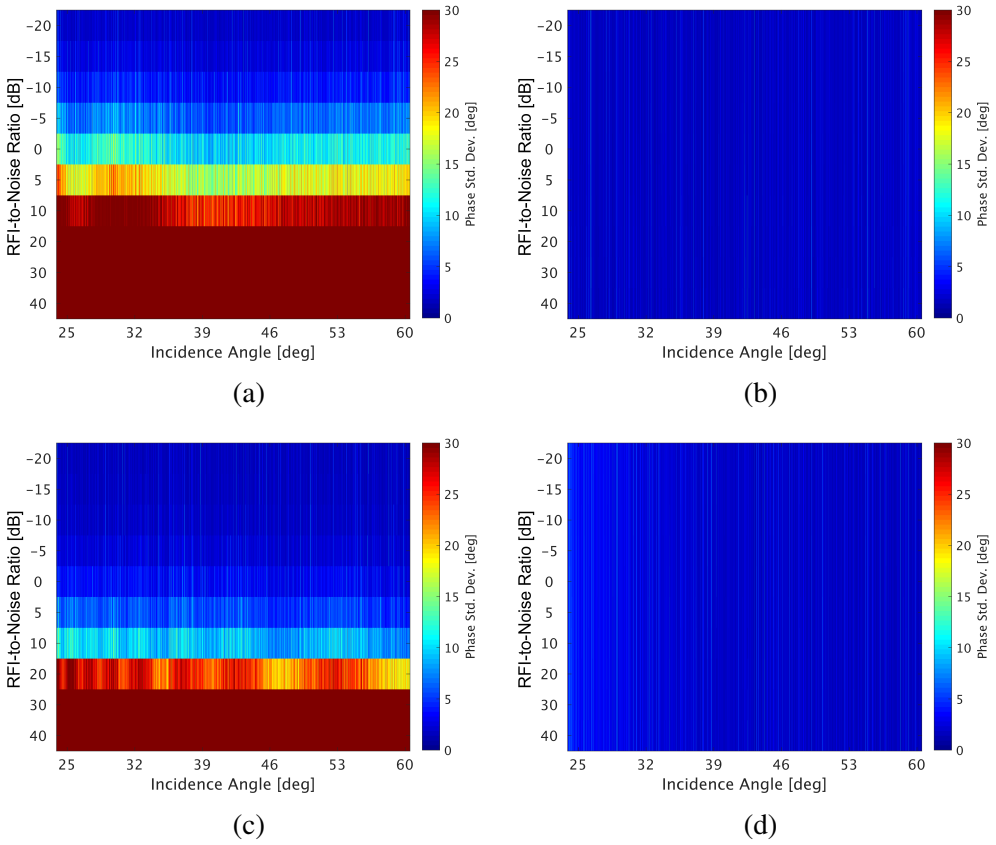

Fig. 3.28.: The phase standard deviation of the residual error image of scenario C for different RFI-to-Noise Ratios vs. the incidence angle of the instantaneous SAR signal. The SNR is 37.36 dB. a) No RFI mitigation for $N = 8$, b) After Range-Dependent Frequency MVDR beamforming for $N = 8$, c) No RFI mitigation for $N = 32$, d) After Range-Dependent Frequency MVDR beamforming for $N = 32$. The results of the Range-Dependent Time MVDR beamforming are similar.

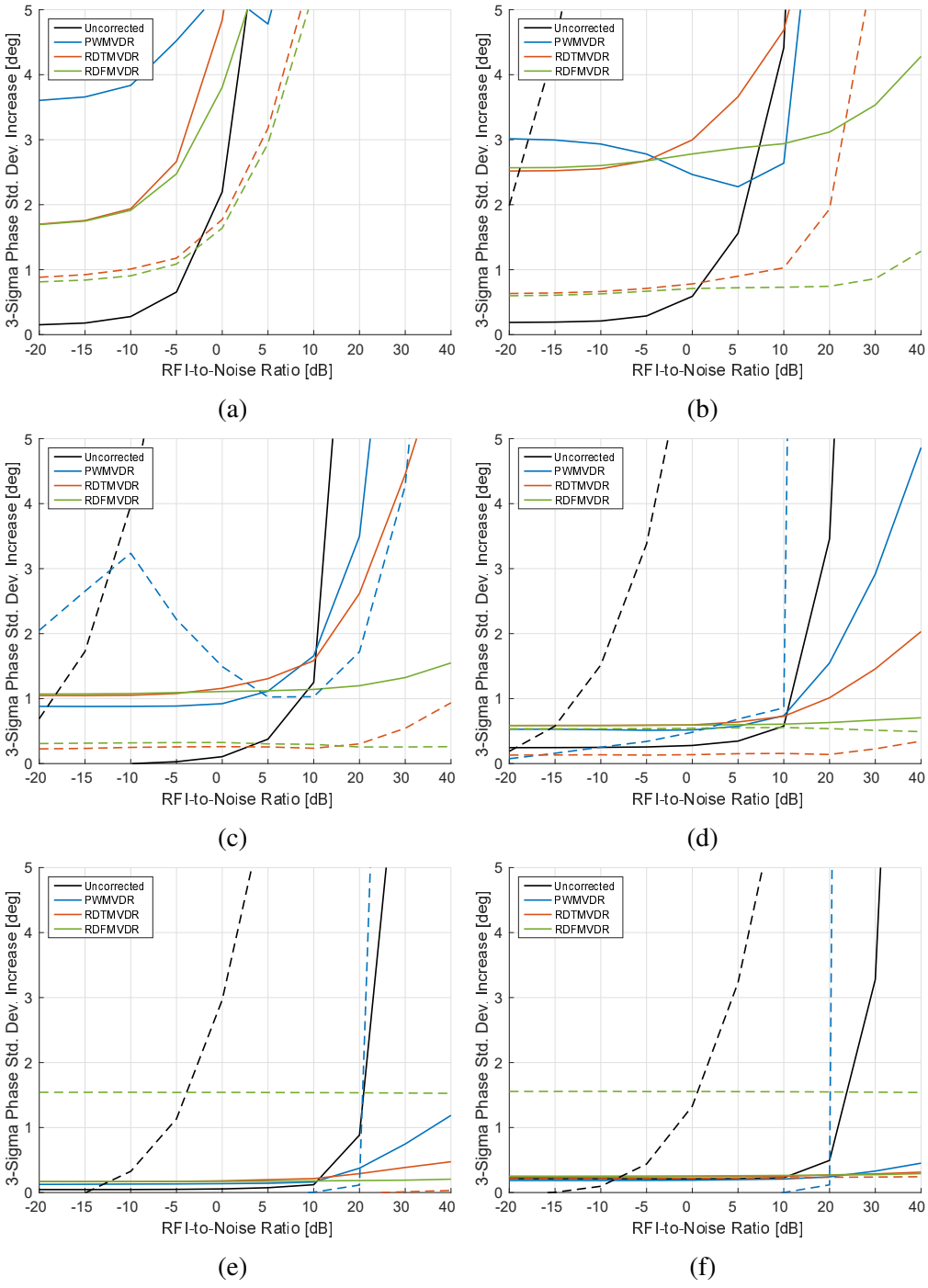

Fig. 3.29.: The 3-sigma phase standard deviation error of the residual error image of scenario C vs. RFI-to-Noise Ratio. The plots are shown for SNR = 0 dB (solid lines) and SNR = 37.36 dB (dashed lines). a) $N = 2$, b) $N = 4$, c) $N = 8$, d) $N = 16$, e) $N = 32$, f) $N = 64$

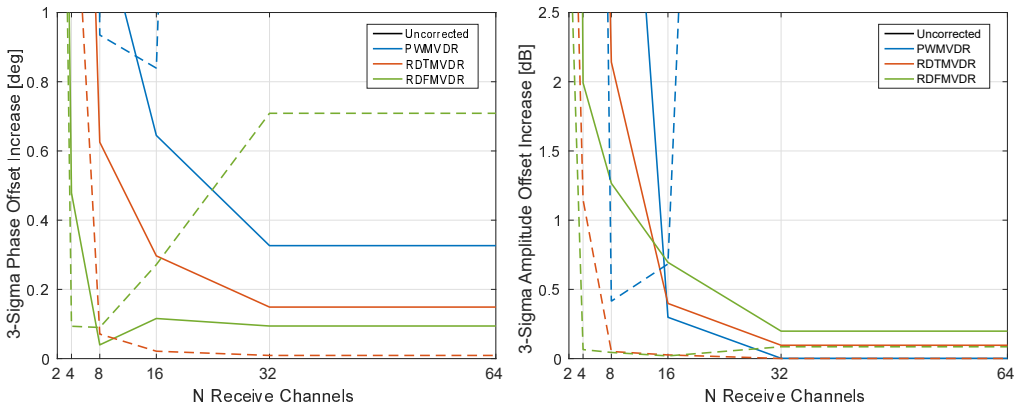

(a) (b)

Fig. 3.30.: The 3-sigma error increase of the residual error image of Scenario C at an RFI-to-Noise Ratio of 40 dB vs the antenna array length. The plots are shown for SNR = 0 dB (solid lines) and SNR = 37.36 dB (dashed lines). a) Phase offset, b) Amplitude offset.

Scenario D

In scenario D, 4 interferers are located inside the swath and 7 interferers outside of the swath. Again, it is expected that only part of the swath can not be recovered due to the in-swath RFI. Figure 3.31 shows the phase standard deviation of the residual error image measured in each range line (SNR = 37.63 dB). Figure 3.31a and Fig. 3.31c show the error before the spatial filter is applied for $N = 8$ and $N = 32$, respectively. For $N = 8$ all simulated RNR show a degradation of the entire swath as the main beam is constantly occupied by one interferer. The more narrow antenna pattern of $N = 32$ (due to the longer antenna) shows the SCORE-typical ripples because the interferers move in and out of the main beam. Again, the increased antenna length (narrower instantaneous SCORE beam) yields an inherent suppression of the in-swath RFI to some extent. The residual phase standard deviation error applying the Range-Dependent Frequency MVDR beamformer is shown in Fig. 3.31b ($N = 8$) and Fig. 3.31d ($N = 32$). The entire swath can be recovered in both cases for a RNR of up to 10 dB. For this value, the interference is about 27 dB lower than the SAR signal. As the RNR values increase, only part of the swath can be recovered. As before, the higher N (which here results in a longer antenna) improves the reconstruction area because of the more narrow antenna pattern. For $N = 8$ the areas overlap and more than half of the first part of the swath is lost. Even though

four interferers are placed in the swath, only three are visible. This can be explained with the fact that the frequency shift of one of the interferers results in an AoA shift at f_c, which moves the interferer outside of the swath from the perspective of the radar's center frequency (as discussed in Section 3.4.3).

The amount of the lost swath is further analyzed in Fig. 3.32. As before, Fig. 3.32a (N = 16) and Fig. 3.32a (N = 64) show the phase standard deviation error at RNR 40 dB for each range line after the mean phase standard deviation error of the noise floor is subtracted. The Pulse-Wise MVDR (blue) curve is comparable to the uncorrected (black) curve. As a matter of fact, the Pulse-Wise MVDR is even degrading the data further at some incidence angles because it is blind to the in-swath interference. The orange curve shows the Range-Dependent Time MVDR, and for the N = 16 and SNR = 0 dB only the far range is corrected. When the SNR (saturated curve) or N is increased, the corrupted area around the interferer position gets smaller (due to the longer antenna) and reveals parts of the swath. The Range-Dependent Frequency MVDR exhibits the same trend but is reducing the error in between the interferers even for low N and low SNR. When N is increased, the Range-Dependent Time MVDR and Range-Dependent Frequency MVDR perform comparably (due to the high number of available notches it is not necessary to perform a frequency-dependent notching).

The percentage of the recovered swath in dependency of N is plotted from Fig. 3.32c through Fig. 3.32e for the phase standard deviation, the phase offset and the amplitude offset, respectively. The recovered swath in the figures has a phase standard deviation error below 20°, a phase offset below 5° and an amplitude offset below 0.5 dB. As in scenario B, the lost swath halfens for a doubling of the antenna length.

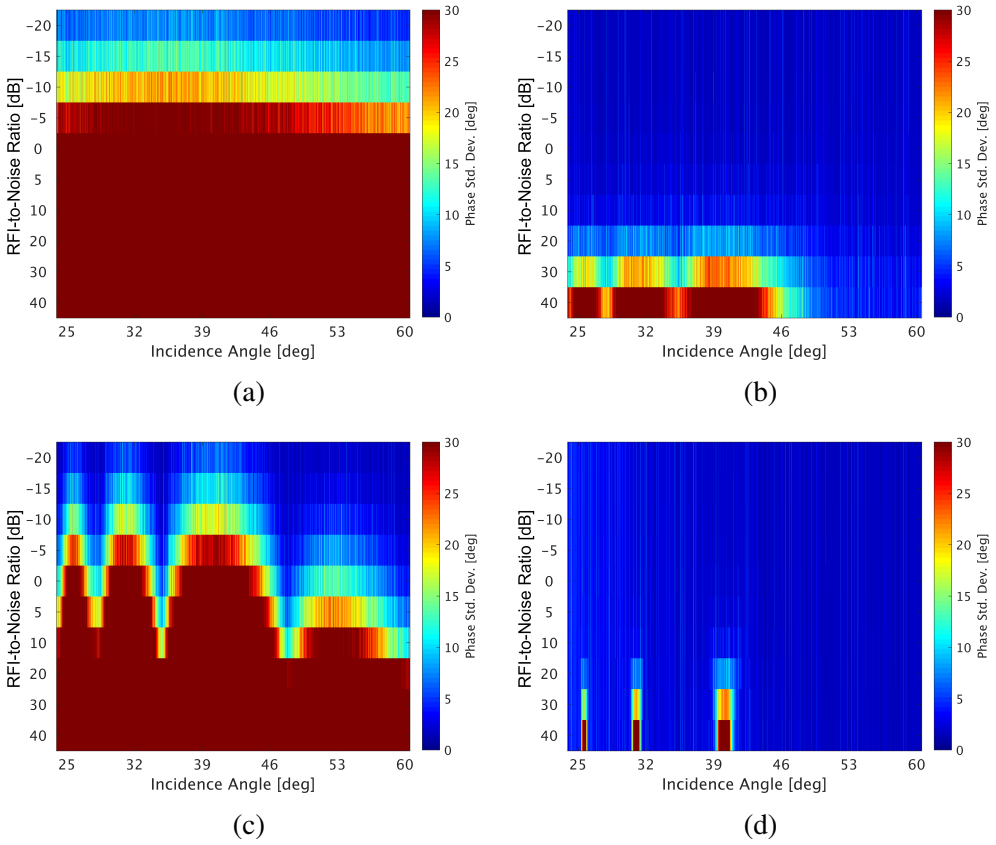

Fig. 3.31.: The phase standard deviation of the residual error image of scenario D for different RFI-to-Noise Ratios vs. the incidence angle of the instantaneous SAR signal. The SNR is 37.36 dB. a) No RFI mitigation for $N = 8$, b) After Range-Dependent Frequency MVDR beamforming for $N = 8$, c) No RFI mitigation for $N = 32$, d) After Range-Dependent Frequency MVDR beamforming for $N = 32$. The results of the Range-Dependent Time MVDR beamforming are similar, though the corrupted area increases slightly in elevation due to the less optimal notch placement.

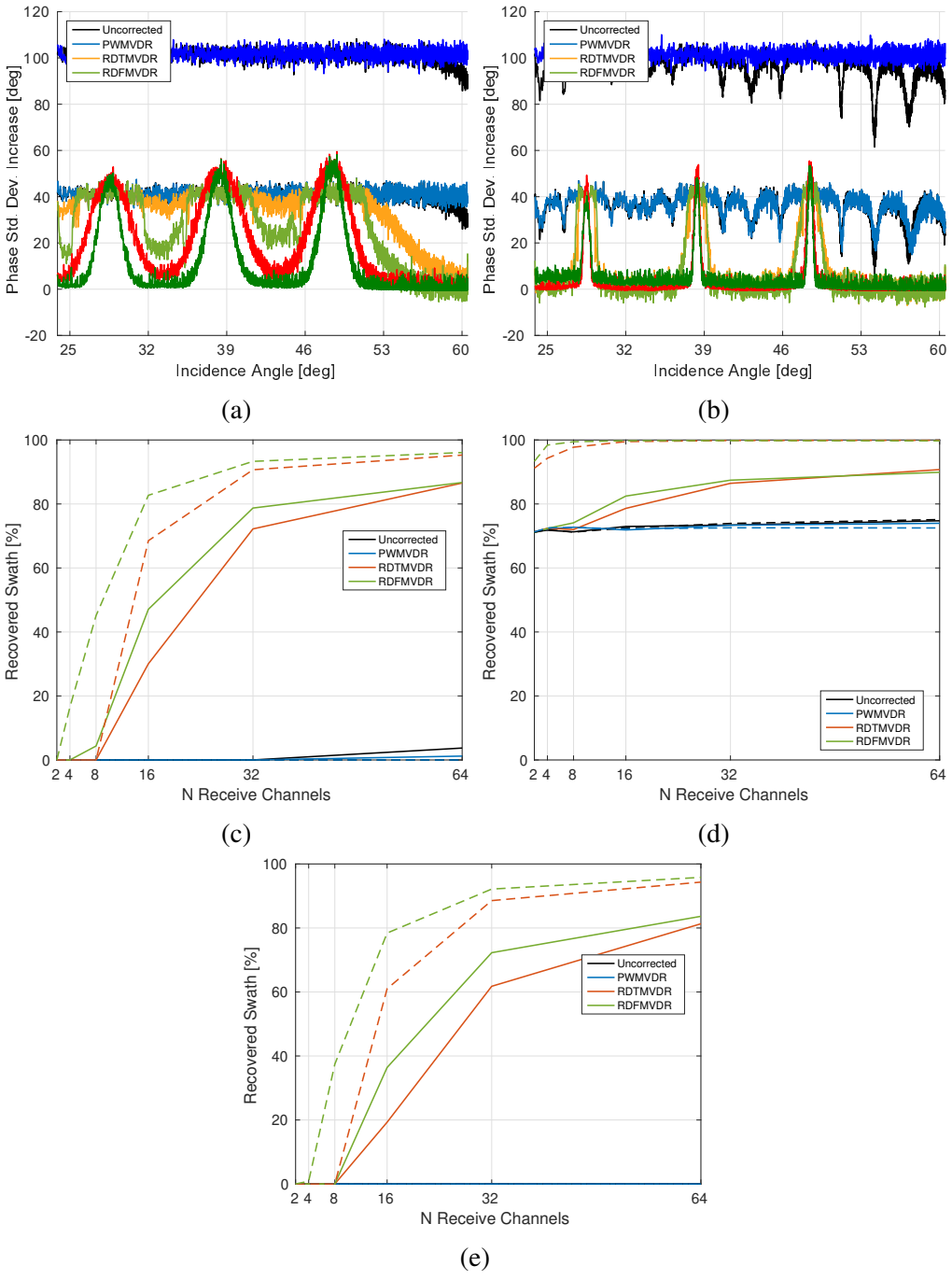

Fig. 3.32.: The phase standard deviation increase of the residual error image for scenario D at an RFI-to-Noise Ratio of 40 dB. SNR = 0 dB (pale and solid lines) and SNR = 37.36 dB (saturated and dashed lines). a) Error plotted vs. incidence angle for N = 16, b) Error plotted vs. incidence angle for N = 64, c) The percentage of the recovered SAR swath that is within the phase std. dev. limits of 20°, d) The percentage of the recovered SAR swath that is within the phase offset limits of 5°, e) The percentage of the recovered SAR swath that is within the absolute amplitude budget of 0.5 dB.

3.5. Remarks

In the absence of in-swath interference and if there are more notches available than interferers (large N), the Pulse-Wise MVDR performs best. This is because the Range-Dependent Time MVDR and Range-Dependent Frequency MVDR introduce a larger processing noise. However, if there are in-swath interferers (or more interferers than notches available) the Pulse-Wise MVDR fails. In that case, the range-dependent algorithms are necessary. The simulation showed that the Range-Dependent Frequency MVDR introduces a higher processing noise than the Range-Dependent Time MVDR but the Range-Dependent Frequency MVDR is also capable to operate at smaller N (because the notches are set frequency-dependent). The advantage of the Range-Dependent Frequency MVDR decreases with increasing N. It is therefore recommended to use the Range-Dependent Frequency MVDR for receive antennas with small N or if many interferers are expected. Another important point is, that the simulations were performed with CW interferers. The notching of a wide-band interferer requires frequency-dependent beamforming weights. Otherwise, the placed antenna pattern notch is only pointing directly towards the interferer position at one frequency and the RFI suppression is degraded. This effect is compensated in the Range-Dependent Frequency MVDR due to the frequency-dependent processing. The Range-Dependent Time MVDR needs to be applied on multiple subbands if the SAR data are corrupted by wide-band interferers. In regard to N it should also be mentioned that many close interferers can be notched with few N because they can be suppressed with the same wide notch. In theory, a single notch is sufficient to notch one interferer but relying on one notch makes the notching sensitive to AoA errors of the RFI. Placing wider notches ensures that the interferer is suppressed well and is beneficial for strong wide-band interferers.

As predicted, in-swath interference can not be removed with antenna pattern notching when the instantaneous main (SCORE) beam looks into the interferer direction. However, the lost swath halfens for a doubling of the antenna length, which is due to the resulting halfening of the beamwidth.

4. Experimental Results

After the introduction of novel RFI mitigation techniques based on DBF in the previous chapter, this chapter presents the RFI analysis and mitigation results obtained from experimental airborne data. Section 4.1 gives an overview of the NASA EcoSAR system that provided the used dataset. The flight campaign that acquired the data is presented in Section 4.2. Based on EcoSAR data, two different methods for the detection and flagging of RFI are presented and evaluated in Section 4.3. The methods are applied to the entire EcoSAR dataset and the measured RFI characteristics are summarized. In Section 4.4, the position of an interfering source in the EcoSAR data is pinpointed and geolocated by utilizing the change of the measured Angle-of-Arrival in elevation. Next, the achieved RFI mitigation results on EcoSAR data with the algorithms from Chapter 3 are presented in Section 4.5. The chapter is concluded with remarks in Section 4.6.
Part of the results presented in this chapter has been published in [94] and in [116].

4.1. EcoSAR System Description

EcoSAR is an airborne DBF SAR instrument developed at the NASA Goddard Space Flight Center [30,117–119]. It was funded through the 2010 ESTO Instrument Incubator Program with the goal to measure forest structure, biomass, ice sheets and dry soils. The radar operates at 435 MHz in P-band, the same center frequency that will be used by ESA's BIOMASS mission [28, 29], with bandwidths of up to 120 MHz in the horizontal (H) polarization and 200 MHz in the vertical (V) polarization. At this low frequency, the radar benefits from the higher sensitivity of the backscatter to high biomass densities [28]. Furthermore, the temporal decorrelation between repeat passes is reduced due to the increased penetration of the signal and the increased signal return from tree stems and trunks, which are stable over time [120]. The system consists of two dual-polarization antennas that are mounted under both wings of the aircraft as illustrated in Fig. 4.1, allowing it to acquire fully-polarimetric single-pass interferometric data with a baseline of 25 m. Each antenna is composed of eight active subelements per polarization that

permit DBF in elevation over a range of ±45°. Therefore, the available EcoSAR dataset enables the verification of the algorithms presented in this work on an interferometric SAR system with multiple elevation channels. The performance is assessed by means of the interferometric coherence. For a general overview of EcoSAR, system parameters are listed in Table 4.1.

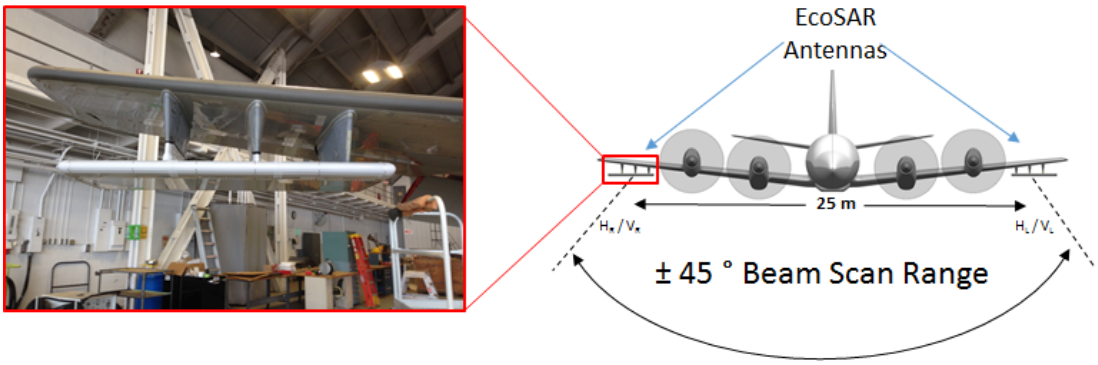

Fig. 4.1.: EcoSAR antenna mounted on a wing of the P3 airplane during the 2014 flight campaign (left) and illustration of antenna positions on each wing (right).

Table 4.1.: Operational range of EcoSAR system parameters.

	Capability
Center Frequency	435 MHz
Bandwidth	up to 120 MHz (H) up to 200 MHz (V)
Pulse Length	1 μs to 50 μs
PRF	100 Hz to 10 kHz
Range Resolution	0.75 m
Azimuth Resolution	0.5 m
Array Power	40 Watt
Physical Baseline	25 m
Antenna elements	8 per antenna and polarization
Antenna element spacing	0.29 cm (0.46λ)

4.2. EcoSAR Dataset Description

EcoSAR's first test flights and science campaign were conducted in March 2014. Data were collected on different days in Corcovado National Park in Costa Rica and on Andros Island in the Bahamas. EcoSAR was operating in dual-track mode, illuminating both sides of the aircraft with a wide transmit beam. Due to EcoSAR's DBF capability, it was possible to electronically steer the antenna beam to both sides of the track in post-processing. The flown areas are shown in Fig. 4.2. Blue lines represent the flight tracks. Green and red boxes in Fig. 4.2 represent the swath on the left and right side of the airplane, respectively. The dates and observation times of the acquired flights are listed in Table 4.2.

Each area in Costa Rica was flown at least once on two different days, allowing the analysis of the RFI data for repeating patterns. For the two tracks in the Bahamas, there is only one acquisition available. In addition to the normal fully polarimetric mode, EcoSAR also performed acquisitions with an interleaved sniffing mode. The transmission of the vertical polarizations from one of the wings was skipped to listen for interference. These flight lines are marked with a red asterisk. For these data sets it is possible to analyze the RFI without being masked or disturbed by an overlapping SAR signal return.

Table 4.2.: Acquisition times of the flight tracks (UTC) and time duration (minutes). Data that were collected in interleaved sniffing mode is marked with a red asterisk. Lowercase letters indicate repeat tracks.

Track	Date	Start Time [UTC]	Length [min]
Osa_T1a	03/30/2014	18:59	3.5
Osa_T1b	03/30/2014	19:50	5.0
Osa_T1c*	03/31/2014	16:23	6.0
Osa_T1d*	03/31/2014	17:28	5.0
Osa_T2a	03/30/2014	16:34	3.5
Osa_T2b*	03/31/2014	16:34	4.5
Osa_T3a	03/30/2014	19:21	6.0
Osa_T3b*	03/31/2014	16:43	7.0
Osa_T4a	03/30/2014	18:47	5.5
Osa_T4b	03/30/2014	19:35	8.5
Osa_T4c*	03/31/2014	16:09	7.5
TB_T1	03/27/2014	18:00	4.0
TB_T2	03/27/2014	17:42	5.0

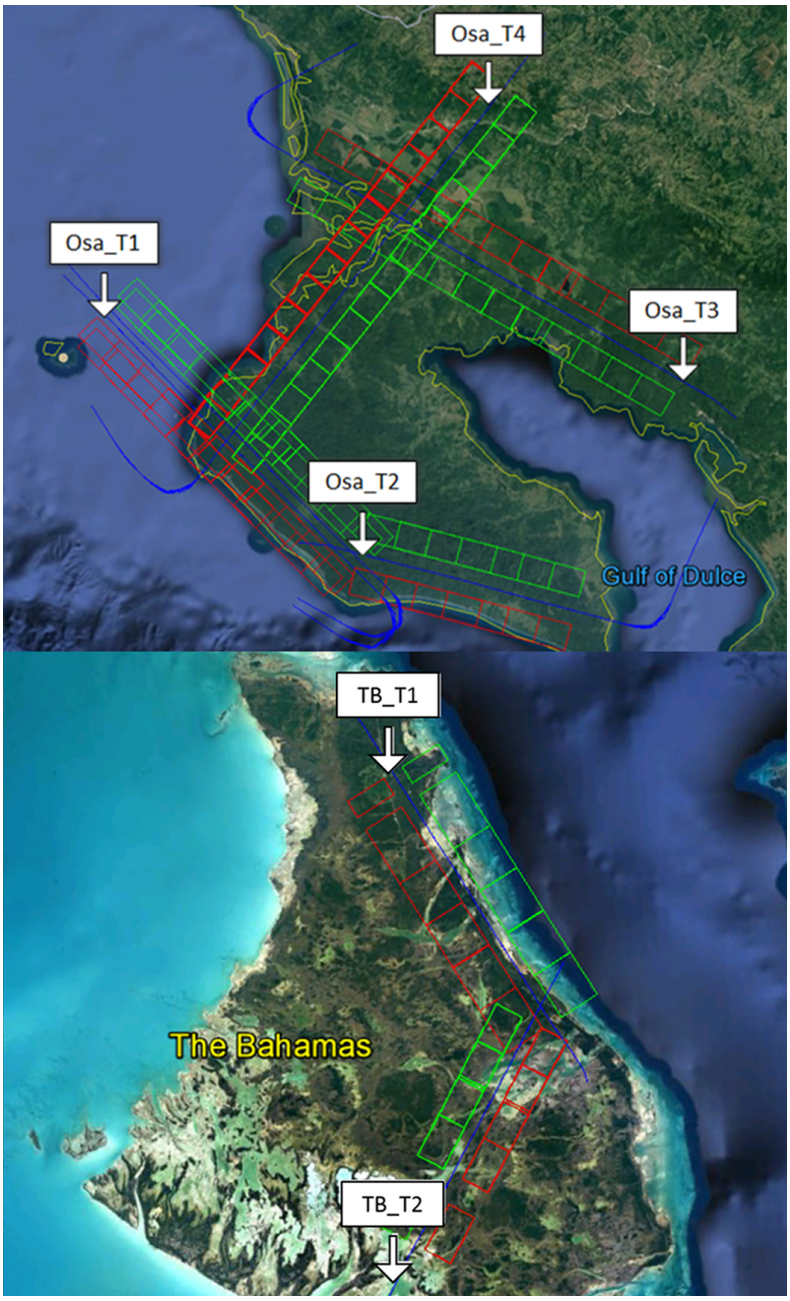

Fig. 4.2.: Flight lines of the collected EcoSAR data in Costa Rica and the Bahamas in March 2014. Green and red boxes represent the image swaths on the left and right side of the trajectory, respectively.

Due to the complexity of the system, there were synchronization issues among the receive channels that appeared in flight, which were undetectable in the lab. These included time delays and phase offsets in range and azimuth between the channels. The range-dependent errors changed abruptly every few minutes, causing about one change within a recorded flight line. A change of the azimuth dependent errors occured every few seconds within a flight line and can be contributed to missing pulses in the raw data. These error sources have now been repaired for future flights and the previously collected data have largely been corrected. Nevertheless, this gave rise to a degraded DBF performance.

4.3. RFI Detection and Analysis

This section presents two different RFI detection methods for SAR. The first method relies on EcoSAR's sniffing mode, which allows for a detection of the RFI signals by omitting SAR pulses. Due to the absence of the SAR signal, this method can even detect weak RFI and is ideal for the creation of reference data. However, this method comes at the loss of SAR information and is therefore disadvantageous for an operational system. The second method detects RFI if no sniffing pulse is available. A performance evaluation of this new method is performed with the reference data created by the first method. It will be shown that the proposed RFI detection method without sniffing pulse is accurate enough to characterize the entire EcoSAR data set. The method is then used to present the RFI observed during EcoSAR's first flight campaign. Note that some of the RFI measured may be due to internal interference of the system itself. To avoid these false detections, the methods presented in this section are performed on each receive channel individually, and only interference mutual to all channels is flagged. An indicator for the adequacy of this method is the consistency of the Angle-of-Arrival (AoA) presented in Section 4.3.1 for repeated flight tracks and the change of the AoA pattern for different flight tracks.

4.3.1. Proposed RFI Detection Methods

To mitigate RFI, EcoSAR has implemented a sniffing pulse during which the radar is switched into listen-only mode to sniff for RFI in alternation with three transmit pulses. This allows for a better understanding of the locally present RFI without it being masked

by the SAR signal itself. This is implemented at the cost of one of the polarization channels. Due to the low flight altitude of 3.6 km, the impact of ambiguous returns from other polarizations can be neglected at the operational pulse repetition frequency (PRF) of 2 kHz. Another way to implement the sniffing pulse is by increasing the PRF, which results in a smaller swath and makes the sniffing pulse susceptible to range ambiguities. Fig. 4.3 shows the averaged frequency spectrum of multiple receive windows in transmit-mode (HH and HV) and in sniffing-mode. Note that without the sniffing pulse large portions of weak RFI that contributes to a SNR degradation goes undetected. In the following, two detection methods are presented. The first one is using the sniffing pulse, the second one is applying bandpass filters in the time domain to the weakest SAR pulse (HV). Both methods are compared to determine the importance of the sniffing pulse for future missions, and to evaluate the accuracy of retrieved RFI from datasets that are lacking a sniffing pulse.

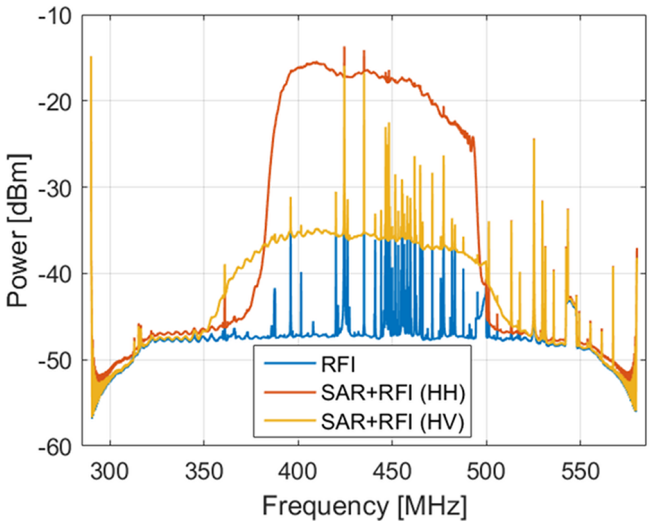

Fig. 4.3.: Range-frequency spectrum when the radar is in transmit-mode (orange, yellow) and in sniffing-mode (blue). Weaker RFI sources are masked by the SAR signal.

Sniffing Pulse

As a first step, the sniffing pulse data were transformed via FFT in range into the range-frequency domain. This yields a spectrum as shown in Fig. 4.4. Next, the noise floor is estimated by averaging the spectrum in slow time. All spikes exceeding a local mean are removed from the averaged spectrum and a polynomial curve is fitted through it. The hereby estimated noise floor is subtracted from the unaveraged data. To reduce false detections, a moving average window of 25 samples in slow time (this equals 1/20 second for EcoSAR's PRF of 500 Hz) is applied and the frequency bins with a resulting magnitude that is 3 dB above the noise floor are flagged as RFI. Sniffed data were collected simultaneously in between imaging pulses yielding a reference for the RFI that is present in the datasets and can be compared to the RFI extracted with the next method.

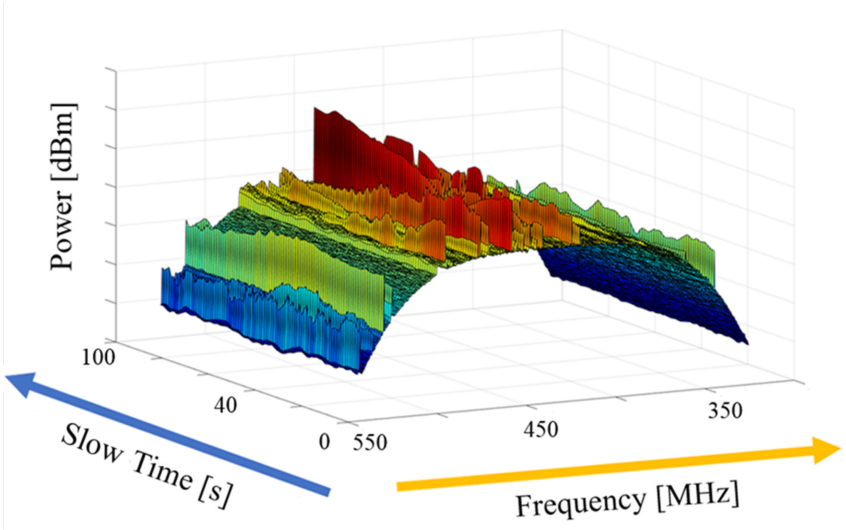

Fig. 4.4.: Time-varying range-spectrum of the sniffing pulse with distinct peaks due to interference.

Time-Bandpass Filters

Time-bandpass filters are applied to the SAR channels with the weakest return (e.g., HV and VH raw data), to minimize the masking of the RFI by a residual SAR signal after bandpass filtering. This takes advantage of the linear frequency dependency of the SAR chirp as displayed in Fig. 4.5a. Assuming a pulse duration of T_{P} and a receive window that spans from the first return of near range targets, to the last return of far range targets. Then the first $T_{\mathrm{P}}/2$ seconds of the receive window will only be occupied in half of the spectrum and the last $T_{\mathrm{P}}/2$ seconds by the other half of the spectrum. Therefore, two separate bandpass filters can be used to get a combined filtered spectrum. The first filter is using the time samples of the first half of Fig. 4.5a, a FFT is performed and only the first half of the frequency spectrum is kept. The second filter is using the samples of the second half (Fig. 4.5a) and the opposite site of the spectrum is kept. This yields the spectra plotted in Fig. 4.5b. It can be noticed, that the second half of the spectrum is not as clean from the SAR signal after filtering. This is due to the fact, that the receive window of the collected EcoSAR data was set too short to capture the complete duration of the chirp in the far range. Therefore, part of the data where only the right half of the spectrum is in use (Fig. 4.5a) was cut off. Based on this filtered spectrum, the same steps that were performed on the sniffing pulse in Section 4.3.1 are applied. To account for residual SAR signals that change over time depending on the environment, the averaged noise floor is estimated every 1000 samples in slow time. For scenes acquired with a PRF of 500 Hz, this equals a new noise floor estimation about every 2 seconds of acquired data. This method does not rely on a sniffing pulse, but can only detect RFI that is present in the first and last $T_{\mathrm{P}}/2$ seconds of the receive window. However, as shown in the next subsection, it is sufficient to detect the RFI present in the EcoSAR data. Note that due to the low flight altitude of 3.6 km, the impact of ambiguous returns from the other polarizations can be neglected. If this were not the case, then the time-bandpass filter would need to be adjusted accordingly. This can be done because the slow time appearance of ambiguities is correlated with their angular position and distance.

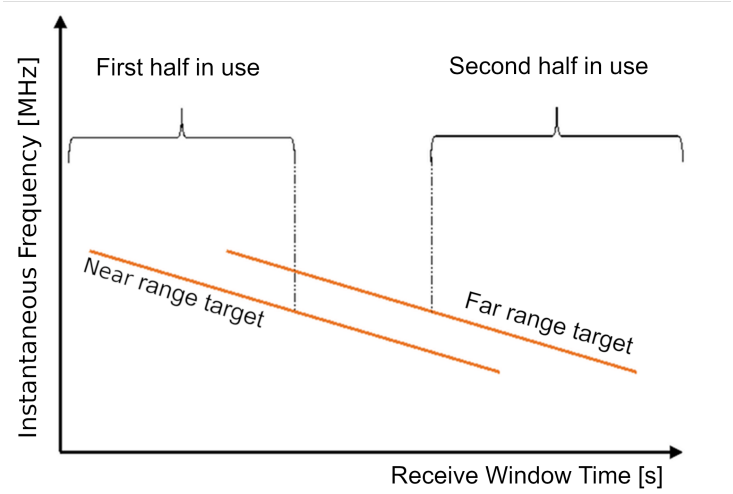

(a)

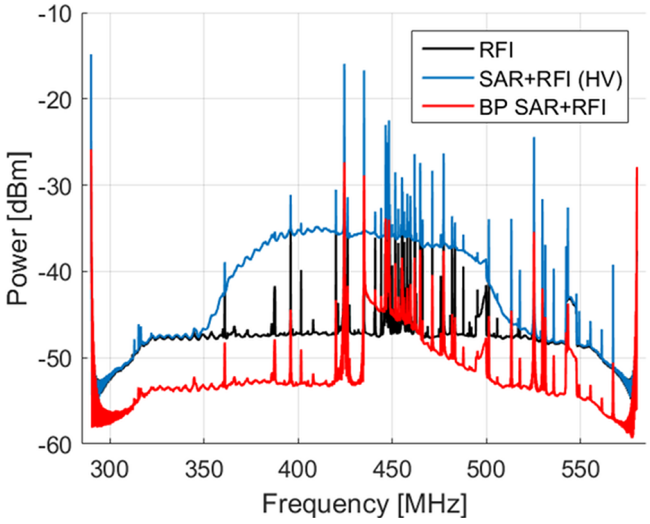

(b)

Fig. 4.5.: a) Illustration of the occupied SAR spectrum for a near and far range target. b) Range-frequency spectrum of single channel when the radar is in transmit-mode (blue) and in sniffing-mode (black), as well as the recovered RFI using time-bandpass filters (red) on the RFI-contaminated SAR signal. A residual SAR signal is visible in the upper spectrum because EcoSAR's receive window was set too short to capture the entire swath.

Method Comparison

Next, the bandpass filter detection is compared to the sniffing pulse method. The bandpass filtered signal yields a lower frequency resolution because it utilizes fewer samples for the FFT operation. The RFI mask created with this method is therefore upsampled to the same number of frequency bins as the RFI mask created by the sniffing pulse. Figure 4.6 shows the differences in the flagged frequency bins as a histogram. They are sorted according to the strength of the RFI above the noise floor. The blue histogram shows bins that have been identically flagged with both detection methods. The red histogram shows only the frequency bins that have only been detected in the sniffing pulse. They represent the RFI that goes undetected in the bandpass filter approach. We conclude that both methods are able to flag the same frequency bins, if the RFI is significantly above the noise floor. Weak RFI is more prone to go undetected with the time bandpass filter. A possible explanation for this is that the RFI is still masked by the residual SAR signal. In general, the detected RFI with the bandpass filter approach will be limited by the strength of the SAR signal. However, this naturally limits RFI detection to a reasonable amount, as RFI that is significantly weaker than the SAR signal will cause little degradation of the SAR image quality. The yellow histogram shows bins that have additionally been flagged in the bandpass filtered data. One reason for this is the reduced frequency resolution, as the windowed FFT is performed on fewer samples for the bandpass filtered signal. Hence, a sharp peak that is flagged in the sniffing pulse in one bin will result in multiple flagged bins that surround this peak in the low-resolution and upsampled, bandpass filtered approach. Overall, both methods are in a good agreement for 88.94% of all bins. The results differ for RFI that is less than 6 dB above the noise floor.

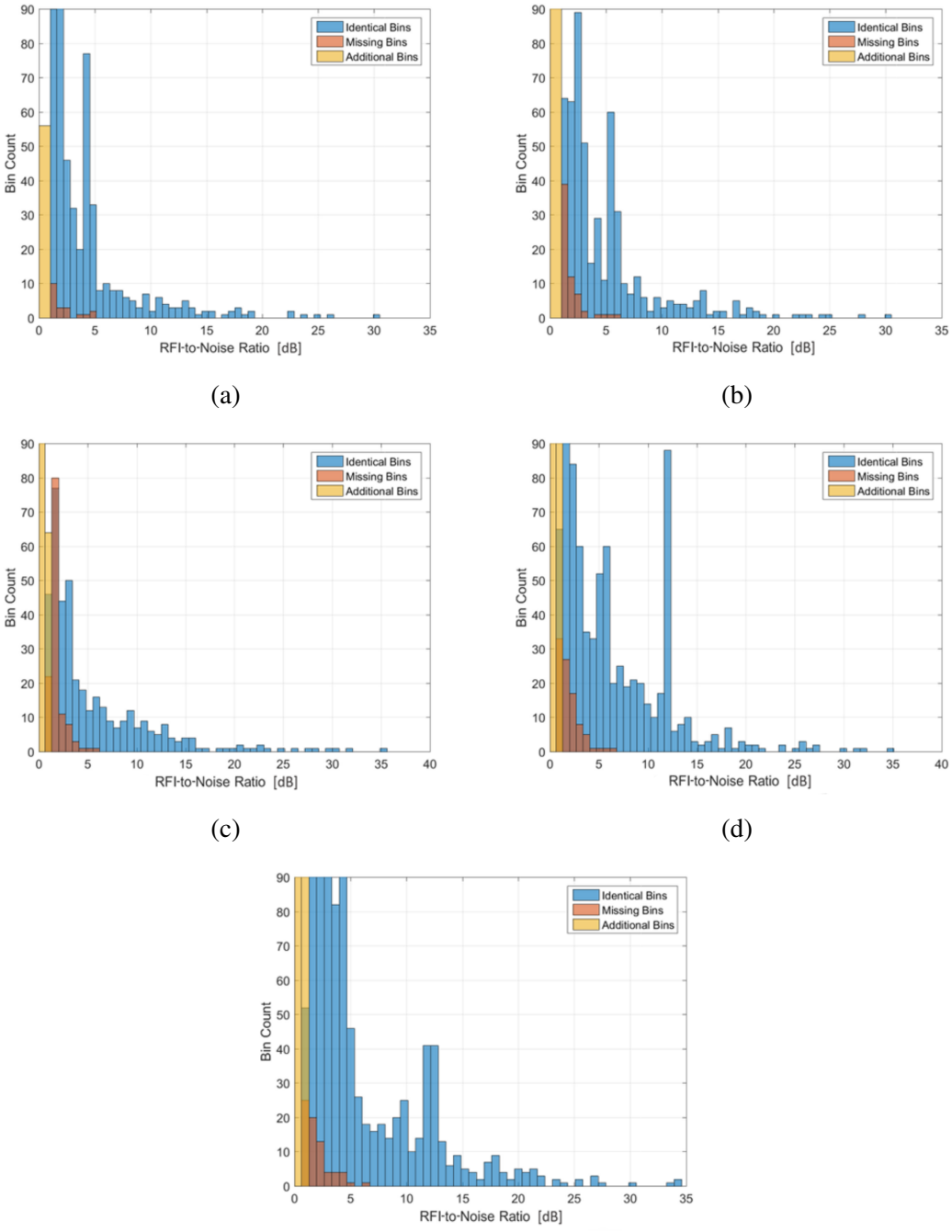

Fig. 4.6.: Differences in the bin flagging for both RFI detection methods as histogram. Blue: Flagged in both methods, Red: Only flagged in the sniffing pulse, Yellow: only flagged in the time bandpass filter. Flight tracks according to Table 4.2: a) Osa_T1c b) Osa_T1d, c) Osa_T2b, d) Osa_T3b, e) Osa_T4c.

Angle-of-Arrival Estimation

A popular algorithm for AoA estimation of multiple signals with a uniform linear array is MUSIC (Multiple Signal Classification) [110]. With an antenna array that consists of N elements, it is possible to estimate the direction of $K = N - 1$ RFI sources. The basis for this is that the eigenvectors of the $N - K$ weakest eigenvalues of the input covariance matrix span a noise subspace that is orthogonal to the signal subspace. Therefore, as a priori information it is necessary to know the number of sources present in the data. If too few sources are assumed, the algorithm will not detect all sources. However, if too many sources are assumed, ghost sources can appear in the estimates. Methods to estimate the number of sources from the data have been developed but require higher computational power and are subject to errors [111, 112]. Further, for an accurate estimation it is necessary to know the frequency of the source. Otherwise the estimated angle is over- or underestimated due to the different phase delay at different frequencies. To avoid this, the MUSIC algorithm is applied here in the range-frequency domain (Fig. 4.4) as well. This allows to perform an estimation on each frequency bin separately. Compared to an estimation in the time domain where the maximum number of sources is limited to $N - 1$ (7 for EcoSAR), it is possible to estimate up to $N - 1$ sources per frequency bin. For simplicity, and to avoid any errors due to a wrong estimation of the number of sources, it is assumed that each flagged frequency bin contains only one major RFI source. This yields an azimuth-dependent AoA for each flagged frequency. Fig. 4.7a and 4.7b display the estimated AoA on the sniffing pulse of Osa_T1c and Osa_T1d, respectively. For each angle estimate the MUSIC algorithm was applied on a 40-sample estimation window in azimuth. The Y-Axis is the nth range-frequency bin flagged with RFI, the X-axis is slow time in seconds and the color represents the AoA in degrees. It is evident, that the AoAs of the same flight track show similar behavior. Because of the short temporal separation on the same day, similar interference is observed (Osa_T1c: 16:23, Osa_T1d: 17:28). The images are slightly shifted in azimuth due to a different aircraft position at recording start time. On the other hand, the AoAs of the different flight track Osa_T3b (same day, 16:28) in Fig. 4.7d show a completely different AoA pattern. This is expected and is an indication of the observed RFI originating from an external source outside of the airplane. Furthermore, Fig. 4.7c shows the differences in estimating the AoA from the sniffing pulse and from the bandpass filtered Osa_T1a data. It can be seen, that most of the samples are colored in dark blue, which is equivalent to a difference in the AoA estimate of much less than 0.5°. There are some areas with larger

errors and some chunks of the image that are completely red due to the necessary corrections mentioned in Section 4.2. The estimated corrections are different for the sniffing pulse data and the bandpass filter data, which introduces differences in the data. Fig. 4.8 shows the AoA estimate as a plot for a single frequency (456.42 MHz, Osa_T1a) for both methods. Both estimates show a similar trend with a slight offset. This offset is a result of the independent error corrections that were needed to correct issues manifested during flight. Individual corrections are applied to the data set used for the sniffing pulse and to the HV-polarization used for the bandpass filter. Future flights without corrupted raw data should not result in an offset between both methods.

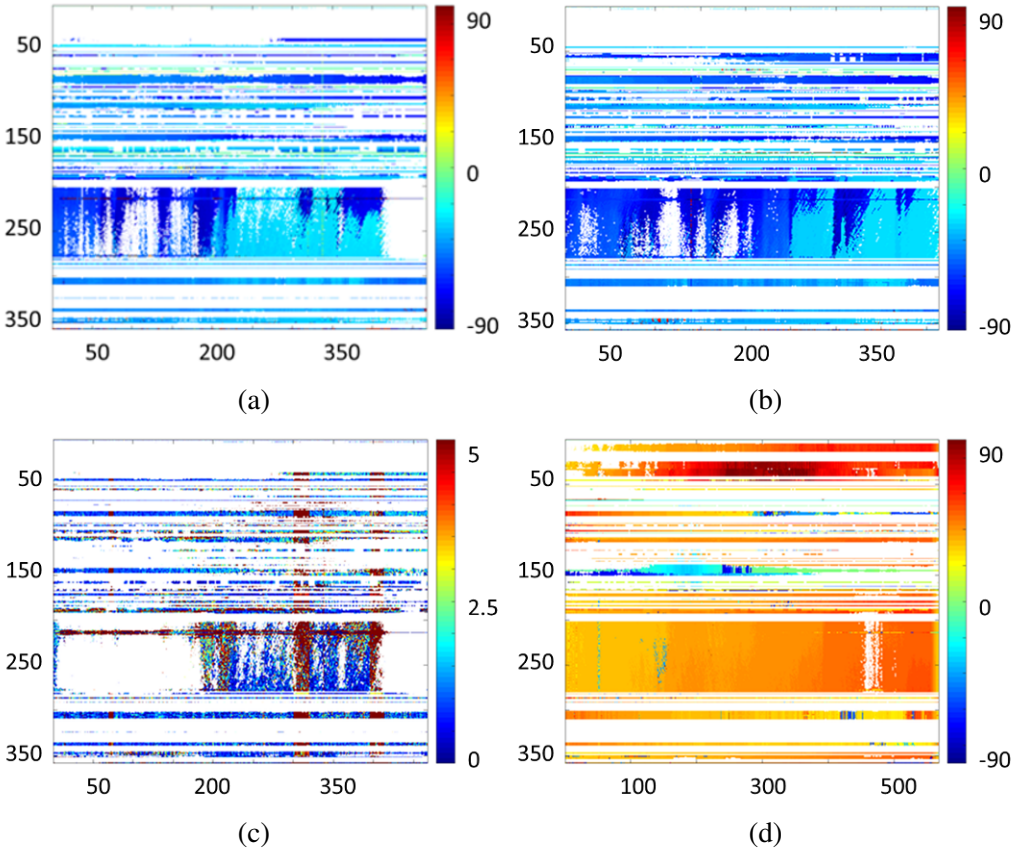

Fig. 4.7.: AoA estimates for the nth RFI-flagged bin (y-axis) in slow time (x-axis): a) Osa_T1c (sniffing pulse), b) Osa_T1d (sniffing pulse), c) Osa_T1c (absolute angle difference between both methods), d) Osa_T3b. Colors indicate AoA in degrees with 0 pointing to nadir. White bins were not flagged with RFI at the shown time instance.

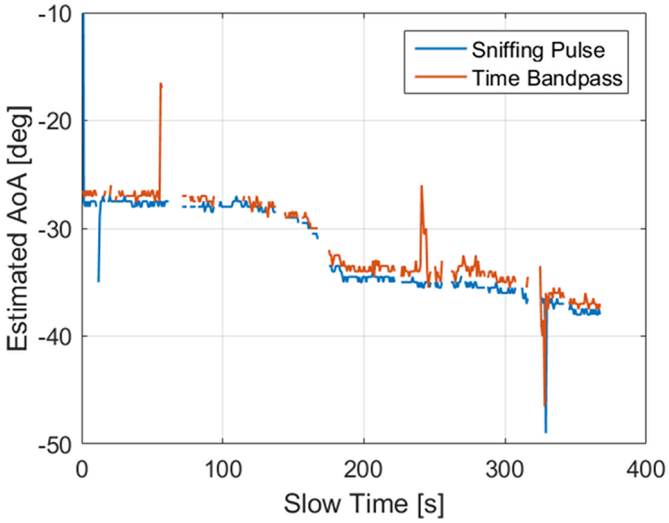

Fig. 4.8.: Estimated AoA of an RFI source at 456.42 MHz captured in Osa_T1c with the sniffing pulse method (blue) and the bandpass filter approach (orange). The sudden change of the angle at 180 seconds could be caused by attitude corrections of the airplane to follow the planned flight path.

4.3.2. RFI Observed with EcoSAR

In the following, the RFI patterns between repeat acquisitions are compared and the overall spectrum occupancy as well as maximum power for each flight track are presented. To do so, the bandpass filter method is applied to the entire EcoSAR 2014 dataset. The detection method is performed on each channel, only keeping mutual interference. This helps to single out interferences that are possibly caused by the system itself. Internal interference common to all channels would still leak through, but the angle of arrival estimation would result to 0° (nadir) at all times for such signals. Fig. 4.9 shows the flagged RFI bins over time for Osa_T3a and Osa_T3b in H-polarization. The y-axis represents the position of the interferer in the baseband frequency (e.g., 0 corresponds to 435 MHz) and the x-axis in slow time. The time difference between both acquisitions is 21 hours. The slow time is shifted by about a minute due to a shift of the swath in azimuth. Reproducible RFI can be observed at roughly 100 seconds (160 seconds in Fig. 4.9b) for a frequency of 20 MHz in baseband (red arrows). Frequency occupations at 36 MHz, 42 MHz and a wide-band source around 62 MHz show repeatable characteristics. However, there are also significant differences. In Fig. 4.9a there is an interfering source at -40 MHz, which does not show up in Fig. 4.9b. Figure 4.9b shows RFI at

-62 MHz and -47 MHz. In Fig. 4.9a these RFI sources are only flagged for a small time period. A potential reason for this is that the signal was too weak to be detected in the first pass.

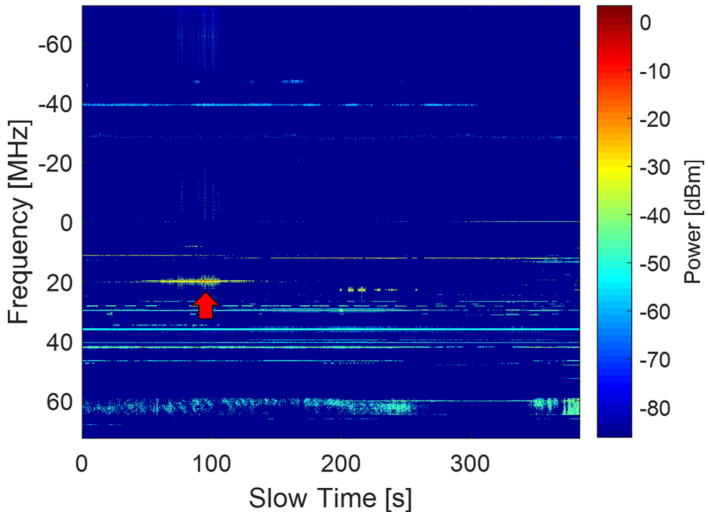

(a)

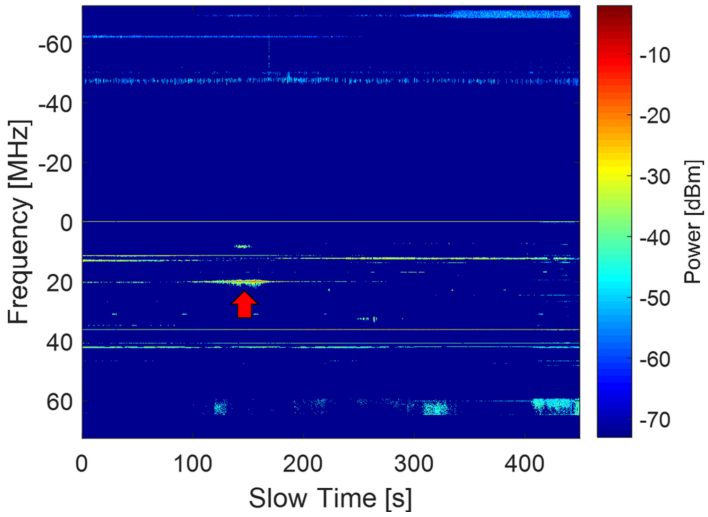

(b)

Fig. 4.9.: Frequency bins flagged with RFI for baseband frequency (y-axis) and slow time (x-axis) for visits with 21 hours difference. Flight tracks according to Table 4.2: a) Osa_T3a, b) Osa_T3b.

Fig. 4.10 shows the occupation of the spectrum in percentage (ratio between interferer transmit duration and receive window duration) for all tracks. Fig. 4.10a and Fig. 4.10b represent the received H-polarization and Fig. 4.10c and Fig. 4.10d the received V-polarization at lower and upper frequency bands. An internal interference source at 435 MHz has been removed from the plots. It can be noticed, that the left side of the spectrum contains far less RFI than the upper frequencies. The spike at 362.5 MHz (-72.5 MHz in Fig. 4.9) that affects all tracks and shows an occupation of 100% is likely internal RFI as well, that was present in all channels. The other spikes however, show different behaviors for each flight track. In the lower frequencies, they are only present in the Costa Rica flight tracks for the H-polarization. The two strongest spikes (yellow) are located at 396.1 MHz and at 406.7 MHz with a spectrum occupation of both about 50%. The Bahamas (H and V) and the Costa Rica V-polarization does not show any RFI in the lower frequencies from 360 MHz to 435 MHz.

The upper frequency spectrum on the other hand shows a large variety of interfering signals. Most of them are very narrow peaks in the frequency domain, which indicates a spread signal in the time domain. Yet, notching all of them would result in a large loss of bandwidth. There are three wide-band interferers at 482.8 MHz - 487.4 MHz (Bahamas H-polarization only), at 494.6 MHz - 498.5 MHz (all tracks and polarizations) and at 506.6 MHz - 507.2 MHz (Bahamas only).

A zoomed in view on the frequencies of concern to ESA's BIOMASS is shown in Fig. 4.10e (H-polarization) and Fig. 4.10f (V-polarization). The BIOMASS spectrum (432 MHz - 438 MHz) is not affected in any of the scenes. There is one main interferer in the Bahamas (both polarizations) at 439.9 MHz - 440.4 MHz with an occupation of close to 70% in H and almost 100% in V-polarization. Less active interferers can be found at 441 MHz and at 446.2 MHz.

The maximum frequency bin power of the interferers is given in Fig. 4.11. All powers are measured at the antenna input. It can be seen in Fig. 4.11e and Fig. 4.11f that the main interferer in the Bahamas adjacent to the BIOMASS band has maximum powers of -10 dBm (H-polarization) and -3.4 dBm (V-polarization). The left side of the entire spectrum (Fig. 4.11a, Fig. 4.11c) has maximum power values of -14 dBm. The RFI in the upper frequencies (Fig. 4.11b, Fig. 4.11d) shows a wide variety with signal powers ranging from +4.3 dBm to below -40 dBm. In conclusion, the high spectrum occupancies at several frequencies (Fig. 4.10) combined with the non-negligible powers (Fig. 4.11) demonstrate the need for advanced RFI filtering methods at P-band.

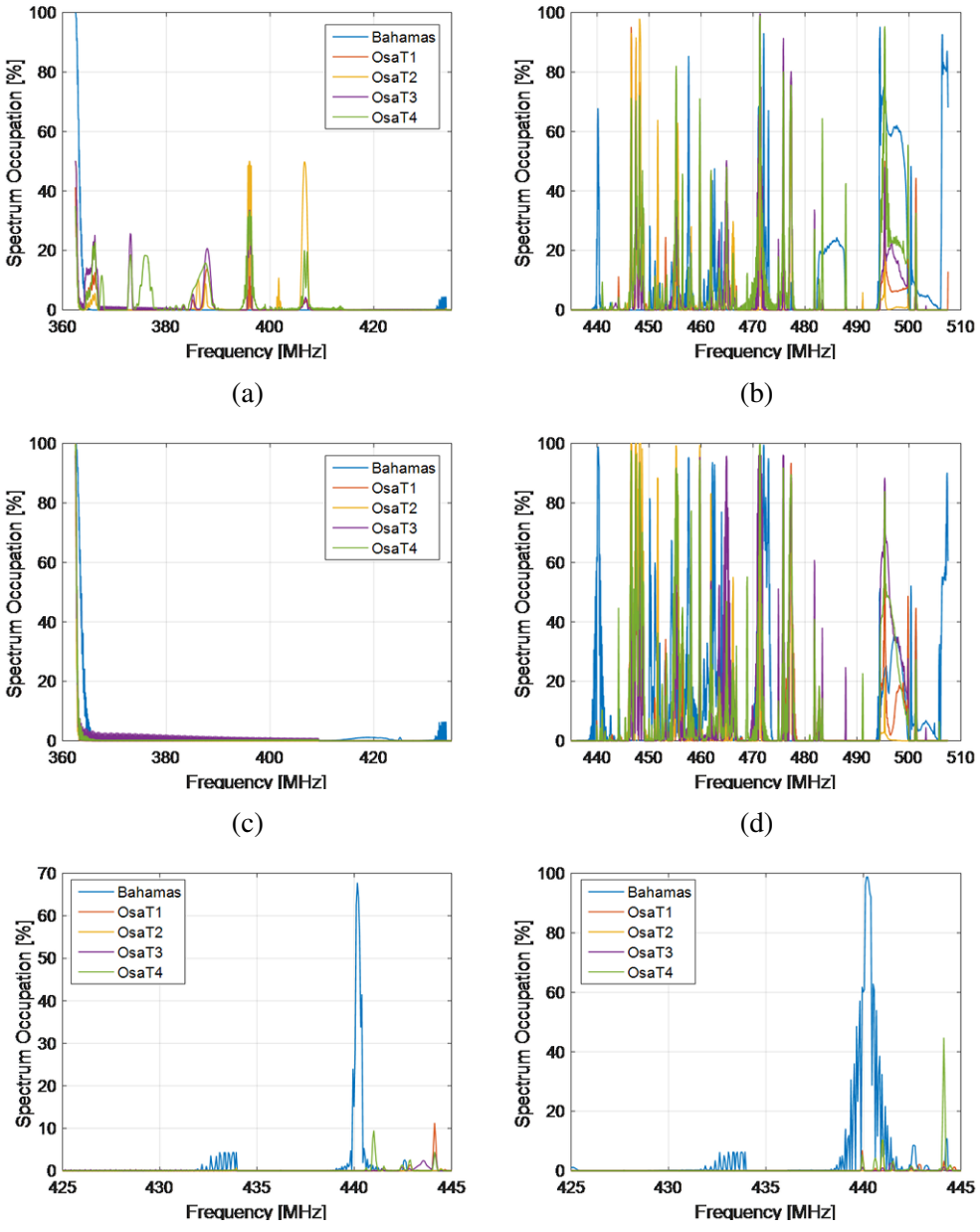

Fig. 4.10.: Spectrum occupancy of RFI detected at each frequency bin in percentage for: a) and b) H-polarization for the lower and higher frequency band, respectively, c) and d) V-polarization for the lower and higher frequency band, respectively, e) H-polarization zoomed, f) V-polarization zoomed.

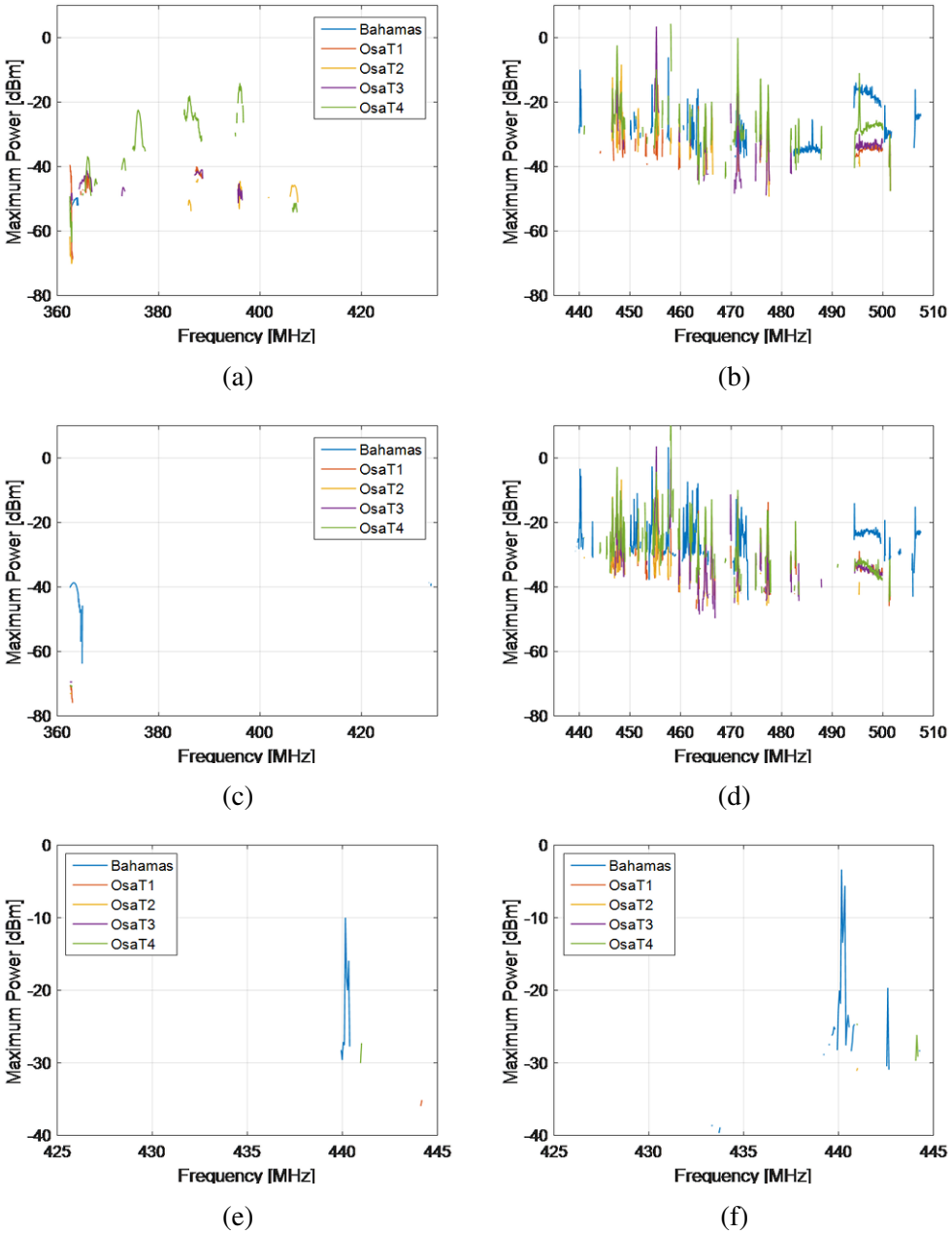

Fig. 4.11.: Maximum RFI power over frequency: a) and b) H-polarization for the lower and higher frequency band, respectively, c) and d) V-polarization for the lower and higher frequency band, respectively, e) H-polarization zoomed, f) V-polarization zoomed.

4.4. Geolocation of RFI

The EcoSAR antenna elements are orthogonally aligned to the flight direction. Therefore it is only able to steer in elevation and to estimate the angle between the line-of-sight to the signal and the axis going through all antenna elements. Depending on the AoA, the RFI source can be positioned on a cone around the axis that is originating in the phase center of the antenna with an opening angle that corresponds to $180° - \theta_{\mathrm{AoA}}$ (Fig. 4.12). Assuming interferers on Earth, possible RFI locations can be reduced to only one half of the cone. This half-cone can be intersected with a model of the Earth, which yields a line with all possible positions of the RFI source. However, because of the relative motion over time, multiple lines can be estimated to narrow down the position of the interferer further. For this approach, it is necessary to account for the relative position and orientation of the radar to the Earth model.

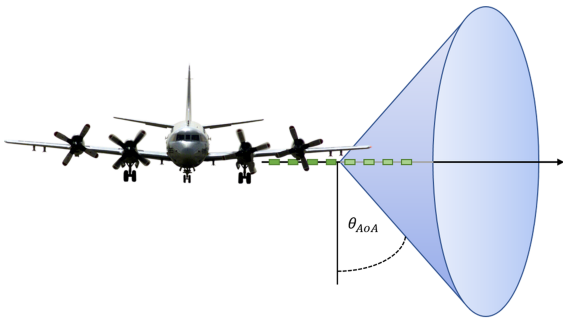

Fig. 4.12.: Cone representing possible locations of RFI source measured at an elevation angle of θ_{AoA}. Green boxes represent antenna elements.

In this section the location of the interferer in the Bahamas at 439.9 MHz - 440.4 MHz is narrowed down. The estimated AoA is shown in Fig. 4.13a for the flight tracks TB_T1 (blue) and TB_T2 (orange). The blue line decreases from -55° until it stabilizes at roughly -72.5°. The reason for this is that as the plane is approaching the target, the previously described cone is narrowing until the target is normal to the flight track. The following abrupt increase of the AoA is then caused by a roll maneuver of the airplane, as it is taking a right turn. The negative angle and the change over time conclude that the target is on the left side of the TB_T1 flight track, approximately orthogonal to the target before plane's right turn. The orange line on the other hand shows positive angles. This indicates that the target is on the right side of flight track TB_2. It initially reads a small AoA that then slowly increases over time. This indicates that the plane is flying

towards the target. It is likely far ahead because of the small AoA. Figure 4.13b shows a map that is separated into three sections: the RFI source is located in the right section that is enclosed with the green lines and is left to TB_T1 and right to TB_T2. Further, a signal that is far ahead of the flight track TB_T2 and normal to TB_T1 before the turn must be located somewhere between Andros Island and Nassau.
Based on the latitude, longitude, altitude, yaw, pitch and roll values recorded with the integrated Inertial Measurement Unit and Global Position System, the instantaneous nadir looking vector $\vec{n}$, forward looking vector $\vec{f}$ and right looking vector $\vec{r}$ of the airplane in the ECEF coordinate system can be calculated. The half-cone towards the RFI source can then be described with the measured looking angle θ_{AoA} and the azimuth angle Ψ as follows:

$$\begin{pmatrix} x \\ y \\ z \end{pmatrix} = \begin{pmatrix} x_0 \\ y_0 \\ z_0 \end{pmatrix} + t \cdot \left[\vec{n} \cos\theta_{\mathrm{AoA}} \cos\Psi + \vec{r} \sin\theta_{\mathrm{AoA}} + \vec{f} \cos\theta_{\mathrm{AoA}} \sin\Psi \right]. \tag{4.1}$$

With x_0, y_0 and z_0 being the instantaneous airplane position in ECEF coordinates and $t \in \mathbb{R}$. This cone is intersected with an ellipsoidal Earth model described by:

$$\frac{x^2}{a} + \frac{y^2}{a} + \frac{z^2}{b} = 1, \tag{4.2}$$

where a is the semi-major axis and b is the semi-minor axis of the WGS84 ellipsoid. The intersections for all Ψ are possible locations of the RFI source. The locations are marked on a map and the procedure is repeated for more steps in time. In the ideal scenario, the interferers position is marked on the map for each time step and the location is narrowed down. The resulting maps are shown in Fig. 4.14. Figure 4.14a shows the observed scene without overlay and Fig. 4.14b shows the computed intersections for flight track TB_T1. Blue means a low number of intersections on the same point and red indicates a high percentage of intersections were located at a point. It is possible to make out the shape of the cones and also one point that shows a high number of hits. This point is likely the location of the interfering signal. The geolocation is also performed for track TB_T2 and shown in Fig. 4.14c. Due to the low nature of the estimated AoA, the cones have a high opening angle. This results in a less defined maxima.
However, the points with the most intersections are located in the same area as in

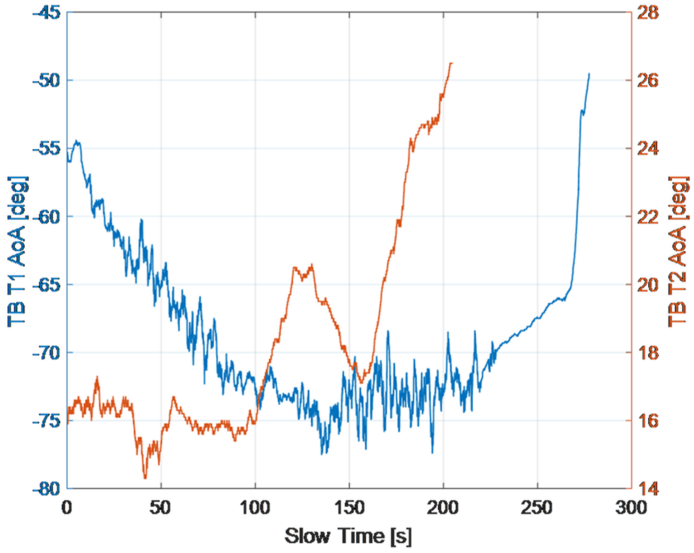

(a)

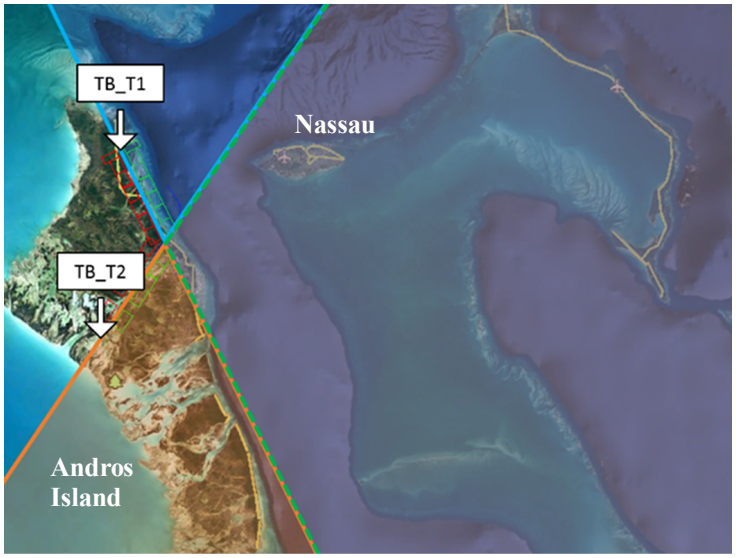

(b)

Fig. 4.13.: a) Estimated AoA of RFI source at 439.9 MHz - 440.4 MHz in TB_T1 (blue) and TB_T2 (orange). b) Map divided into three areas. Blue: possible RFI location based on AoA of TB_T1, Orange: possible RFI location based on AoA of TB_T2, Purple: Overlap of both areas.

Fig. 4.14b. The location of the RFI source is independently reproduced from both flight tracks. A merged map of the intersections is given in Fig. 4.14d. The resulting location is

in agreement with the expected result derived from Fig. 4.13a above, and the estimated position is in the ocean, potentially originating from a marine vessel. The location is located 16 km WSW of a base of the Royal Bahamas Defence Force and 30 km NNE of the U.S. Navy's AUTEC base. The target is located outside of EcoSAR's imaging swath and no other unobstructed satellite data were available for this day over the area.

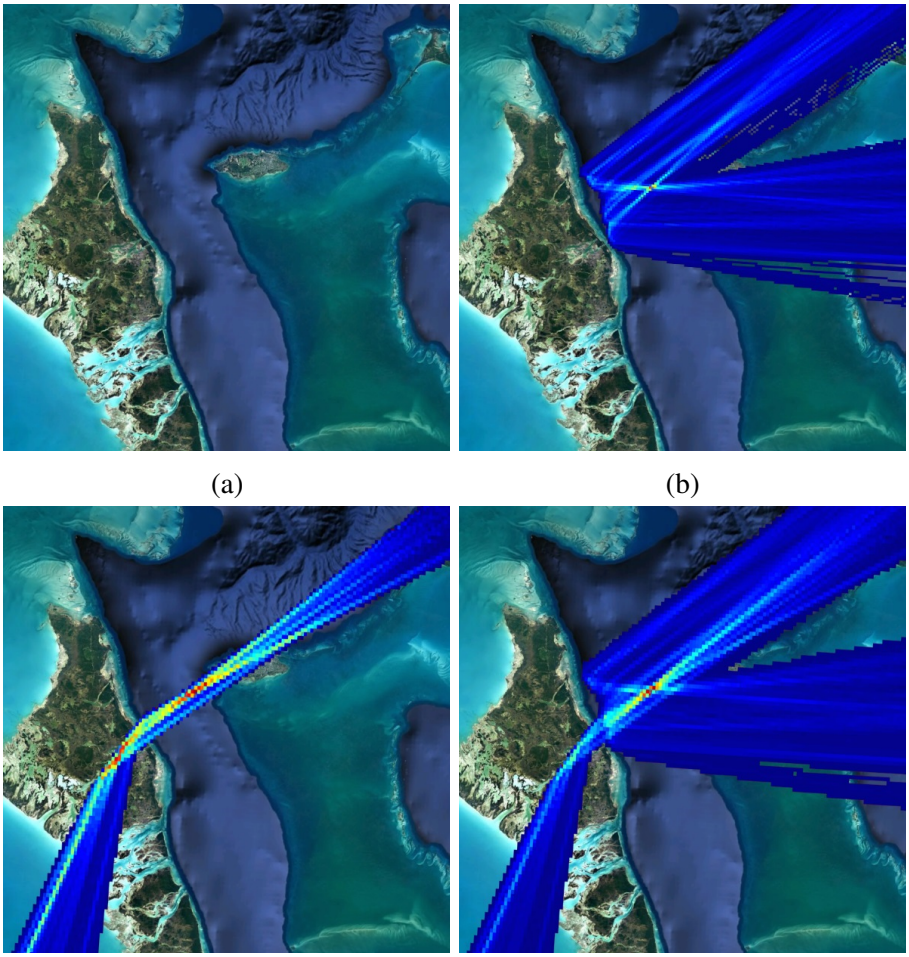

(a) (b)

(c) (d)

Fig. 4.14.: a) Aerial image. Intersections of possible RFI locations for TB_T1 (b), TB_T2 (c), and mean of both (d). The color scale is going from 0% (blue) to 100% (dark red) and visualizes the percentage of the cones that intersect in one point.

4.5. Adaptive Antenna Pattern Notching Results

In Chapter 3, antenna pattern notching with the MVDR beamformer was adapted to the filtering of SAR images by utilizing time- and frequency-varying algorithms in range and azimuth. Based on these previous simulations, the Range-Dependent Time MVDR and Range-Dependent Frequency MVDR are applied to real EcoSAR data with multiple elevation channels in this section. The effectiveness of the algorithms is evaluated based on the inferferometric coherence before and after RFI filtering. Note that synchronization issues between the receive windows of each antenna and polarization, as well as a too short receive window, decreased the common spectral overlap between interferometric pairs. The processed range bandwidth therefore needed to be reduced to 20 MHz, with only 2.5 μs of the pulse recovered for the H-polarization (1.5 μs for the V-polarization). This affected the SNR and resulted in noisy interferograms. In addition, the transmit power of the V-polarization was lower than intended, further decreasing the SNR of interferograms that utilize the V-polarization in transmit. After all error sources were corrected, only the flight line Osa_T1 (Fig. 4.2) was of good enough quality to produce interferograms. The geocoded HH image of this flight line is shown in Fig. 4.15. The shown image covers the entire processed bandwidth of 120 MHz for the H-polarization, thus the swath size in range is decreased for the interferograms because the common bandwidth is only 20 MHz. The parameters of the dataset are summarized in Table 4.3.

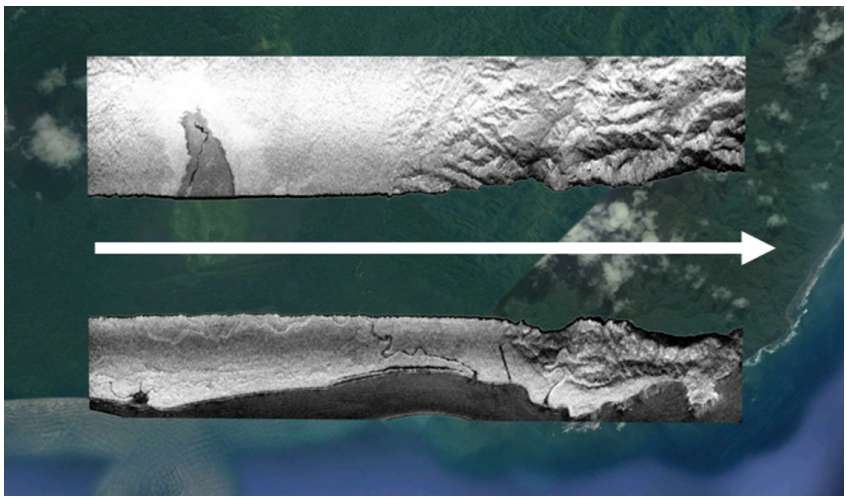

Fig. 4.15.: The geocoded EcoSAR HH image of Osa_T1 that is analyzed in this section. Data were acquired on both sides of the flight track simultaneously (right).

Table 4.3.: EcoSAR system parameters of analyzed dataset.

	Dataset
Center Frequency	479 MHz
Bandwidth	20 MHz
Pulse Length	2.5 μs (H) 1.5 μs (V)
PRF	500 Hz
Range Resolution	7.5 m
Azimuth Resolution	0.675 m
Flight Altitude	3.7 km
Platform Velocity	136 m/s

Figure 4.16a shows the averaged frequency spectrum of the HH and VH image. Multiple peaks due to narrowband RFI are clearly visible in the right half of the SAR spectrum. If the entire bandwidth was used for the interferograms, it would be recommended to apply the RFI filtering on multiple sublooks to make best use of the number of available notches. However, Fig. 4.16b shows the part relevant to the interferograms that are filtered to a common bandwidth with the spectrum ranging from 469 MHz to 489 MHz. In the processed bandwidth only three peaks can be made out in the HH and five peaks in the VH image. EcoSAR's antenna is made of 8 elements and hence 7 notches can be placed towards interference. The dual-track mode doubles the covered swath, though this makes it necessary to reserve notches for ambiguity suppression to suppress signals from the opposite side. These ambiguities are handled by the Range-Dependent Time MVDR and Range-Dependent Frequency MVDR as if they were interferences and no modification of the algorithms are needed. However, the ability to notch external interferences is reduced compared to single-track mode. Because about three notches are required to suppress these ambiguities, this leaves four notches for interference. Therefore, the HH image should show a good RFI filter behaviour as more notches than interferers are available. The VH image on the other hand has not enough notches available and the filter capabilities might be reduced. In addition, the power (and hence SNR) in the VH image is weaker than the HH image, partially due to the weaker transmit power and partially because the power is spread over a higher total bandwidth (H: 120 MHz, V: 200 MHz) even though only 20 MHz are processed. Overall, the total coherence and the improvement due to the RFI mitigation is expected to be higher for the HH interferogram.

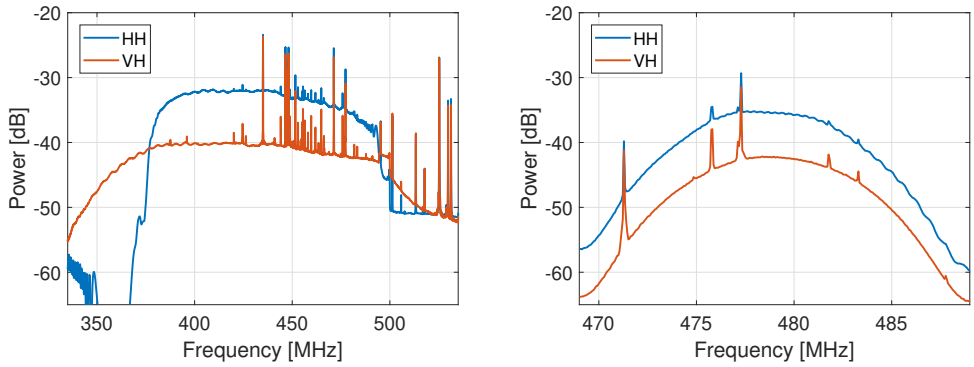

Fig. 4.16.: Averaged range-frequency spectrum of the available EcoSAR scene for the HH (blue) and VH (orange) image: a) Entire recorded spectrum with cut-off chirp due to too short receive window; b) Spectrum after Hamming window is applied to keep common spectrum only.

Computed HH and VH coherence histograms for both sides are plotted in Fig. 4.17. The blue curve represents uncorrected data and shows the worst coherence in all four cases. It can be noticed that the improvement for the left side (Fig. 4.17a and Fig. 4.17c) is higher than for the right side (Fig. 4.17b and Fig. 4.17d). A possible explanation for this is, that external interferers are located on the left side of the track and are already suppressed well by the sidelobes when the beam is steered towards the right side. This also seems logical because the right side is looking towards the sea, where the likelihood for interference is expected to be lower. After a manual notching of the antenna pattern towards the expected direction of the ambiguities (orange curve), the coherence moves to higher values. The performance of the Range-Dependent Time MVDR and Range-Dependent Frequency MVDR is similar, making the faster Range-Dependent Time MVDR the better choice. The better performance of the Range-Dependent Frequency MVDR in the simulations can be contributed to the larger bandwidth (120 MHz). Because the processed bandwidth of the available dataset is only 20 MHz, the frequency resolution of the Range-Dependent Frequency MVDR can not utilize its full potential. The coherence gains are also higher compared to the manual notching of the ambiguities. In Fig. 4.17b and Fig. 4.17c, the tail ends of the manual notching approach reach into higher coherences but the overall coherence values are improved with the automated methods. Possible reasons for this include the high coherence seen in the mountains. As the MVDR beamformer is sensitive to a wrong steering direction of the main beam, a degradation

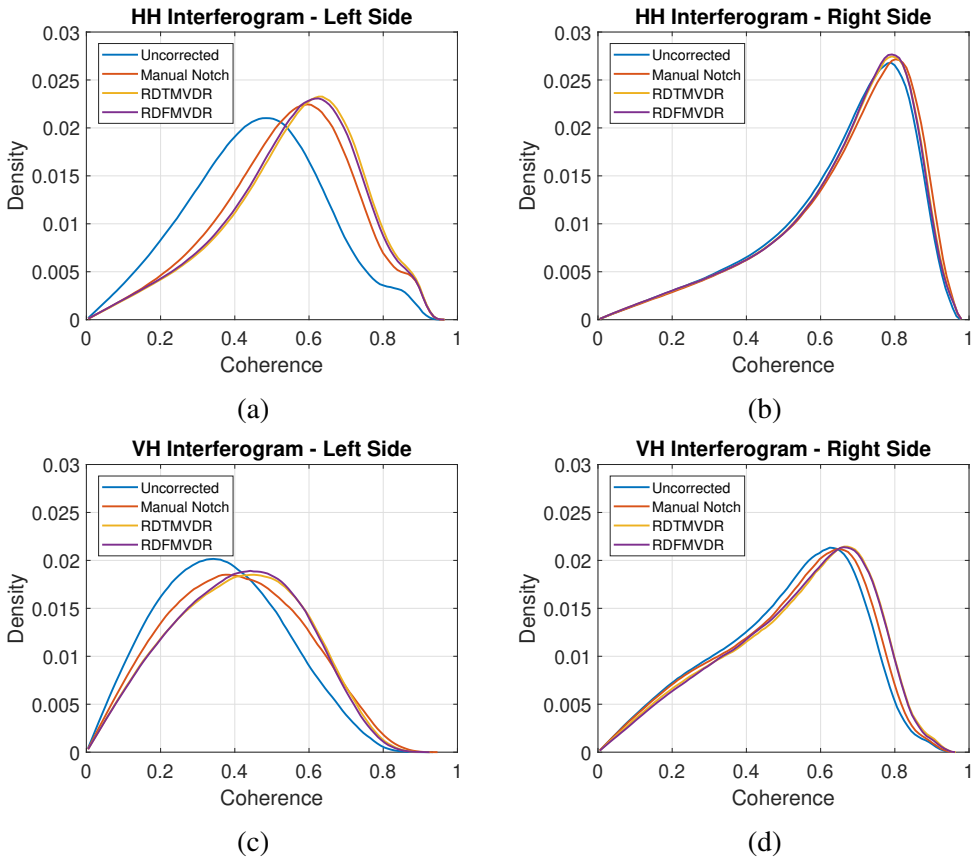

Fig. 4.17.: Coherence histograms for uncorrected, manually notched, Range-Dependent Time MVDR filtered and Range-Dependent Frequency MVDR filtered image for a) HH interferogram of left side, b) HH interferogram of right side, c) VH interferogram of left side, d) VH interferogram of right side.

is caused by the filter and hence the SNR drops. A solution for this would be an additional constraint to widen the main beam (at the cost of one notch) or to implement a topography-dependent steering rather than assuming a flat Earth model.

Coherence images for the HH interferogram of the left side, which showed the biggest improvement according to the histograms, are shown in Fig. 4.18. The improvement from the uncorrected image (second from top) to the manually notched image (third from top) is evident and marked with red boxes. Fringes in the middle of both images could be caused by the narrow band interferences observed in the spectrum of Fig. 4.16b. After implementing the Range-Dependent Time MVDR (bottom row), the fringes van-

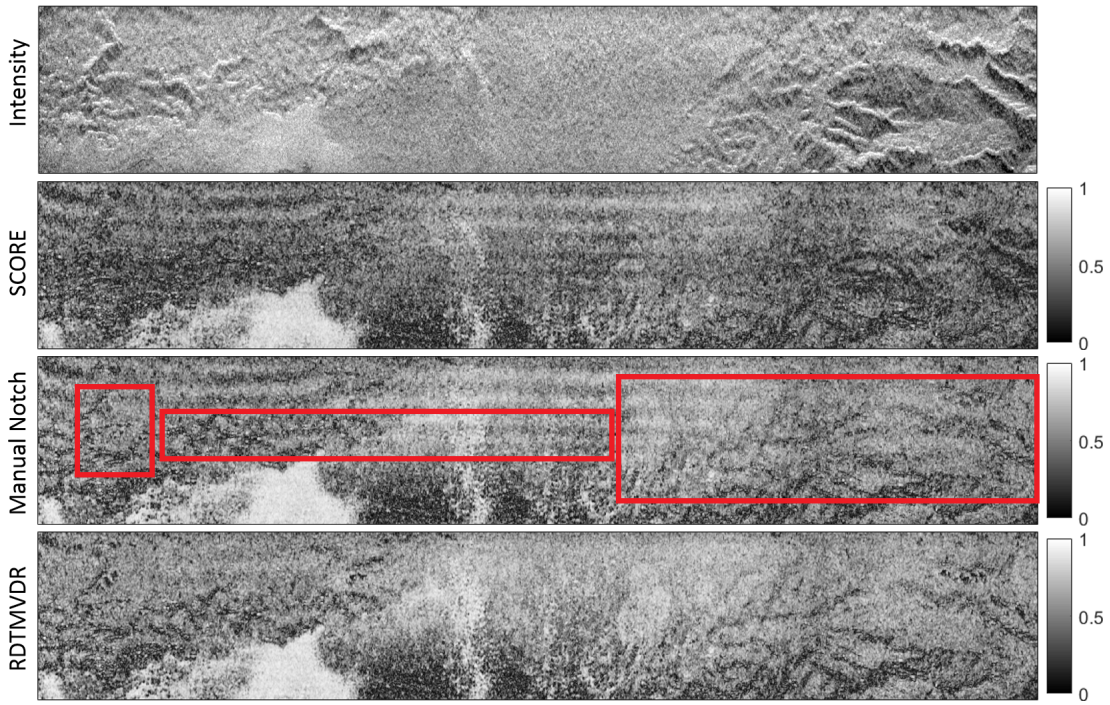

Fig. 4.18.: Top to bottom: Intensity of focused SAR image, HH coherence with Scan-On-Receive, HH coherence with a manual notching of the ambiguities, and HH coherence with adaptive Range-Dependent Time MVDR for ambiguity and RFI suppression. Fringes due to interference are visible in the uncorrected image and in the manually notched image. Red boxes mark areas of most evident coherence improvement after notching ambiguities from the other side. After the RFI mitigation, the fringes disappear.

ish, producing a clearer coherence image with higher coherence values.

4.6. Remarks

An analysis of the RFI encountered during EcoSAR's first flight was performed. Herefore, the use of an interleaved sniffing pulse for RFI detection was compared to the RFI detection from recorded SAR data. The interference that could be observed in the EcoSAR data is narrow band interference. It is well located in the frequency domain and spread in the time domain. Therefore, the approach to separate the RFI from the SAR signal with timed bandpass filters proved to be effective for detection and analysis. Pulsed RFI was not experienced, however, a pulsed signal is expected to be captured at least partially with a bandpass filter and should therefore also be detectable when the radar is operating in transmit mode. The relative accuracy of RFI AoA estimates in the presence of the SAR signal compared to the sniffing pulse was also investigated. Offsets in the angle estimate of up to 1° compared to an estimate on RFI only data were measured. One potential reason for this offset is independent error corrections that needed to be applied to the EcoSAR data to compensate for hardware glitches.
An important aspect of detecting RFI threats is the geolocation of the RFI source. For example RFI measured during airborne campaigns may originate from sidelobes. Strong interference that is far away from the flight track will still be seen in the data. Unlike conventional radars, the DBF capability enables to estimate the direction of the impinging RFI signal. In this chapter, the RFI direction estimation for an interfering signal in the Bahamas was demonstrated. The accuracy of this method is expected to be improved for DBF data that were not exposed to hardware glitches.
In addition, RFI mitigation based on time and frequency adaptive antenna pattern notching (Chapter 3) was applied to EcoSAR imagery and first results were presented. Even though the EcoSAR data were corrupted due to hardware glitches and affected by uncalibrated channels, the applied techniques showed a good improvement of the coherence. Further, ambiguities from the opposite side of the flight track caused by a dual-track imaging mode were treated as interference and handled well by the algorithm. This concludes that the algorithm is also able to handle an automatic notching of, for example, orthogonal waveforms in MIMO-SAR [81, 121] or multiple elevation beams [121], which are both sensitive to inaccuracies of the estimated signal AoAs [79, 102] (e.g., due to topography). The notches were adaptively driven towards the ambiguity and towards external interference for the best result in each range line. A further improvement of the RFI filtering is expected from uncorrupted DBF data.

5. RFI Mitigation with Auxiliary Beams

5.1. Chaper Overview

The previous chapter verified the novel DBF-based RFI mitigation algorithms of Chapter 3 with experimental airborne SAR data. However, the implementation of these new algorithms is challenging for a spaceborne DBF SAR. A spaceborne DBF SAR that implements antenna pattern notching needs to be equipped with sufficient processing power or the capability to transmit the increased data volume to the ground. If processed on board, any errors induced by the notching, such as caused by insufficient calibration or lack of knowledge about topography, are irreversibly applied to the data. Therefore, this chapter investigates a new method [122] for spaceborne systems to supplement on-ground RFI mitigation with additional information that can be gathered with DBF SAR. Auxiliary beams can be used to measure the interferer signals and to subtract RFI from the SAR beam. With this novel RFI mitigation method based on DBF, there is no need for auxiliary antennas (and their disadvantages), as a formation of additional auxiliary beams can be achieved with the main antenna. In addition, DBF allows to adaptively notch the signal of interest in the auxiliary beams, which improves the performance.
The presented methods inherently result in short time gaps in the reconstructed signal for time instances when the position of the RFI and instantaneous SAR signal is identical. This is the case because the removal of the RFI signal from the SAR data requires that both signals are orthogonal in the filtering space. For example, in a general SAR system, interfering signals can be removed with a bandpass filter from a SAR image if they are received at a different frequency (Fig. 5.1a). Multi-channel systems are capable of a spatial filtering and open additional filtering space in the elevation angle and Doppler angle direction as illustrated in Fig. 5.1a. All DBF RFI mitigation methods only work as long as the interferer and instantaneous SAR signal are viewed from different angles (and thus they can be separated). However, this chapter shows that autoregressive modelling can be used to reconstruct the SAR signal in these short time gaps to overcome this limitation under certain conditions (Section 5.3).

The idea behind the auxiliary beams is proposed in Section 5.2. Different concepts for systems with DBF in elevation and/or azimuth are discussed in Section 5.2.2. In addition, Section 5.2.2 also introduces a way to overcome a fundamental limitation of DBF: to remove in-beam interference. Finally, simulations for a system with DBF in elevation are conducted in Section 5.5 to investigate the performance.

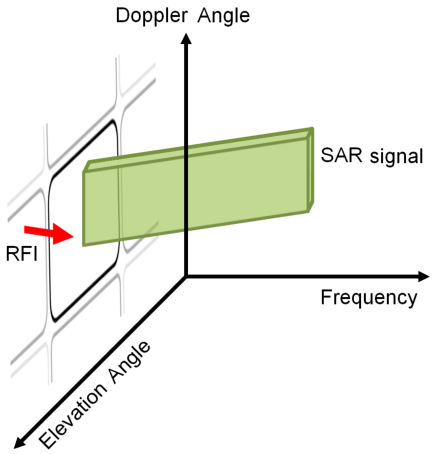

(a)

Fig. 5.1.: SAR (green) and RFI signal (red) that arrive at the antenna at the same time instance are distributed over frequency, Doppler angle and elevation angle. They are orthogonal to each other if they can be separated in one of these directions, which allows for RFI mitigation. Depending on the direction of the impinging signal, it is inherently modulated by the antenna pattern gain in that direction.

5.2. The Concept of Auxiliary Beams

The Sidelobe Canceller (SLC) [47–49, 123] is the foundation of the novel RFI mitigation method presented in this chapter. The SLC makes use of auxiliary antennas to gather information about interferers in the sidelobes of the main antenna. Hereby, the interfering signal is observed with a higher gain than in the main antenna. While the main antenna is pointing towards the direction of the signal of interest, the auxiliary antenna covers

a wide angular area (e.g., close to isotropic) to record interference from unknown directions (Fig. 5.2b). By this means, two different signals are recorded, that yield two independent combinations of the SAR and RFI signal according to:

$$\mathbf{s}_{\mathrm{M}} = \mathbf{s}_{\mathrm{SOI}} \cdot G_{\mathrm{M,SOI}} + \mathbf{s}_{\mathrm{RFI}} \cdot G_{\mathrm{M,RFI}} \tag{5.1}$$

$$\mathbf{s}_{\mathrm{A}} = \mathbf{s}_{\mathrm{SOI}} \cdot G_{\mathrm{A,SOI}} + \mathbf{s}_{\mathrm{RFI}} \cdot G_{\mathrm{A,RFI}} \tag{5.2}$$

Note that $\mathbf{s}_{\mathrm{M}}$ is the signal at the main antenna, where the signal of interest is modulated with the complex gain $G_{\mathrm{M,SOI}}$ and the interferer is modulated with the complex gain $G_{\mathrm{M,RFI}}$. $\mathbf{s}_{\mathrm{A}}$ is the signal at the auxiliary antenna with the corresponding gains $G_{\mathrm{A,SOI}}$ and $G_{\mathrm{A,RFI}}$. Neglecting the effect of relative motion within a single receive window, the interfering signal can then be subtracted from the main data by a scaling k of the auxiliary data according to Fig. 5.2a. In the conventional Sidelobe Canceller, this is commonly achieved with a second antenna that affects the payload or reduces the size of the main antenna. DBF overcomes this disadvantage by synthesizing arbitrary antenna patterns post-acquisition. The auxiliary antenna can be replaced with digital auxiliary beams that are formed by the main antenna. In addition, the shape and number of the auxiliary beams can even be changed adaptively, which offers great flexibility. Another advantage

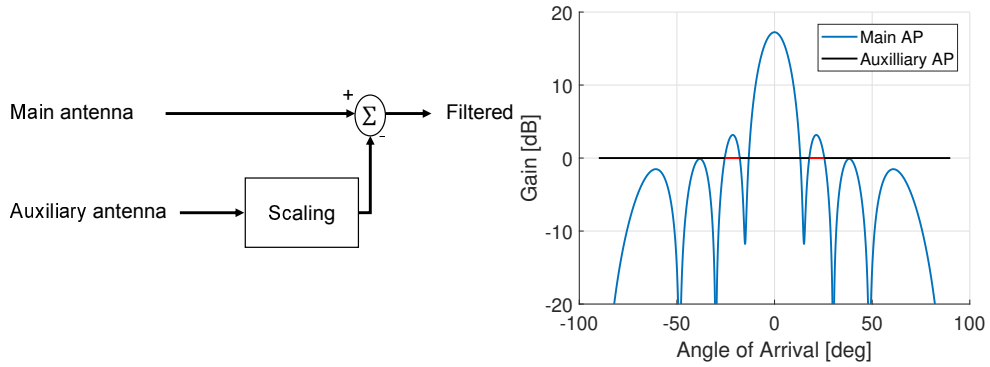

(a) (b)

Fig. 5.2.: a) Block diagram of the Sidelobe Canceller (SLC), b) The antenna pattern of the main antenna (blue) and of an auxiliary antenna (black) with isotropic gain. The information collected with the auxiliary antenna can be used to mitigate interference in the sidelobes. For angles where the auxiliary antenna has lower gain than the main antenna (red), this mitigation can result in an increased noise floor due to the scaling of the signal.

is that the signal of interest can be adaptively notched in the auxiliary beam towards the instantaneous direction of the signal of interest. This improves the performance further. The approach proposed in this chapter is an advanced RFI mitigation method for multi-channel systems that uses advanced DBF and outperforms the SLC by the use of adaptive, digital auxiliary beams. The payload is reduced compared to the SLC which comes at the cost of a slightly increased data rate. Note that the transmission of few additional auxiliary beams results in a reduced data rate compared to transmitting all N receive channels to the ground, as is required for on-ground antenna pattern notching.

5.2.1. Conditions for a Least-Mean-Square Subtraction

The gain of a DBF system in the main beam and the digital auxiliary beam depends on the chosen beamforming weights **w** and the steering vector **a**:

$$G_{\mathrm{M,SOI}}(\theta_{\mathrm{d}}) = \mathbf{w}_{\mathrm{M}}^{H}\, \mathbf{a}(\theta_{\mathrm{d}}) \tag{5.3}$$

$$G_{\mathrm{M,RFI}}(\theta_{\mathrm{RFI}}) = \mathbf{w}_{\mathrm{M}}^{H}\, \mathbf{a}(\theta_{\mathrm{RFI}}) \tag{5.4}$$

$$G_{\mathrm{A,SOI}}(\theta_{\mathrm{d}}) = \mathbf{w}_{\mathrm{A}}^{H}\, \mathbf{a}(\theta_{\mathrm{d}}) \tag{5.5}$$

$$G_{\mathrm{A,RFI}}(\theta_{\mathrm{RFI}}) = \mathbf{w}_{\mathrm{A}}^{H}\, \mathbf{a}(\theta_{\mathrm{RFI}}). \tag{5.6}$$

θ_{d} is the angle of arrival of the signal of interest and θ_{RFI} is the angle of arrival of the interferer. Unless the system is ideally calibrated (and thus **a** is well known) and the angle of arrival of the interferer is known (an estimation can only be performed at the expense of additional computational load), the linear system given by (5.1) and (5.2) remains underdetermined. The complex scaling coefficient k is therefore chosen in a least mean square manner according to [124]

$$k = (\mathbf{s}_{\mathrm{A}}^{H}\, \mathbf{s}_{\mathrm{A}})^{-1}\, \mathbf{s}_{\mathrm{A}}^{H}\, \mathbf{s}_{\mathrm{M}}, \tag{5.7}$$

assuming the matrix inverse of $\mathbf{s}_{\mathrm{A}}^{H}\, \mathbf{s}_{\mathrm{A}}$ exists. Note that $\mathbf{s}_{\mathrm{A}}$ and $\mathbf{s}_{\mathrm{M}}$ are column vectors. Further, to avoid an amplification of the noise in the auxiliary signal, the beam patterns must be chosen so that $|k| < 1$ and thus the gain of the interferer in the auxiliary beam needs to be larger than in the main beam. This is illustrated in Fig. 5.2b for a directive main antenna and an isotropic auxiliary antenna. The red lines mark the angular area that is impacted by the noise degradation.

After an ideal estimation of k, the reconstructed signal of interest after LMS filtering is:

$$\mathbf{s}_{\mathrm{SOI}} = \frac{\mathbf{s}_{\mathrm{M}} - k \cdot \mathbf{s}_{\mathrm{A}}}{G_{\mathrm{M,SOI}}} = \mathbf{s}_{\mathrm{SOI}} \cdot \left(1 - \frac{G_{\mathrm{A,SOI}} \cdot G_{\mathrm{M,RFI}}}{G_{\mathrm{A,RFI}} \cdot G_{\mathrm{M,SOI}}}\right). \tag{5.8}$$

As seen from Eq. (5.8), the LMS filter subtracts an attenuated version of the signal of interest, as well. Assuming $G_{\mathrm{A,SOI}} < G_{\mathrm{A,RFI}}$ and the worst case of an isotropic auxiliary beam, this requires

$$\frac{G_{\mathrm{M,RFI}}}{G_{\mathrm{M,SOI}}} << 1. \tag{5.9}$$

This condition is satisfied if the interferer is located in the sidelobes of the main antenna and the PSLR of the antenna pattern is high enough. If the interferer is close to or inside the main beam, then Eq. (5.9) is not satisfied anymore. However, note that DBF gives the flexibility to notch the signal of interest in the auxiliary beam, which can soften the impact of Eq. (5.9).

5.2.2. Auxiliary Beam Constellations

A DBF instrument is recording each channel individually to form the digital antenna pattern after data acquisition, which allows for the generation of multiple simultaneous beams. This means that unlike conventional phased array radars, auxiliary beams can be acquired in the absence of auxiliary antennas. In contrast to [53], the entire main antenna can be utilized for recording the SAR signal and measuring the RFI. In addition, the angular distribution of the SAR signal that depends on fast time can be utilized to notch the auxiliary beams towards the signal of interest at each time instance. This reduces the error of the RFI subtraction (Eq. (5.8)) and thus allow for a cancellation of the interference closer to the signal of interest (otherwise the high gain of the signal of interest in the auxiliary beam affects the performance). The resulting antenna patterns for the system simulated in Section 5.5 ($N = 63$) are shown in Fig. 5.3. For an isotropic auxiliary beam (in the absence of noise), the residual LMS error of Eq. (5.8) is a result of the main antenna pattern shape. For an interferer at -5°, it is only about 1.73 dB. However, the new notched auxiliary beam receives an additional suppression (Eq. (5.8)) of more than 20 dB. This additional suppression strongly depends on how accurately the signal of interest is notched. Hence, it is affected by errors of the angle of arrival introduced by topography. To avoid this, the notch can be widened by placing more than

one null. For the simulations in this work, it is assumed that the signal of interest is known and thus only one notch is placed. The generation of the auxiliary beams can either be performed on range-compressed data or by using dispersive beams [75]. The following subsections present auxiliary beam constellations for DBF SAR systems.

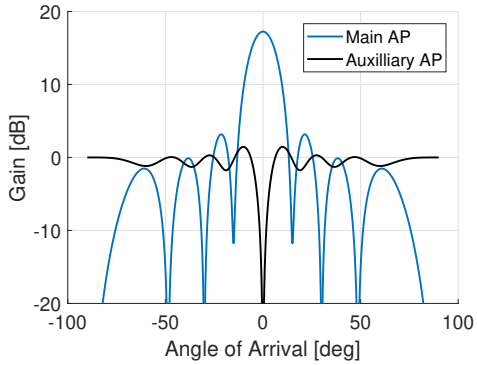

Fig. 5.3.: Main antenna pattern and auxiliary beam pattern with a notch towards the signal of interest. The notching reduces the error of the subtraction in Eq. (5.8).

Application to a Scan-on-Receive System

A digital auxiliary elevation beam that measures RFI in all directions but the SAR signal direction (Fig. 5.4a) has to move its notch along the ground. Thus, the gain experienced by a fixed interferer in the digital auxiliary beam is changing during the receive window (in the same manner, the interferer gain in the main beam is changing due to the scan-on-receive operation). The received power of an interferer at 30° is shown in Fig. 5.4b (system simulated in Section 5.5 with $N = 63$). While the interferer is outside of the scan-on-receive beam, it experiences a high gain in the auxiliary beam (red curve). Note that the received power is computed with normalized antenna patterns. When the SAR and RFI signal direction are identical, the interferer moves into the notch of the auxiliary beam and the received power drops. A spatial filtering of SAR and RFI with DBF is not possible for these angles (no angular orthogonality). The green curve shows the received power of the interferer in the scan-on-receive beam, which resembles the antenna pattern of the main antenna. As the interferer moves into the SAR beam, the power increases and is the highest at 30°.

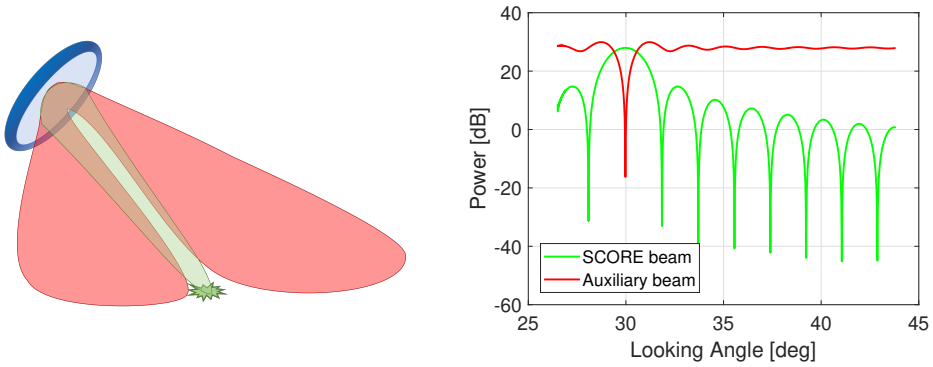

(a) (b)

Fig. 5.4.: a) Illustration of scan-on-receive (SCORE) beam (green) and a wide auxiliary beam (red) with notch, b) Received power of interferer at 30° in auxiliary beam and SCORE beam.

On the other hand, the SAR signal of an extended target receives a flat gain in the scan-on-receive beam (green curve in Fig. 5.5a) because the main antenna pattern is constantly pointing towards the instantaneous return. In the auxiliary beam, the SAR signal is notched and thus suppressed (red curve in Fig. 5.5a). As a result, the combination of SAR and RFI signal in Fig. 5.5b allows for measuring the same RFI in the auxiliary beams, as if the SAR signal was not present.

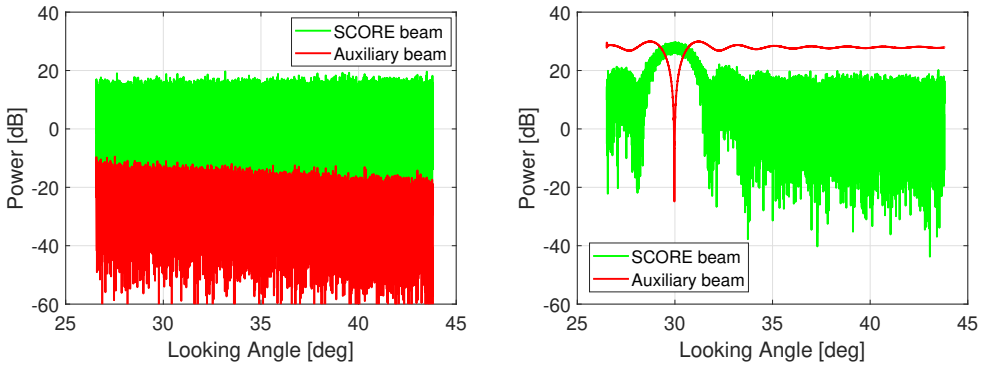

(a) (b)

Fig. 5.5.: a) Received power of extended SAR target in auxiliary beam and SCORE beam. The element factor of the antenna array equals one, b) Received power of extended SAR target and interferer in auxiliary beam and SCORE beam.

The correction of the data can be performed on-ground according to the LMS approach of Eq. (5.7). However, in the conventional SLC this is performed pulse-wise or on multiple pulses. Thus the SLC requires the scaling k between scan-on-receive beam and auxiliary beam to be constant. As evident from Fig. 5.4b, this is not the case. The scaling is changing with range due to the modulation of the interferer in both, the scan-on-receive and the notch-on-receive antenna pattern. It is an inherent property of scan-on-receive systems that the complex scalar k depends on fast-time and is thus a complex vector $\mathbf{k}$. If both, the antenna pattern and the angle of arrival of the interferer, were known, this variation of $\mathbf{k}$ could be removed.
A much better option is to perform the LMS filter in the azimuth direction. This way, $\mathbf{k}$ can be estimated for each range bin. As the radar is moving, the interferer modulation is changing due to the 2D antenna pattern, though for a couple of hundred pulses this variation can be neglected. $\mathbf{k}$ can be assumed constant in azimuth. Therefore, the estimation is performed on short segments in each range line as shown in Fig. 5.6.

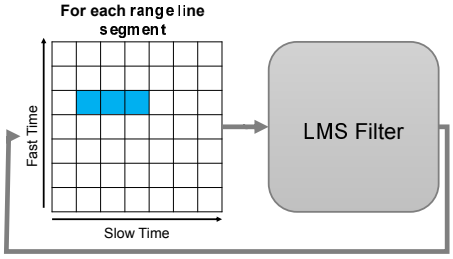

Fig. 5.6.: Application of auxiliary beams to a SAR with scan-on-receive (SCORE) in the range direction. The scaling factor $\mathbf{k}$ varies with range but can be estimated on short azimuth segments, which allows for the assumption of an azimuth invariant k.

By inserting Eq. (5.7) into Eq. (5.8), the filtered image $\mathbf{s}_\mathrm{F}$ can be computed to:

$$\mathbf{s}_\mathrm{F}(\tau) = \mathbf{s}_\mathrm{M}(\tau) - \mathbf{k}(\tau)\,\mathbf{s}_\mathrm{A}(\tau) = \mathbf{s}_\mathrm{M}(\tau) - \left(\mathbf{s}_\mathrm{A}^H(\tau)\,\mathbf{s}_\mathrm{A}(\tau)\right)^{-1}\mathbf{s}_\mathrm{A}^H(\tau)\,\mathbf{s}_\mathrm{M}(\tau)\,\mathbf{s}_\mathrm{A}(\tau). \quad (5.10)$$

Moving from the time domain to a two-dimensional matrix that contains multiple pulses, this can be efficiently computed via

$$\mathbf{s}_\mathrm{F} = \mathbf{s}_\mathrm{M} - \left[\frac{1}{\mathrm{diag}(\mathbf{s}_\mathrm{A}^H\,\mathbf{s}_\mathrm{A})} \otimes \mathrm{diag}(\mathbf{s}_\mathrm{A}^H\,\mathbf{s}_\mathrm{M})\right]\mathbf{s}_\mathrm{A}, \quad (5.11)$$

where $\otimes$ represents an element-wise multiplication.

Wide Elevation Beam

The simplest approach to generating a notched auxiliary beam in elevation is to generate a wide beam pattern as shown in the example of Fig. 5.3, which is notched towards the SAR signal. Because the SAR angle of arrival is changing and captured with scan-on-receive, the notch of the auxiliary beam is changing as well. The wide beam is the inverted scan-on-receive beam. As the scan-on-receive weights are predetermined for the acquired scene, the auxiliary beam weights can be precalculated in the same manner. An optimization of the beam pattern on the ground is possible before the scene is acquired. In case of a reflector antenna, the auxiliary beam coverage depends on the physically available feed elements and it might not be possible to achieve a high gain outside of the swath. However, reflector antennas benefit from a high sidelobe suppression and do not necessarily require an out-of-swath RFI mitigation.

Narrow Elevation Beam Steered Towards RFI

The previously presented wide auxiliary beam has the advantage of measuring RFI in all directions (except the signal of interest direction). This allows for the optimization of the beamforming weights on the ground. However, the noise floor in the auxiliary beam is increased. Thus, interference signals that are spatially close to the instantaneous notch in the auxiliary beam might be masked by noise. This does not impact the filtering of out-of-swath interference but will impact the removal of RFI close the instantaneous main beam (inside the swath).
Another option is to form a narrow auxiliary beam towards the direction of the interferer as shown in Fig. 5.7a. While the narrow auxiliary beam is measuring the RFI signal, a notch is again placed towards the SAR signal (Fig. 5.7b). The method achieves a noise floor in the auxiliary beam that is equivalent to the noise floor in the scan-on-receive beam. This comes at the cost of losing RFI information that is not in the narrow beam. It is therefore necessary to either estimate the RFI angle of arrival on-board or to steer the auxiliary beam towards the expected RFI direction. For example, this is useful for interference emitted by a fixed source on the ground that does not change position.

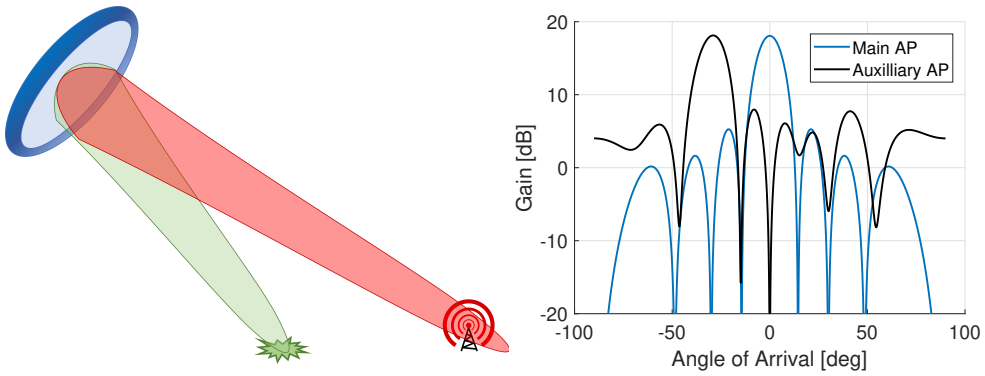

(a) (b)

Fig. 5.7.: a) Illustration of scan-on-receive (SCORE) beam (green) and narrow auxiliary beam (red) pointing towards interferer, b) Narrow auxiliary beam pattern.

Narrow Elevation Beams Surrounding SCORE Beam

As mentioned before, a reflector antenna benefits from a high suppression of the higher order sidelobes. If this suppression is high enough to remove the RFI, then the auxiliary beam is only needed to gather information about RFI in the first sidelobes and close to the main beam. Hence, the narrow antenna pattern can be set to follow and preceed the scan-on-receive beam as shown in Fig. 5.8a. This can be achieved with two separate auxiliary beams or with a single auxiliary beam, such as is shown in Fig. 5.8b. The

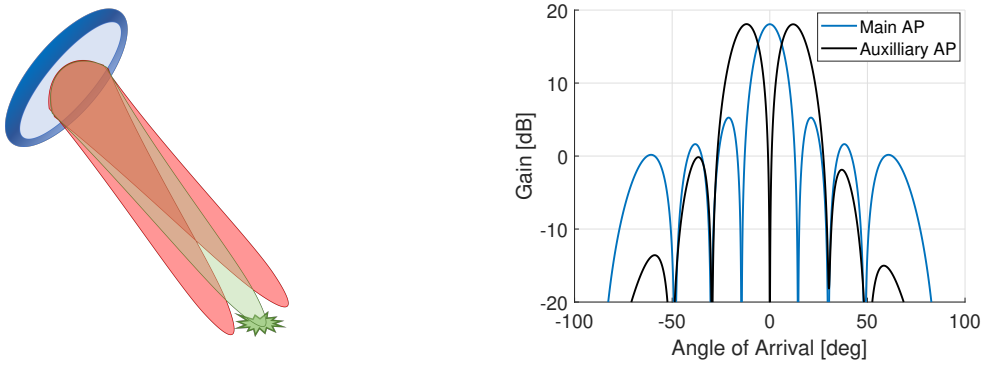

(a) (b)

Fig. 5.8.: a) Illustration of SCORE beam (green) and narrow auxiliary beams (red) surrounding the SCORE beam, b) Two auxiliary beams surrounding the SCORE beam.

width of the notch and the two peak positions of the auxiliary beam can be optimized on-ground without the need of estimating the angle of arrival of the RFI. Additional beams can be placed if necessary.

Azimuth Beams

The previously presented methods for elevation beams can be directly transfered to a SAR system with steerable azimuth beams. The digital auxiliary beams are either pointed towards the interferer or they cover a wide aperture that is notched towards the instantaneous Doppler frequency (this needs to be performed on-board in the range-Doppler domain). On the ground, the LMS filter is applied in the range-Doppler domain for each Doppler bin and in small range segments as shown in Fig. 5.9 (each Doppler bin of the main beam is filtered with the corresponding digital auxiliary beam). This makes it possible to assume that $\mathbf{k}$ is constant during each segment.

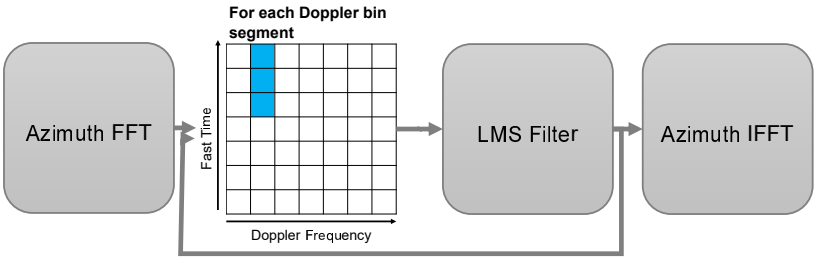

Fig. 5.9.: Application of auxiliary beams for a DBF SAR with multiple azimuth channels. The scaling factor $\mathbf{k}$ varies with azimuth but can be estimated on short range segments, which allows for the assumption of a range invariant $\mathbf{k}$.

Two-dimensional Beams

For SAR systems that are capable of DBF in both dimensions, the area covered by a single antenna element (and covered by the wide, digital auxiliary beam) increases significantly as shown in Fig. 5.10a. Simultaneously, the wide aperture in both dimensions decreases the antenna gain in the wide auxiilary beam, which results in a higher noise floor. This can make the wide beam an unfavorable choice for a two-dimensional system. On the other hand the narrow auxiliary beam (Fig. 5.10b), requires knowledge about the interferer angle of arrival in both dimensions and is thus more sensitive to mispointing. The best choice for a two-dimensional system is a narrow auxiliary beam that is wrapping around the scan-on-receive beam, which is shown in Fig. 5.10c. Compared to the

wide beam, the lower coverage of the auxiliary beam improves the noise floor and the predetermined position of the scan-on-receive beam allows for an exact placement of the auxiliary beam. For a reflector antenna, this can be sufficient. However, a planar antenna will still be subject to interference in the higher order sidelobes that are not measured with this auxiliary beam. To circumvent this, a windowing of the DBF weights could be applied to lower the sidelobes at the expense of a wider main beam.

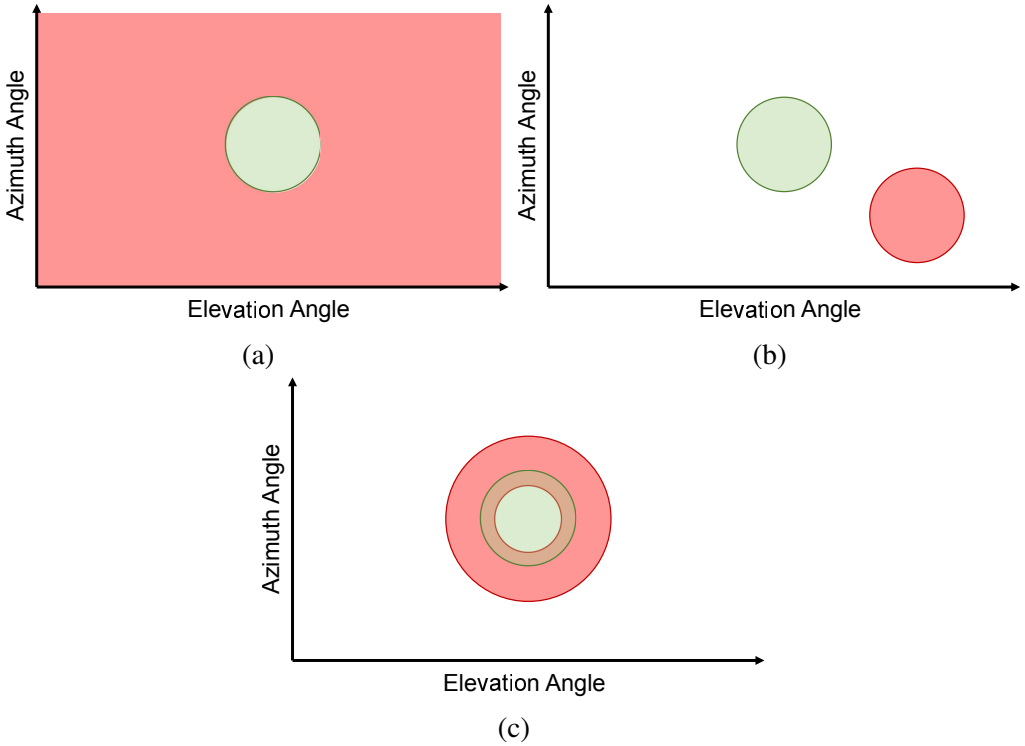

Fig. 5.10.: Illustration of two-dimensional auxiliary beams: a) A wide beam notched towards the signal of interest, b) A narrow beam steered towards the known RFI position, c) A narrow beam that wraps around the scan-on-receive beam.

An additional constraint for a two-dimensional system is the range and azimuth variant scaling factor **k**. In the range-Doppler domain, **k** can be estimated on small windows (Fig. 5.11). This allows for the same sample size as the one-dimensional estimation but with a smaller extent in range and in azimuth. The stationarity of **k** during the small window is dependent on the system parameters and the imaging geometry.

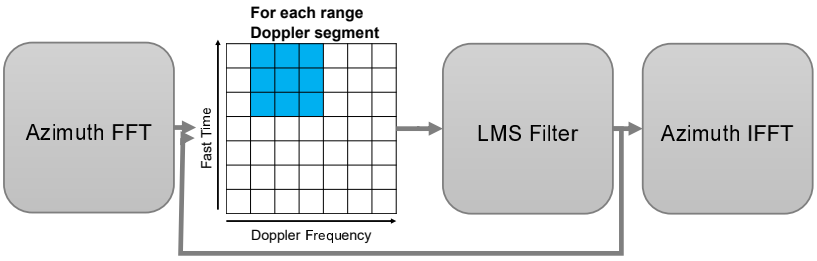

Fig. 5.11.: Application of two-dimensional auxiliary beams. The scaling factor **k** varies in both dimensions. The variation is minimized by updating **k** on small windows. The variation can be further decreased with knowledge about the antenna patterns.

5.3. Autoregressive Modelling for In-Beam Reconstruction

The receive beam in a scan-on-receive (SCORE) system is scanning in elevation to follow the travelling pulse along the ground. If an interferer is located inside the swath, the auxiliary beam and the main beam look into the same direction when the instantaneous SAR direction is originating from the same angle as the interferer. This overlap results in a gap in the reconstructed signal that can not be recovered. However, especially in elevation, this gap is in the order of a few tens of microseconds and defined by the imaging geometry and the main beamwidth. In these instances, an autoregressive model [125, 126] can be used to predict future samples or fill gaps in a time series, which is commonly applied in the restoration of digital audio signals [127, 128]. The signal reconstruction can be achieved if a relation between the missing sample y_n and its preceeding values y_{n-i} $(i \in \mathbb{I})$ can be formed so that

$$y_n = -\sum_{i=1}^{m} a_i y_{n-i}. \tag{5.12}$$

In other words, Equation (5.12) weighs each known sample with a coefficient a_i and recovers y_n by means of a summation of the weighted outputs. This is illustrated with a block diagram in Fig. 5.12. Several autoregressive methods exist that estimate the

weighting coefficients by optimizing

$$\min \; y_n + \sum_{i=1}^{m} a_i y_{n-i}, \tag{5.13}$$

which can be simplified by moving y_n into the sum as $a_0 y_n$ where $a_0 = 1$:

$$\min \; \sum_{i=0}^{m} a_i y_{n-i}. \tag{5.14}$$

A stable method that minimizes the error of both forward and backward estimation (inversion of the sample order) is the recursive Burg's method [129–132]. A detailed description of the method and its derivation as well as the implementation can be found in [133]. The main criterion for the signal reconstruction with an autoregressive is that the signal is stationary during the duration of the gap length and thus requires the signal to have a constant mean, variance and covariance.

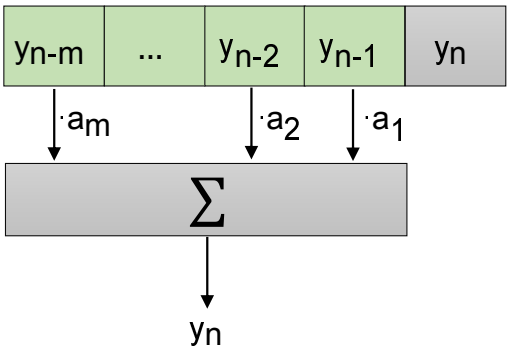

Fig. 5.12.: Illustration of Eq. (5.12): autoregressive modelling estimates the next sample y_n by a weighting and summation of the previous samples (green boxes).

5.3.1. On the Performance Limit of the Signal Reconstruction

Auxiliary beams can not remove interference with the same angle of arrival as the instantaneous SAR signal. This results in a gap width with time duration t_g in the data that can not be recovered (Fig. 5.13). The lower limit for t_g is when the signal positions overlap and is thus influenced by the pulse duration T_p. Note that only the bandwidth B_RFI of the pulse that has the same frequency contributions as the RFI is of interest. The remainder of the pulse can be recovered with a filtering in the frequency domain.

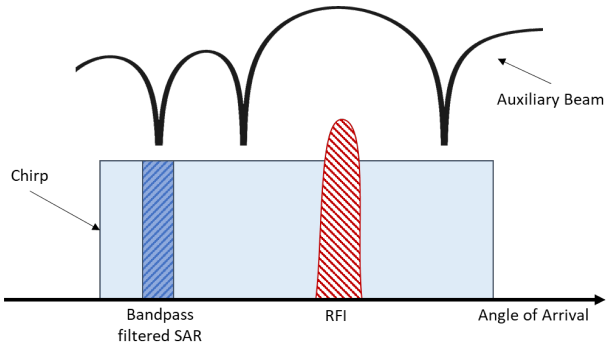

Fig. 5.13.: An instantaneous SAR signal (light blue rectangle) that occupies the entire chirp bandwidth arrives at the antenna simultaneously with an RFI signal. After bandpass-filtering of the received data to the RFI bandwidth, only part of the instantaneous SAR signal remains and is non-orthogonal to the RFI (dark blue-striped box). The RFI and SAR signal are still orthogonal if they can be spatially filtered, for example by spatially notching the SAR signal in the auxiliary beam. If the SAR signal is too close to the main beam of the auxiliary beam, a gap occurs in the filtered data due to the non-orthogonality. The gap width depends on how close to the main beam a notch can be placed in the auxiliary beam.

Therefore, the theoretical lower limit of gap width is given by

$$t_{\mathrm{g}} = T_{\mathrm{p}} \frac{B_{\mathrm{RFI}}}{B_{\mathrm{W}}} \tag{5.15}$$

for $B_{\mathrm{RFI}} < B_{\mathrm{W}}$. In a dispersive system, B_{RFI} can be replaced with the bandwidth of each subband. In addition, the goal of the auxiliary beams is to measure the RFI with a higher gain than the signal of interest. As the signal angle of arrival difference gets smaller, so does the gain difference. Therefore the shape of the antenna pattern is limiting the achievable t_{g} (this is illustrated in Fig. 5.14). The longer the antenna array compared to the wavelength, the sharper the notch that can be placed in the auxiliary beam (red curve). Thus, t_{g} improves for a longer antenna. However, inaccuracies in the SAR angle of arrival knowledge (e.g., due to topography) require a placement of a wider notch. The inaccuracies also come at the cost of an increased t_{g}.

Another factor is the RFI-to-Noise Ratio (RNR) in the auxiliary beam that also impacts t_{g}. As shown in Fig. 5.14, if the RNR increases, the width of the notch that is below the noise floor becomes larger. RFI signals below the noise floor in the auxiliary beam

can not be measured and thus the sensitivity to weak RFI is limited. Because the main beam and auxiliary beams are generated from the same antenna array, this can only be influenced by narrowing the auxiliary beam. Again, this comes at the cost of not capturing RFI from all directions. Note that a larger gain is also desired to restrict $k < 1$ close to the main beam. If $k > 1$, the performance of the interferer subtraction is degraded by an injection of noise during the LMS subtraction. For strong RFI-to-Signal Ratios (RSR), the image is improved despite the noise injection. However, for low RSR this is effectively increasing t_g.
As the auxiliary beam is steered across the image in a scan-on-receive fashion, t_g depends on the time derivative of the incidence angle. Thus, t_g increases with altitude.

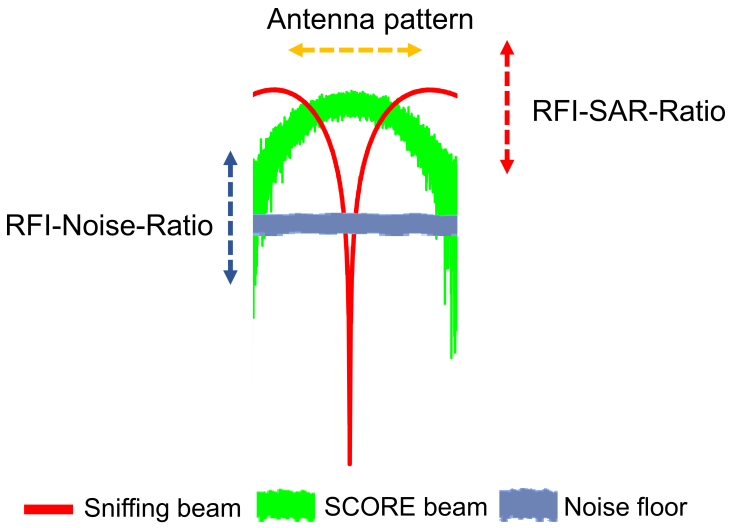

Fig. 5.14.: Illustration of parameters that impact the gap width duration t_g: 1) The auxiliary beam antenna pattern shape defines the width of the notch (red), 2) The RFI-to-Noise Ratio (blue) in the auxiliary beam increases the gap width for weak RFI, 3) the RFI-to-Signal Ratio affects the benefit for $k > 1$, when noise is injected by the LMS filter into the main signal (green).

5.3.2. The Gap Width of the Autoregressive Model

The lower limit of t_g after bandpass-filtering is given by Eq. (5.15) and limited by the pulse duration in each subband. However, according to Section 5.3.1, t_g depends also on N, platform altitude, as well as noise floor in the SCORE beam and auxiliary beam,

which might prevent the SAR system to achieve the limit given by Eq. (5.15). A narrow receive beam minimizes the noise in both beams; thus, this section investigates the impact of antenna height and platform altitude on t_g. The dependency on antenna height (expressed with N receive channels with a half-wavelength spacing) is shown in Fig. 5.15a. The plot indicates that t_g is inversively proportional to the antenna height (and thus here N). As the antenna height decreases, the notch in the auxiliary beam widens (and the minimum spatial separation of instantaneous SAR signal and RFI signal that can be resolved increases). In addition, t_g decreases with altitude because the SCORE beam needs to be scanned faster, which moves the notch in the auxiliary beam faster over the ground. The dependency of t_g on altitude is proportional and shown in Fig. 5.15b.

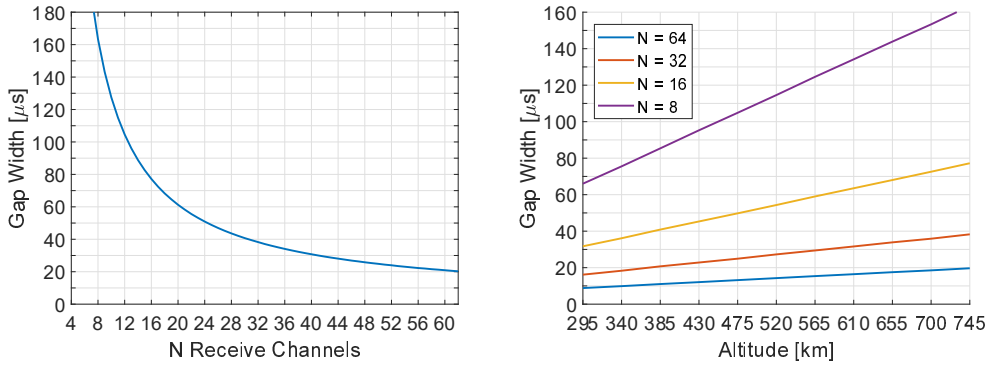

(a) (b)

Fig. 5.15.: Dependency of t_g on: a) Number of receive channels N with half-wavelength spacing that cause the notch in the auxiliary beam to widen, b) Platform altitude that defines the angular velocity of the steered beams.

5.3.3. Overcoming the Performance Limit with Signal Reconstruction

As discussed, a gap width exists for in-beam interference that can not be recovered with adaptive antenna pattern notching nor with auxiliary beams. If this is the case, the RFI signal in this gap needs to be estimated based on the surrounding information. This can either be achieved by fitting a known model of the RFI to the data (e.g., periodic interferer such as a surveillance radar with a fixed transmit chirp), or by assuming the local

stationarity of the RFI signal for the duration of the gap. Then an autoregressive model can be applied to the gap. This is performed in the steps presented in Fig. 5.16. First, the RFI is estimated (blue-dashed line) for the time instances surrounding the gap (LMS filter output). To increase the stationarity of the signal, an estimation of the main-beam antenna pattern shape is removed from both the SAR beam (green) and the RFI estimate (step 2). Inaccuracies in the antenna pattern knowledge will decrease the stationarity of the signal, though this will be reversed in the final step. Also, removing the antenna pattern will increase the noise floor of the RFI estimate at the edges. Yet, for a narrow auxiliary beam, the noise floor will be smaller than it was in the auxiliary beam before scaling with k (red). Next, the gap of the SAR signal is modelled (e.g., autoregressive model or systematic model) in step 3 (white-dashed). In the end, the signal is weighted by the main beam antenna pattern shape from step 2. The RFI in the corrupted gap is restored and can be coherently subtracted.

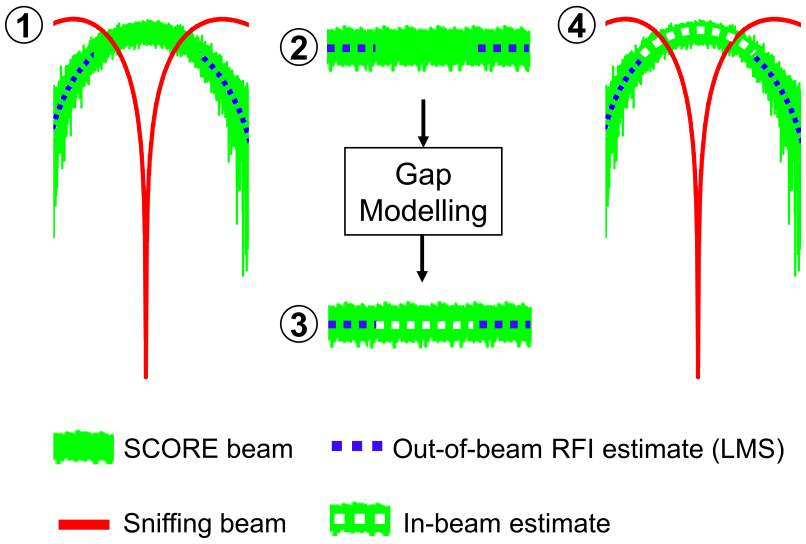

Fig. 5.16.: Reconstruction of the corrupted gap for an in-swath interferer: 1) The out-of-beam RFI signal in the scan-on-receive (SCORE) main beam (green) is estimated (blue-dashed) by means of the auxiliary beam (red) and the LMS filter. 2) The estimated antenna pattern shape in the main beam is removed from the estimated RFI signal and the SCORE beam. This increases the stationarity of the signal. 3) The gap is reconstructed with an autoregressive or systematic model (white-dashed). 4) The reconstructed gap is weighted by the previously removed estimate of the antenna pattern.

Note that the signal reconstruction can only be performed for elevation beams where the resulting gap (number of samples with residual RFI) can be reduced to a length in the order of a few tens of microseconds. For a system with DBF in azimuth, the sampling in azimuth is given by the PRF, which results in azimuth time gaps on the order of milliseconds. Thus, the application of the signal reconstruction for systems with DBF in azimuth is limited as the RFI needs to be stationary for the time duration of the gap.

5.3.4. The Impact of Quantization

After the SAR and RFI signals are received at the antenna, they are quantized on board of the satellite. This is illustrated in Fig. 5.17. The number of bits used for this quantization is hereby also determined by the maximum data rate that can be transmitted to the ground. Due to the quantization, quantization noise is injected into the data which can be significant if the number of bits is set too low, which results in a large spacing between the quantization steps. To capture the data with a minimum number of bits, the dynamic range of the Analog-to-Digital Converter needs to be adjusted to the expected maximum signal power. This is necessary, because even for a fixed number of bits, an increase of the dynamic range will result in an increased spacing of the quantization levels and thus increase the quantization noise again. On the other hand, if the dynamic range is set too low, clipping effects occur. Power levels above the dynamic range are cropped: the signal is restricted to the highest available quantization level which does not represent the accurate state of the signal.

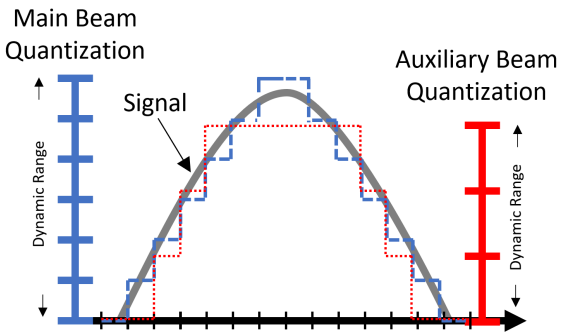

Fig. 5.17.: The signals received with the main and auxiliary beam are quantized on board of the SAR system. The available quantization levels are distributed within the dynamic range of the Analog-to-Digital Converters (colored level bars). If the dynamic range is set too low, clipping effects occur (visible in red quantized signal) and the signal is not fully captured.

A fundamental requirement for the removal of the interference is that neither main beam nor the auxiliary beam experience clipping effects. Regardless of that, the quantization noise that is introduced by the Analog-to-Digital Converter may degrade the filtering performance. The impact of the quantization is investigated with the implemented simulator in Section 5.5.4. The main and auxiliary beams are quantized with a varying number of bits during this analysis. In addition, an implementation of the auxiliary beams with fewer bits than the main beam can reduce the data rate that is transmitted by a spaceborne system to the ground station and is thus investigated as well.

5.4. Summary of Auxiliary Beam Implementations

The methods proposed in this chapter are summarized and compared to the conventional Sidelobe Canceller in Table 5.1.

Type	Advantages	Disadvantages
Sidelobe Canceller	- simple implementation	- increased payload or smaller main antenna - preselected number and shape of beams
All Auxiliary DBF Beams	- payload and main antenna size unaffected - flexible number and shape of beams	- increased complexity (due to DBF architecture)
Wide Auxiliary Beam	- precalculated steering weights - covers all sidelobes	- reduced gain - limited gap reconstruction
Narrow Auxiliary Beam	- highest gain - best gap reconstruction	- on-board AoA estimation / weight computation
Surrounding Auxiliary Beam	- precalculated steering weights - improved gain - improved gap reconstruction	- on-board AoA estimation / weight computation - only measures RFI in first sidelobes

Table 5.1.: Summary of the presented auxiliary beam methods.

5.5. Simulations for Auxiliary Beams in Elevation

In the following subsections, the performance of the methods proposed in Section 5.2.2 is analyzed with a simulator that was implemented for this thesis according to the signal model of Section 2.5. For all simulations, the system parameters in Table 5.2 are used. The simulated swath width is 350 km. Range ambiguities are neglected since the simulated system is utilizing multiple elevation beams (here: five simultaneous beams). The Signal-to-Noise Ratio (SNR), RFI-to-Signal Ratio (RSR) and RFI-to-Noise Ratio (RNR) values given in this section are based on the average power of signal, RFI and noise after beamforming. This is for two reasons: first, the power in the beamformed data of a planar array can be related to the power at a single (active) feed element of a reflector antenna. Second, this excludes the increasing RFI suppression in the sidelobes that is inherent to an increasing array size N from the analysis.

Table 5.2.: Parameters used for the simulations to investigate the performance of the auxiliary beam based methods.

Parameter	**Value**
Elevation Channels	2 to 63
Channel Spacing	0.5λ
Sample Frequency	100 MHz
Center Frequency	1.2575 GHz
Chirp Bandwidth	80 MHz
Pulse Duration	20 μs
Near Range Incidence Angle	26.3°
Far Range Incidence Angle	43.9°
Array Tilt	45°
Platform Altitude	745 km
Swath Width	350 km
Number of Pulses	500
Backscatter Amplitude	Rayleigh distribution
Backscatter Phase	Uniform distribution between 0° and 360°
SNR	0 dB to 40 dB
RFI Type	Continuous Wave, Binary Frequency Key Shifting

5.5.1. Out-of-Beam Interference

Dependence on RNR and SNR

This section uses the implemented simulator to investigate the performance of the proposed auxiliary beam method for RFI mitigation in DBF SAR systems. As a first step,

the number of receive channels N is fixed at 63 for simulations and a wide auxiliary beam is used for the RFI extraction. An interferer is placed outside of the swath at an incidence angle of -20° and at a baseband frequency of 40 MHz. The simulated interferer signal is a continuous-wave signal with a phase offset for each pulse (total pulse number: 500) according to the PRF. The resulting residual 3-sigma errors of the error model discussed in Section 2.5.3 are shown in Fig. 5.18.

The phase standard deviation in the absence of noise (which can be fully contributed to the RFI) is plotted in Fig. 5.18a before (blue) and after (orange) the LMS filter is applied. In the uncorrected case, the error begins to move towards unacceptable values as the RSR approaches about -20 dB. The proposed method achieves a removal of the RFI signal, returning the residual errors back close to zero for high RSR. For low RSR however (smaller than -40 dB), a degradation of the performance is visible. In the absence of noise and interference, the auxiliary beam contains only the notched SAR signal. Even though the SAR signal is mostly notched, the auxiliary beam is still correlated with the SAR signal in the SCORE beam. Therefore, the subtraction of the auxiliary beam with the LMS filters results in a degradation of the signal. Note that this effect disappears in the presence of noise or RFI and could also be avoided with a threshold for the LMS filter.

Next, thermal noise is injected into the data. In the following, we refer to the increase of the standard deviation (which is caused by the RFI) compared to the standard deviation which would result if only noise and no RFI were present. All four residual error parameters of the error model presented in Section 2.5.3 are plotted in Fig. 5.18b through Fig. 5.18f. When the RFI is above the noise floor (RNR > 0 dB), and thus detectable, the LMS output error remains at zero (no standard deviation increase above the normal noise floor) for all parameters regardless of SNR. The RFI mitigation with auxiliary beams is successful. If the interferer is below the noise floor (RNR < 0 dB), the filtering introduces a degradation as discussed above. It can be observed that the degradation (when the method is applied in the absence of detectable RFI) increases with the SNR but is neglectable for SNR = 0 dB. This is the same effect that was observed before in the absence of noise: the auxiliary beam is correlated with the SAR beam and thus the LMS error minimizes part of the SAR signal.

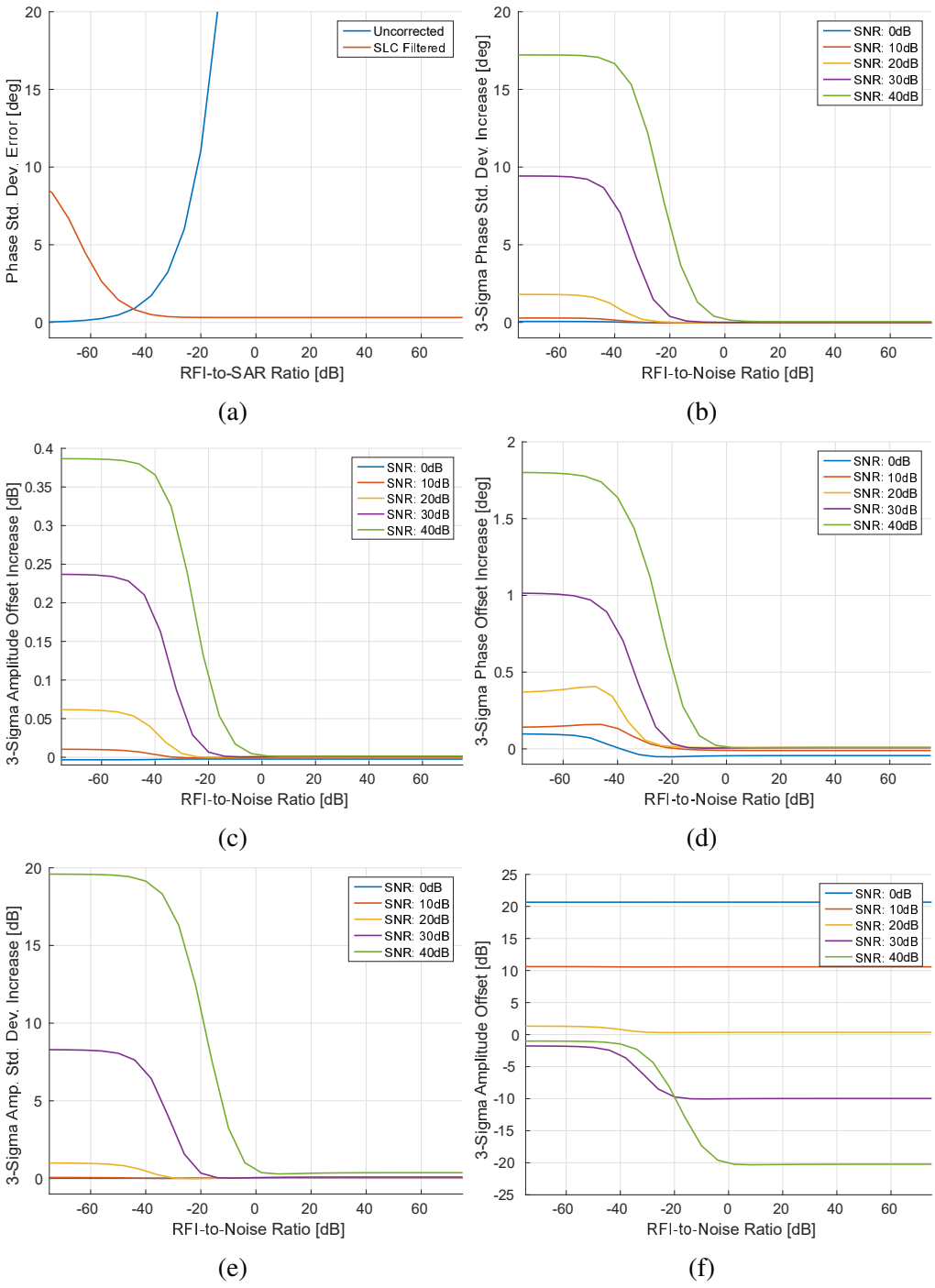

Fig. 5.18.: The 3-sigma error increase (error model of Section 2.5.3) vs. RFI-to-Noise Ratio (x-axis) for $N = 63$ in the presence of a continuous-wave, out-of-swath interferer at -20° and baseband frequency of 40 MHz. The SNR is in reference to the SAR signal: a) Phase standard deviation in absence of noise, b) Phase standard deviation increase with noise, c) Amplitude offset increase with noise, d) Phase offset increase with noise, e) Amplitude standard deviation increase with noise, f) Absolute amplitude standard deviation error with noise.

SNR values of greater than 20 dB are generally expected from point targets only. Because the focusing of point targets will reduce the phase and amplitude standard deviation errors (unlike for extended targets), the degradation is here compensated by the SNR focusing gain. This results in all standard deviation errors to be acceptable for extended targets and point targets. The offset errors for point targets on the other hand are not improving in the focusing process. The shown errors for SNR = 40 dB represent the worst case after focusing. The maximum amplitude offset increase of 0.4 dB (Fig. 5.18c) directly affects the radiometric budget. The maximum phase offset increase (Fig. 5.18d) is below 2° and is acceptable. Note that the amplitude standard deviation increase for SNR = 40 dB is close to 20 dB (Fig. 5.18e), which seems high. A look at the absolute amplitude standard deviation errors (Fig. 5.18f) reveals, however, that for such high SNR an error decrease by 20 dB is still acceptable for point targets (Section 2.5.3). Therefore, a thresholding should be applied to only activate the filter in the presence of RFI for SAR products that need to meet a radiometric budget.

Dependence on Filter Length

Table 5.3 summarizes the maximum error degradation for RNR smaller than 0 dB in dependence of the filter length (which is applied in azimuth direction because of the varying scaling factor in range). An increase of the error with decreasing filter length is evident. All measured values show a good performance.
Next, Table 5.4 summarizes the maximum error degradation when the RFI is below the noise floor. Again the error increases for shorter filter lengths. While the amplitude offset increase of point targets is small for a reduction from 500 pulses to 300 pulses (0.39 dB to 0.6 dB), the error increases significantly for 100 pulses (1.6 dB). Errors of this magnitude affect the radiometric budget. The other error parameters show a good performance. This means a shorter filter window can be implemented if the radiometric budget is not important for the application or if a thresholding is applied to activate the LMS filter only in the presence of RFI above the noise floor.

Table 5.3.: Maximum residual error increase for RFI above the noise floor (RNR > 0 dB). In cells with two values, the first value is the error for extended targets and the value in paranthesis is the error for point targets.

	500 pulses	**300 pulses**	**100 pulses**
Phase standard deviation [deg]	0.2	0.4	1.5
Phase Offset [deg]	0.04	0.05	0.24
Amplitude Offset [dB]	0.01	0.01	0.04
Amplitude standard deviation [dB]	0.58 (0.03)	0.44 (0.03)	4.4 (0.03)

Table 5.4.: Maximum residual error increase for RFI below the noise floor (RNR < 0 dB). In cells with two values, the first value is the error for extended targets and the value in paranthesis is the error for point targets.

	500 pulses	**300 pulses**	**100 pulses**
Phase standard deviation [deg]	1.8 (17.2)	3.0 (22.1)	8.3 (37.3)
Phase Offset [deg]	0.4 (1.8)	0.49 (3.0)	1.9 (8.2)
Amplitude Offset [dB]	0.06 (0.39)	0.1 (0.6)	0.34 (1.6)
Amplitude standard deviation [dB]	1.0 (19.6)	1.1 (21.3)	2.9 (27.2)

Dependence on Array Size

As a next step, the filter length is fixed to 500 pulses and only interference above the noise floor is assumed. The performance of the proposed method for a changing array of size N is shown in Fig. 5.19 by means of the 3-sigma phase standard deviation error increase. Note that, as before in Chapter 3, the array element spacing is fixed at half a wavelength and thus the increasing antenna height results in a narrower main beam. The interferer angle is changed in increments of 5°. The first row shows the result for a wide auxiliary beam with SNR = 0 dB (Fig. 5.19a) and SNR = 40 dB (Fig. 5.19b). For a high SNR, all out-of-swath interference is compensated with an error increase of less than 10° if $N > 6$. The error in a 5° area on both sides of the swath (when the interferer is still out-of-beam but close to the main beam) shows a decreasing error as N gets larger. For $N = 32$, the error is below 5°. On the other hand for the low SNR, residual errors are present on both sides of the swath even for $N = 62$. The angular area that remains contaminated increases for lower N. A reason for this is that $k > 1$ close to the main beam for a wide auxiliary beam because the increased coverage of the auxiliary beam

results in a lower gain. Thus, noise is injected in the first sidelobes when the LMS filter is applied. The second row of Fig. 5.19 shows the error for a narrow auxiliary beam that is pointing towards the RFI. It is evident that all out-of-swath interference can now be recovered for both SNR if $N > 16$. The sacrificed area around the swath for lower N is decreased over the wide beam.

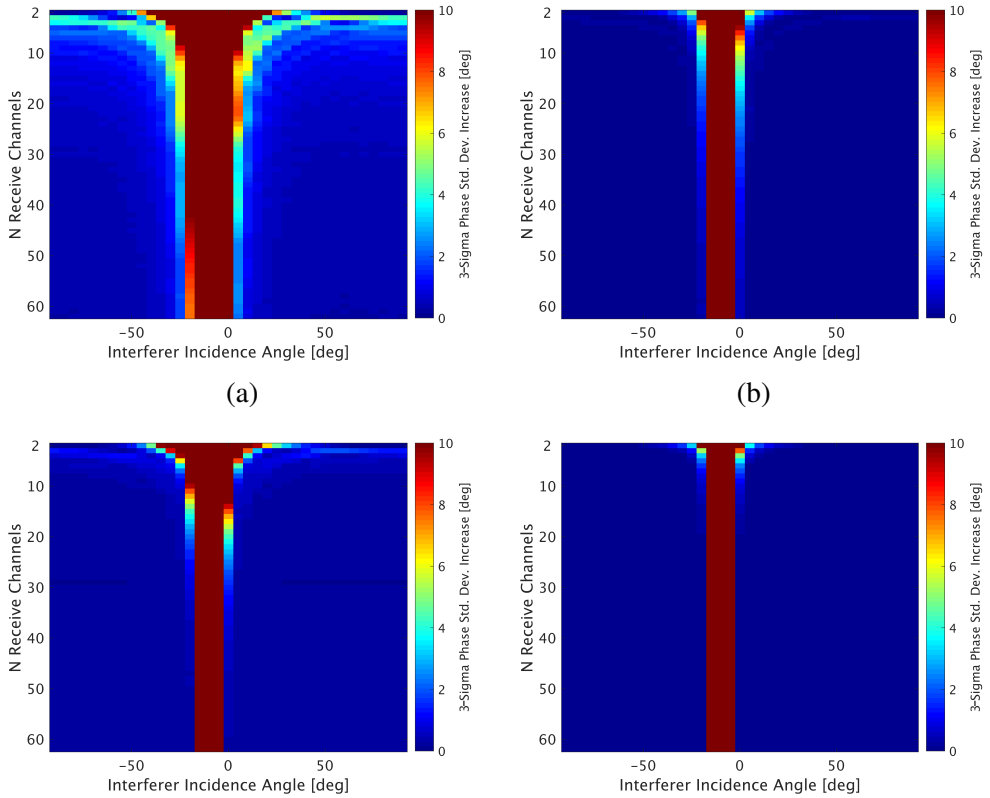

Fig. 5.19.: Maximum 3-sigma phase standard deviation increase (error model of Section 2.5.3) for RNR > 0 dB in dependence on N and the interferer position θ_{RFI}. The SAR return is ranging from an incidence angle of about -20° to 0° due to the antenna tilt. a) Wide auxiliary beam for SNR = 0 dB, b) Wide auxiliary beam for SNR = 40 dB, c) Narrow auxiliary beam for SNR = 0 dB, d) Narrow auxiliary beam for SNR = 40 dB.

5.5.2. In-Beam Interference

The performance of the proposed method has been demonstrated in the previous subsections for the case of out-of-beam interference. However, a main limitation of RFI mitigation methods is that they are incapable of filtering in-swath interferers while the SCORE beam is looking into the direction of RFI (no orthogonality). Therefore the implemented simulator is used in the following to investigate the impact of in-swath interference. Figure 5.20 shows the residual phase standard deviation error of an in-swath interferer (incidence angle 40°, baseband frequency 25 MHz) for different SNR levels. N is fixed to 63. The first plot shows the case of a wide auxiliary beam (Fig. 5.20a). The interferer is removed from the data while it is out-of-beam but a spike of the error remains once it is in-beam. The width of the spike decreases with improving SNR. In addition, a low SNR results in side peaks that are degraded as well. This is related to $k > 1$ for the wide auxiliary beam. A noise injection inhibits the filtering when the RFI is in the mainlobe or in the first sidelobes. Because five simultaneous elevation beams need to be used to acquire the simulated swath, this would result in a degradation of five times the shown area and thus renders the entire swath useless. An approach to combat this is to reduce the noise in the auxiliary beam with a bandpass filter in the frequency domain. Only the spectrum occupied by the interferer is of interest. The result is shown in Fig. 5.20b. The side peaks vanish and the main error peak reduces in size for low SNR. However, the width of the peak is still too large for five simultaneous elevation beams.

It is therefore necessary to use a narrow auxiliary beam if in-beam interference is present. This requires a knowledge or estimation of the RFI AoA. For a reflector antenna, the narrow beam can be formed by thresholding the power of the feed elements. The resulting error is shown in Fig. 5.20c. The error peak is narrow for all SNR. Accounting for five simultaneous elevation beams, the corrupted data due to the estimation gap is occupying less than 33% of each elevation beam. This allows for a reconstruction of the estimation gap as discussed in the next subsection.

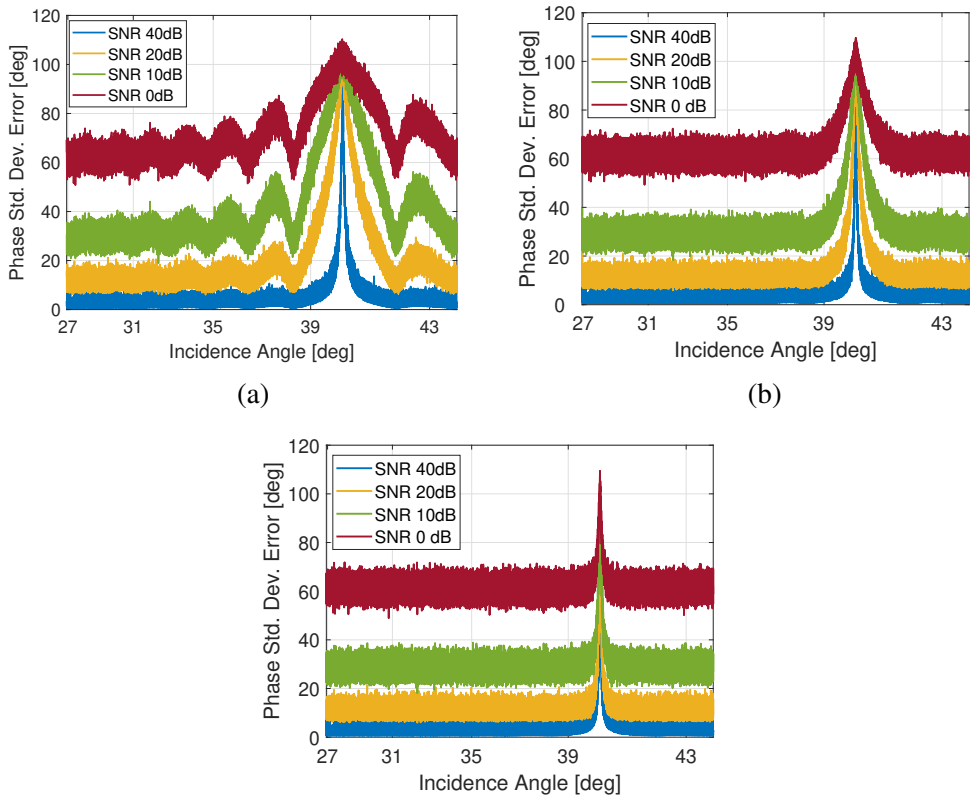

Fig. 5.20.: Residual phase standard deviation error for an in-swath interferer (incidence angle 40°, baseband frequency 25 MHz). The auxiliary beam is formed as: a) Wide beam, b) Wide beam with frequency bandpass filtering for noise reduction, c) Narrow beam.

5.5.3. In-Beam Reconstruction

To overcome the fundamental limitation that prevents the removal of in-beam interference, a reconstruction of the signal with an autoregressive model (Burg's method) is performed. The results of this approach depend on the gap width t_g as well as the stationarity of the interference over this time period. In this section, the implemented simulator is used to simulate a continuous interferer with gap widths from 80 μs to 10 μs to find the optimal gap width for the reconstruction at $N = 63$. Next, the continuous signal is replaced with a random communication signal, which is modulated with binary frequency shift keying (BFSK) for different symbol lengths. The performance of each error parameter is analyzed.

CW Signal

The residual phase standard deviation error results for a continuous-wave interferer (incidence angle 40°, baseband frequency 25 MHz) are shown in Fig. 5.21 for a SNR of 40 dB. Figure 5.21a shows the error before the gap is reconstructed. The corrupted gap is visible for RNR above 14 dB. However, if the signal is reconstructed for a gap width of 80 μs (Fig. 5.21b), the degradation disappears for RNR lower than 56 dB. For higher RNR, the signal worsens over the entire extent of the gap width and thus corrupts the data. Therefore, it is important to set the gap width as small as possible. When the gap width is reduced to 20 μs and 10 μs, the degradation onset is pushed to 74 dB and 80 dB,

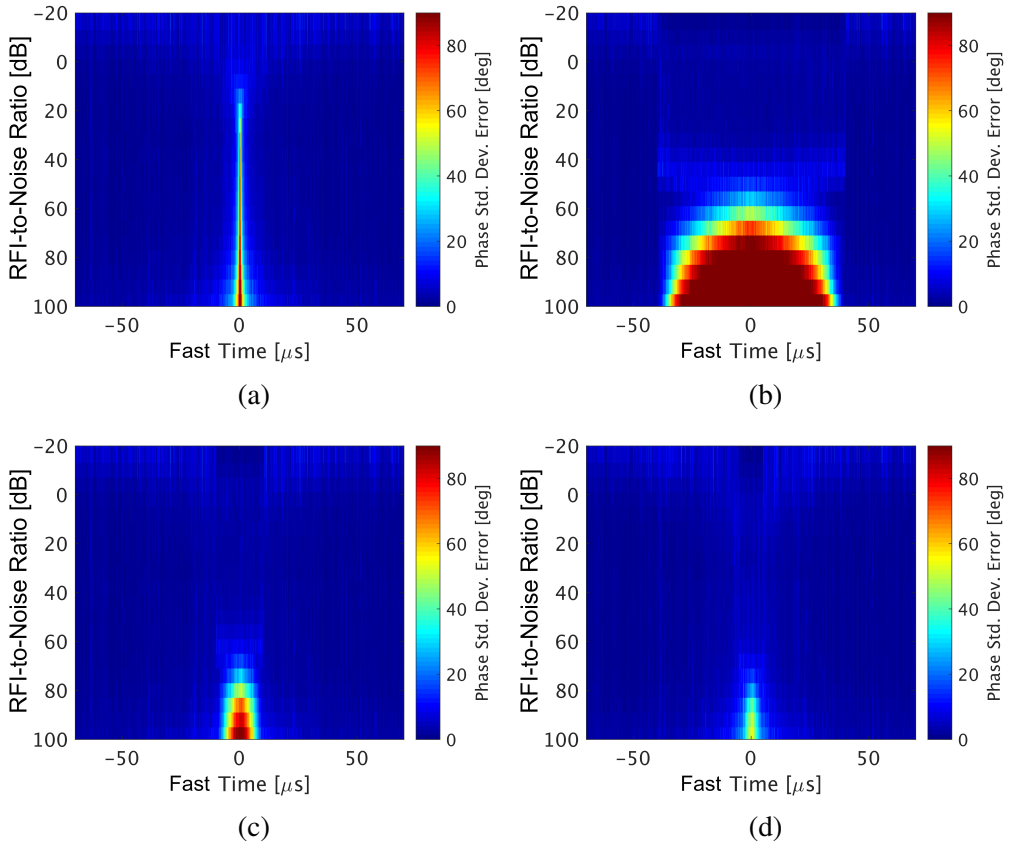

Fig. 5.21.: Residual phase standard deviation error vs. fast time (centered on interferer position) dependent on RNR (SNR = 40 dB): a) No autoregressive model (LMS and bandpass only), b) autoregressive model with gap width of 80 μs, c) autoregressive model with gap width of 20 μs, d) autoregressive model with gap width of 10 μs.

respectively (Fig. 5.21c and Fig. 5.21d). As a reminder, the RNR represents the average power ratios after beamforming. For the simulated interferer, the peak RFI power is about 11 dB above the average power. This means that RFI can be restored up to a peak RNR of 91 dB for SNR = 40 dB, which is exceeding the dynamic range of a common SAR system.

The reconstruction of the gap is repeated in Fig. 5.22 for a SNR level of 0 dB. Before reconstruction (Fig. 5.22a), the degradation starts at a RNR of -14 dB. Gap width sizes of 80 μs, 20 μs and 10 μs move the RNR limit to 16 dB, 40 dB and 28 dB, respectively (Fig. 5.22b through Fig. 5.22d). Note that the best result is achieved with a gap width of

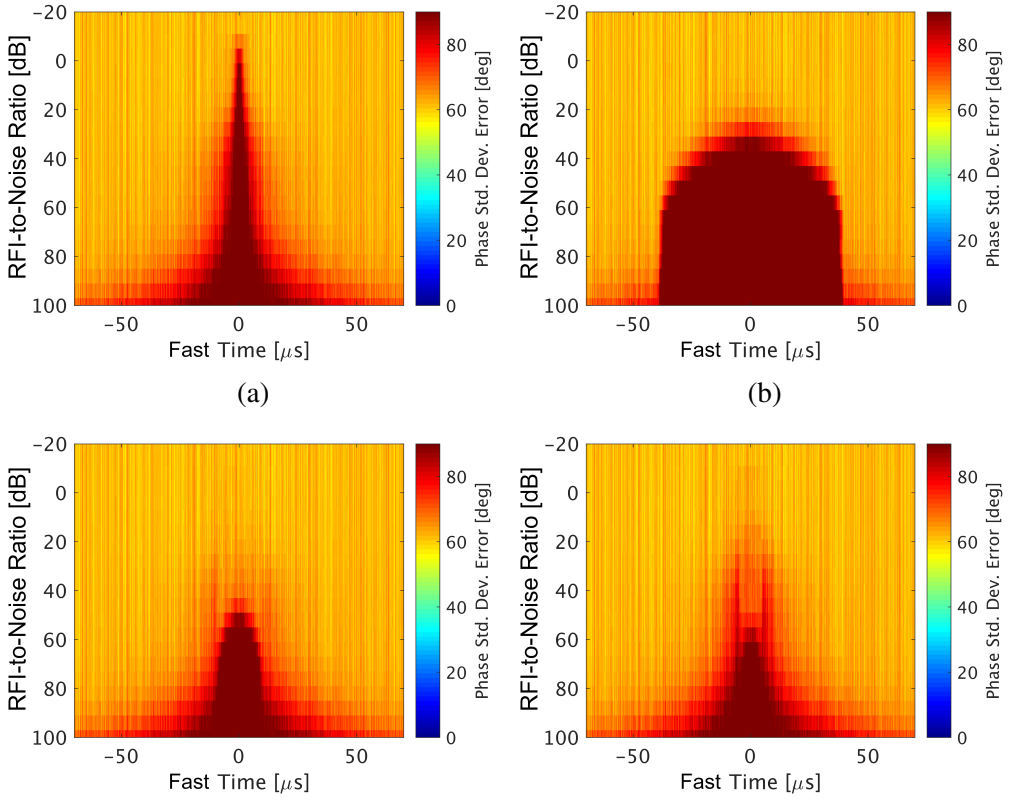

Fig. 5.22.: Residual phase standard deviation error vs. fast time (centered on interferer position) dependent on RNR (SNR = 0 dB): a) No autoregressive model (LMS and bandpass only), b) autoregressive model with gap width of 80 μs, c) autoregressive model with gap width of 20 μs, d) autoregressive model with gap width of 10 μs.

20 μs. Because of the lower SNR, the noise increases the optimal gap width. For a gap width of 10 μs, the reconstruction is not performing optimally. For the best gap width setting, the peak RFI power that can be restored is 51 dB.

The results obtained in Fig. 5.21 and Fig. 5.22 can be represented with the one-dimensional plots shown in Fig. 5.23a and Fig. 5.23b, respectively. The plots show the 3-sigma phase standard deviation increase in a 80 μs window centered on the interferer position for each line of the 2D plot. For high SNR (Fig. 5.23a), a reduction of the gap width size can move the critical RNR from the previously mentioned 14 dB without correction to values greater than 80 dB. For low SNR (Fig. 5.23b), an improvement is only visible up until a gap width size of 20 μs and for RNR lower than 40 dB. The degradation of the reconstruction for smaller gap width is clearly visible in the one-dimensional plot.

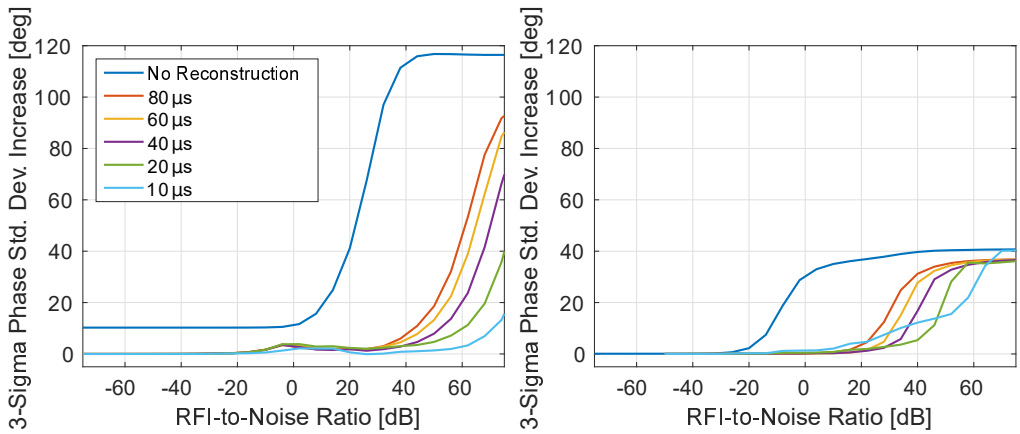

Fig. 5.23.: 3-sigma phase standard deviation (error model of Section 2.5.3) increase computed in a 80 μs window centered on the interferer position for a) SNR = 40 dB and b) SNR = 0 dB.

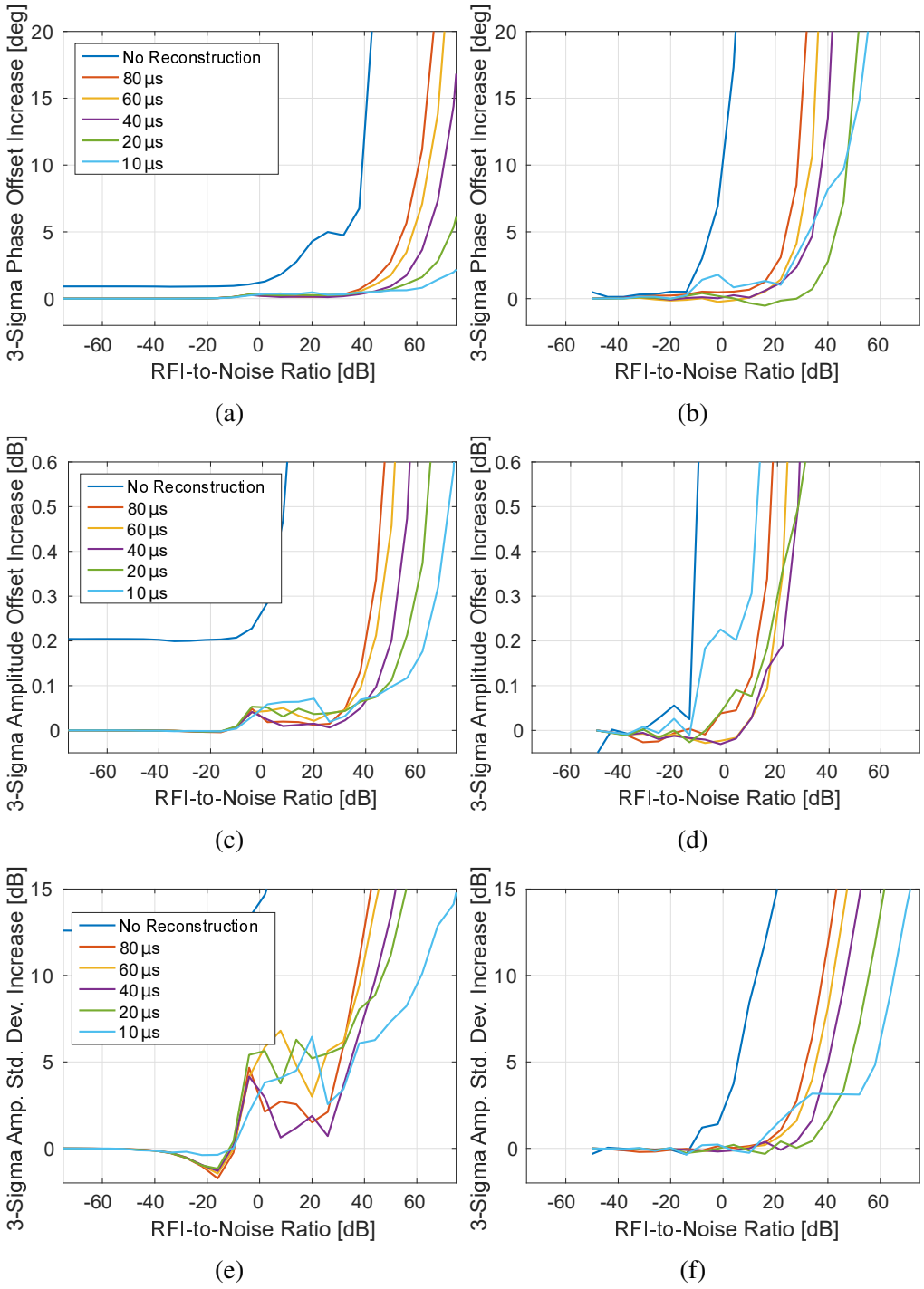

Fig. 5.24.: 3-sigma error increase (error model of Section 2.5.3) computed in a 80 μs window centered on the interferer position. a) Phase offset at SNR = 40 dB, b) Phase offset at SNR = 0 dB, c) Amplitude offset at SNR = 40 dB, d) Amplitude offset at SNR = 0 dB, e) Amplitude standard deviation at SNR = 40 dB, f) Amplitude standard deviation at SNR = 0 dB.

The remaining error parameters are shown in Fig. 5.24a through Fig. 5.24f. The phase offset shows a sudden increase once the RNR exceeds the SNR (Fig. 5.24a and Fig. 5.24b). After reconstruction, the phase offset can be pushed below 5° for all simulated values at SNR = 40 dB and for RNR up to 43 dB at SNR = 0 dB. This is comparable to the performance of the phase standard deviation error. However, the amplitude offset shows a worse performance (Fig. 5.24c and Fig. 5.24d). At the high SNR, a degradation can not be avoided for values higher than RNR = 40 dB. The exact breaking point depends on the radiometric budget. Assuming an allowable error of up to 0.3 dB, the reconstruction starts to fail for RNR > 65 dB. For low SNR and with the same gap width as before (20 μs), the break point is at RNR = 20 dB. This is 20 dB below the RNR that can be reconstructed for the phase errors. In contrast, the amplitude standard deviation error (Fig. 5.24e and Fig. 5.24f) can be recovered for RNR values close to 40 dB (SNR = 0 dB). Applications that do not require a radiometric budget (e.g., interferometry) can therefore handle RFI that is 20 dB stronger than applications that utilize the backscatter amplitude.

Random BFSK Signal

In the following pages, the interfering signal of the implemented simulator is modelled as a random binary communication signal that is encoded with a BFSK modulation. The carrier frequencies are selected to be 25 MHz and 27 MHz in baseband. The spacing of both frequencies is chosen to be 2 MHz to reduce the similarity between symbols. The start position of a symbol within each pulse's receive window is varied. The resulting RFI signal is random in azimuth direction and thus will demonstrate the capabilities of the proposed RFI mitigation method. Note that any aliasing effects in the azimuth spectrum are identical in the SCORE beam and the auxiliary beam. The symbol length is set to 150 μs, 80 μs and 40 μs in different simulations (according to Section 2.4.2). As the symbol length is shortened, the stationarity of the RFI signal is decreased and this is expected to impact the autoregressive performance. On the other hand, the longest selected symbol length (150 μs) should result in a good signal reconstruction.
Figure 5.25a shows a 2D plot of the phase standard deviation error in each range line for different RNR and incidence angles before RFI mitigation is applied. The BFSK in the plot has a symbol length of 150 μs at SNR = 0 dB. The modulation of the RFI with the SCORE pattern is evident and the degradation of the phase begins at RNR = -20 dB in the main beam and at RNR = 0 dB when the interferer is in the SCORE sidelobe.

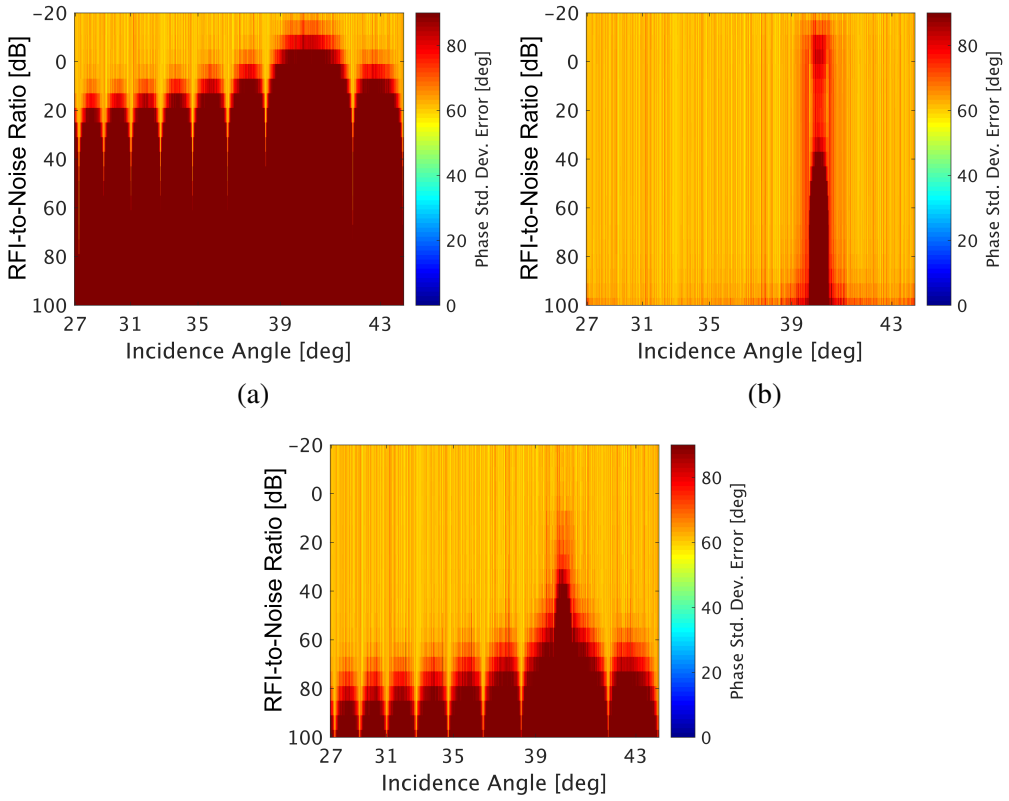

Fig. 5.25.: Phase standard deviation error vs. RNR for a BFSK signal with symbol length equals 150 μs and SNR = 0 dB: a) No RFI mitigation, b) LMS filter and autoregressive reconstruction (gap width equals 80 μs), c) LMS filter and autoregressive reconstruction (gap width equals 80 μs) with frequency bandpass for auxiliary beam noise reduction.

Next, the LMS filter is applied in combination with an autoregressive reconstruction (gap width equals 80 μs, Fig. 5.25b). The residual error while the interferer is out-of-beam drops below the noise and thus the image is successfully filtered. However, the error spike that is caused when the RFI is inside the main beam is not fully removed. The error does drop but a degradation remains. The noise is too high and obstructs the reconstruction of the BFSK signal. Therefore, the noise is decreased with a bandpass filter in the frequency domain. The result is shown in Fig. 5.25c. The in-beam interference is improved and removed for RNR < 10 dB. This threshold can be further moved by reducing the gap width. On the other hand, interference does appear in the sidelobes. This

can be contributed to the convolution with a sinc-function in the time domain caused by the bandpass filter. As a result, the RFI signal in the auxiliary beam is not perfectly matching the RFI signal in the SCORE beam. A small residual error is introduced, which is affecting the reconstruction for large RNR when the energy of the residual error becomes larger than the SAR signal. Note that this only affects the sidelobes for RNR far higher than 50 dB and thus might be exceeding the dynamic range of the SAR system. If necessary, this can be avoided by applying the bandpass filter only for the autoregressive reconstruction and not for the LMS filtering.

The reconstruction performances of the autoregressive is shown in Fig. 5.26 by means of the 3-sigma phase standard deviation increase computed in a 80 μs window centered on the BFSK interferer position. The left side of the figure shows the results for a SNR of 40 dB, while the right side is simulated with SNR = 0 dB. The symbol length of the first row is 150 μs, the symbol length in the middle row is 80 μs and in the last row the symbol length is 40 μs. If the symbol length is 150 μs, the error increase stays below 10° for RNR of up to 55 dB for high SNR. For low SNR, the error increase stays below 10° for RNR of up to 40 dB. This is about double the phase standard deviation error experienced for a continuous interferer at these RNR and SNR levels. Similar values can be seen for a symbol length of 80 μs, though a worsening of the performance for larger gap width is noticed. However, if the symbol length is decreased to 40 μs, the autoregressive performance drops. The RNR thresholds are lowered to 8 dB and -2 dB for SNR = 40 dB and 0 dB, respectively. While the autoregressive reconstruction does improve the signal, it is not able to fully recover the image quality.

The phase offset is plotted in Fig. 5.27 and the plots are arranged in the same manner as before. For the previous thresholds, the phase offset increase is below 3° for SNR = 40 dB and all three symbol lengths. The phase offset increase for SNR = 0 dB is below 4°, 6° and 1° for symbol lengths of 150 μs, 80 μs and 40 μs, respectively. Hence, the performance range for phase offset and standard deviation are comparable.

The amplitude offset is plotted in Fig. 5.28. To achieve amplitude offsets of less than 0.5 dB, the previous thresholds need to be lowered. For a radiometric budget that allows an offset of up to 0.5 dB (gap width equals 20 μs), the new thresholds for high SNR are about 50 dB for the symbol lengths 150 μs and 80 μs. At low SNR the thresholds are 0 dB and -4 dB. The threshold is even lower for the shortest symbol length (-7 dB). Thus, the autoregressive reconstruction performs worse for amplitude.

Last, the amplitude standard deviation is plotted in Fig. 5.29. For the high SNR plots, an

increase of the amplitude standard deviation of 15 dB is acceptable without degrading the image. It is evident that the degradation can be avoided up to RNR of about 20 dB (symbol lengths 150 μs and 80 μs) and 0 dB (symbol length of 40 μs). For low SNR, the degradation can be avoided up to RNR of about 0 dB (symbol lengths 150 μs and 80 μs) and -15 dB (symbol length of 40 μs). This is limiting the autoregressive reconstruction, which is experiencing amplitude errors.

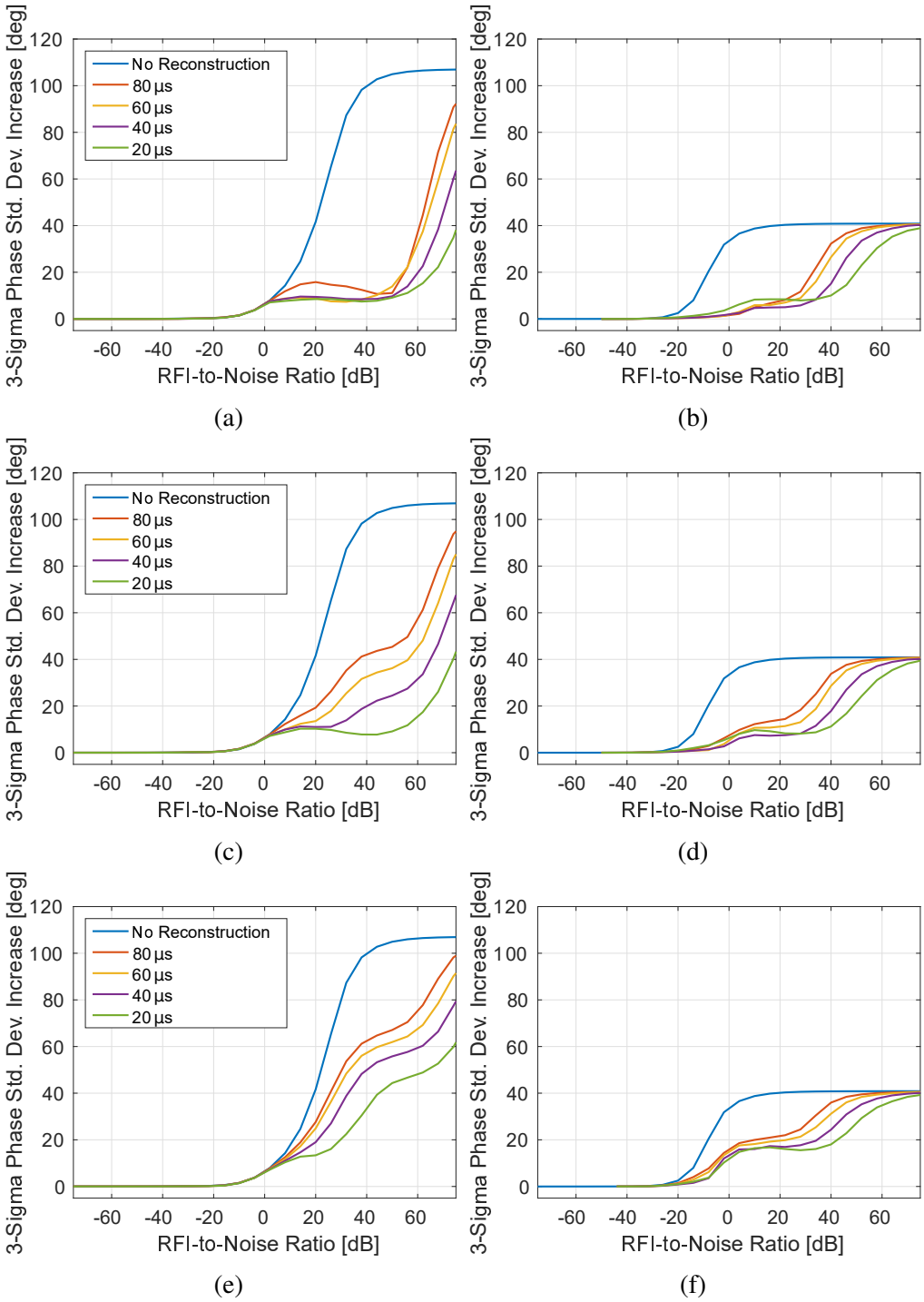

Fig. 5.26.: 3-sigma phase standard deviation increase computed in a 80 μs window centered on the BFSK interferer position. a) symbol length equals 150 μs, SNR = 40 dB, b) symbol length equals 150 μs, SNR = 0 dB, c) symbol length equals 80 μs, SNR = 40 dB, d) symbol length equals 80 μs, SNR = 0 dB, e) symbol length equals 40 μs, SNR = 40 dB, f) symbol length equals 40 μs, SNR = 0 dB.

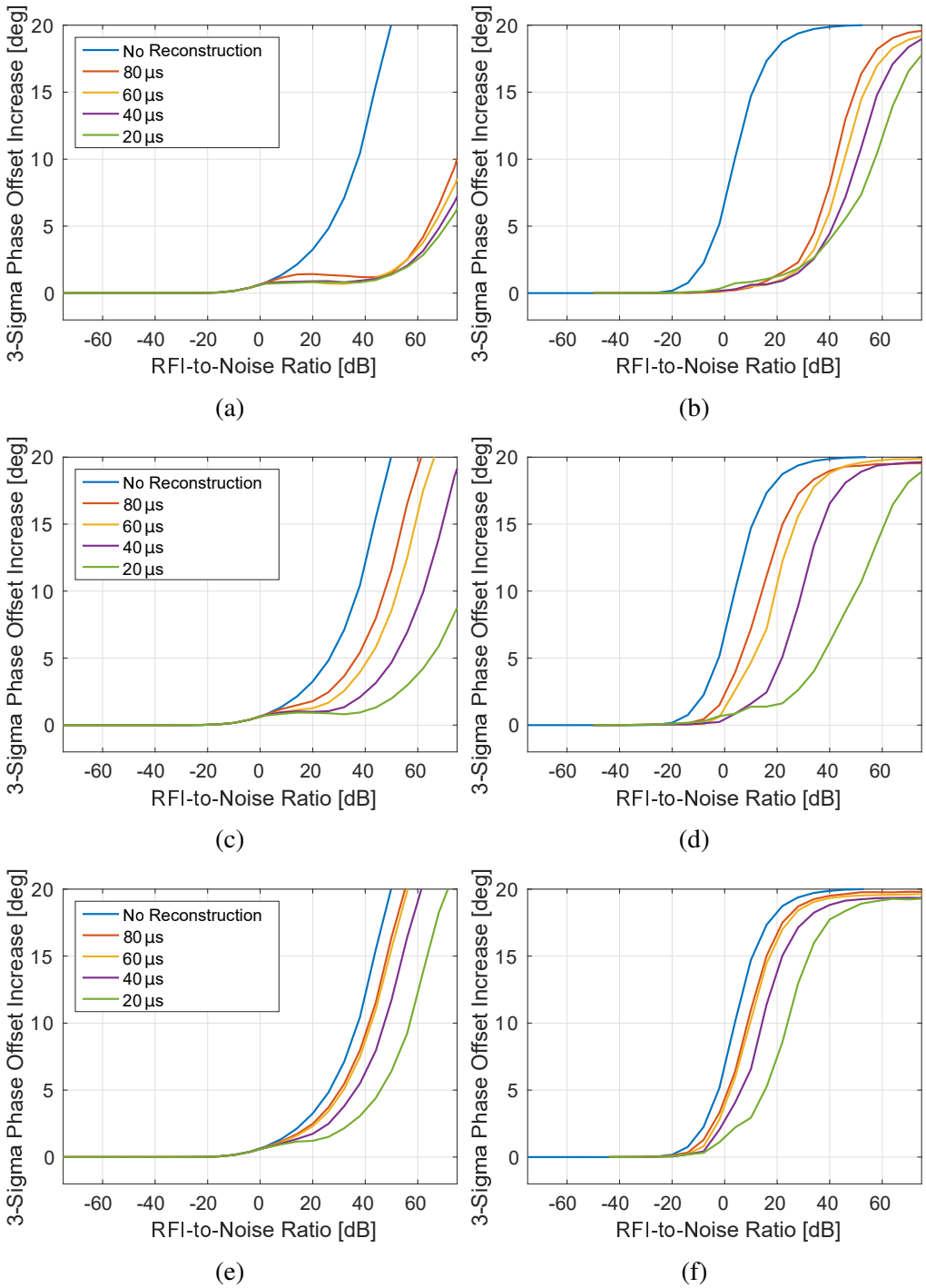

Fig. 5.27.: 3-sigma phase offset increase computed in a 80 μs window centered on the BFSK interferer position. a) symbol length equals 150 μs, SNR = 40 dB, b) symbol length equals 150 μs, SNR = 0 dB, c) symbol length equals 80 μs, SNR = 40 dB, d) symbol length equals 80 μs, SNR = 0 dB, e) symbol length equals 40 μs, SNR = 40 dB, f) symbol length equals 40 μs, SNR = 0 dB.

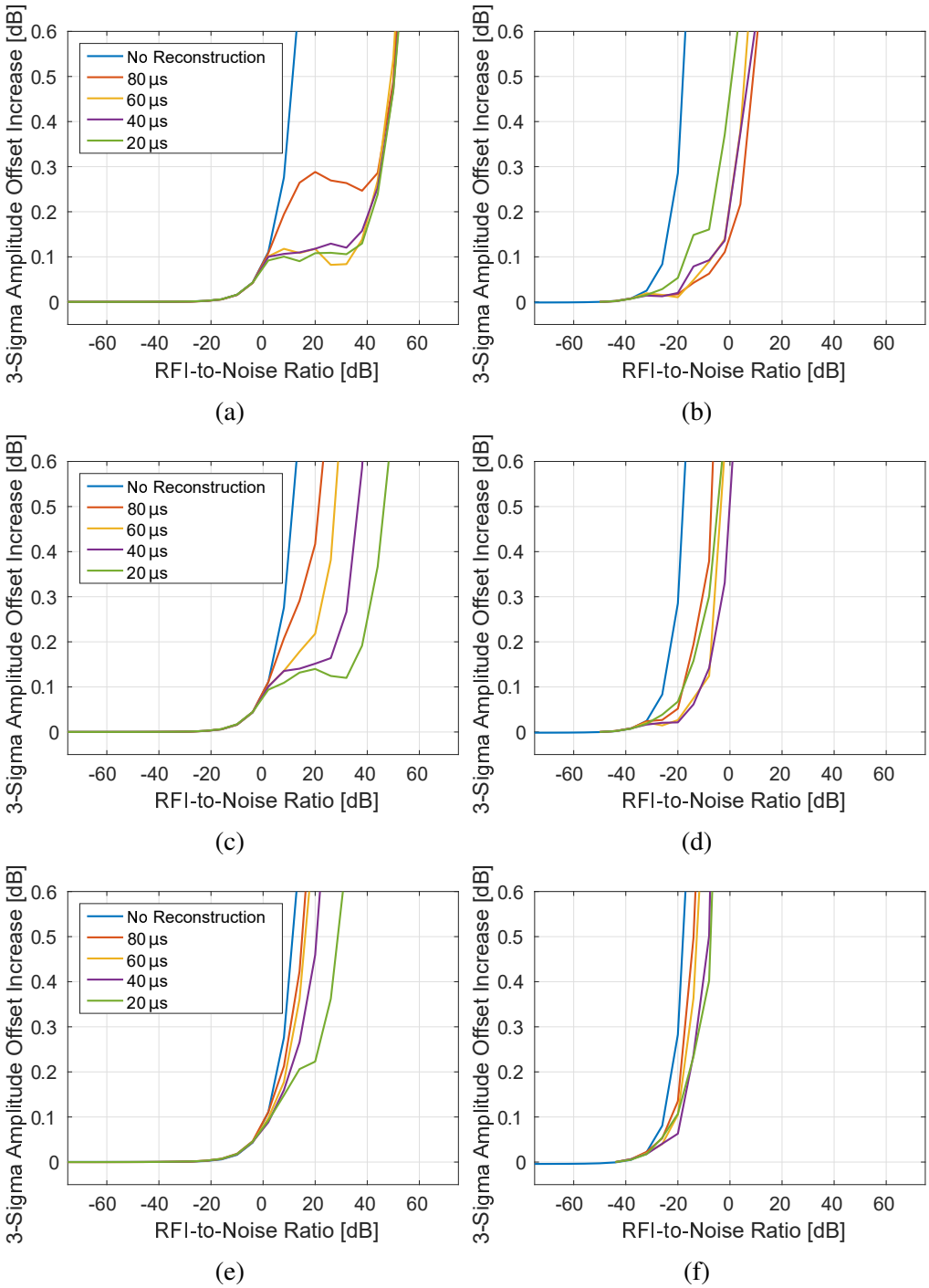

Fig. 5.28.: 3-sigma amplitude offset increase computed in a 80 μs window centered on the BFSK interferer position. a) symbol length equals 150 μs, SNR = 40 dB, b) symbol length equals 150 μs, SNR = 0 dB, c) symbol length equals 80 μs, SNR = 40 dB, d) symbol length equals 80 μs, SNR = 0 dB, e) symbol length equals 40 μs, SNR = 40 dB, f) symbol length equals 40 μs, SNR = 0 dB.

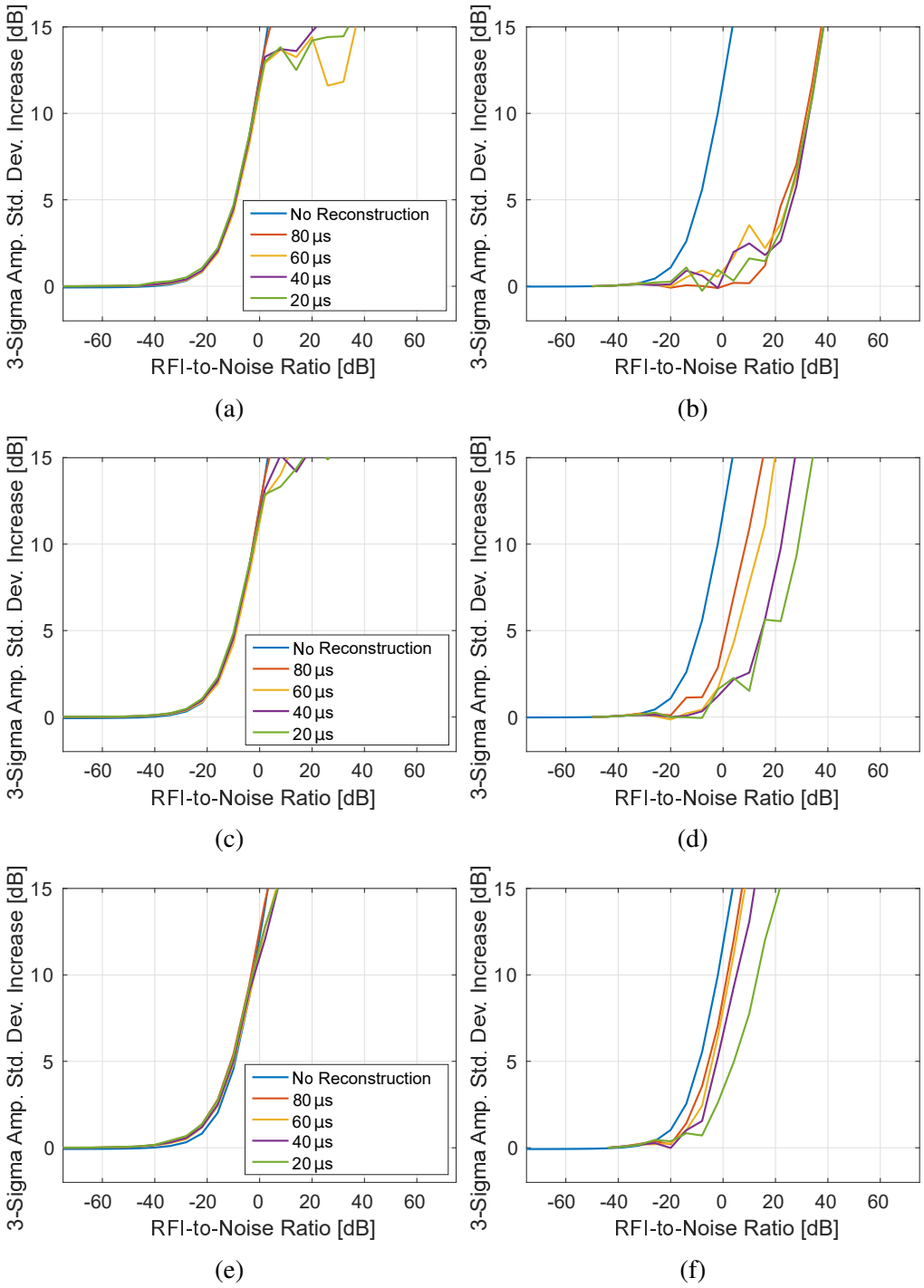

Fig. 5.29.: 3-sigma amplitude standard deviation increase computed in a 80 μs window centered on the BFSK interferer position. a) symbol length equals 150 μs, SNR = 40 dB, b) symbol length equals 150 μs, SNR = 0 dB, c) symbol length equals 80 μs, SNR = 40 dB, d) symbol length equals 80 μs, SNR = 0 dB, e) symbol length equals 40 μs, SNR = 40 dB, f) symbol length equals 40 μs, SNR = 0 dB.

5.5.4. Quantization Effects

For a satellite down-link, the number of bits available to quantize the beams is limited and thus it is necessary to investigate the impact of quantization on the corrections. Therefore the implemented simulator is expanded with an Analog-to-Digital Converter. The dynamic range for the quantization simulations in this section is set to 60 dB. Fig. 5.30 shows the impact before (a) and after (b) RFI mitigation with a 10 bit quantization at a SNR of 40 dB by means of the phase standard deviation error. The RFI is removed from the data until a RNR of about 49 dB, which is when the peak of the RFI signal drives the Analog-to-Digital Converter into saturation and clipping effects appear. On the other hand for a SNR of 0 dB, a 10 bit quantization prevents a full removal of the RFI impact as seen in Fig. 5.31b. Compared to no RFI mitigation, the data are improved (Fig. 5.31a) but the previously contaminated area is still detectable. The quantization of the auxiliary beam is doubled to 20 bits in Fig. 5.31c while the SCORE beam quantization is left at 10 bits. However, increasing the quantization of the auxiliary beam does not improve the result. It is necessary to quantize SCORE beam and auxiliary beam with more bits. A quantization with 12 bits is shown in Fig. 5.31d. Now, the RFI mitigation is working and only limited by the autoregressive reconstruction performance defined by the gap width. A quantization of the SCORE beam with 12 bits and the auxiliary beam with 6 bits would enable a downlinking of an additional auxiliary beam.

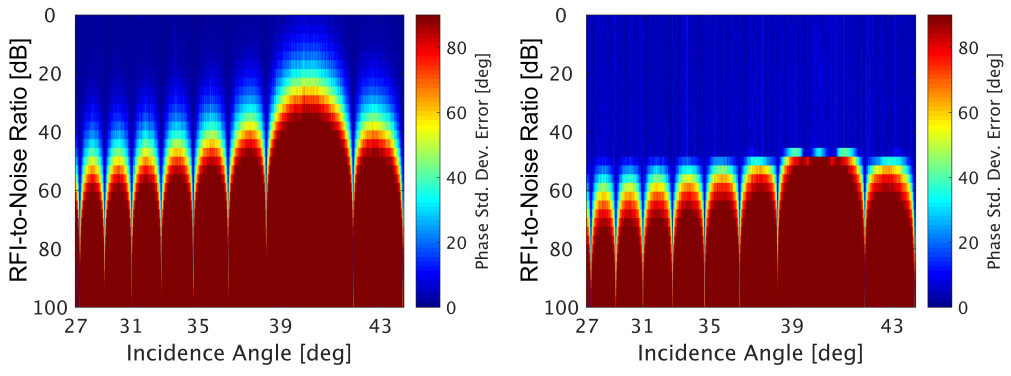

Fig. 5.30.: Phase standard deviation error vs. RNR for a BFSK signal with symbol length equals 150 μs and SNR = 40 dB. The SCORE beam and auxiliary beam are quantized with 10 bits. a) Before RFI Mitigation, b) After LMS filter and autoregressive reconstruction.

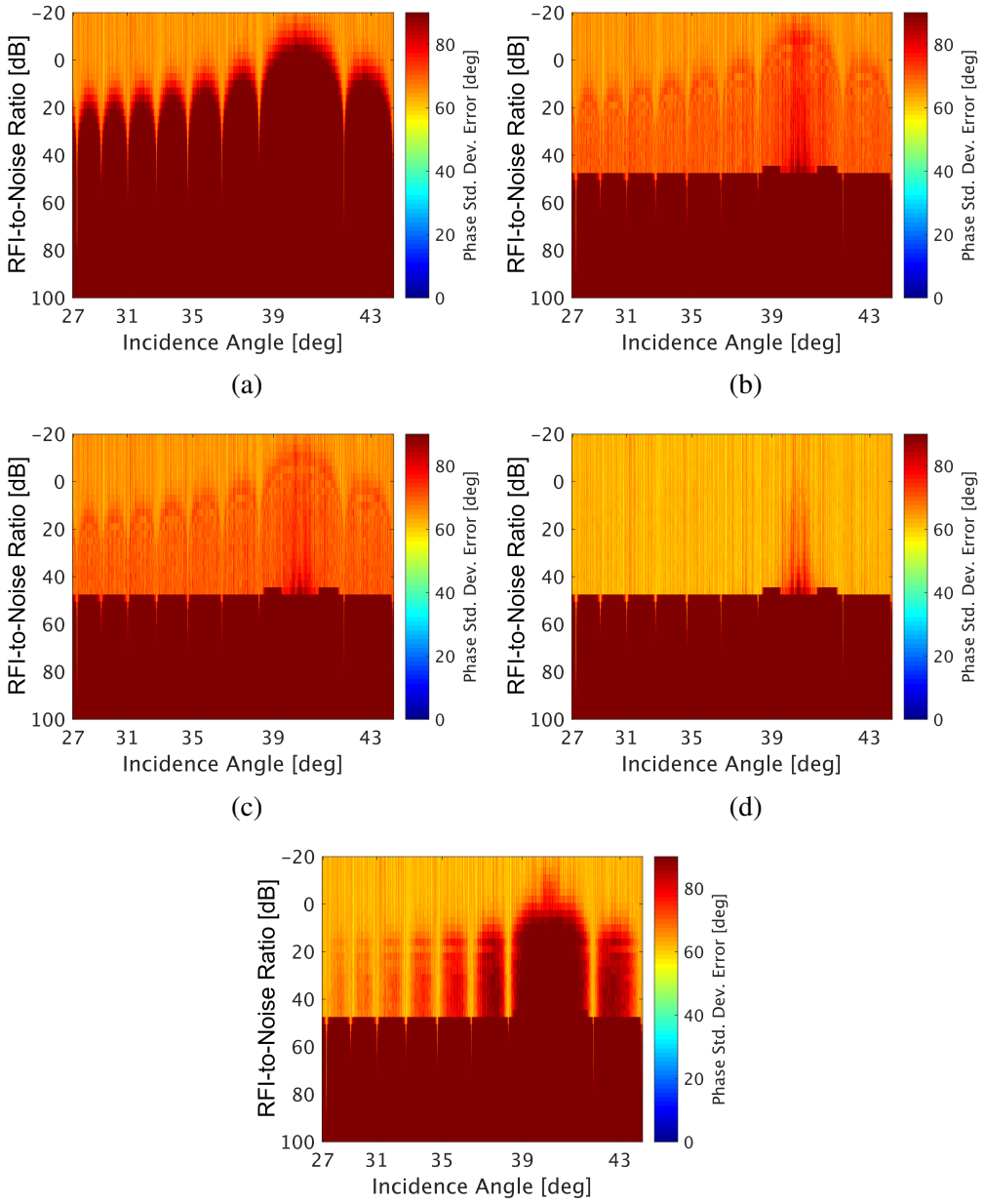

Fig. 5.31.: Phase standard deviation error vs. RNR for a BFSK signal with symbol length equals 150 μs and SNR = 0 dB. The SCORE beam and auxiliary beam are quantized. a) Before RFI Mitigation (SCORE 10 bits), b) After LMS filter and autoregressive reconstruction (SCORE 10 bits, auxiliary beam 10 bits), c) After LMS filter and autoregressive reconstruction (SCORE 10 bits, auxiliary beam 12 bits), d) After LMS filter and autoregressive reconstruction (SCORE 12 bits, auxiliary beam 12 bits), e) After LMS filter and autoregressive reconstruction (SCORE 12 bits, auxiliary beam 6 bits).

The result is shown in Fig. 5.31e but the resulting performance loss renders the RFI mitigation useless. The 3-sigma phase standard deviation error before and after quantization with 10 and 12 bits is shown in Fig. 5.32. For a SNR of 40 dB (Fig. 5.32a), the combination of SLC and autoregressive reconstruction yields a residual error of 4-6° if quantized with double precision (orange curve, up to RNR = 45 dB). Note that the 3-sigma phase standard deviation error caused by the noise floor is 3°. This error is about the same after quantization with 10 bits (yellow curve) or 12 bits (purple curve) while the RFI is below the noise floor. For 0 < RNR < 45 dB, the error increases to 10-13°. The quantization degrades the performance and the curves are identical for 10 bits and 12 bits. When the peak of the RFI signal approaches the saturation voltage of the Analog-to-Digital Converter, the clipping begins and the performance drops. This is evident by the jump of the curves close to RNR = 49 dB. The same plot is shown for SNR = 0 dB in Fig. 5.32b. The phase error caused by the noise floor is about 69°. The double precision curve remains at this level for values up to RNR = 15 dB and thus the filters do not introduce errors in this RNR region. The error then increases slowly to 75° at RNR = 34 dB and continues to rise faster afterwards. After quantization with 12 bits, the error is about 2-5° higher but still shows a good performance compared to no filtering (blue curve). On the other hand, the 10 bit quantization shows a degradation of the data by 15° for RNR < -3 dB compared to not filtering the data. As a consequence, the 10 bit quantization performs worse

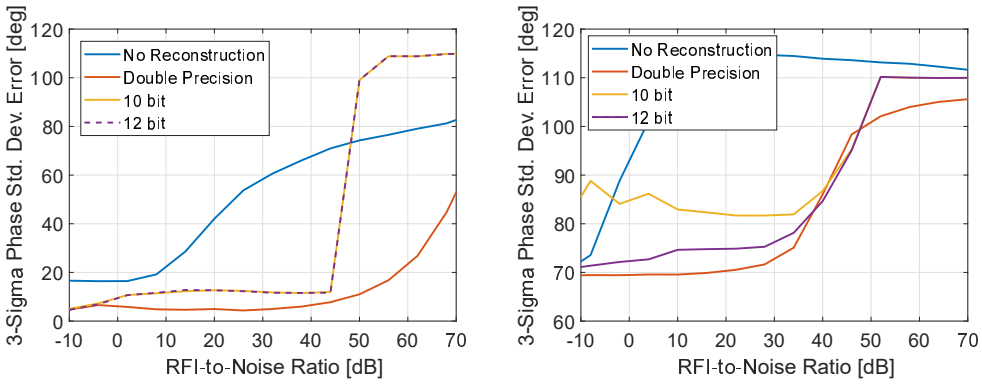

Fig. 5.32.: 3-sigma phase standard deviation errors computed in a 80 μs window centered on the BFSK interferer position. Plot shows errors without RFI mitigation (blue) and after LMS filter and autoregressive reconstruction with double precision (orange), 10 bits (yellow) and 12 bits (purple): a) SNR = 40 dB, b) SNR = 0 dB.

than the 12 bit quantization by about 17°. The error difference slowly decreases until the Analog-to-Digital Converter saturates. For RNR = 10 dB, the 10 bit quantization performs about 10° worse than if quantized with 2 additional bits.
The remaining error parameters are shown in Fig. 5.33. The left column shows the error for SNR = 40 dB, while the right column shows the error for SNR = 0 dB. It is evident that for high SNR, the quantization error is identical for 10 and 12 bits. The phase offset is shown in the first row. In the dynamic range of the Analog-to-Digital Converter, the phase offset error for double precision is 1° after correction and up to 4° without correction. After quantization, the error increases up to 1.5°. Again, the low SNR shows a degradation of the data for 10 bits compared to no correction for low RNR values. This degradation is about 2°. The 12 bit quantization is on the same level as the double precision at low RNR and diverges by about 4° at RNR = 45 dB.
The amplitude offset error is shown in the middle row. Without correction, the error exceeds 0.2 dB at RNR= 4 dB. After correction with double precision, this limit is exceeded at RNR = 54 dB. After quantization it is exceeded at RNR = 40 dB. The quantization degrades the performance by up to 0.15 dB for RNR < 40 dB and then the error increases when clipping takes effect. At low SNR, a degradation of 0.2-1.5 dB can be seen when the 12 bit quantization is compared to the double precision. The 10 bit quantization introduces errors of more than 2 dB.
The amplitude standard deviation error is shown in the bottom row. For high SNR, the error is not affecting the image quality regardless of quantization up to RNR = 40 dB. The double precision is performing well up to RNR = 55 dB because it is not exposed to clipping effects. At low SNR, the error after quantization is increased by 3 dB for 12 bits at RNR = 20 dB. The 10 bit quantization shows a degradation by more than 4 dB at this point. The amplitude standard deviation error for high RNR is already degraded without quantization, as shown in the previous sections. The performance is further restricted by the quantization. Nevertheless, it is moving the curve prior to corrections by about 20 dB to the right.
The simulation results show that the interference can still be removed from the data in presence of quantization noise as long as no clipping effects occur and the main and auxiliary beam is sampled with sufficient bits. Hereby, the auxiliary beam can be sampled with fewer bit than the main beam, though the performance depends on the dynamic range covered with the Analog-to-Digital Converter and the expected SNR of the scene.

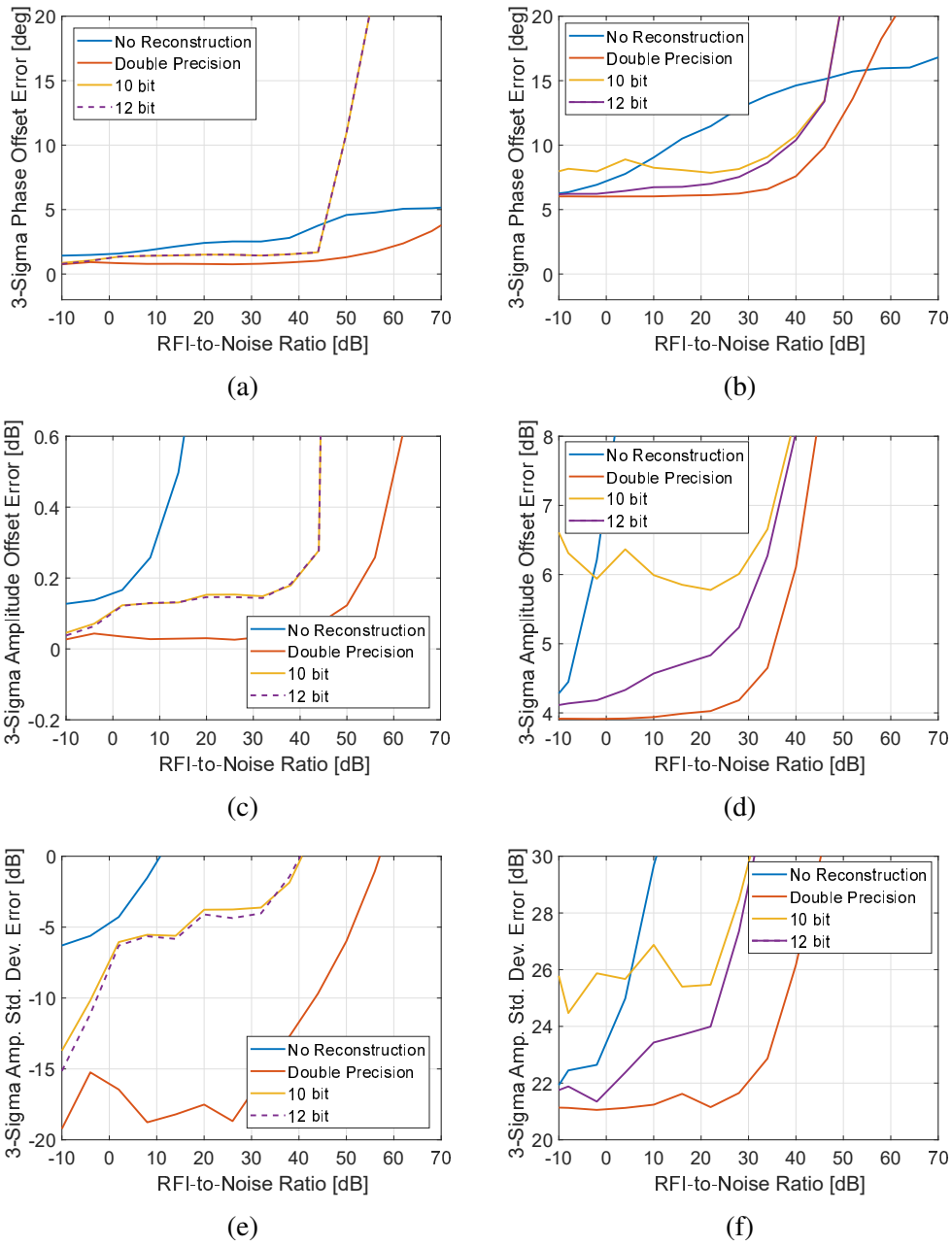

Fig. 5.33.: 3-sigma errors (error model of Section 2.5.3) computed in a 80 μs window centered on the BFSK interferer position. Plot shows errors without RFI mitigation (blue) and after LMS filtering and autoregressive model with double precision (orange), 10 bits (yellow) and 12 bits (purple): a) Phase offset for SNR = 40 dB, b) Phase offset for SNR = 0 dB, c) Amplitude offset for SNR = 40 dB, d) Amplitude offset for SNR = 0 dB, e) Amplitude standard deviation for SNR = 40 dB, f) Amplitude standard deviation for SNR = 0 dB.

5.6. Remarks

A novel method for DBF-based RFI mitigation in spaceborne systems was presented, which avoids the need to perform computational on-board beamforming and does not require the transmission of all receive channels to the ground. The introduced technique is based on digital auxiliary beams that are synthesized simultaneously to the digital SAR main beam. These digital auxiliary beams allow recording the RFI signals in the absence of the SAR signal, which can be used to subtract the signal of one interferer per auxiliary beam and frequency from the data on ground. One possible implementation uses a wide auxiliary beam that covers a wide area except for the direction of the instantaneous SAR signal return. This comes at the advantage that no AoA estimation needs to be performed for the RFI signals.

However, the RFI subtraction with auxiliary beams only performs well while the SAR and RFI signals are spatially orthogonal. Residual RFI remains in the image for time instances when this is not the case. For a DBF system in elevation, this results in short time gaps on the order of microseconds due to the SCORE operation and the time-varying AoA of the SAR signal, which is predetermined by the geometry. Therefore, this work proposed to model the RFI in these short time gaps with an autoregressive model based on the information collected about the RFI outside of the gaps. Simulations show that the removal of the residual RFI with the autoregressive model performs well if a narrow auxiliary beam is used (which reduces the noise level compared to a wide auxiliary beam) and if the interferer signal is stationary for the time duration of the gap. Hence, this innovative method comes with the trade-off that the interferer position needs to be estimated before it can be recorded with the narrow auxiliary beam but allows the removal of RFI even when it can not be filtered spatially. Another proposed implementation synthesizes a narrow digital auxiliary beam that measures only the directions of the first sidelobes of the SAR main beam (and is notched towards the peak of the SAR main beam). The resulting auxiliary beam steers alongside the SCORE beam and does not require an estimation of the interferer positions. This approach combines the advantages of a wide and a narrow auxiliary beam, if the interference in the higher sidelobes can be neglected.

Further, a random BFSK interferer signal was simulated to validate the RFI mitigation performance for the subtraction and the autoregressive modelling. The simulation also accounted for the impact of quantization. The results showed that the subtraction always

performed well and the autoregressive modelling of the residual RFI performed well for the phase and acceptably for the amplitude information.

6. Conclusions and Outlook

Radar remote sensing instruments have played an increasingly important role in understanding Earth and its dynamic processes. Their operational frequencies are predetermined based on the physical properties that are to be retrieved. Consequently, their ability to operate at alternative frequency bands is limited. Simultaneously, the demand for wireless services has been increasing, which resulted in a more crowded frequency spectrum. This observed trend is expected to continue in the future. Measures to suppress RFI are therefore critical for future Earth observation missions. Not only is it necessary for future instruments to tackle existing RFI sources but they also need to be prepared for new RFI-causing services that arise during their development or operational phase.
Conventional methods for RFI suppression are grouped into three categories. Methods of the first category remove RFI from the data in a way that results in the simultaneous loss of parts of the SAR signal and thus distort the data (i.e., loss of resolution or gaps in the image). The second category aims at subtracting an estimate of the RFI from the data. These are based on interferer modeling, which requires a-priori knowledge about the interfering signal characteristics. Methods from the third group are based on filtering and depend on the careful selection of scene- and interferer-dependent filter parameters.

Because the new baseline for SAR-based Earth observation are multichannel radars capable of DBF, these systems give rise to new opportunities for RFI mitigation. The main contributions of this work are the development of novel methods for an adaptive antenna pattern notching that is applicable to airborne DBF SAR systems (Chapter 3), as well as a novel use of simultaneous, digital auxiliary beams that allow for an on-ground RFI mitigation in spaceborne DBF SAR systems with a limited downlink capacity (Chapter 5). In addition, this work contributes a novel DBF-based RFI mitigation approach that can estimate and filter the interference signal even when the SAR and RFI signal overlap spatially (Chapter 5).
To achieve this, this work proposed for the first time to utilize the spatial distribution of

the SAR signal for RFI mitigation. This spatial distribution in the range-Doppler domain is inherent to the imaging geometry. Thus, this distribution is variable in time and yet predictable because the arrival time of the radar return is determined by the distance. The Doppler frequency of the radar return is directly related to the range history and the relative motion between the platform and the target. This can be used as a-priori information on the SAR signal and helps to characterize unwanted RFI signals in the data. The angle of arrival of the interferers can thus be estimated for all time instances when the RFI signal position is not identical to the instantaneous SAR signal return position (and thus orthogonal).
An extensive analysis of the interference suppression performance in dependence of various SAR system parameters was performed in this work.

Multiple novel adaptive antenna pattern notching methods, which were developed during this work, are presented in Chapter 3. The methods are based on placing nulls in the antenna pattern towards the direction of the interferer and require the usage of all receive channels. For a system with DBF in elevation, the proposed Range-Dependent Time MVDR allows for a range-dependent and adaptive notching of the RFI throughout the image. Not only is this method capable of notching the strongest interferer in each range line but the Range-Dependent Time MVDR can also adaptively notch range ambiguities and orthogonal waveforms for scenes with unknown topography. The proposed Range-Dependent Frequency MVDR extends the concept of the Range-Dependent Time MVDR in the frequency domain for an additional adaption of the notches with frequency, applicable when further processing capabilities are available. The composition of both algorithms is well suited for an implementation of parallel processing, which can compensate for the increased computational load. In the same manner, methods for azimuth DBF were introduced, which utilize the Doppler dependency of the angle of arrival of the SAR signal to detect and notch RFI coming from other angles adaptively for each Doppler frequency, as well as for 2D DBF systems.
A simulation of different interference scenarios illustrated the capabilities of the novel methods for DBF in elevation and clearly showed the superiority of the new algorithms of this work over a traditional pulse-wise notching of the antenna pattern. This work concluded that for out-of-swath interference, the number of available notches $N - 1$ can be smaller than the number of interferers without limiting the RFI mitigation performance. This is the case because a small number of well placed nulls in the antenna pattern can

suppress out-of-swath interference over a wide angular area. This is especially significant for the observation of rural and forest areas with no expected RFI. In this case, an airborne SAR benefits from its smaller swath compared to a satellite mission, which keeps all interfererers out of the swath.
On the other hand, if in-swath interference is present, $N-1$ has to exceed the number of interferers. It was observed that the advantage of the Range-Dependent Frequency MVDR over the Range-Dependent Time MVDR diminished for large N and thus the algorithm of choice depends on the system parameters. This work demonstrated that by doubling the antenna height, the lost ground coverage due to RFI halfened. In addition, the RFI gap was half the size at high SNR compared to an SNR of 0 dB.
A weakness of the above algorithms is the angular resolution of the estimated power spectrum. For low SNR, the used Capon estimate is subject to a worsening of the resolution, which results in a less efficient placement of the antenna pattern nulls. Based on the findings of this work, it makes sense to look at alternative spectral estimators such as MUSIC, which were excluded from this work due to their obstruction by false peaks (if there is no knowledge about the number of interferers as it is usually the case). If a spectral estimator can be found that combines the high resolution of spectral estimators such as MUSIC and the stability against false peaks by Capon, then this would result in a more efficient placement of the notches for low SNR and thus would increase the overall performance.

The effectiveness of the RFI mitigation techniques developed in Chapter 3 is verified with experimental data in Chapter 4. Airborne SAR data from NASA's airborne EcoSAR system was used for this purpose. An analysis of the experienced RFI during the flight campaign was presented. Two novel methods for RFI detection in SAR were proposed and evaluated for their performance with the experimental data. The methods were able to detect weak RFI by means of a time-varying bandpass filter at the beginning and end of the receive window, which takes advantage of the time-frequency dependency of the SAR signal. Next, the newly developed RFI mitigation algorithms from the previous chapter were applied to the data. The effectiveness was measured based on the interferometric coherence of a single-pass image acquired over forest areas. Despite the lack of calibration measurements, the adaptive antenna pattern notching showed promising results. Artifacts due to RFI were removed from the data and ambiguities from the opposite side of the flight track (the scene was imaged with a

wide transmit beam to allow for a simultaneous acquisition of both sides) were treated as interference and automatically notched. In addition, the experimental data were used to demonstrate the geolocating capabilities of DBF by evaluating the time-varying angle of arrival of an interferer in the Bahamas, which is an inherent result of the moving SAR platform.

The novel RFI mitigation techniques, which were presented in Chapter 3 and verified by experimental data in Chapter 4, are difficult to implement for a spaceborne SAR system with limited processing capabilities and downlink capacity. Therefore, Chapter 5 presented another novel contribution of this work: the use of digital auxiliary beams to measure RFI, which can then be downlinked to the ground for further processing. This is especially interesting for DBF systems since the main antenna can be used to form these digital auxiliary beams simultaneously without affecting the main SAR beam. An additional innovation of this work is a notch towards the instantaneous SAR signal in the auxiliary beam that is moving along the ground based on the imaging geometry. This allowed for the removal of interference closer to the angle of arrival of the instantaneous SAR signal. To increase the number of simultaneous interferers per subband that can be mitigated, the number of auxiliary beams can be increased.
Different implementations of the auxiliary beam were proposed along with techniques that increase the time-stability of the scaling factor in the SAR image. Simulations showed the ability to notch out-of-beam RFI with a wide auxiliary beam, which improved with increasing antenna size. In addition, the proposed method of this work was able to restore in-swath interferers with a narrow auxiliary beam for time instances when instantaneous SAR signal and RFI were orthogonal (as with the methods in Chapter 3).

The significant advantages of this new approach from Chapter 5 over the antenna pattern notching (Chapter 3) are the on-ground processing with a minimum increase of the data rate, as well as the possibility to overcome a fundamental limitation of non-orthogonality: the filtering of in-beam interference for all time instances. The innovative reconstruction and subsequent subtraction methods developed during this work showed promising results for the removal of non-orthogonal RFI signals (spatially overlapping with the SAR signal) with an autoregressive model: if the RFI signal is stationary for the time duration in which it was non-orthogonal to the SAR signal, it

was possible to recover the data. The signal phase was restored at RFI-to-Noise Ratios (RNR) up to 40 dB but the reconstruction was suffering from residual amplitude errors at low SNR and RNR > 0 dB. Based on the findings of this work it is recommended to assume a constant amplitude for the reconstructed interferer, which is a valid assumption during the symbol length of a digitally modulated signal. This is expected to remove the residual amplitude errors and thus may allow for a full reconstruction at RNR up to 40 dB regardless of SNR.

This work showed that DBF is a powerful tool, that can suppress most RFI in future SAR systems. Unlike conventional methods, the mitigation performance is independent of the scene and RFI characteristics but defined by system design parameters, such as antenna size, receive channels N, platform altitude, etc. However, even with DBF, the SAR and RFI signal become non-orthogonal when the main beam looks into the interferer direction, which prevents RFI mitigation. The underlying work shows that this can be overcome by a SCORE system with systematic or autoregressive modelling of the interferer based on measured out-of-beam information.
A potential direction of future DBF SAR systems is the transmission of multiple orthogonal waveforms that allow for an a posteriori change of the transmit pattern. Although, a steering of the transmit beam manipulates the interference in the receive beam and these systems can not directly measure interference by moving the transmit beam away from the swath. However, this allows for a measurement of the in-beam RFI characteristics and the angle of arrival in the absence of the SAR signal, which will benefit both the in-beam reconstruction and antenna pattern notching. It is also conceivable that the increased information content due to the transmit-steering can increase the number of effective channels N for the antenna pattern notching. Furthermore, the additional gain of a scan-on-transmit approach will result in an inherent reduction of the RFI by means of an increased SAR signal power.
Another major step towards a decreased RFI sensitivity in SAR systems can be expected from future New Space systems. These concepts, such as MirrorSAR [134], consider the use of one dedicated transmitter satellite that is flying in formation with a swarm of lightweight, cheap receiver satellites. The resulting multitude of physical baselines between the receivers allows for the simultaneous measurement of various shifted versions of the ground reflectivity spectrum. This effect, also commonly known as the spectral shift or spatial decorrelation [135], is caused by the incidence-angle-dependent projection

of the transmitted radar wavelength on the ground. The difference in the RFI signals at each receiver depends on the interferer's transmit antenna pattern and propagation effects. Thus, the decorrelation of the SAR signal can be used to further improve the RFI estimation, especially for interference that can not be filtered spatially. Further, the suppression of interference that is orthogonal to the SAR signal can be realized by forming auxiliary beams with the well-synchronized swarm of receivers. A deployment of multiple transmit satellites allows for the recording of even more auxiliary beams, which can improve the suppression further.

Nevertheless, the frequency spectrum is expected to become even more crowded in the future. It is therefore important to find other ways of sharing the same frequencies. One option would be to use communication satellites as transmitters of opportunity [136]. However, this requires good knowledge about the transmitted communication signal. A better approach is to combine the SAR and communication satellite on the same platform. Studies in the automotive radar sector demonstrated that the communication signal can be modulated onto the radar transmit signal via Orthogonal Frequency Division Multiplexing (OFDM) [137, 138]. In addition, the use of OFDM as SAR waveform has been proposed in the past [139, 140]. This concept could be adopted for joint SAR and communication satellites. As a result, the spectrum could be used for communication purposes and for remote sensing at the same time without giving rise to mutual RFI.

A. SAR Processing Gain

Let the received power of an uncompressed point target be ${\sigma_\mathrm{s}}^2$, as illustrated in Fig. A.1 by the blue rectangle. If circular-symmetric complex Gaussian noise with variance ${\sigma_\mathrm{n}}^2 = {\sigma_\mathrm{s}}^2$ is added (red-dashed line in Fig. A.1), then the SNR_raw in the raw data equals 0 dB. This can be improved by matched filtering the image, which results in a coherent integration of $N_\mathrm{P} = B_\mathrm{W} T_\mathrm{p} \cdot T_\mathrm{Int} PRF$ samples. Hence, the peak signal power is increased to ${N_\mathrm{P}}^2 {\sigma_\mathrm{s}}^2$. On the other hand, the noise is being added incoherently, increasing the noise variance to $N_\mathrm{P} {\sigma_\mathrm{n}}^2$. As a result, the SNR of the focused image [59] SNR_foc is

$$SNR_\mathrm{foc} = \frac{{N_\mathrm{P}}^2 {\sigma_\mathrm{s}}^2}{N_\mathrm{P} {\sigma_\mathrm{n}}^2} = N_\mathrm{P} \cdot SNR_\mathrm{raw}. \tag{A.1}$$

This is commonly referred to as the SAR processing gain. Note that the SNR gain is only a result of redistributing the signal energy in the time domain when the SAR IRF (green line in Fig. A.1) is formed. The integrated signal power before and after focusing remains the same [141]. This is evident as the focusing operation is a phase multiplication in the frequency domain, leaving the power spectrum density unchanged. The SNR improvement is only achieved in the mainlobe where the SAR energy is concentrated because noise is spread across the image.

This is not the case for the extended target with variance ${\sigma_\mathrm{s}}^2$ that was simulated in Section 2.2.1. The raw signal is the result of an integration of the backscattering coefficient over the pulse extent. The measured raw signal power due to the overlapping chirps is therefore $N_\mathrm{P} {\sigma_\mathrm{s}}^2$ (green-dashed line in Fig. A.1). Assuming the same noise, the SNR of the raw signal is

$$SNR_\mathrm{raw,ext} = \frac{N_\mathrm{P} {\sigma_\mathrm{s}}^2}{{\sigma_\mathrm{n}}^2} \tag{A.2}$$

When a matched filter is applied, the Gaussian raw signal is being added incoherently - as is the noise. Hence the resulting SNR is

$$SNR_\mathrm{foc,ext} = \frac{{N_\mathrm{P}}^2 {\sigma_\mathrm{s}}^2}{N_\mathrm{P} {\sigma_\mathrm{n}}^2} = SNR_\mathrm{raw,ext} \tag{A.3}$$

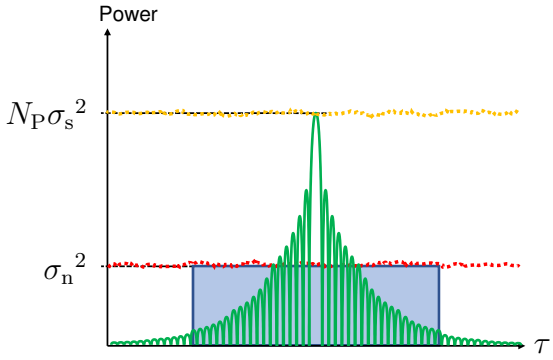

Fig. A.1.: Power of received signals: the blue rectangle represents the power received of an ideal point target with $\sigma_n^2 = \sigma_s^2$. The time extent is given by the pulse duration. After range compression, the power is defined by the IRF. The power at the peak is equivalent to $N_P^2\sigma_s^2$. The power received of an extended target is plotted as a yellow-dashed line. After range compression, the power stays the same. The noise floor is plotted as a red-dashed line.

This implies that the SNR of an extended target is not improved in the focused image. Note that each infinitisemal small point of the extended target is still experiencing the processing gain of Eq. (A.1) in the mainlobe. However, the redistribution of the energy of multiple overlapping rectangular chirps (green-dashed line in Fig. A.1) to multiple overlapping IRFs (green-dashed line in Fig. A.1) does not change the visible signal power.
In Section 2.5.2, the RFI model for the simulations in this thesis is outlined and an error model is presented to measure the data degradation due the RFI. Simulations of the impact on the SAR performance parameters from Section 2.2.3 are presented in Section 2.5.3.

B. Impact of RFI on SAR Performance Parameters

This section completes the analysis of the error model (Section 2.5.3) for the remaining SAR performance parameters based on the assumptions made in Section 2.5.3.

Resolution

A simulation of the resolution of a point target shows a detoriation on the order of 5 cm (Fig. B.1). Hence, no further restriction of the errors is necessary.

Peak-to-Sidelobe Ratio

The PSLR of a point target in dependence of time-varying amplitude and phase errors with normal distribution is shown in Fig. B.2a. The one-dimensional plots for point targets and a normal RFI distribution and for a CW interferer is shown in Fig. B.2b-B.2c. The PSLR is more sensitive to the errors introduced by a CW interferer. However, a drop by 1 dB is only exceeded for $\sigma_\Phi > 18°$. Hence, the PSLR is acceptable for the previously defined error range with a maximum degradation of 0.62 dB.

Integrated Sidelobe Ratio

A drop of the Integrated Sidelobe Ratio (ISLR) by 0.5 dB is caused for $\sigma_\Phi > 22°$ or $\sigma_\mathrm{A} > -9$ dB. The previously defined error range causes acceptable ISLR values with a maximum ISLR drop of 0.4 dB.

Coherence

Next, the spatial interferometric coherence for normally distributed errors is computed. It is evident from Fig. B.4a that amplitude phase deviations smaller -10 dB have no impact on the coherence. A phase standard deviation of $\sigma_\Phi \leq 18°$ results in a coherence

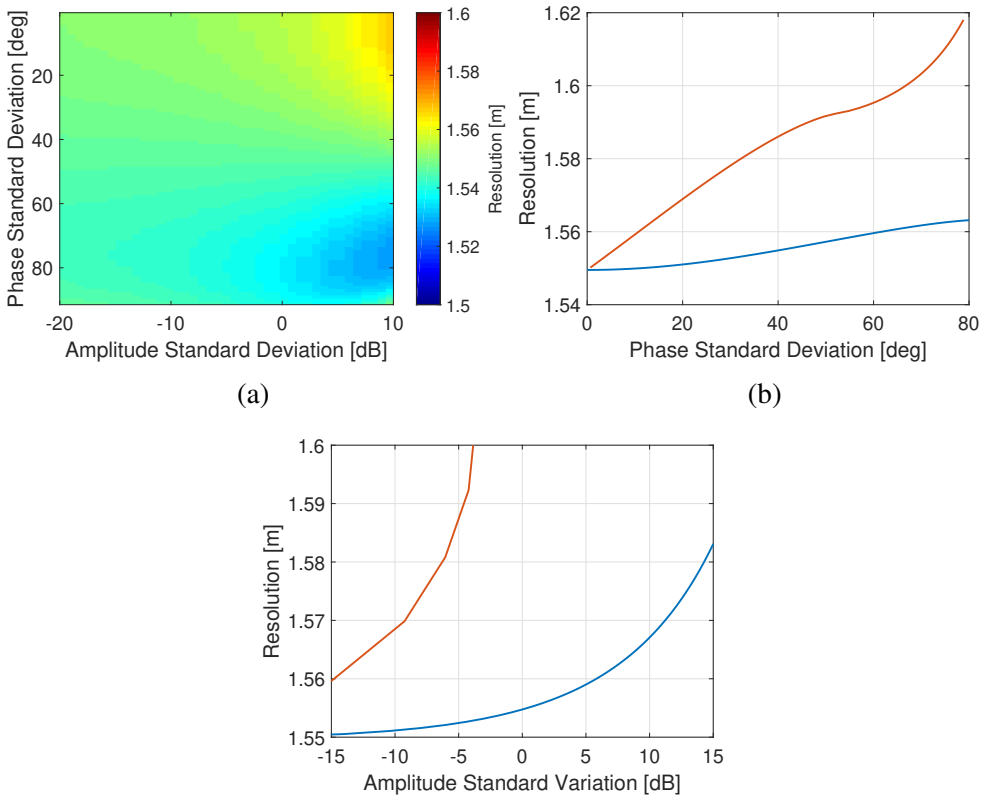

Fig. B.1.: a) Impact of time-varying normal errors on the point target resolution, b) Impact of time-varying phase errors on the point target resolution, c) Impact of time-varying amplitude errors on the point target resolution. The orange curves represent the maximum error for a CW interferer.

drop of 0.956 for an otherwise coherent signal. The combination of σ_{Φ} and σ_{A} is shown in Fig. B.4c and is in agreement with the one dimensional plots. Hence, the values are in alignment with the interferometric budget and do not require a further restriction of the errors.

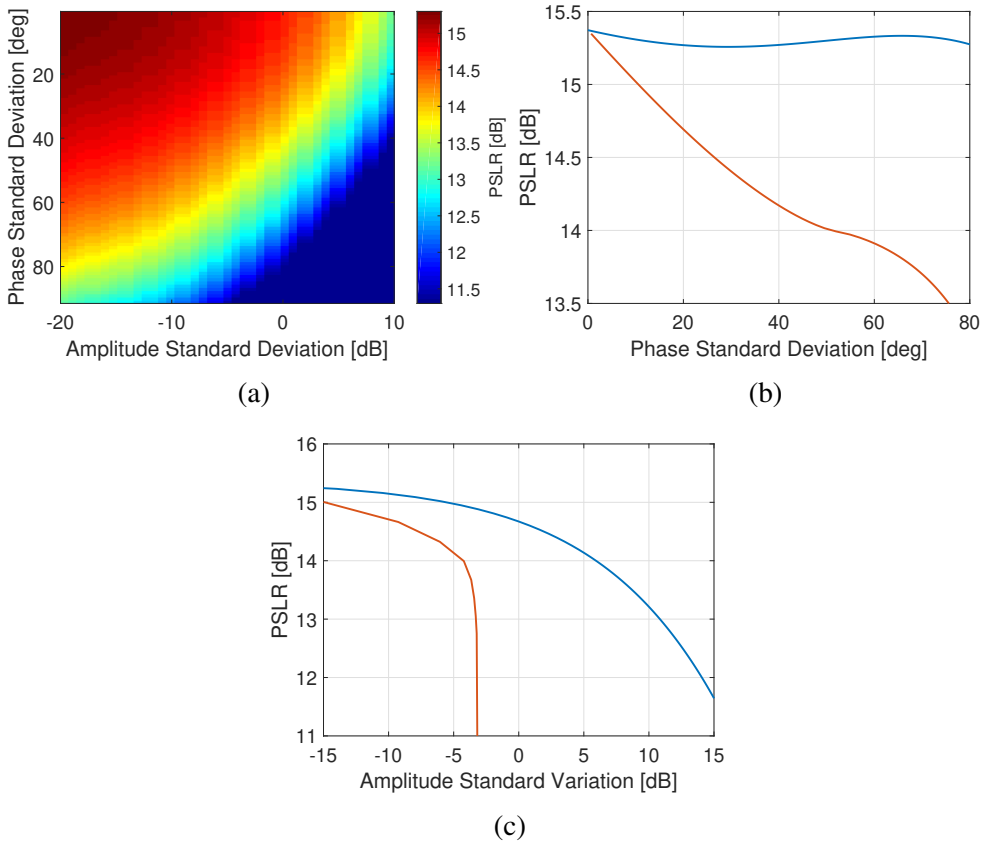

Fig. B.2.: a) Impact of time-varying errors with normal distribution on the point target PSLR, b) Impact of time-varying phase errors on the point target PSLR, c) Impact of time-varying amplitude errors on the point target PSLR. The orange curves represent the maximum error for a CW interferer.

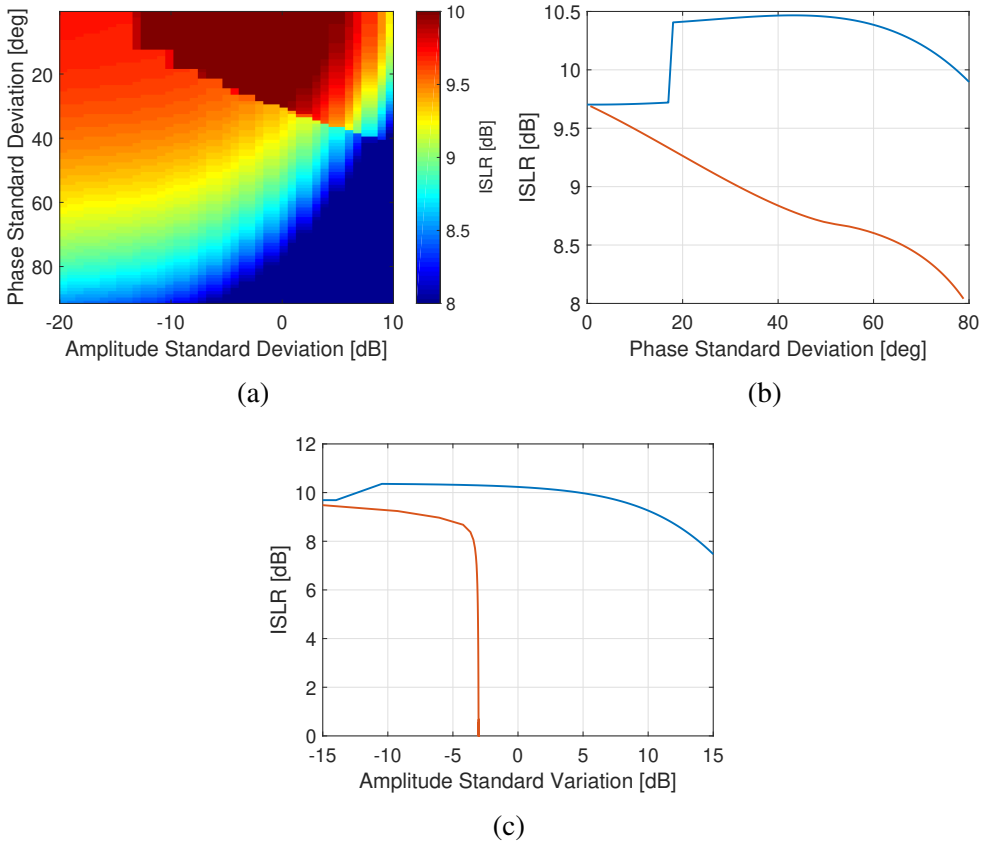

Fig. B.3.: a) Impact of time-varying errors with normal distribution on the point target ISLR, b) Impact of time-varying phase errors on the point target ISLR, c) Impact of time-varying amplitude errors on the point target ISLR. The orange curves represent the maximum error for a CW interferer.

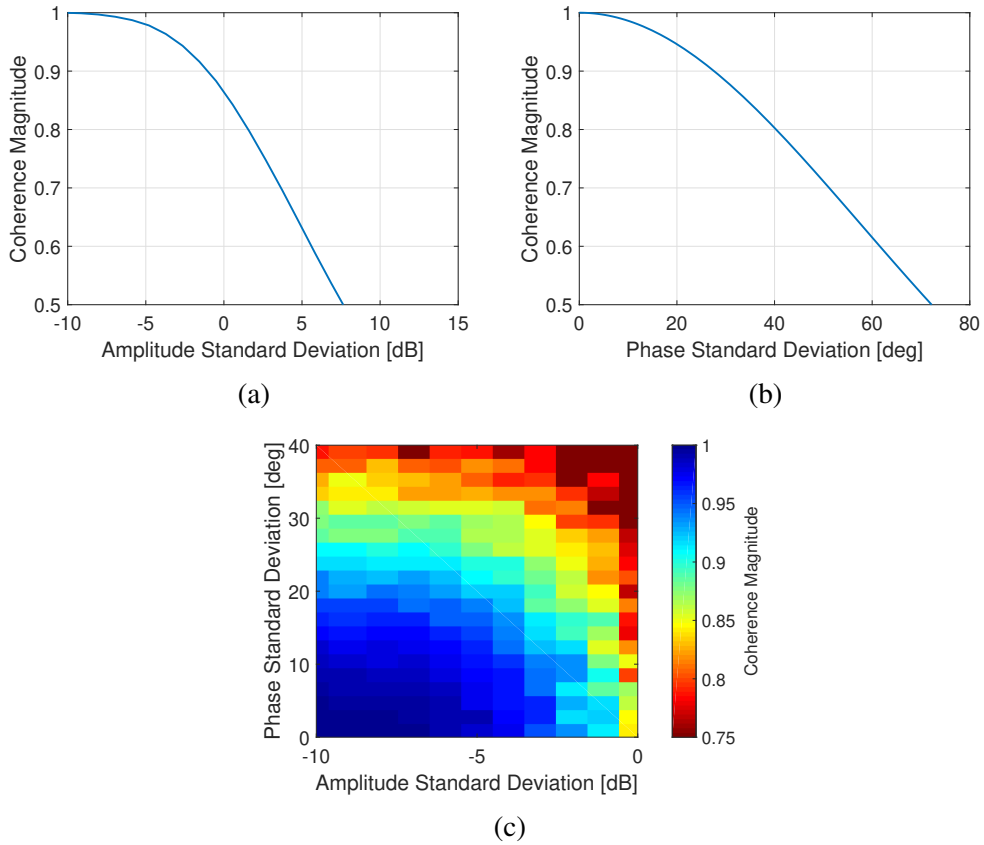

Fig. B.4.: a) Impact of time-varying amplitude errors on the coherence, b) Impact of time-varying phase errors on the coherence, c) Impact of time-varying amplitude and phase errors on the coherence

C. Bibliography

[1] D. J. Cichon and W. Wiesbeck, "The Heinrich Hertz wireless experiments at Karlsruhe in the view of modern communication," 1995.

[2] C. A. Wiley, "Pulsed doppler radar methods and apparatus," Jul. 20 1965, US Patent 3,196,436.

[3] H. Mazar, *Radio Spectrum Management: Policies, Regulations and Techniques*. John Wiley & Sons, 2016.

[4] L.-L. Fu and B. Holt, *Seasat views oceans and sea ice with synthetic-aperture radar*. California Institute of Technology, Jet Propulsion Laboratory, 1982, vol. 81.

[5] P. A. Rosen, S. Hensley, and C. Le, "Observations and mitigation of RFI in ALOS PALSAR SAR data: Implications for the DESDynI mission," in *2008 IEEE Radar Conference*, May 2008, pp. 1–6.

[6] D. M. L. Vine, F. Pellerano, G. S. E. Lagerloef, S. Yueh, and R. Colomb, "Aquarius: A mission to monitor sea surface salinity from space," in *2006 IEEE MicroRad*, 2006, pp. 87–90.

[7] A. Freedman, D. McWatters, and M. Spencer, "The aquarius scatterometer: An active system for measuring surface roughness for sea-surface brightness temperature correction," in *2006 IEEE International Symposium on Geoscience and Remote Sensing*, July 2006, pp. 1685–1688.

[8] D. M. L. Vine and P. de Matthaeis, "Aquarius active/passive RFI environment at L-band," *IEEE Geoscience and Remote Sensing Letters*, vol. 11, no. 10, pp. 1747–1751, Oct 2014.

[9] D. M. L. Vine, "ESTAR experience with RFI at L-band and implications for future passive microwave remote sensing from space," in *IEEE International Geoscience and Remote Sensing Symposium*, vol. 2, June 2002, pp. 847–849 vol.2.

[10] A. Rosenqvist, M. Shimada, N. Ito, and M. Watanabe, "ALOS PALSAR: A pathfinder mission for global-scale monitoring of the environment," *IEEE Transactions on Geoscience and Remote Sensing*, vol. 45, no. 11, pp. 3307–3316, Nov 2007.

[11] F. J. Meyer, J. B. Nicoll, and A. P. Doulgeris, "Correction and characterization of radio frequency interference signatures in L-band synthetic aperture radar data," *IEEE Transactions on Geoscience and Remote Sensing*, vol. 51, no. 10, pp. 4961–4972, Oct 2013.

[12] ——, "Characterization and extent of randomly-changing radio frequency interference in ALOS PALSAR data," in *2011 IEEE International Geoscience and Remote Sensing Symposium*, July 2011, pp. 2448–2451.

[13] J. E. Belz, B. L. Huneycutt, and M. W. Spencer, "A study of radio frequency interference in the space-to-Earth exploration allocation at L-band," in *2011 Aerospace Conference*, March 2011, pp. 1–10.

[14] S. Mecklenburg, M. Drusch, Y. H. Kerr, J. Font, M. Martin-Neira, S. Delwart, G. Buenadicha, N. Reul, E. Daganzo-Eusebio, R. Oliva, and R. Crapolicchio, "ESA's soil moisture and ocean salinity mission: Mission performance and operations," *IEEE Transactions on Geoscience and Remote Sensing*, vol. 50, no. 5, pp. 1354–1366, May 2012.

[15] R. Oliva, E. Daganzo, Y. H. Kerr, S. Mecklenburg, S. Nieto, P. Richaume, and C. Gruhier, "SMOS radio frequency interference scenario: Status and actions taken to improve the RFI environment in the 1400-MHz 1427-MHz passive band," *IEEE Transactions on Geoscience and Remote Sensing*, vol. 50, no. 5, pp. 1427–1439, May 2012.

[16] *Radio regulations*. Geneva: ITU, 2016.

[17] M. Spencer and F. Ulaby, "Spectrum issues faced by active remote sensing: Radio frequency interference and operational restrictions technical committees," *IEEE Geoscience and Remote Sensing Magazine*, vol. 4, no. 1, pp. 40–45, March 2016.

[18] E. R. Stofan, D. L. Evans, C. Schmullius, B. Holt, J. J. Plaut, J. van Zyl, S. D. Wall, and J. Way, "Overview of results of spaceborne imaging radar-C, X-band synthetic aperture radar (SIR-C/X-SAR)," *IEEE Transactions on Geoscience and Remote Sensing*, vol. 33, no. 4, pp. 817–828, 1995.

[19] T. Kawanishi, T. Sezai, Y. Ito, K. Imaoka, T. Takeshima, Y. Ishido, A. Shibata, M. Miura, H. Inahata, and R. W. Spencer, "The advanced microwave scanning radiometer for the Earth observing system (AMSR-E), NASDA's contribution to the EOS for global energy and water cycle studies," *IEEE Transactions on Geoscience and Remote Sensing*, vol. 41, no. 2, pp. 184–194, Feb 2003.

[20] P. S. Narvekar, T. J. Jackson, R. Bindlish, L. Li, G. Heygster, and P. Gaiser, "Observations of land surface passive polarimetry with the WindSat instrument," *IEEE Transactions on Geoscience and Remote Sensing*, vol. 45, no. 7, pp. 2019–2028, July 2007.

[21] D. McKague, J. J. Puckett, and C. Ruf, "Characterization of K-band radio frequency interference from AMSR-E, WindSat and SSM/I," in *2010 IEEE International Geoscience and Remote Sensing Symposium*, July 2010, pp. 2492–2494.

[22] A. Panetti, F. Rostan, M. L'Abbate, C. Bruno, A. Bauleo, T. Catalano, M. Cotogni, L. Galvagni, A. Pietropaolo, G. Taini, P. Venditti, M. Huchler, R. Torres, S. Lokas, D. Bibby, and D. Geudtner, "Copernicus Sentinel-1 satellite and C-SAR instrument," in *2014 IEEE Geoscience and Remote Sensing Symposium*, July 2014, pp. 1461–1464.

[23] E. M. Team, "Sentinel-1 Radarsat-2 mutual interference," 2017.

[24] *An Introduction to National Aeronautics and Space Administration Spectrum Management*. NASA, 2016.

[25] D. Giudici, P. Guccione, D. Geudtner, and R. Torres, "RLAN impact on Sentinel-1 C-band SAR performance," in *EUSAR 2018; 12th European Conference on Synthetic Aperture Radar*, June 2018, pp. 1–6.

[26] *An Introduction to the WRC - A beginner's guide to the World Radiocommunication Conference*. GSMA, 2017.

[27] S. Misra and P. de Matthaeis, "Passive remote sensing and radio frequency interference (RFI): An overview of spectrum allocations and RFI management algorithms [technical committees]," *IEEE Geoscience and Remote Sensing Magazine*, vol. 2, no. 2, pp. 68–73, 2014.

[28] T. L. Toan, S. Quegan, M. Davidson, H. Balzter, P. Paillou, K. Papathanassiou, S. Plummer, F. Rocca, S. Saatchi, H. Shugart, and L. Ulander, "The BIOMASS mission: Mapping global forest biomass to better understand the terrestrial carbon cycle," *Remote Sensing of Environment*, vol. 115, no. 11, pp. 2850 – 2860, 2011, dESDynI VEG-3D Special Issue.

[29] J. M. Carreiras, S. Quegan, T. L. Toan, D. H. T. Minh, S. S. Saatchi, N. Carvalhais, M. Reichstein, and K. Scipal, "Coverage of high biomass forests by the ESA BIOMASS mission under defense restrictions," *Remote Sensing of Environment*, vol. 196, pp. 154 – 162, 2017.

[30] R. F. Rincon, T. Fatoyinbo, B. Osmanoglu, S. Lee, K. J. Ranson, G. Sun, and T. Bollian, "EcoSAR: P-band digital beamforming polarimetric and single pass interferometric SAR: Instrument performance," in *Proceedings of EUSAR 2016: 11th European Conference on Synthetic Aperture Radar*, June 2016, pp. 1–5.

[31] L. J. Harcke and C. T. C. Le, "AirMOSS P-band RF interference experience," in *2014 IEEE Radar Conference*, May 2014, pp. 0761–0764.

[32] R. F. Rincon, T. Fatoyinbo, J. Ranson, G. Sun, M. Perrine, Q. Bonds, S. Valett, and S. Seufert, "Digital beamforming synthetic aperture radar (DBSAR) polarimetric operation during the Eco3D flight campaign," in *2012 IEEE International Geoscience and Remote Sensing Symposium*, July 2012, pp. 1549–1552.

[33] R. Rincon, T. Fatoyinbo, B. Osmanoglu, S.-K. Lee, K. J. Ranson, V. Marrero, and M. Yeary, "Next generation digital beamforming synthetic aperture radar (DBSAR-2)," in *Geoscience and Remote Sensing Symposium (IGARSS), 2015 IEEE International*. IEEE, 2015, pp. 2774–2777.

[34] Y. Kankaku, M. Sagisaka, and S. Suzuki, "PALSAR-2 launch and early orbit status," in *2014 IEEE Geoscience and Remote Sensing Symposium*, July 2014, pp. 3410–3412.

[35] Y. Okada, Y. Yokota, A. Karasawa, M. Matsuki, M. Arii, and S. Nakamura, "Hardware performance of PALSAR-3 onboard ALOS-4," in *IGARSS 2018-2018 IEEE International Geoscience and Remote Sensing Symposium*. IEEE, 2018, pp. 4175–4176.

[36] P. Rosen, S. Hensley, S. Shaffer, W. Edelstein, Y. Kim, R. Kumar, T. Misra, R. Bhan, R. Satish, and R. Sagi, "An update on the NASA-ISRO dual-frequency DBF SAR (NISAR) mission," in *2016 IEEE International Geoscience and Remote Sensing Symposium (IGARSS)*, July 2016, pp. 2106–2108.

[37] A. E. Giraldez, "SAOCOM-1 Argentina L-band SAR mission overview," in *Coastal and Marine Applications of SAR Symp*, 2003.

[38] M. Younis, S. Huber, C. T. Herrero, G. Krieger, A. Moreira, A. Uematsu, Y. Sudo, R. Nakamura, Y. Chishiki, and M. Shimada, "Tandem-L instrument design and SAR performance overview," in *2014 IEEE Geoscience and Remote Sensing Symposium*, July 2014, pp. 88–91.

[39] M. Shimada, O. Isoguchi, T. Tadono, and K. Isono, "PALSAR radiometric and geometric calibration," *IEEE Transactions on Geoscience and Remote Sensing*, vol. 47, no. 12, pp. 3915–3932, Dec 2009.

[40] R. T. Lord and M. R. Inggs, "Approaches to RF interference suppression for VHF/UHF synthetic aperture radar," in *Communications and Signal Processing, 1998. COMSIG '98. Proceedings of the 1998 South African Symposium on*, Sep 1998, pp. 95–100.

[41] J. L. W. CHANG and X. LI, "The effect of notch filter on RFI suppression," *Wireless Sensor Network*, vol. 1, no. 3, pp. 196–205, 2009.

[42] A. Reigber and L. Ferro-Famil, "Interference suppression in synthesized SAR images," *IEEE Geoscience and Remote Sensing Letters*, vol. 2, no. 1, pp. 45–49, Jan 2005.

[43] A. Potsis, A. Reigber, and K. P. Papathanassiou, "A phase preserving method for RF interference suppression in P-band synthetic aperture radar interferometric data," in *Geoscience and Remote Sensing Symposium, 1999. IGARSS '99 Proceedings. IEEE 1999 International*, vol. 5, 1999, pp. 2655–2657 vol.5.

[44] D. A. S. Matthew Braunstein, James M. Ralston, "Signal processing approaches to radio frequency interference (RFI) suppression," pp. 2230 – 2230 – 19, 1994.

[45] R. T. Lord and M. R. Inggs, "Efficient RFI suppression in SAR using LMS adaptive filter integrated with range/doppler algorithm," *Electronics Letters*, vol. 35, no. 8, pp. 629–630, Apr 1999.

[46] C. T. C. Le, S. Hensley, and E. Chapin, "Removal of RFI in wideband radars," in *Geoscience and Remote Sensing Symposium Proceedings, 1998. IGARSS '98. 1998 IEEE International*, vol. 4, Jul 1998, pp. 2032–2034 vol.4.

[47] S. Applebaum, "Adaptive arrays," *IEEE Transactions on Antennas and Propagation*, vol. 24, no. 5, pp. 585–598, Sep 1976.

[48] A. Farina, "Single sidelobe canceller: Theory and evaluation," *IEEE Transactions on Aerospace and Electronic Systems*, vol. AES-13, no. 6, pp. 690–699, Nov 1977.

[49] ——, "Evaluation of sidelobe-canceller performance," *Communications, Radar and Signal Processing, IEE Proceedings F*, vol. 129, no. 1, pp. 52–58, February 1982.

[50] M. Sedehi, D. Cristallini, J. Marini, and P. Lombardo, "Impact of an electromagnetic interference on imaging capability of a synthetic aperture radar," in *2007 IEEE Aerospace Conference*, March 2007, pp. 1–8.

[51] M. Sedehi, F. Colone, D. Cristallini, and P. Lombardo, "A reduced order jammer cancellation scheme based on double adaptivity," in *2008 IEEE Radar Conference*, May 2008, pp. 1–6.

[52] P. Lombardo, M. Sedehi, F. Colone, M. Bucciarelli, and D. Cristallini, "Dual channel adaptive antenna nulling with auxiliary selection for spaceborne radar," in *2008 IEEE Aerospace Conference*, March 2008, pp. 1–8.

[53] M. Sedehi, D. Cristallini, M. Bucciarelli, and P. Lombardo, "Constrained adaptive beamforming for electromagnetic interference cancellation for a synthetic aperture radar," in *2007 IET International Conference on Radar Systems*, Oct 2007, pp. 1–5.

[54] M. Younis, C. Fischer, and W. Wiesbeck, "Digital beamforming in SAR systems," *IEEE Transactions on Geoscience and Remote Sensing*, vol. 41, no. 7, pp. 1735–1739, July 2003.

[55] B. D. V. Veen and K. M. Buckley, "Beamforming: a versatile approach to spatial filtering," *IEEE ASSP Magazine*, vol. 5, no. 2, pp. 4–24, April 1988.

[56] M. Suess, B. Grafmueller, and R. Zahn, "A novel high resolution, wide swath SAR system," in *IGARSS 2001. Scanning the Present and Resolving the Future. Proceedings. IEEE 2001 International Geoscience and Remote Sensing Symposium (Cat. No.01CH37217)*, vol. 3, 2001, pp. 1013–1015 vol.3.

[57] M. Suess and W. Wiesbeck, "Side-looking synthetic aperture radar system," Sep. 2002, european Patent EP 1 241 487 B1.

[58] K. Tomiyasu, "Tutorial review of synthetic-aperture radar (SAR) with applications to imaging of the ocean surface," *Proceedings of the IEEE*, vol. 66, no. 5, pp. 563–583, 1978.

[59] J. C. Curlander and R. N. McDonough, "Synthetic aperture radar: Systems and signal theory," *John Willey & Sons*, 1991.

[60] A. Moreira, *Radar mit synthetischer Apertur*. Oldenbourg Verlag, München, 1999.

[61] A. Moreira, P. Prats-Iraola, M. Younis, G. Krieger, I. Hajnsek, and K. P. Papathanassiou, "A tutorial on synthetic aperture radar," *IEEE Geoscience and remote sensing magazine*, vol. 1, no. 1, pp. 6–43, 2013.

[62] A. Martinez and J. Marchand, "SAR image quality assessment," *Revista de Teledeteccion*, vol. 2, pp. 12–18, 1993.

[63] X. Lu and H. Sun, "Parameter assessment for SAR image quality evaluation system," in *Synthetic Aperture Radar, 2007. APSAR 2007. 1st Asian and Pacific Conference on*. IEEE, 2007, pp. 58–60.

[64] V. T. Vu, T. K. Sjögren, M. I. Pettersson, and A. Gustavsson, "Definition on SAR image quality measurements for UWB SAR," in *Image and Signal Processing for Remote Sensing XIV*, vol. 7109. International Society for Optics and Photonics, 2008, p. 71091A.

[65] R. Bamler and D. Just, "Phase statistics and decorrelation in SAR interferograms," in *Geoscience and Remote Sensing Symposium, 1993. IGARSS'93. Better Understanding of Earth Environment., International*. IEEE, 1993, pp. 980–984.

[66] R. N. Treuhaft, S. N. Madsen, M. Moghaddam, and J. J. Zyl, "Vegetation characteristics and underlying topography from interferometric radar," *Radio Science*, vol. 31, no. 6, pp. 1449–1485, 1996.

[67] E. Rodriguez and J. Martin, "Theory and design of interferometric synthetic aperture radars," in *IEE Proceedings F (Radar and Signal Processing)*, vol. 139, no. 2. IET, 1992, pp. 147–159.

[68] B. Forman, "Directivity characteristics of scannable planar arrays," *IEEE Transactions on Antennas and Propagation*, vol. 20, no. 3, pp. 245–252, May 1972.

[69] H. Steyskal, "Digital beamforming antennas - an introduction," *Microwave journal*, vol. 30, p. 107, 1987.

[70] P. Barton, "Digital beam forming for radar," *Communications, Radar and Signal Processing, IEE Proceedings F*, vol. 127, no. 4, pp. 266–277, August 1980.

[71] H. M. Aumann, A. J. Fenn, and F. G. Willwerth, "Phased array antenna calibration and pattern prediction using mutual coupling measurements," *IEEE Transactions on Antennas and Propagation*, vol. 37, no. 7, pp. 844–850, Jul 1989.

[72] A. Currie and M. A. Brown, "Wide-swath SAR," *IEE Proceedings F - Radar and Signal Processing*, vol. 139, no. 2, pp. 122–135, April 1992.

[73] G. Krieger, N. Gebert, and A. Moreira, "SAR signal reconstruction from non-uniform displaced phase centre sampling," in *IGARSS 2004. 2004 IEEE International Geoscience and Remote Sensing Symposium*, vol. 3, Sept 2004, pp. 1763–1766 vol.3.

[74] N. Gebert, G. Krieger, and A. Moreira, "Digital beamforming on receive: Techniques and optimization strategies for high-resolution wide-swath SAR imaging," *IEEE Transactions on Aerospace and Electronic Systems*, vol. 45, no. 2, pp. 564–592, April 2009.

[75] M. Younis, T. Rommel, F. Bordoni, G. Krieger, and A. Moreira, "On the pulse extension loss in digital beamforming SAR," *IEEE Geoscience and Remote Sensing Letters*, vol. 12, no. 7, pp. 1436–1440, 2015.

[76] J. Castillo, M. Younis, and G. Krieger, "A HRWS SAR system design with multibeam imaging capabilities," in *2017 European Radar Conference (EURAD)*, Oct 2017, pp. 179–182.

[77] T. Yang, X. Lv, Y. Wang, and J. Qian, "Study on a novel multiple elevation beam technique for HRWS SAR system," *IEEE Journal of Selected Topics in Applied Earth Observations and Remote Sensing*, vol. 8, no. 11, pp. 5030–5039, Nov 2015.

[78] J. H. Kim, M. Younis, P. Prats-Iraola, M. Gabele, and G. Krieger, "First spaceborne demonstration of digital beamforming for azimuth ambiguity suppression," *IEEE Transactions on Geoscience and Remote Sensing*, vol. 51, no. 1, pp. 579–590, Jan 2013.

[79] G. Krieger, S. Huber, M. Villano, M. Younis, T. Rommel, P. L. Dekker, F. Q. de Almeida, and A. Moreira, "CEBRAS: Cross elevation beam range ambiguity suppression for high-resolution wide-swath and MIMO-SAR imaging," in *2015 IEEE International Geoscience and Remote Sensing Symposium (IGARSS)*, July 2015, pp. 196–199.

[80] R. F. Rincon, M. A. Vega, M. Buenfil, A. Geist, L. Hilliard, and P. Racette, "NASA's L-band digital beamforming synthetic aperture radar," *IEEE Transactions on Geoscience and Remote Sensing*, vol. 49, no. 10, pp. 3622–3628, Oct 2011.

[81] G. Krieger, "MIMO-SAR: Opportunities and pitfalls," *IEEE Transactions on Geoscience and Remote Sensing*, vol. 52, no. 5, pp. 2628–2645, May 2014.

[82] M. Younis, P. Lopez-Dekker, and G. Krieger, "MIMO SAR operation modes and techniques," in *EUSAR 2014; 10th European Conference on Synthetic Aperture Radar*, June 2014, pp. 1–3.

[83] T. Rommel, M. Younis, and G. Krieger, "An orthogonal waveform for fully polarimetric MIMO-SAR," in *2014 IEEE Radar Conference*, May 2014, pp. 0887–0891.

[84] G. Krieger, T. Rommel, and A. Moreira, "MIMO-SAR tomography," in *Proceedings of EUSAR 2016: 11th European Conference on Synthetic Aperture Radar*, June 2016, pp. 1–6.

[85] G. Adamiuk, C. Heer, and M. Ludwig, "DBF technology development for next generation of ESA C-band SAR mission," in *Proceedings of EUSAR 2016: 11th European Conference on Synthetic Aperture Radar*, June 2016, pp. 1–4.

[86] A. Reigber, A. Nottensteiner, M. Limbach, M. Jäger, A. Kosc, R. Scheiber, J. Fischer, A. D. Maria, G. Müller, R. Que, M. Künemund, K. Trappschuh, S. Pasch, D. Geßwein, D. Höflmayr, B. Gabler, M. Keller, R. Horn, and A. Moreira, "DBF-SAR: An airborne very high-resolution digital beamforming SAR system," in *2017 European Radar Conference (EURAD)*, Oct 2017, pp. 175–178.

[87] R. Wang, Y. Deng, and P. Wang, "Recent progress of airborne X-band SAR with two-dimensional digital beamforming," in *Proceedings of EUSAR 2016: 11th European Conference on Synthetic Aperture Radar*, June 2016, pp. 1–4.

[88] H. Wang, H. Zhang, S. Dai, and Z. Sun, "Azimuth multichannel GMTI based on Ka-band DBF-score SAR system," *IEEE Geoscience and Remote Sensing Letters*, vol. 15, no. 3, pp. 419–423, March 2018.

[89] A. Moreira, G. Krieger, I. Hajnsek, K. Papathanassiou, M. Younis, P. Lopez-Dekker, S. Huber, M. Villano, M. Pardini, M. Eineder, F. De Zan, and A. Parizzi, "Tandem-L: A highly innovative bistatic SAR mission for global observation of dynamic processes on the Earth's surface," *IEEE Geoscience and Remote Sensing Magazine*, vol. 3, no. 2, pp. 8–23, June 2015.

[90] P. A. Rosen, S. Hensley, S. Shaffer, L. Veilleux, M. Chakraborty, T. Misra, R. Bhan, V. R. Sagi, and R. Satish, "The NASA-ISRO SAR mission-an international space partnership for science and societal benefit," in *2015 IEEE Radar Conference (RadarCon)*. IEEE, 2015, pp. 1610–1613.

[91] J. Mittermayer and H. Runge, "Conceptual studies for exploiting the TerraSAR-X dual receive antenna," in *IGARSS 2003. 2003 IEEE International Geoscience and Remote Sensing Symposium. Proceedings (IEEE Cat. No.03CH37477)*, vol. 3, July 2003, pp. 2140–2142.

[92] ITU, *Handbook on Amateur and Amateur-Satellite Services*. Geneva: International Telecommunication Union, 2014.

[93] ITU-R, *Recommendation M.1732-2. Characteristics of systems operating in the amateur and amateur-satellite services*. International Telecommunication Union, 2017.

[94] T. Bollian, B. Osmanoglu, R. Rincon, S.-K. Lee, and T. Fatoyinbo, "Adaptive antenna pattern notching of interference in synthetic aperture radar data using digital beamforming," *Remote Sensing*, vol. 11, no. 11, p. 1346, 2019.

[95] J. Capon, "High-resolution frequency-wavenumber spectrum analysis," *Proceedings of the IEEE*, vol. 57, no. 8, pp. 1408–1418, Aug 1969.

[96] H. Trees, "Optimum array processing (detection, estimation, and modulation theory, part iv) wiley-interscience," *New York, NY, USA*, 2002.

[97] R. G. Lorenz and S. P. Boyd, "Robust minimum variance beamforming," *IEEE Transactions on Signal Processing*, vol. 53, no. 5, pp. 1684–1696, May 2005.

[98] H. Cox, "Resolving power and sensitivity to mismatch of optimum array processors," *The Journal of the acoustical society of America*, vol. 54, no. 3, pp. 771–785, 1973.

[99] A. Vural, "Effects of perturbations on the performance of optimum/adaptive arrays," *IEEE Transactions on Aerospace and Electronic Systems*, no. 1, pp. 76–87, 1979.

[100] R. Compton, "The effect of random steering vector errors in the Applebaum adaptive array," *IEEE Transactions on Aerospace and Electronic Systems*, no. 4, pp. 392–400, 1982.

[101] M. Wax and Y. Anu, "Performance analysis of the minimum variance beamformer in the presence of steering vector errors," *IEEE Transactions on Signal Processing*, vol. 44, no. 4, pp. 938–947, Apr 1996.

[102] F. Bordoni, M. Younis, E. M. Varona, and G. Krieger, "Adaptive scan-on-receive based on spatial spectral estimation for high-resolution, wide-swath synthetic aperture radar," in *2009 IEEE International Geoscience and Remote Sensing Symposium*, vol. 1, July 2009, pp. I–64–I–67.

[103] O. L. Frost, "An algorithm for linearly constrained adaptive array processing," *Proceedings of the IEEE*, vol. 60, no. 8, pp. 926–935, 1972.

[104] M. Sedehi, M. Bucciarelli, D. Cristallini, S. Scolamiero, and P. Lombardo, "Interference covariance matrix estimation for a multi-channel synthetic aperture radar," in *7th European Conference on Synthetic Aperture Radar*, June 2008, pp. 1–4.

[105] M. Villano, G. Krieger, and A. Moreira, "Staggered SAR: High-resolution wide-swath imaging by continuous PRI variation," *IEEE Transactions on Geoscience and Remote Sensing*, vol. 52, no. 7, pp. 4462–4479, 2014.

[106] ——, "A novel processing strategy for staggered SAR," *IEEE Geoscience and Remote Sensing Letters*, vol. 11, no. 11, pp. 1891–1895, 2014.

[107] M. Villano, G. Krieger, M. Jäger, and A. Moreira, "Staggered SAR: Performance analysis and experiments with real data," *IEEE Transactions on Geoscience and Remote Sensing*, vol. 55, no. 11, pp. 6617–6638, 2017.

[108] F. Q. de Almeida, M. Younis, G. Krieger, and A. Moreira, "Multichannel staggered SAR azimuth processing," *IEEE Transactions on Geoscience and Remote Sensing*, 2018.

[109] Y. Gu and A. Leshem, "Robust adaptive beamforming based on interference covariance matrix reconstruction and steering vector estimation," *IEEE Transactions on Signal Processing*, vol. 60, no. 7, pp. 3881–3885, 2012.

[110] R. Schmidt, "Multiple emitter location and signal parameter estimation," *IEEE Transactions on Antennas and Propagation*, vol. 34, no. 3, pp. 276–280, Mar 1986.

[111] H.-T. Wu, J.-F. Yang, and F.-K. Chen, "Source number estimators using transformed Gerschgorin radii," *IEEE Transactions on Signal Processing*, vol. 43, no. 6, pp. 1325–1333, Jun 1995.

[112] Z. Qiu, Z. He, and M. Cui, "A method for signal source number estimation based on MUSIC algorithm," in *2015 IEEE International Conference on Communication Problem-Solving (ICCP)*, Oct 2015, pp. 344–346.

[113] S. Rapuano and F. J. Harris, "An introduction to FFT and time domain windows," *IEEE instrumentation & measurement magazine*, vol. 10, no. 6, 2007.

[114] A. F. Yegulalp, "Fast backprojection algorithm for synthetic aperture radar," in *Proceedings of the 1999 IEEE Radar Conference. Radar into the Next Millennium (Cat. No.99CH36249)*, 1999, pp. 60–65.

[115] M. I. Duersch, *Backprojection for synthetic aperture radar*. Brigham Young University, 2013.

[116] T. Bollian, B. Osmanoglu, R. F. Rincon, S.-K. Lee, and T. E. Fatoyinbo, "Detection and geolocation of P-band radio frequency interference using EcoSAR," *IEEE Journal of Selected Topics in Applied Earth Observations and Remote Sensing*, vol. 11, no. 10, pp. 3608–3616, 2018.

[117] R. F. Rincon, T. Fatoyinbo, K. J. Ranson, B. Osmanoglu, G. Sun, M. Deshpande, M. Perrine, C. D. Toit, Q. Bonds, J. Beck, and D. Lu, "The ecosystems SAR (EcoSAR) an airborne P-band polarimetric InSAR for the measurement of vegetation structure, biomass and permafrost," in *2014 IEEE Radar Conference*, May 2014, pp. 1443–1445.

[118] R. F. Rincon, T. Fatoyinbo, B. Osmanoglu, S. Lee, K. J. Ranson, G. Sun, M. Perrine, and C. D. Toit, "EcoSAR: P-band digital beamforming polarimetric and single pass interferometric SAR," in *2015 IEEE Radar Conference (RadarCon)*, May 2015, pp. 0699–0703.

[119] B. Osmanoglu, R. Rincon, S. Lee, T. Bollian, and T. Fatoyinbo, "Forest structure retrieval from EcoSAR P-band single-pass interferometry," in *2017 IEEE International Geoscience and Remote Sensing Symposium (IGARSS)*, July 2017, pp. 4296–4305.

[120] P. C. Dubois-Fernandez, T. L. Toan, S. Daniel, H. Oriot, J. Chave, L. Blanc, L. Villard, M. W. J. Davidson, and M. Petit, "The TropiSAR airborne campaign in French Guiana: Objectives, description, and observed temporal behavior of the backscatter signal," *IEEE Transactions on Geoscience and Remote Sensing*, vol. 50, no. 8, pp. 3228–3241, Aug 2012.

[121] G. Krieger, N. Gebert, and A. Moreira, "Multidimensional waveform encoding: A new digital beamforming technique for synthetic aperture radar remote sensing," *IEEE Transactions on Geoscience and Remote Sensing*, vol. 46, no. 1, pp. 31–46, Jan 2008.

[122] T. Bollian, M. Younis, and G. Krieger, "TO BE SUBMITTED - digital beamforming based RFI extraction for an on-ground correction of spaceborne SAR data," *IEEE Journal of Selected Topics in Applied Earth Observations and Remote Sensing*.

[123] M. I. Skolnik, "Radar handbook," 1970.

[124] T. L. Lai, H. Robbins, and C. Z. Wei, "Strong consistency of least squares estimates in multiple regression," *Proceedings of the National Academy of Sciences of the United States of America*, vol. 75, no. 7, p. 3034, 1978.

[125] R. Steele and F. Benjamin, "Sample reduction and subsequent adaptive interpolation of speech signals," *Bell Labs Technical Journal*, vol. 62, no. 6, pp. 1365–1398, 1983.

[126] A. Janssen, R. Veldhuis, and L. Vries, "Adaptive interpolation of discrete-time signals that can be modeled as autoregressive processes," *IEEE Transactions on Acoustics, Speech, and Signal Processing*, vol. 34, no. 2, pp. 317–330, 1986.

[127] S. V. Vaseghi and P. J. Rayner, "A new application of adaptive filters for restoration of archived gramophone recordings," in *Acoustics, Speech, and Signal Pro-*

cessing, 1988. ICASSP-88., 1988 International Conference on. IEEE, 1988, pp. 2548–2551.

[128] S. Godsill, P. Rayner, and O. Cappé, "Digital audio restoration," in *Applications of digital signal processing to audio and acoustics*. Springer, 2002, pp. 133–194.

[129] J. P. Burg, "Maximum entropy spectral analysis," in *37th Annual International Meeting, Soc. of Explor. Geophys., Oklahoma City, Okla., Oct. 31, 1967*, 1967.

[130] R. Shibata, "Selection of the order of an autoregressive model by Akaike's information criterion," *Biometrika*, vol. 63, no. 1, pp. 117–126, 1976.

[131] M. B. Priestley, "Spectral analysis and time series," 1981.

[132] M. De Hoon, T. Van der Hagen, H. Schoonewelle, and H. Van Dam, "Why Yule-Walker should not be used for autoregressive modelling," *Annals of nuclear energy*, vol. 23, no. 15, pp. 1219–1228, 1996.

[133] C. Collomb, "Burg's method, algorithm and recursion," *K. Elissa, unpublished*, 2010.

[134] G. Krieger, M. Zonno, M. Rodriguez-Cassola, P. Lopez-Dekker, J. Mittermayer, M. Younis, S. Huber, M. Villano, F. Q. de Almeida, P. Prats-Iraola, and A. Moreira, "MirrorSAR: A fractionated space radar for bistatic, multistatic and high-resolution wide-swath SAR imaging," in *2017 IEEE International Geoscience and Remote Sensing Symposium (IGARSS)*, July 2017, pp. 149–152.

[135] F. Gatelli, A. M. Guamieri, F. Parizzi, P. Pasquali, C. Prati, and F. Rocca, "The wavenumber shift in SAR interferometry," *IEEE Transactions on Geoscience and Remote Sensing*, vol. 32, no. 4, pp. 855–865, July 1994.

[136] M. Cherniakov, R. Saini, R. Zuo, and M. Antoniou, "Space-surface bistatic synthetic aperture radar with global navigation satellite system transmitter of opportunity-experimental results," *IET Radar, Sonar & Navigation*, vol. 1, no. 6, pp. 447–458, 2007.

[137] C. Sturm, E. Pancera, T. Zwick, and W. Wiesbeck, "A novel approach to OFDM radar processing," in *2009 IEEE Radar Conference*. IEEE, 2009, pp. 1–4.

[138] C. Sturm, T. Zwick, and W. Wiesbeck, "An OFDM system concept for joint radar and communications operations," in *VTC Spring 2009-IEEE 69th Vehicular Technology Conference*. IEEE, 2009, pp. 1–5.

[139] D. S. Garmatyuk, "Simulated imaging performance of UWB SAR based on OFDM," in *2006 IEEE International Conference on Ultra-Wideband*. IEEE, 2006, pp. 237–242.

[140] W. Wiesbeck and L. Sit, "Radar 2020: The future of radar systems," in *2014 International Radar Conference*. IEEE, 2014, pp. 1–6.

[141] M. Younis, P. Lopez-Dekker, and G. Krieger, "Signal and noise considerations in multi-channel SAR," in *2015 16th International Radar Symposium (IRS)*, June 2015, pp. 434–439.